THE UNIVERSITY *of* EDINBURGH

Development of high pressure and cryogenic techniques, and their application to neutron diffraction

Christopher J Ridley

THE UNIVERSITY *of* EDINBURGH

Doctor of Philosophy
The University of Edinburgh
June 2017

Lay Summary

Temperature can cause considerable changes to the physical properties of a material, such as altering optical, mechanical, electrical, and magnetic behaviour. Familiar examples include the freezing/melting of water ice, or the need to reach low temperatures to allow certain materials to conduct electricity without resistance. Similarly, pressure is another tool which can be used to alter the behaviour of a material. For example, the structure of a material may change when all the atoms are compressed closer together. Using both temperature and pressure together can lead to a wealth of new exotic properties, aiding our understanding of materials.

The main challenge is in obtaining useful measurements of the sample in these circumstances, since it must be enclosed in a chamber or cell to be pressurised. One technique uses the principle of diffraction to measure how the structure of a material changes. The main work of this thesis has been in developing a new cell to enable high pressure, low temperature neutron diffraction to be performed over a wider range of pressures/temperatures than currently available. Small samples are easier to contain to higher pressures, but also limit the quality of the measurements achievable with some techniques. This project has performed extensive research into techniques to improve the quality of data from extremely small sample (less than $1\,\mathrm{mm}^3$).

Diffraction measurements can provide useful data on material structure, but must sometimes be used alongside other measurements to fully understand certain properties. Where data is compared between different measurements, there is always uncertainty whether the sample is under exactly the same conditions. This thesis presents a cell capable of performing simultaneous diffraction and electrical measurements, removing this source of uncertainty. Aside from developing new equipment, several short studies are presented to demonstrate the information obtainable using pressure and temperature as variables.

Abstract

Neutron diffraction is an extremely powerful technique in condensed matter research; it can be used to measure crystallographic structures, including some of those undeterminable using X-rays. It is also perhaps the most powerful technique for determining magnetic structures, and for probing the strength of magnetic interactions, revealing information beyond that extractable from a magnetometer. High pressure is used by many condensed matter researchers as an additional thermodynamic variable, or tool to perturb otherwise stable systems, and has been used with neutron diffraction for many years. When coupled with low temperatures, this has led to the discovery of an enormous range of non-ambient phases of matter, with a range of exotic properties, some of which are discussed in this thesis. Pressure has a very strong effect on the magnetic properties of a material, with many of the most unusual magnetic phases existing only at extremely low temperatures, or pressures which can only be reached on very small samples. The main topic for this thesis is the study, development, and implementation of new techniques to combine low temperatures, high pressures, and neutron diffraction measurements from micro sized samples.

A new pressure cell has been designed, tested, and commissioned with neutron beam time on the WISH diffractometer at the ISIS neutron facility. The cell is compact, with a total mass of approximately 5 kg, and is capable of generating large loads in excess of 4.5 tonnes force. Depending on the sample size used with the cell, the opposed anvil system is capable of generating a range of different pressures beyond what is widely available for low temperature neutron diffraction measurements. To save wasted experimental time in cooling and warming the device, the cell is capable of varying the applied load continuously down to 5 K, whilst the sample pressure can also be measured in-situ using a compact spectrometer system. Obtaining refineable neutron diffraction data from the small samples ($< 1\,\mathrm{mm}^3$) possible in an opposed anvil pressure cell is challenging

due to extremely low ratios of signal-to-background when compared with large volume pressure cells. Finite element analysis (FEA) was performed to minimise the mass of the cell, whilst also minimising the amount of supporting material in the beam. Despite this, the signal from the sample is typically very weak; to overcome this, a novel 3D printed device has been designed and tested to collimate extremely small samples, removing much of the background signal from the surrounding material. It has enabled neutron data to be collected from samples an order of magnitude smaller than previously measurable in the cell. To maximise the pressures achievable in the pressure cell, for a given sample volume, an extended FEA study was performed to understand the evolutions of stresses in the cell, and understand the limitations of using sapphire as an anvil material.

To complement this work, a compact piston cylinder cell has also been designed for a combination of different measurements. One of the key challenges in high pressure research is in knowing, or ensuring, that the conditions the sample is under are approximately the same for a variety of different measurements. Since different instruments, and techniques, may not allow for the same apparatus to be used between them, this is not always possible. A compact clamped piston cylinder cell has been designed, suitable for in-situ electrical measurements, with additional potential for simultaneous neutron diffraction measurements. The device is demonstrated through an ultrasonic characterisation of the compound UGe_2.

In addition to the information obtainable from neutron diffraction, much can be learnt from studying the transport properties of a material. This information can be used alongside neutron data to provide a full understanding of how a material behaves. One technique of interest measures how the electrical properties of a material changes under applied magnetic field. This is difficult to achieve under pressure due to the often anisotropic construction of the pressure cell affecting the magnetic field on the sample in different orientations, and the challenge in getting wires to the sample under pressure. This thesis presents the design, and preliminary testing, of an ultra compact high symmetry piston cylinder cell designed to be taken to sub-Kelvin temperatures and rotationally oriented in applied magnetic field. The spherical construction of the cell means that the field on the sample position is, to a very close approximation, identical in all orientations.

Finally, this thesis presents a study of the binary alloy Pd_3Fe under pressure. Pd_3Fe was recently reported to undergo a large-volume collapse under high

pressure at room temperature, resulting in near zero thermal expansion [1]. There are several competing theories on the mechanism behind this process. To investigate further, a series of single crystal Pd_3Fe samples were grown, cut, prepared, and extensively analysed. The results of this study suggest that the cause for the large volume collapse may not be magnetic in nature, as previously expected.

Declaration

I declare that this thesis has been composed by myself and that it has not been submitted, in whole or in part, in any previous application for any degree or professional qualification. Except where otherwise acknowledged, the work presented is entirely my own.

Parts of this work have been published in [2–6].

(*Christopher J Ridley, June 2017*)

Acknowledgements

The work presented in this thesis would not have been possible if it weren't for the help and support of many people. I would like to thank Konstantin Kamenev for supervising me on this project; our discussions together, and his input have been essential to helping me achieve during this project. His ability to find the best aspects of sometimes bad situations has been incredibly motivating.

I would also like to thank Oleg Kirichek for supervising me during my time at the ISIS neutron facility, his willingness to share his experiences in developing sample environment for neutron experiments was very helpful in helping this project achieve its goals. Oleg seems to have an interesting story applicable to any situation, which has improved my morale even when at its lowest.

Thank you also to Matt Jacobsen, whose support early in my PhD helped define my project, and taught me many important aspects of becoming a researcher. I am also grateful to all my colleagues in the Centre for Science at Extreme Conditions for their kindness and support, and many hours of entertainment. I am particularly grateful to the other members of the Kamenev group; Xiao Wang, and Juan Carlos Fallas for fruitful discussions regarding finite element analysis, and Christopher Woodall for his collaboration on many projects.

I am also indebted to many from other research groups in CSEC; Angel Arevalo Lopez and Graham McNally for their extensive collaboration performing high pressure neutron experiments, and the entire Huxley group for their assistance in growing, and characterising the Pd_3Fe crystals, particularly William Whitley, and Dmitry Sokolov. I also want to thank Michal Kepa for his extensive collaboration on multiple experiments in CSEC, and his support on occasions when everything needed rewiring late at night!

This PhD would have been empty without the support from the physics and engineering workshops. Particular thanks for Rob Louden, and Dave McCabe for their machining expertise, and entertaining conversations. They have both, on occasion, worked on timescales beyond what can be reasonably expected under any circumstances, thank you.

Pascal Manuel and Dmitry Khalyavin have been a great support to me during the many WISH experiments performed together. I truly appreciate the late nights,

and time they both invested to help me with these. I would also like to thank Craig Bull for his support performing various high pressure experiments, and for giving me the opportunity to work with him on PEARL for several months. I am grateful to the Cryogenics, and Pressure & Furnace technicians at ISIS, for there support and advice, even when they have many other tasks to deal with. I would particularly like to thank Colin French, and John Crawford, for their help with machining parts on short timescales.

I am most grateful to Yasmeen who has dealt with my long periods of absence for experiments, late nights, and focus on work for the full 4 years of my PhD. I am extremely lucky to have her love and support during both the good and the hard times, without which I wouldn't have got this far. Thank you also to my family, who have been a constant source of support and encouragement to me during this period.

Contents

List of Figures

List of Tables

Glossary

$\boldsymbol{\sigma_r}$, $\boldsymbol{\sigma_t}$, $\boldsymbol{\sigma_z}$	Radial, tangential and axial components of stress respectively
$\boldsymbol{\epsilon_r}$, $\boldsymbol{\epsilon_t}$, $\boldsymbol{\epsilon_z}$	Radial, tangential and axial components of strain respectively
$\boldsymbol{\sigma_1}$, $\boldsymbol{\sigma_2}$, $\boldsymbol{\sigma_3}$	Maximum, middle and minimum principal stresses respectively
$\boldsymbol{\epsilon_1}$, $\boldsymbol{\epsilon_2}$, $\boldsymbol{\epsilon_3}$	Maximum, middle and minimum principal strains respectively
$\boldsymbol{\sigma_x}$, $\boldsymbol{\sigma_y}$, $\boldsymbol{\sigma_z}$	x, y, and z components of stress
$\boldsymbol{\sigma_{VM}}$	Von-Mises equivalent stress
$\boldsymbol{\sigma_{yield,\,y}}$	Yield stress
$\boldsymbol{E}$, $\boldsymbol{E_0}$	Elastic modulus (Young's modulus)
$\boldsymbol{E_{plastic}}$	Plastic modulus (tangent modulus)
$\boldsymbol{\mu}$	Poisson's ratio
$\boldsymbol{\tau}$	Shear stress
$\boldsymbol{\tau_{max}}$	Maximum shear stress
$\boldsymbol{\tau_{yield,\,y}}$	Shear yield stress
$\boldsymbol{\rho}$	Radius of plastically deformed region in thick cylinder
$\boldsymbol{\delta}$	Radial interference between two press fit cylinders
$\boldsymbol{f}$	Frictional force
$\boldsymbol{\mu}$	Static coefficient of friction, or relative permeability
$\boldsymbol{\varnothing}$	Diameter
$\boldsymbol{\mu_B}$	Bohr magneton, unit of magnetic moment (SI $9.274 \times 10^{-24}\,\mathrm{J\,T^{-1}}$)
$\boldsymbol{\mu_r}$	Relative permeability
$\boldsymbol{\mu_0}$	Permeability of free space

M_s	Saturated magnetic moment
M	Magnetic moment
H	Applied magnetic field
T_c	Curie temperature
T_s	Superconducting transition temperature
χ	Magnetic susceptibility
γ	Curie critical exponent
a	Inner radius of cylinder
b	Outer radius of cylinder
c	Radius of interference fit in compound cylinder
u	Radial displacement in Lamé formulation
ϕ_s	Sample diameter
ϕ_c	Culet diameter
ϕ_g	Gasket diameter
t_0	Unindented gasket thickness
t_{max}	Maximum stable thickness
t	Indented gasket thickness
θ	Angle of cylindrical element in Lamé formulation
	& half cone angle in massive support analysis
b, $\bar{b}$	Scattering length, and average over system respectively
σ_{coh}	Coherent scattering cross-section
σ_{inc}	Incoherent scattering cross-section
$\vec{Q}$	Scattering vector
Q	Diffraction momentum transfer (magnitude of scattering vector)
B_0	Bulk modulus
B'	Pressure derivative of bulk modulus
λ	Wavelength, or thermal conductivity coefficient
C_p	Specific heat (isobaric)

Chapter 1

Introduction

1.1 Motivation

Temperature and pressure are powerful tools to extend our understanding of materials. Varying them causes variations in the physical structure, mechanical behaviour, transport properties, and magnetic properties of a material, revealing a wealth of information which is otherwise inaccessible [12, 13]. It is currently possible to generate static pressures exceeding 750 GPa [14], and to reach temperatures as low as 250 pK [15], though taking measurements at either, and particularly at both conditions, is highly limited. This thesis aims to address how to start to overcome these limitations; the benefits of this work will be motivated here.

There is a variety of apparatus available for reaching low temperatures, but for the generation of sizeable pressures, there is one commonly used instrument, the diamond anvil cell (DAC) [16]. This generates pressure through compressing the sample between two flat surfaces on a pair of gem diamonds, whilst the sample is contained using a gasket to prevent extrusion. This technique is widespread due to its deceptive simplicity, however the mechanics of the cell are complex [17], such that few users have a full understanding.

Measurement techniques possible with a DAC include Raman spectroscopy, resistivity, susceptibility, and X-ray diffraction among others. The important comparison to be drawn is that, whilst it might reduce error on the data, the sample is not required to be particularly large. An enormous amount of data

may be obtained using these techniques, but limitations on sample size preclude the measurement of an even greater amount of information. The most in demand of these measurements are those obtained using neutron diffraction, which has distinct benefits over X-ray diffraction in certain cases [18]. The charge neutrality of neutrons enables them to penetrate deeply into the bulk of a material, unlike X-rays which are more limited to surface studies. This property has enabled the use of larger alternative pressure devices to reach moderate pressures, though the pressure range remains limited by the much larger forces required, and upper limits on the size of the cell. Larger cells also limit the use of low temperatures, as the increase in mass requires more cooling power. This means that the time required to cool the sample may increase exponentially [19], whilst base temperature may never be reached. This thesis presents and overview of these technical difficulties, and the design of a novel pressure device for cryogenic neutron diffraction under pressure.

The main objective of most scientific studies is not to reach the highest pressures at the lowest temperatures, but is to measure sufficient data to thoroughly understand what is happening to a material in these conditions. Neutron diffraction is a very powerful measurement technique, but not all samples are well suited to it due to the weakness of their interaction with neutrons, whilst there is plenty of information which cannot be provided by neutrons. For example, a study of a superconducting material may be interested in the electrical transport properties and the electronic band structure. A variety of resistivity measurements, often using magnetic fields to probe the system, or ultrasound excitation techniques to probe the Fermi surface of a metallic sample can be used to understand how the electrons in a material interact with the atomic structure [20]. Whilst attaching wires to a sample in a DAC is possible, it is challenging to obtain reliable and repeatable data. This thesis presents the design of two more reliable pressure devices suitable for these measurement techniques at lower pressures.

The study of materials under pressure directly benefits our understanding of how they behave under ambient conditions, which consequently leads to improved technology using these materials. An example of this is the family of materials which exhibit the Invar behaviour, zero thermal expansion over a given temperature range. These materials are particularly important to engineers, for use in situations where large thermal changes in dimensions can lead to structural problems. It was recently reported that the material Pd_3Fe displays Invar

behaviour under pressure [1], presenting an opportunity to tune the onset of the behaviour using external parameters, in a material other than Fe-Ni alloys. This thesis presents additional studies into this behaviour using neutron diffraction.

1.2 Neutron diffraction

Neutron diffraction uses the wave-like nature of neutrons to investigate periodic structures, such as an atomic lattice. It is well known that in order for a wave to diffract strongly through a gap or slit, the size of the gap must be comparable or smaller than the wavelength of the wave. In order to achieve this on the atomic scale this means that the wavelength must be of the order 1-10 Å. These wavelengths may be achieved in the electromagnetic spectrum using X-rays, but also coincide with the wavelength of medium to low energy neutrons. Both neutrons and X-rays can be used to provide similar information about a material, but can also provide complementary information due to the nature of their interaction with matter. One key advantage of neutrons is their sensitivity to isotopic content, which cannot be distinguished via X-rays.

1.3 Pressure devices

The use of pressure in crystallographic studies pre-dates the development of the DAC by almost 30 years [21, 22]. This period showed an enormous advance in the development of high pressure instrumentation, including the first synthetic growth of diamond itself, which itself opened a new branch of accessible chemical syntheses [23]. The DAC is now the most commonly used pressure device due to the pressure range it offers, its compactness, and relatively safe operation. However, the advantages of the DAC for certain measurements are disadvantages for others, such that a review of previously developed devices remains useful for further development. There are three broad classes of pressure cell, each containing variations along a common theme; gas cells, piston-in-cylinder cells, and opposed anvil cells.

The gas cell applies pressure to a sample in a sealed vessel through exposure to a pressurised gas medium. This class of cell is limited in pressure ($P_{max} \approx 0.3\,\mathrm{GPa}$) by the dangers involved in working with large volumes of highly compressed

gas, the difficulties involved in sealing the gas, and the mechanical strength of the vessel used. These cells may be used with large sample volumes ($V_{max} > 1000\,\mathrm{mm}^3$), and the pressure may be controlled with great precision using modern compressors.

The piston-in-cylinder class of cells generate pressure through compressing the sample, surrounded by a compressible liquid medium which is easier to seal than gaseous medium, in a cylindrical vessel using a hard piston (such as tungsten carbide). These devices are typically much safer to operate than gas cells, with the pressure fluid contained entirely in the cell, and can reach much greater pressures. However, cylinder strength limitations mean that these cells are limited to smaller sample volumes at these greater pressures. Piston-in-cylinder cells also don't have the continuous pressure control available with gas cells.

Opposed anvil cells compress the sample and surrounding pressure medium between two hard anvils. These may be made from naturally hard gemstones, or composite materials such as tungsten carbide. To achieve the most uniform pressures on the sample, it must be contained in a gasket, and surrounded with a compressible pressure medium. The anvils then deform the gasket material, which supports the sample volume, pressurising it whilst also containing it between the anvils. These devices can generate pressures many times greater than the measured yield strengths of both the gasket and the anvil material, due to the principle of massive support. The level of support provided is determined by several critical dimensions of the system. Whilst support in the system is essential, more support requires larger applied loads to reach a given pressure. Much of the work of this thesis will be in understanding this effect, in order to maximise its efficiency.

1.4 Computer aided design and finite element modelling

Difficulties in machining traditionally meant that metallic parts with a complex geometry would need to be die-cast, a technique which is costly for small scale production. Improvements in machining techniques, and the development of increasingly mechanised equipment (such as multi-axis mills), means that this is no longer always the case. Furthermore, the more recent revolution of 3-

dimensional printing means that it is possible to print complex parts from metals and plastics, to a precision approaching that achievable through manual machining, but in a fraction of the time, with fewer geometric constraints.

Computer aided design (CAD) allows designers to construct parts virtually, and then set the structure to draft digitally, significantly reducing the difficulties in visualising complex geometries ćiteMedland2012. A knowledge of how the parts will be machined is still essential, imposing limitations on the type of features that may be included in the models. Digital models of the parts are also compatible with other modelling software, which can be used to understand the structural behaviour of the part when placed under external forces. For example, the development of a piston-in-cylinder pressure cell may be interested in how the stresses grow in the wall of the cylinder as the pressure is increased, in order to optimise the thickness of the wall. Finite element analysis (FEA) provides a tool for the numerical determination of full stress-strain tensors at any point in the model, at any applied pressure. It achieves this through splitting the model up into a series of smaller elements, a process called 'meshing' [24]. Material data, loads, and constraints must then be placed on the model before it can then be 'solved'. The solver finds approximate solutions to a series of linear and partial differential equations prescribed by the conservation laws used in continuum mechanics.

Further detail of how the solution is arrived at is superfluous to the needs of this thesis, but it must be understood that the solutions are only ever an approximation, and will contain errors and misleading results. For this reason careful comparison of the results is needed with theory, and experiment. Despite these limitations FEA is a powerful tool for engineers. The use of FEA in the design of scientific apparatus has been demonstrated elsewhere, but it is still a relatively underused tool. The work shown in this thesis uses FEA extensively, to optimise systems to fit tight design parameters.

1.5 Thesis layout

This thesis is split into two parts. Part I (chapters 3 to 6) is focussed on the development of high pressure techniques for, or motivated by, neutron diffraction studies. Part II (chapters 7 and 8) is more concerned with the magnetic characterisation of two materials of interest. Whilst this includes some neutron

diffraction characterisation, it is not focussed on the development of high pressure techniques for neutron diffraction. Otherwise, the chapters are structured as below.

Chapter 2 both introduces the fundamental principals of, and provides an in depth review of previously reported research, in several areas relevant to the techniques used in the work of this thesis. Existing instrumentation for achieving high pressures at low temperatures, and variants for incorporating diffraction measurements, are discussed, and key design challenges are identified. The technique of finite element analysis is reviewed in the context of pressure cell design.

Chapter 3 presents the design of a load cell for opposed-anvil high pressure neutron diffraction measurements. The geometry, mechanism, and overall mass of the cell was optimised using finite element analysis to fulfil several key criteria. The cell uses gas pressure, contained in an actuating single unit (or 'bellows'), to generate 45 kN using standard 200 bar bottle pressure. The maximum extension of the unit is approximately 1.5 mm. If used with a pressure intensifying unit the cell is capable of generating 100 kN without further adaptation. The compact design of the cell ($M_{total} \approx 3.5$ kg) allows it to be cooled using conventional closed cycle refrigerators (T_{base}=5 K) and cryostats (T_{base}=2 K), and large bore dilution refrigerators (T_{base}=600 mK). As the load is controlled using helium gas, it can be continuously monitored, and varied over the full temperature range of the cell without needing to warm the cell back to room temperature. The cell was designed to house a variety of different anvil materials: WC, sapphire and diamond anvils have been tested in the cell.

Chapter 4 considers the mechanics of pressure generation within a gasket compressed between two anvils. As the total sample volume is a critical parameter for neutron diffraction measurements, finite element analyses were performed in order to understand and optimise the pressure achievable with a given sample volume. The simulations provided insight into the stresses developed within the anvils and gasket, and were used to determine the most robust anvil design for use in the cryogenic load cell presented in Chapter 3.

Chapter 5 presents the design of a compact collimator designed to be attached directly to the load cell presented in Chapter 3. Collimation is used to reduce diffraction contributions from sources other than the sample. Selective laser sintering (or '3D printing') allowed for the geometry of the collimator to be

miniaturised and fully customised to meet the requirements of the cell, leading to a significant reduction in the background signal from the cell. The parameters involved in the design of the collimator were optimised through the use of multiple simulations. Monte-Carlo ray tracing was used to simulate the effect of introducing a collimator so close to the sample, and classical ray-tracing simulations were used to estimate the optical profile of the collimator.

Chapter 6 covers the development and testing of a clamped piston-cylinder cell for low temperature neutron diffraction. The cell was originally developed at the Institut Laue Langevin, and was subsequently adapted at the University of Edinburgh to incorporate a simpler sealing mechanism, and a reliable mechanism to introduce wires to the pressurised sample volume. This was done primarily to allow the pressure to be measured continuously over the full temperature range of operation, though the inclusion of additional electrical connections allows for other measurements on the sample which could be combined with neutron diffraction or inelastic scattering data. To show the potential for simultaneous measurements the cell was used to perform ultrasonic measurements of the unconventional superconductor UGe_2.

Chapter 7 presents the design of a spherical pressure vessel designed to rotated in high magnetic fields, at sub-Kelvin temperatures.

Chapter 8 outlines an investigation into the high pressure magnetic behaviour of the binary alloy Pd_3Fe. Large crystals of the material were grown using the Czochralski technique, and characterised using SQUID magnetometry, X-ray Laue, powder X-ray diffraction and X-ray fluorescence to verify the structure and composition of the sample. High pressure single crystal data was collected on the WISH diffractometer at room temperature, and high pressure room temperature powder data was collected on the PEARL diffractometer at the ISIS muon and neutron facility.

Chapter 9 summarises the work reported in, and highlights significant outcomes of this thesis.

Chapter 10 discusses potential future applications of high pressure to neutron diffraction, and further developments in high pressure technology.

Chapter 2

Literature Review

A review of existing pressure cell designs is given; fundamental principles, design concepts, material properties, and low temperature design considerations are discussed. The basic principles of diffraction are outlined, and the applicability of existing high pressure cells is critiqued, highlighting the need for a careful balance of material properties for optimal performance. This thesis has developed several new pressure devices for different purposes. As FEA is used extensively in the design stage a review of FEA techniques and similar previous studies is presented. Background and theory regarding the properties of Invar alloys is introduced.

2.1 High pressure instrumentation

2.1.1 Motivation

Hydrostatic pressure is a thermodynamic variable which can be measured and controlled to partially determine the equilibrium state of a material. This can be used with other variables such as temperature, volume, and chemical composition, to fully define the state of the system. These variables are macroscopic, and are often inter-dependent, but influence the microscopic character of the material too, possibly leading to structural changes, or magnetic transitions, which can lead to new macroscopic properties. Pressure is therefore a broad but powerful tool for tuning the properties of a material or substance, understanding its properties and process of formation, and forming unique and otherwise unseen phases. Aside

from a useful scientific tool, high pressure has many commercial and industrial applications ranging from synthesising diamonds (typically for abrasive purposes), to 'pascalisation' the pressure treatment of food stuffs to deactivate bacteria, and preserve goods.

2.1.2 Pressure cell classification

The range equipment used to generate pressures is reflective of the diversity of its applications. The suitability of a design for a particular application is largely determined through specifying the required sample volume. Large samples are more difficult to contain at high pressures than smaller samples; this restriction will be further discussed in this section. Pressure cells can generally be categorised to belong to one of three main classes. The main design and operating principles of each of these classes, and examples are discussed here.

Externally pressurised fluid cell

This class of cell applies pressure to an enclosed sample through applying an externally pressurised fluid medium, which may be gaseous or a compressible liquid such as methanol/ethanol or light mineral oils. The sample may be enclosed in either a capillary or in a cylindrical vessel with much thicker walls which are able to withstand much larger pressures but may be less preferable depending on the measurement technique. The pressure range for capillary cells is typically $10 - 50\,\mathrm{MPa}$, but may reach significantly higher pressures of $\approx 0.7\,\mathrm{GPa}$ where thicker cylinders are used. The samples may be solid, mounted in the cell prior to introduction of the pressure medium, or may be the pressure medium itself; helium, for example, has a rich P-T phase diagram but remains hydrostatic up to approximately 40 GPa. Choosing an appropriate pressure medium is discussed further in 2.1.3.

Since the pressure medium, or sample, is pressurised externally to the cell, this class of cell offers unrivalled control over the pressure; commercially available compressors may offer precision better than 0.1 %. This may be essential if a the sample is extremely delicate, and poorly suited to large sudden changes in pressure, or for characterising very rich P-T phase diagrams, where high resolution is needed. The sample volume for these systems is large, $\approx 1000\,\mathrm{mm}^3$, making it preferable for industrial applications, or for studies where a large amount of

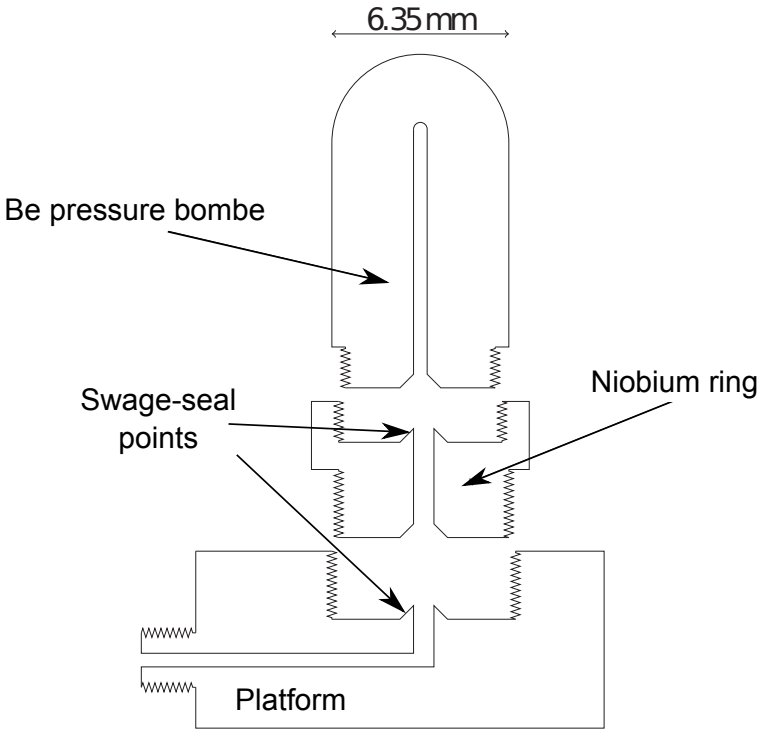

Figure 2.1 *Cell developed by Morosin and Schirber [25] for low pressure, low temperature X-ray studies.*

sample is needed to improve data quality. However there are safety concerns with externally pressurised pressure cells. Compressing large volumes of pressure medium stores a significant amount of energy. If the system leaks at a connection point, or if the compressor is not properly maintained, then this energy can be released suddenly and dangerously. It is particularly difficult to seal high pressure gases such as helium or hydrogen due to their high compressibility, and in the case of hydrogen its ability to permeate many materials. As many of these media are also flammable such as ethanol or hydrogen, these cells can be very dangerous to operate.

Capillary cells are optimal for measurements where the sample needs to be highly visible, either optically or to X-rays or neutrons, since the ratio of sample to background material can be high. One example is the beryllium pressure bombe (see figure 2.1) [25], designed for single crystal X-ray diffraction studies up to 0.4 GPa at 80 K. The system is relatively easy to load and operate; the beryllium container is loaded with kerosene (or an alternative pressure medium) and the sample, and then attached to the pressurising platform. The kerosene line is then pressurised externally with a compressor. The shape of the beryllium piece is such as to reduce stresses at the end of the cylinder, whilst also maintaining

a uniform thickness. This is important for accurate intensity corrections in the diffraction data. The design is also adapted to account for the brittle nature of Be at low temperatures, through using Nb ring, allowing the cell to be removed cold without risk of thread failure. The system is sealed through swaging the various components together at conical joints through applying torque to the threads. This deforms a small protruding conical section against the countersunk conical section on the mating part. The mismatch in the thermal expansion properties of the the materials used here may cause the swaged fittings to leak at very low temperatures, however, no issues were reported down to liquid nitrogen temepratures.

Piston-cylinder cell

Piston-cylinder cells are the most widely used pressure cell for achieving moderate pressures ($1 - 4\,\mathrm{GPa}$) on smaller sample volumes ($200 - 500\,\mathrm{mm}^3$). The sample volume is limited by the length of the cell, and the relative volume reduction required to generate the desired pressure; this is not the case for gas cells where the pressure medium is compressed externally. The sample is contained inside a cylinder, and surrounded by liquid or solid pressure medium, which is then isothermally compressed with a piston using an external hydraulic press. The piston may then be locked in position, such that the pressure cell is then entirely self contained. Reaching high pressures is limited by large stresses in the wall of the cylinder as the load is increased. There are various design techniques which can extend the range, which may also be applied to externally pressurised pressure cells, these are discussed in section 2.1.5 (p18).

A variant of the piston-cylinder cell is the belt type press, first used to synthesise diamonds for General Electric [26]. This was developed since it was observed that even tungsten carbide pistons failed at the point where they were no longer supported by the bore of the cylinder, the belt press evolved to use a short truncated piston design, itself supported by press fit surrounding cylinders. The belt press also altered the design of the cylinder of the cell. Instead of a straight bore, a conical bore made from tungsten carbide is adopted, which is then supported with binding rings of steel. This design allows the piston to be increasingly supported by the cylinder, and visa-versa as the piston is advanced further. The conical shape of the bore also allows much greater pressures ($10 - 15\,\mathrm{GPa}$) to be sustained by the cylinder prior to failure using the principle

of 'massive support' [27]. This is discussed in depth in section 2.1.5 (p24). The achievable pressures were increased from simple piston-cylinder cells by drastically reducing the initial sample volume, and consequently the required travel of the piston. Although this system was originally developed some time ago, it is still commercially significant, used for mass synthesis of diamond grit, and continues to be developed for other measurements [28, 29].

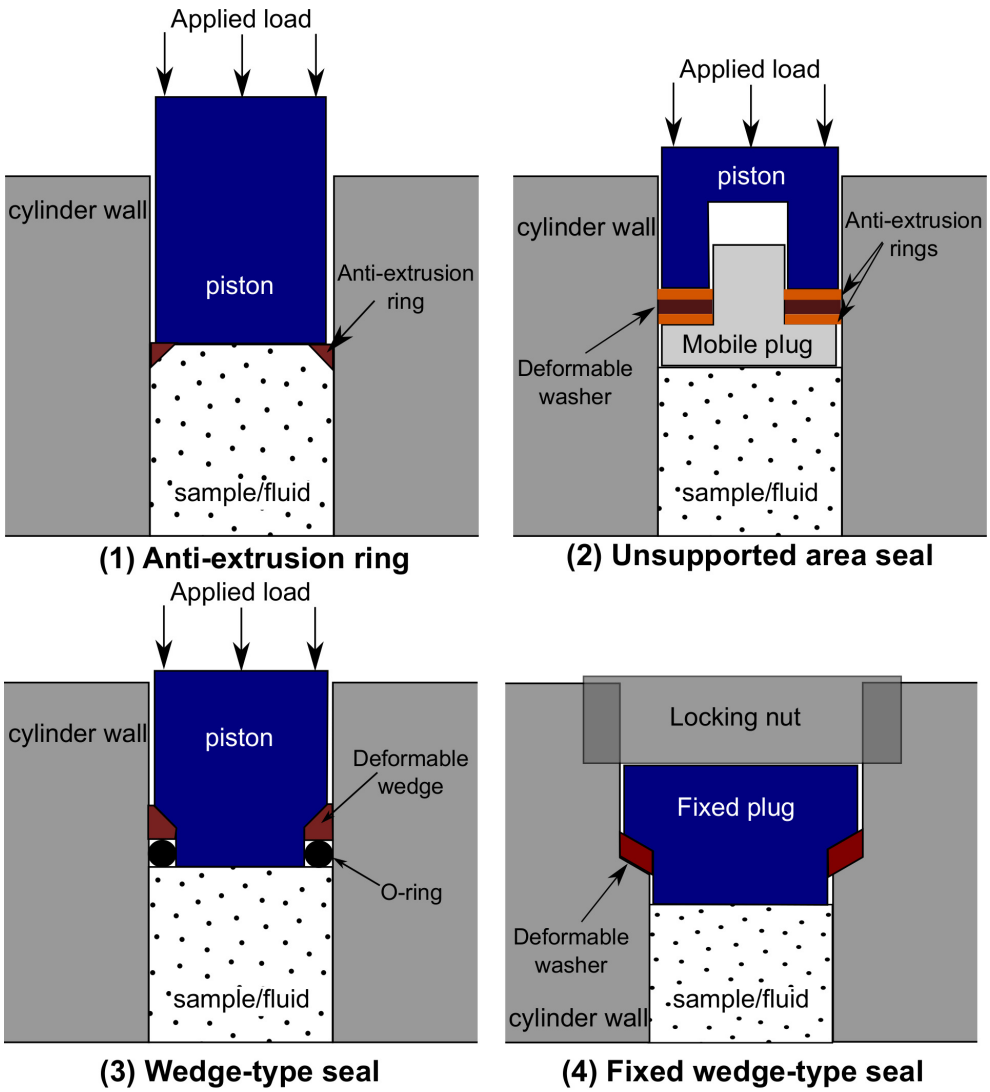

Figure 2.2 *Illustrating different commonly used seal types. All work on the concept that the pressure in the seal should remain larger than that in the sample region.*

A major disadvantage of piston-cylinder cells over externally pressurised fluid cells is that the pressure cannot be continuously controlled, or applied with the same level of precision due to the high loads involved, and the effects of friction between the piston and the cylinder wall. In cases where the cell is not physically accessible during measurements, such as with experiments involving extreme temperatures

where the cell may be inside a furnace or refrigerator, this can make measurements at multiple pressure points very time consuming. In addition, as the temperature of the cell is changed the pressure in the cell will differ from that set at room temperature. Temperature effects are further discussed in section 2.1.6 (p25).

One of the main challenges in designing a pressure cell is successfully sealing the pressure medium in the cylinder to high pressures, often over a broad temperature range. Whilst liquids and solids are easier to seal in the cylinder (due to a higher bulk modulus), maintaining a seal whilst allowing the piston to continue compressing the pressure medium is challenging. There are several seal designs for achieving this, though all seals work on the principle that the pressure in the seal should remain larger than that in the sample volume to maintain the sample pressure (see figure 2.2). **(1)** Anti-extrusion ring. **(2)** Unsupported area seal. **(3)** Wedge-type seal. **(4)** Fixed wedge-type seal (where motion isn't required). The belt type variant uses an alternative 'gasket' sealing system which is discussed further in the following section. Types **(1-3)** are used where the seal is required to move with the piston. The load applied to the piston concentrates the generated pressure at the seals in each case. This prevents the sample from extruding around the seal.

An example of a piston cylinder cell is presented by Zimmermann et al. [30] (see figure 2.3), designed for high energy X-ray diffraction up to 3 GPa at $\approx$ 10 K. Initially the base of the cell is sealed via a locking nut, the sample is then loaded into the cylinder, the seals are then inserted with the piston which is then pushed to be hand tight using the top locking nut. High pressures are then generated using an external press, and gradually tightening the locking nut.

Opposed anvil cell

Opposed anvil cells can generate significantly greater static pressures $5-200$ GPa (and upwards of 750 GPa in more complex variants [14]) depending on the size of the sample volume. The first opposed anvil system was designed by Percy Bridgman, decades prior to the invention of the belt system by the General Electric team [31–34]. Bridgman produced several different designs of opposed anvil cells, the most commonly referred to of which contains the sample between the faces (culets) of two conical anvils within a pyrophyllite gasket. Early gasket designs used a small disc of gasket material, located only between the central flats of the anvils (see figure 2.4). The advancing anvil crushes the deformable gasket

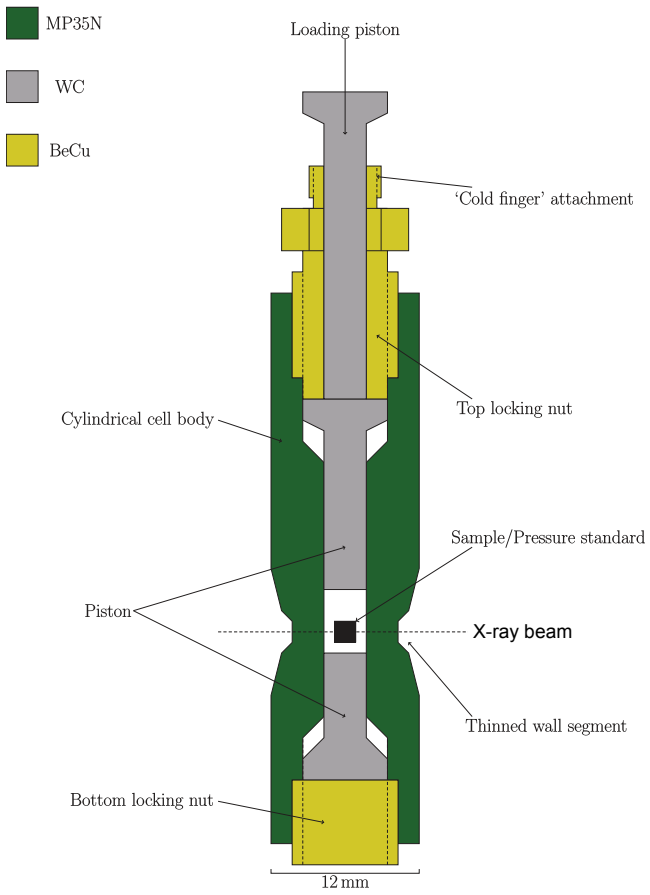

Figure 2.3 *Cell developed by Zimmermann et al. [30] for high energy, low temperature high energy X-ray studies to* 2.7 GPa

and sample; the sample pressure then increases as its volume is reduced. The gasket prevents extrusion of the sample from between the anvils due to contact friction with the flat surface of the anvil. Internal friction within the gasket (i.e its shear strength) prevents the sample from simply pushing the gasket apart. The same principles are used in the belt press which uses a deformable gasket to support the truncated piston and contain the sample at high pressures beyond the yield strength of the gasket material itself.

Another type of anvil cell, known as the Drickamer cell, allows for optical access to the sample through tightly packing NaCl pellets into a conical window to form a single transparent salt crystal. Despite the relatively soft window material, the long narrow holes they are formed in allow for pressures of 20 GPa to be generated without considerable extrusion of the NaCl [35].

To achieve higher still pressures the compressive strength of diamond is used. The earliest diamond anvil cell experiments placed the sample onto the culet of one of the diamonds, and then compressed it directly using the face of the other. Charles

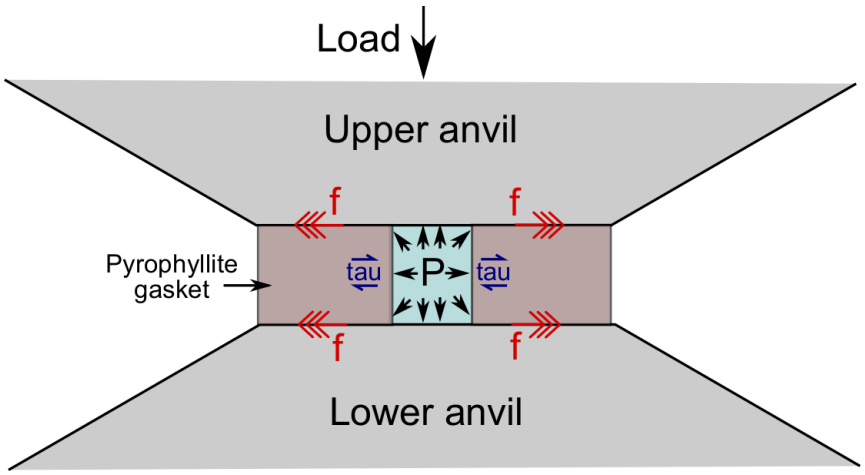

Figure 2.4 *Figure demonstrating the operation of a simple opposed anvil cell. f indicates friction between the gasket and the anvil, tau indicates the shear strength holding the sample pressure, P, within the gasket.*

Weir and Alvin van Valkenberg are both credited with the first use of single crystal diamond as an anvil material [23], both inspired by the work of Bridgman with tungsten carbide anvils. The sample would extrude from between the anvils, the outer regions of which supported the inner regions creating a smooth pressure distribution over the sample. The use of gaskets with diamond anvil cells improved the uniformity of the sample pressure (hydrostaticity), increasing the volume of sample at a given pressure, and the maximum pressure achievable. The small dimensions of the culets of diamond anvils means that significant pressures can be generated with forces generated by the turn of a bolt. This extended pressure range, without the need for high loads or large volumes of compressed fluids, and the relative simplicity of their operation, has made diamond anvil cells the most ubiquitous pressure instrument. Despite the simplicity of the DAC as a device, explaining how it achieves such high pressures is often confused, hampering attempts to push to higher pressures. Section 2.1.5 (p18) highlights the main design considerations for all high pressure cells, including opposed anvil systems.

2.1.3 Pressure media

Pressure experiments depend on the use of a pressure transmitting medium to ensure that the pressure applied to a sample is uniform over the volume of the sample (or hydrostatic). Deviatoric elements of pressure may not be considered as thermodynamic variables, and may cause secondary effects with the behaviour

of the sample. The pressure medium may be solid, liquid or gaseous, though at low temperatures and high pressures, all will eventually solidify. Solids typically have stronger anisotropic mechanical properties than liquids/gases in their solid phases at high pressure, so it is preferable to have pressure media with low freezing temperatures and high solidification pressures. However some fluid pressure media, such as light mineral oils, may become less hydrostatic at higher pressures than some soft solids such as NaCl or Pb. Here soft refers to the low resistant to plastic deformation, and low shear strength, which reduces the build-up of local stresses within the medium. Some stress gradients due to inhomogeneous pressure in the sample area are inevitable at the highest pressures due to the anisotropic behaviour of dense solids.

Aside from important mechanical characteristics, pressure media may need to satisfy a large number of other constraints. Since the pressure media completely surrounds the sample, it is fully exposed to the X-ray/neutron beam during diffraction measurements. It is therefore important that the pressure medium has a high beam transparency, weak coherent scattering cross-section with a low incoherent background (i.e. be hydrogen in the case of neutrons, see section 2.1.7, p27), and contributes few parasitic peaks to the diffraction pattern. The medium mustn't react with the sample, and for neutron studies must not be magnetic, and shouldn't be readily activated by the beam. It is also desirable that the pressure medium is cheap and readily available as a disposable commodity [36].

Despite the huge number of constraints, there are several commonly used pressure media each with their own limitations. The properties of different pressure media at low temperatures have been discussed elsewhere [37–39], though helium is by far the most hydrostatic medium, giving gas cells a distinct advantage over other cell designs. Though it is possible to gas load opposed anvil cells, the large volume changes required to increase the pressure of helium mean that it must be loaded in a highly compressed state, which complicates the procedure, and raises safety concerns. This must be done with the gas either in a cooled condensed state, or through immersing the anvils in a gas-'bombe' containing the pressurised gas. The latter method requires that there is a suitable method for locking the anvils in place to seal the gas within the gasket [40]. Solid and liquid pressure media are easier to load, though do not remain isotropically stressed up to the highest pressures [41]. Liquid pressure media with low boiling temperatures, such as pentane-isopentane (1:1) (which remains hydrostatic to 7.4 GPa) are also challenging to load, as the medium evaporates quickly at room temperature [42].

For opposed anvil cells, the surface finish of the anvil must be considered when choosing the pressure medium. If a very hydrostatic medium, such as a fluid is used, then this can permeate into micro-cracks on the surface of the culet and cause premature failure. This may be avoided if the surface of the anvil is protected by a thin film of auxiliary material to fill the cracks. This may be achieved using aluminium foil, or through sputter coating the anvil. It is worth noting that the significantly higher strength of diamond anvils, makes this less of an issue. For this reason, helium may not be used as a pressure medium for micro-porous samples, such as ice. Argon gas has a well characterised melting curve [43], and being a larger element, can used as an alternative.

2.1.4 Pressure measurement

Measuring the pressure generated by a pressure cell can be achieved using several different techniques depending on the type of measurement being performed, the required accuracy and pressure range. In the case of externally pressurised pressure cells, an in-line transducer can be used to measure the pressure of the fluid being pumped into the cell to good accuracy (typically 0.5 %). These electromechanical sensors vary in achievable range, the best of which are typically limited to 750 MPa. For piston cylinder cells, where the pressure will exceed this limit, pressure measurement is complicated by the fluid being entirely contained in the pressure cell. If diffraction experiments are to be performed then the inclusion of a pressure standard/marker is common. These are materials with a known equation of state up to the desired pressure, and can yield extremely accurate measurements perhaps an order of magnitude better than transducers, depending on the instrument resolution. The disadvantage of this technique is that it reduces the volume of sample that can be included, and by necessity generates parasitic diffraction peaks which may overlap with the sample peaks, obscuring the data. Another concern is that the pressure marker may be reactive with the sample under the application of pressure. For neutron diffraction the most common pressure markers are NaCl and Pb, or MgO for high temperature measurements.

An alternative technique measures the change in resistance in a manganin wire with pressure. Manganin resistivity has a linear response to pressure, enabling extrapolation to determine the pressure at any given resistance. This technique is limited only by the accuracy to which the resistance of the wire can be measured

in the pressure cell. The obvious disadvantage of this method is the need to feed wires into the pressure cell, and the small sample volume reduction due to the inclusion of the wire in the sample chamber. The wires must be fed into the cell using a plug, which seals the wires using an adhesive. If the adhesive deforms excessively under pressure the plug might leak, or the wires might break inside the plug. Preparing the correct adhesive to prevent this is essential.

Where optical access to the cell is possible, the excitation of chromium ions in a chip of ruby can be used as a manometer [44, 45]. If excited with the correct wavelength (532 nm) then Cr^{3+} ions can be excited to higher energy levels with a short lifetime, quickly relaxing to a metastable energy level of longer lifetime. The relaxation of the ions from this state emits light at approximately 694 nm, the so called ruby R1 line. The energy of the metastable energy state has a strong pressure dependency, such that the position of the R1 line has been calibrated to a pressure scale. This technique is very commonly used for diamond anvil cells, or any cell where there is optical access. The ruby chip need only be small if the laser is suitably focussed, such that the loss of sample volume is not a major concern. In addition, the hydrostaticity of the pressure in the cell can be monitored qualitatively through measuring the FWHM of the R1 line. The accuracy of the ruby pressure is limited by the precision with which the R1 peak position can be measured, and may be used up to approximately 100 GPa at which point the effect seems to vanish. The ruby pressure line has been calibrated against known gas pressures [46]. Measuring pressures beyond this in a diamond anvil cell requires use of a Raman spectrometer. The absorption edge of diamond has been approximately calibrated up to several times this pressure. This pressure range is beyond the scope of this project.

For the reader's interest it is worth noting that all the above pressure markers are essentially calibrated against some 'zero' absolute pressure, a perfect vacuum. Shock-physics, Brillouin scattering, and ultrasonic interferometry are all commonly used to derive absolute pressure scales [47], diffraction may also be used to infer additional pressure calibrations from known equations of state.

2.1.5 Key design principles

Although pressure cells can be broadly characterised as above, the specifics of their designs are far more varied, with different aspects tailored to the experimental requirements in question. The decisions to be made are similar

in each case, but designs often require a careful balance of properties, and these will be prioritised differently in each case. This section will outline the mechanical considerations in the design of cylindrical, and opposed anvil cells.

Cylindrical pressure vessels: Lamé formulation

The analysis of cylindrical vessels under internal or external pressure has been reported extensively elsewhere [17, 48–51]; here we are exclusively concerned with the analysis of thick walled cylinders (approximately where thickness, $t \geqslant \frac{\emptyset_{cylinder}}{20}$), as they can contain the greatest pressures. Layering cylinders (press-fitting), and autofrettage (plastically pre-stressing) can improve the pressure range of the thick walled cylinder [52]; an overview of these techniques, and a review of the key stress analysis for internally pressurised thick walled cylinders is presented here.

For a thick cylinder the stresses are not uniform in the wall, requiring the Lamé formulation to describe the stress distribution. Figure 2.5 illustrates the approach, which uses two assumptions: (1) that the material is isotropic and homogeneous; (2) that the axial stress remains constant along the thickness of the cylinder; that the axial symmetry of the cylinder means that the radial profile is maintained, and that all elements at a given radius are deformed equally, such that planes remain plane so there is *n*o shear in these three principle directions [50]. These assumptions are valid in the limit of a long cylinder, where calculations are considered only far from the ends of the cylinder, and where the cylinder is made from a metallic alloy which may be assumed to be approximately isotropic, with a uniform profile. The three principal stresses/strains are respectively: the axial σ_z/ϵ_z, hoop σ_t/ϵ_t, and radial σ_r/ϵ_r. The formulation uses an infinitesimal approach, based on the assumption already mentioned, to derive an expression for any point in the cylinder wall.

Using the above assumptions the radial and tangential strains can be written in terms of the radial displacement [50], u, as

$$\epsilon_r = \frac{du}{dr}, \epsilon_t = \frac{u}{r} \tag{2.1}$$

Balancing the radial forces in the element, using the small angle approximation, and neglecting products of infinitesimal elements, the following may be derived

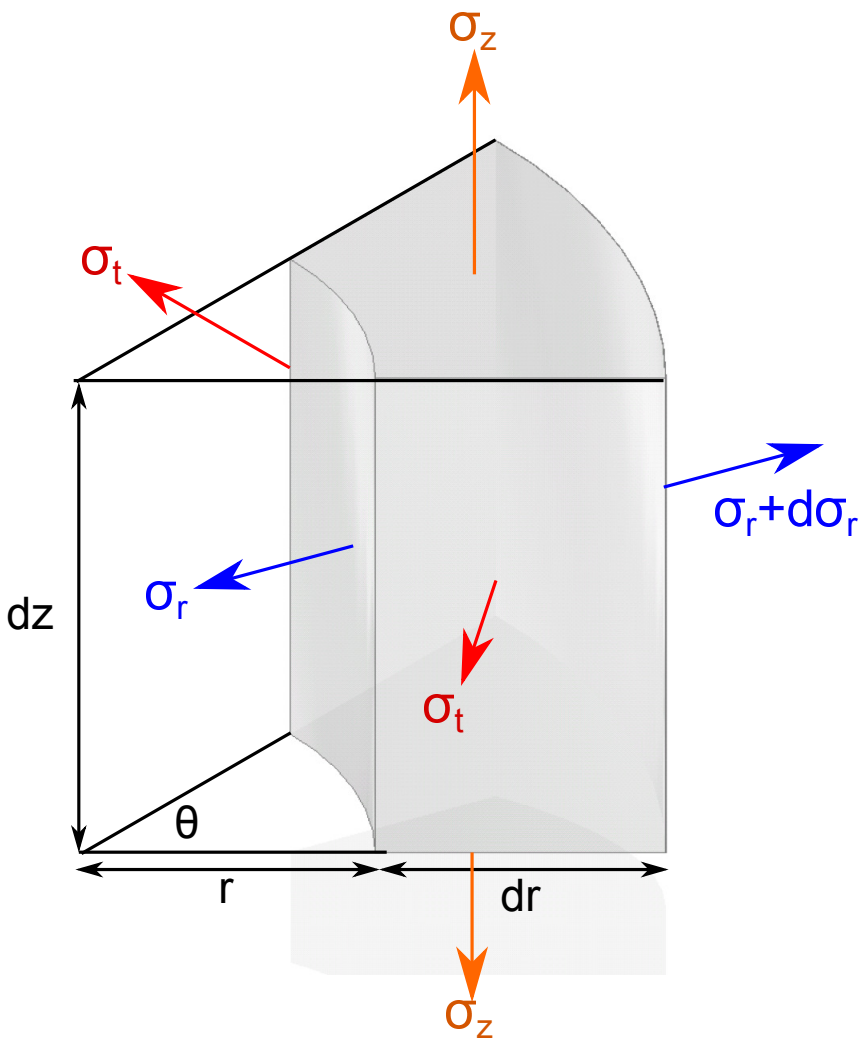

Figure 2.5 *Element of a Lamé cylinder, showing the three principal stresses on the device.*

(see [50]):

$$\sigma_r - \sigma_t + \frac{d\sigma_r}{dr} r = 0 \tag{2.2}$$

If the generalised Hooke's law for axial strain in a material, of Poisson ratio μ, can be written $\epsilon_z = \frac{1}{E}\big(\sigma_z - \mu(\sigma_r + \sigma_t)\big)$, then the assumption that $\epsilon_z, \sigma_z = constant$ in the wall of the cylinder dictates that

$$\sigma_r + \sigma_t = const. = 2A$$

$$2\sigma_r - 2A + \frac{d\sigma_r}{dr} r = 0$$

Integrating this expression gives two expressions for the radial and tangential stress components, with constants A, and B, which are fixed by the boundary

conditions that $\sigma_r = -P_a$ at the inside radius, a, and $\sigma_r = -P_b$ at the outer radius, b, of the cylinder, such that at a radial position r of a cylinder with inner radius a, and outer radius b:

$$\sigma_{t,r} = \frac{P_a a^2 - P_b b^2}{b^2 - a^2} \pm \frac{a^2 b^2}{r^2} \frac{P_a - P_b}{b^2 - a^2} \tag{2.3}$$

In the case where $P_a = P$ and $P_b = 0$ this reduces to:

$$\sigma_{t,r} = \frac{Pa^2}{b^2 - a^2}\left(1 \pm \frac{b^2}{r^2}\right)$$

$$\sigma_z = \frac{Pa^2}{b^2 - a^2}$$

where σ_z is estimated using a simple force/area approximation.

The maximum values of $\sigma_{r,t}$ are, as expected, at the inside diameter of the cylinder. This can be used to determine the elastic pressure limit of the cylinder where $\sigma_r = P$ and $\sigma_t = \frac{P(b^2+a^2)}{(b^2-a^2)}$, such that tangential stresses grow faster in the cylinder than radial stresses, and are always larger than axial stresses. For this reason, a loaded thick cylinder often forms tangential cracks during failure.

These expressions can be used to determine the pressure which the cylinder can elastically withstand. For isotropic materials there are two popular failure criteria. The maximum shear (Tresca) failure, and maximum distortion failure (Von-Mises) [53]. The former assumes that it is shear stresses that initiate failure, maximum shear can be calculated by the difference between the maximum and minimum principle stress $\frac{\sigma_t - \sigma_r}{2}$, whilst the latter (which provides a closer match to observed failure limits) assumes that uniform compression of an element doesn't cause failure, but non-uniform compression results in a stress gradient which if large enough *w*ill result in failure. The Von-Mises criterion can be summarised in this case as:

$$2\sigma_{VM}^2 = (\sigma_t - \sigma_r)^2 + (\sigma_r - \sigma_z)^2 + (\sigma_z - \sigma_t)^2$$

where failure would be expected where $\sigma_{VM} = \sigma_{yield}$. This leads to the result that the maximum pressure in a cylinder is determined by:

$$P_{max,Tresca} = \frac{b^2 - a^2}{2b^2}\sigma_{yield} \tag{2.4}$$

$$P_{max,VM} = \frac{b^2 - a^2}{\sqrt{3}b^2}\sigma_{yield}$$

Where the yield stress under shear is approximated to be $0.5 \times \sigma_{yield}$ (it is generally found that shear strength is between 0.5 and 0.75 times the tensile strength of many metallic alloys, taking the lower limit is advisable for safe operation). These are both plotted in figure 2.6 as a function of $\frac{b}{a}$ where $\sigma_{yield} = 1000\,\text{MPa}$. These expressions are bound, as $\frac{b}{a} \to \infty$, $P_{max,Tresca} \to \frac{\sigma_{yield}}{2}$ and $P_{max,VM} \to \frac{\sigma_{yield}}{\sqrt{3}}$.

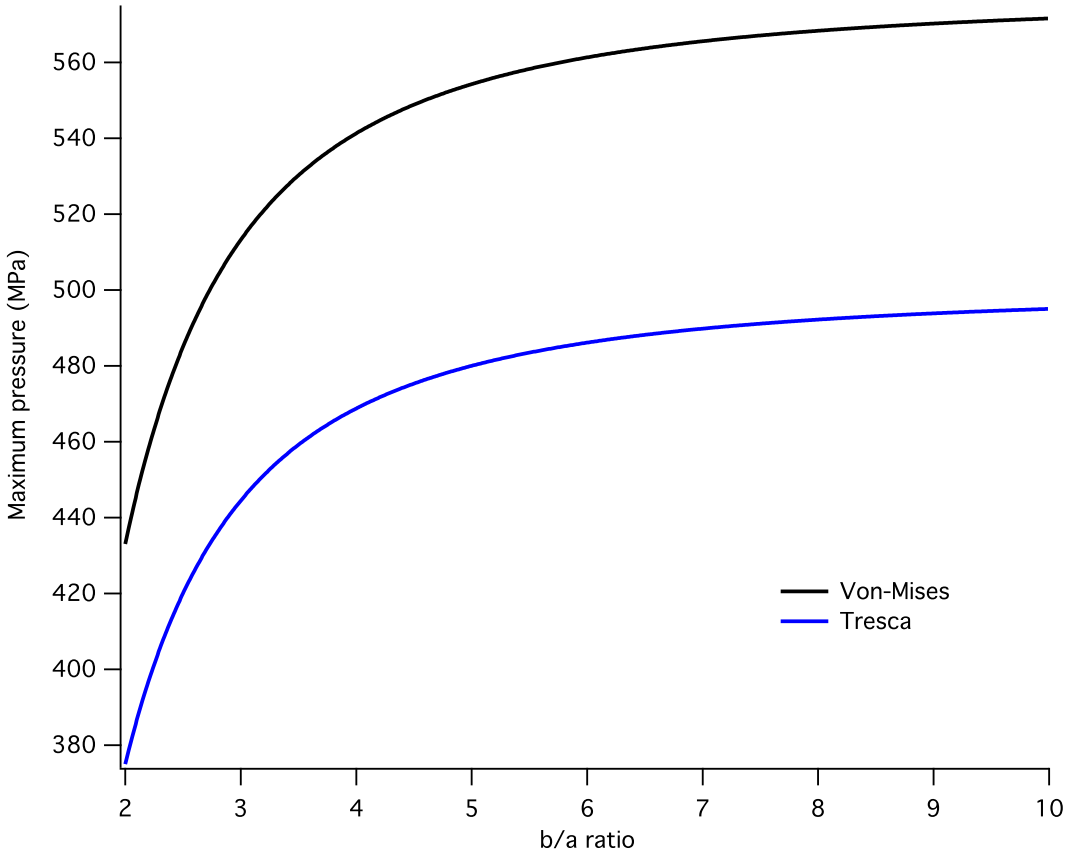

Figure 2.6 *Comparison of pressure limit for elastic operation as a function of wall thickness for material with* $\sigma_{yield} = 1000\,\text{MPa}$ *for both Tresca and Von-Mises criteria.*

Cylindrical pressure vessels: press fitting & autofrettage

From the Lamé formulation it is clear that tangential stresses severely limit the pressures which a cylinder can hold in the elastic limit. This limit can be overcome using press fitting, where the cylinder is compressively strained by an outer cylinder, greatly extending the pressure range. Alternatively the cylinder can be autofrettaged, where it is is initially machined with a smaller bore size,

and then loaded to beyond the elastic limit. This forms a region of plastically strained material in the wall of the cylinder. The bore can then be machined to the desired size, but the cylinder is now compressively supported by the plastic region. Both these techniques work on the same principle, where the region at $r = a$ is compressively strained before loading, increasing the pressure achievable before further plastic deformation. Autofrettage may be thought of as the extreme case of press fitting; without careful calculations, the process can be relatively dangerous.

For the case of press fitting the Lamé formulation can be used to consider the displacement of the outer radius of the inner cylinder, and the inner radius of the outer cylinder. This is done using equations 2.1 & 2.3 with the generalised Hooke's law. From this an interference pressure at the interface between the two can be determined, where a is the inner radius of the inner cylinder, b is the outer radius of the outer cylinder, and c is the radius of the interface between the two, with interference δ, where the elastic modulus E is assumed to be the same for both cylinders [17]:

$$P_c = \frac{E\delta}{2c^3}\frac{(c^2 - a^2)(b^2 - c^2)}{b^2 - a^2}$$

Through subtracting the stresses calculated from the press fit from the stresses determined by equation 2.3, the effects of press fitting on an internally loaded cylinder can be calculated. With an applied pressure inside the compound cylinder, stresses grow at both the inner diameter, and at the interface between the two cylinders. It is sub-optimal for either of these to reach the elastic limit before the other does. Ensuring that the stresses at the interface grow at the same rate as at the inner bore the value of c is optimal when $c = \sqrt{ab}$, [52]. This result is only valid where the yield strength and elastic modulus of the two cylinders is identical. If this condition is fulfilled, then $P_{max,VM} = \frac{2(b-a)}{\sqrt{3}b}\sigma_{yield}$, as $\frac{b}{a} \to \infty$, $P_{max,Tresca} \to 1.15\sigma_{yield}$.

Equation 2.2 can be used to understand the autofrettage process by considering the elastic and plastic region of the cylinder separately. If the cylinder is plastically deformed from the inner surface up to a radius ρ then at $r = \rho$ the radial stress must be equal to the stress required for yielding, equation 2.4 if the Tresca criteria is used. Integrating equation 2.2 with this boundary condition, and the condition that $\sigma_r(r = a) = -p$, the internal pressure to cause plastic

deformation to a radius ρ is given by:

$$p = \sigma_{yield}\Big[\ln\frac{\rho}{a} + \frac{b^2 - \rho^2}{2b^2}\Big]$$

This suggests that there is no upper limit to the pressures which can be contained within an autofrettaged cylinder, provided that the outer diameter is large enough. In practice, excessive autofrettage can result in large compressive residual strains, which results in reverse yielding after unloading, where the prestress is sufficient to cause secondary plastic deformation inwards back towards the inner cylinder surface. Provided that the thickness of the wall is sufficient, this can be contained within the cylinder wall, allowing much high pressures to be generated.

Massive support

In belt presses, the piston and belt can generate pressures well beyond their reported yield strengths; similarly in Drickamer cells, the piston and window materials can withstand higher pressures than expected. The same is true for the anvil and gasket material in an opposed anvil system. This is due to the principle of 'massive support'. For example, in a simple conical angle, the tapered shape reduces the level of critical stresses in the anvil, allowing it to generate much larger pressures. In the gasket, similar reasoning can be applied to understand why much larger pressure can be generated than would be expected from a simple cylindrical Lamé analysis. It has been further suggested that a thick cylinder, operated in a 'short' geometry, where the pressurised volume is considerably smaller than the supporting volume, that massive support allows greater pressures to be generated [17].

Bundy [7] derived a simple expression to demonstrate this; figure 2.7 gives an overview of the analytic model used. Through balancing vertical forces in the model between the face of the anvil, and a region within the body of the anvil defined by the extent of gasket support, and integrating with suitable boundary conditions, the result that $P(x) = P_0 - S - 2\ S\ \ln(\frac{x}{x_0})$, where $S = 2\ \tau_y$ of the anvil material, can be derived. If one further assumes that the gasket extends to the unsupported periphery at $x = x_1$ where the pressure must be zero, then

$$P_0 = S\Big[1 + 2\ \ln(\frac{x_1}{x_0})\Big]$$

so that $P(x) = 2\ S\ \ln(\frac{x_1}{x})$.

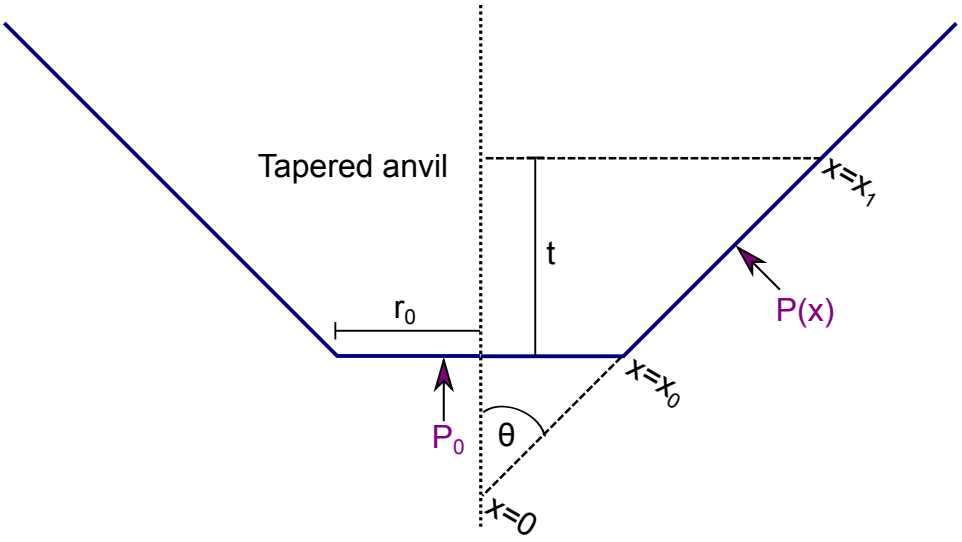

Figure 2.7 *Model used for analytic solution to massive support derived by Bundy [7]. A tapered anvil with culet radius r_0, is used to generate a face pressure of P_0. A gasket is included extending the pressurised region (P_x) along the flank of the anvil to $x = x_1$.*

This reasoning was later applied to the gasket by Dunstan [54]. It is also worth noting that this expression is similar to that derived for the analysis of autofrettaged cylinders.

2.1.6 Thermal and thermo-mechanical properties

Cooling can be achieved through immersion of the device in cryogen such as liquid nitrogen or liquid helium. This process uses the cryogen very inefficiently, which can be expensive in the case of liquid helium. Cryostats are more efficient alternatives for reaching temperatures below 70 K through operating the cryogen in a closed system controlling the cryogen using a small needle valve, and evacuating the boil off. Closed-cycle refrigerators can mechanically drive gaseous helium through a thermodynamic cycle removing the need for cryogens, reaching base temperatures around 5 K. Cryostats and CCRs are more controllable, allowing the cooling rate to be set, whilst the sample is kept in near vacuum, avoiding disruption due to aggressive cryogen boil off. From a neutron scattering perspective this is advantageous, as liquid helium/nitrogen scatter quite strongly, increasing the background. Where small sample containers are cooled, such as vanadium cans, CCRs and cryostats are very quick and effective.

To reach temperatures below 1 K, cryogens are used in dilution refrigeration, and

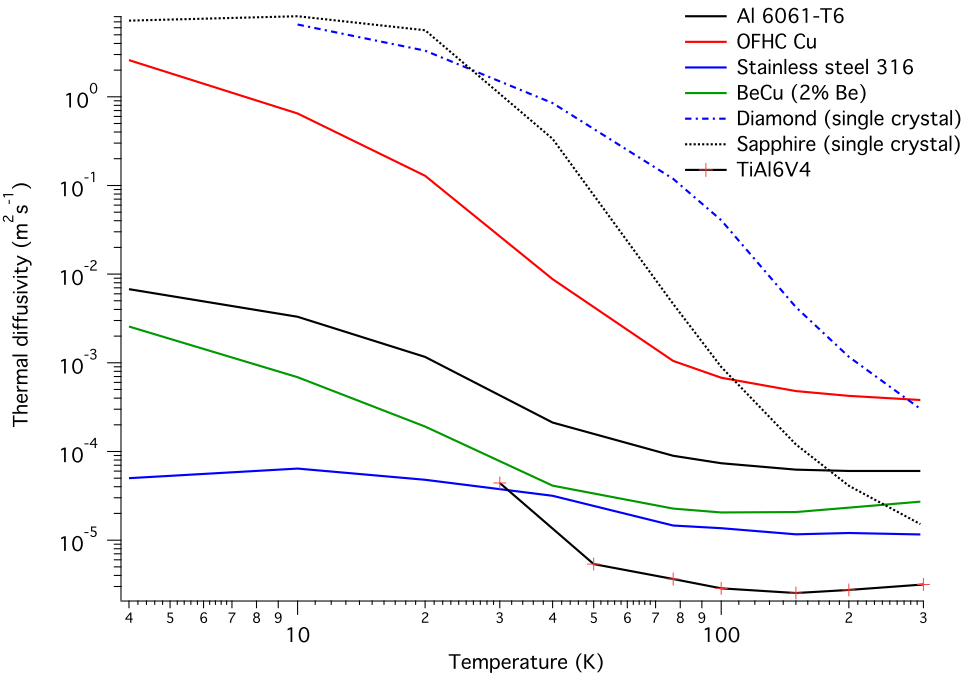

Figure 2.8 *Thermal diffusivity versus temperature for some common cryogenic alloys, compared with single crystal sapphire and diamond. Data compiled from [55–58]*

the cooling power drops considerably. Cryogen free dilution systems have been developed which use CCR systems to condense the mixture of helium to start the dilution process. The increased efficiency of these systems allows them to be upscaled to work with larger sample volumes.

For large pressure systems the high thermal load, and limited cooling power of the CCR/cryostat/fridge, mean that it can take several hours to reach base temperature. Convective cooling using the exchange gas dominates in the CCR/cryostat, whereas in the dilution fridge, the cell is cooled through mechanical contact with the mixing chamber, where the cooling power is derived from a phase separation of liquid helium. To avoid thermal gradients across the sample position, either between the mixing chamber and the end of the cell, or between the inner and outer portions of the pressure cell in exchange gas, the thermal conductivity must be high. The thermal diffusivity, the ratio of thermal conductivity to heat capacity and mass density, provides an easily comparable measure of a material's cryogenic suitability. Since heat capacity is an extensive property, minimising the mass of the pressure cell, whilst also choosing materials with high thermal diffusivity is essential. The thermal diffusivity of some common construction materials is shown in figure 2.8.

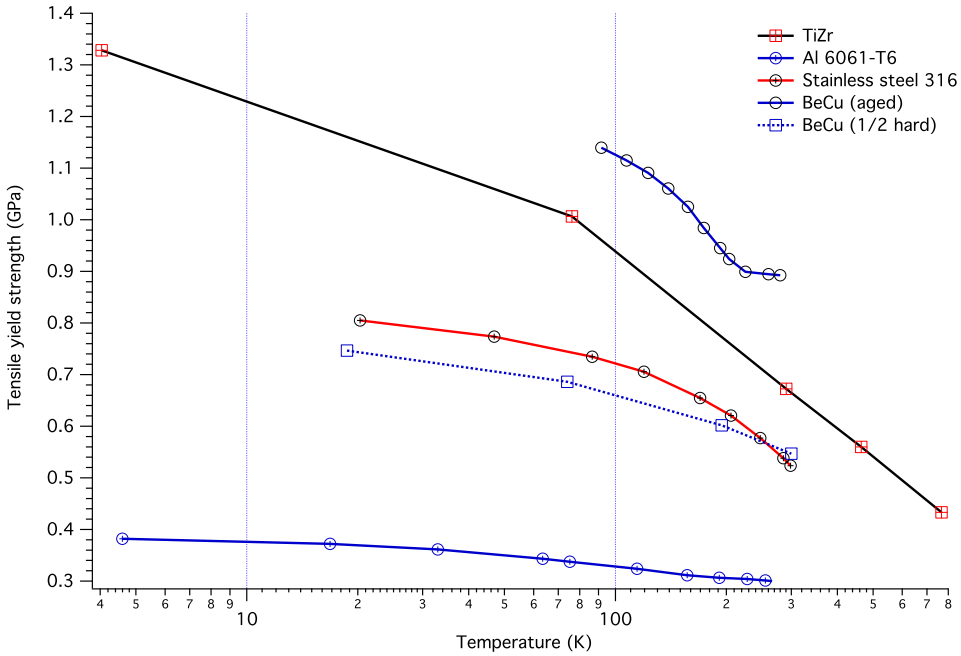

Figure 2.9 *Temperature dependence of tensile yield strengths for some commonly used structural materials in cryogenic, and neutron diffraction suitable, high pressure cell designs. Data compiled from [36, 55, 59–61]*

It is also important that the thermo-mechanical properties of the cell are considered. Many bcc structured metals undergo a ductile to brittle transition at low temperatures[1]. Fatigue, where a material may eventually fail below the stated yield strength due to repeated stress cycling, is typically reduced at cryogenic temperatures in fcc metals. Creep is also negligible, even for materials highly susceptible to creep at room temperature. These trends are likely due to the increased yield strength of most metals at these temperatures (see figure 2.9). The forces required to pressurise increased sample volumes are large, and pressure vessels need to be able to transmit this force safely to the sample without brittle failure, plastic, or extensive elastic, deformation over the full temperature range of operation.

2.1.7 Neutron interactions

Due to charge neutrality, there are only two fundamental forms of interaction between an incident neutron, and the sample. Principally, neutrons are scattered

[1]Ni based steels, and certain titanium alloys can reduce in fracture toughness to at least 50% of their room temperature values [55]

due to short range ($\sim$ fm) nuclear forces between them and the nuclei of the sample. Secondarily, the intrinsic spin (magnetic moment) of the neutron allows it to interact with magnetic moments in the sample (unpaired orbital electrons) via a dipole-dipole interaction. Due to the short range nuclear interaction, the scattering density of the sample is orders of magnitude lower than the mass density of the sample; this means that interactions between neutrons and the sample are infrequent when compared to the rate of interaction of X-rays. When this is coupled with the lower intensity of neutron sources compared to synchrotrons, scattering statistics from neutrons are many orders of magnitude weaker than for X-rays. However, the penetrability of neutrons can be greatly advantageous, allowing data to be collected from samples contained in large pieces of sample environment (cryostats, pressure cells etc) without the need for windows.

$$\sigma_{coh} = 4\pi(\bar{b})^2$$

$$\sigma_{inc} = 4\pi\{\bar{b^2} - (\bar{b})^2\}$$

The short range interaction of neutrons with the nucleus provides information that can be separated into two measurable contributions; a coherent and an incoherent part. The equations above represent the total scattering cross-section for each, as a function of the scattering length, b. σ has units of area, giving a measure of the target size, defined as the ratio of the total number of neutrons scattered per second and the incident flux. b, has units of length, and determines the strength of resulting scattering. The coherent contribution provides information from the average interaction with the sample, a measure of the correlation between the positions of the same nucleus at different times, and between other nuclei at different times, whereas the incoherent contribution provides information on the deviation from average scattering, only the correlation between the position of the same nucleus at different times. Physically, this could be due to either isotopic content, random deviations from the mean scattering interaction, or spin orientation of the neutron relative to the sample [62].

Despite high penetrability, additional material still attenuates the incident neutron beam, but over longer length scales than for a typical X-ray beam. From the perspective of pressure cell design, such as for a cylindrical pressure vessel, a balance must be found between structural and neutronic properties.

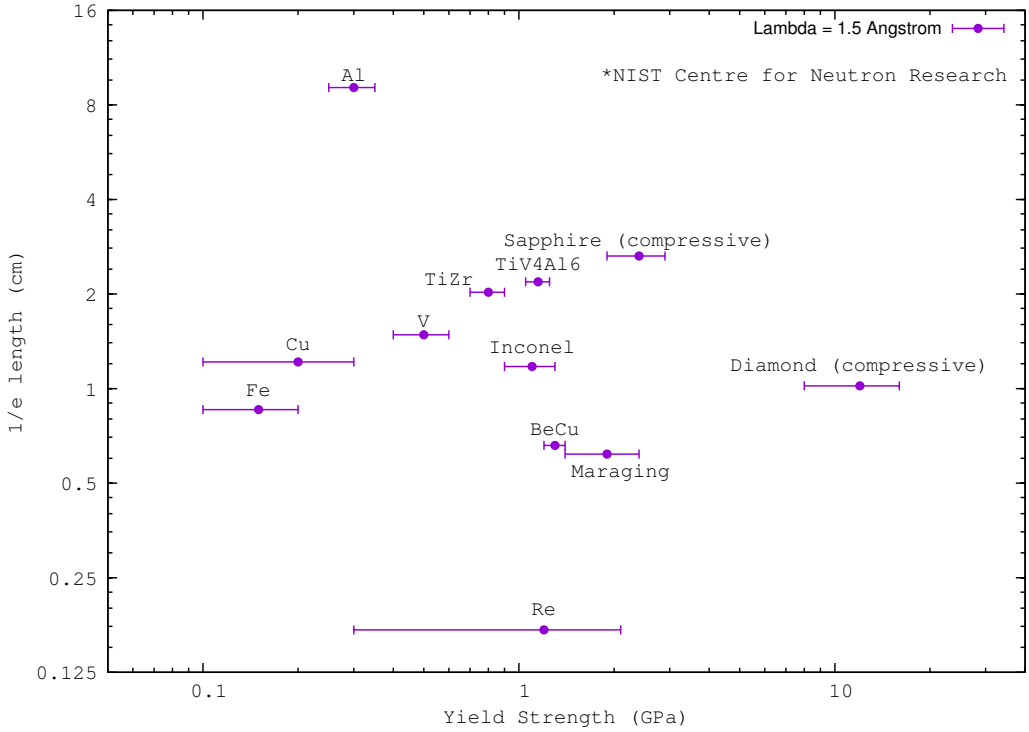

Figure 2.10 *Plot of neutron 1/e length versus material yield strength, for some commonly used structural, gasket, and anvil materials at* 1.5 Å*. Data compiled from [63, 64]. Taking into account worst case scenario coherent contributions for each material.*

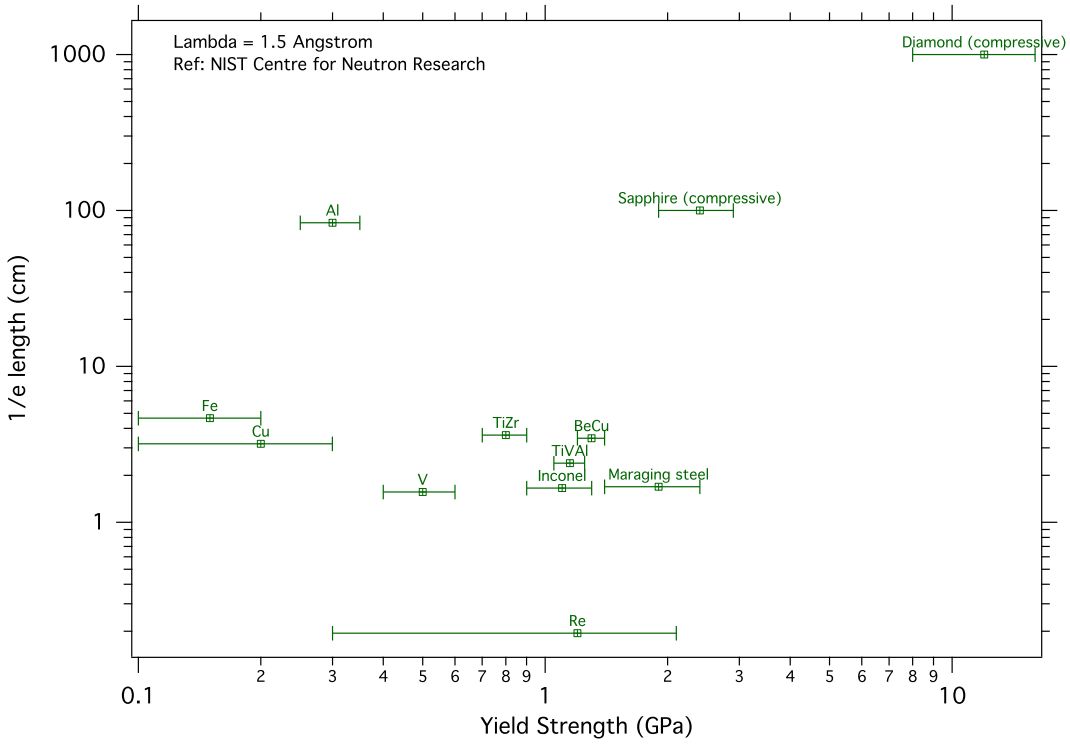

Figure 2.11 *1/e length versus yield strength not accounting for coherent contributions.*

Figure 2.10 shows how the neutron transmission (at 1.5 Å) of a variety of materials compares with their yield strengths[2]. This figure takes into account the absorption, incoherent scattering, and coherent scattering from the sample, but doesn't account for the wavelength dependence of the latter. As such the figure shows a comparison of neutron transparency in the worst case for each material, assuming that 1.5 Å satisfies some diffraction criterion for all materials. Ignoring the coherent contribution, and therefore comparing the transmission properties of each material in a situation where no Bragg conditions are met, is also helpful, allowing the derivation of a linear attenuation coefficient (see figure 2.11). At longer wavelengths these values decrease, by as much as 40% at 6 Å (see supplementary material in Appendix B, p179). The 1/e length is a useful metric for beam attenuation, but it is also important to consider diffraction from the sample.

The coherent scattering contribution can show interference effects caused by the structure and symmetry of the material, where the coherent scattered intensity cancels to zero in some directions, and adds constructively in others. Using purely classical arguments for a wave of wavelength λ incident at an angle θ on a set of planes, equally separated by distance d, Bragg's equation can be derived for integer, n:

$$\mathrm{n}\lambda = 2\mathrm{d}\sin\theta$$

This defines the condition for maximum scattering intensity, as a function of wavelength and lattice spacing. Although incoherent scattering cannot show interference effects, due to being sourced from self correlation, it will still contribute to the measured signal as a general isotropic background, which scales with the volume of material such that it can easily mask coherent diffraction peaks. Magnetic interactions do provide interference effects, but unlike coherent nuclear scattering, are not isotropic in nature, due to the dipole interaction being dependent on the relative alignment of the magnetic moments.

From the perspective of pressure cell design, and the choice of pressure medium/markers, it is important that the diffraction signal from the sample can be easily disentangled from the contribution from the pressure cell over the full range of pressures and temperatures of interest. The pressure cells need to minimally attenuate the beam reaching the sample, have low incoherent levels of scattering, and contribute as few Bragg peaks as possible, avoiding

[2]The 1/e length is the distance travelled through the material where a neutron beam is attenuated to 1/e (approximately 1/3) it's original intensity.

overlap with sample data. In reality, no materials fulfil all of these criteria in addition to the extensive mechanical requirements already discussed, and a balance must be found. For example, null-scattering materials such as the binary alloy TiZr contribute no Bragg reflections due to the scattering lengths of a precise stoichiometry of Ti and Zr resulting in $\bar{b} \approx 0$. However, the material still contributes a strong incoherent scattering signal, subsequently attenuating the beam relatively strongly. This can be overcome through careful geometry design, minimising pressure cell material in crucial regions, masking the incident beam, and treating the collected data.

2.2 FEA optimisation of diamond anvils

It is counterintuitive that a stainless steel gasket, compressed between two gem diamonds, can be used to contain pressures many orders of magnitudes greater than it's expected yield stress from tensile and compressive tests. The diamond anvil cell is conceptually a remarkably simple device, however, reaching the highest pressures remains more of an art than a science, with most loading practices being based on previous trial and error. The dimensions of the device, and the extreme pressures, make it difficult to measure what is happening to the gasket and anvils with high spatial resolution, data which is essential to test theories of how the cell operates, and how it may be improved further. A study by Hemley et al. [65] measured the pressure distribution along the culet of a bevelled diamond anvil cell during indentation of a gasket without a sample hole, and subsequently determined the gasket thickness profile under load using X-ray transmission. This demonstrated that the bevel angle flattens, and then cups as the pressure reaches 3 Mbar, see figure 2.12, but fails to explain how this is beneficial to the operation of the anvil, providing no data on the stress state of the anvil itself.

The non-linear behaviour of the gasket, and the complex onset of support provided between it and the anvil, makes the ab-initio calculation of full stress patterns challenging. Previous studies have looked for analytical solutions to the problem of anvil optimisation [7, 17, 67], though the results tend to underestimate the capabilities of the anvils. Finite element analysis offers a pseudo-alternative to performing physical measurements, or finding an analytical solution, whereby the stress state of the cell is computationally simulated, outputting full stress/strain tensors at any stage of the loading.

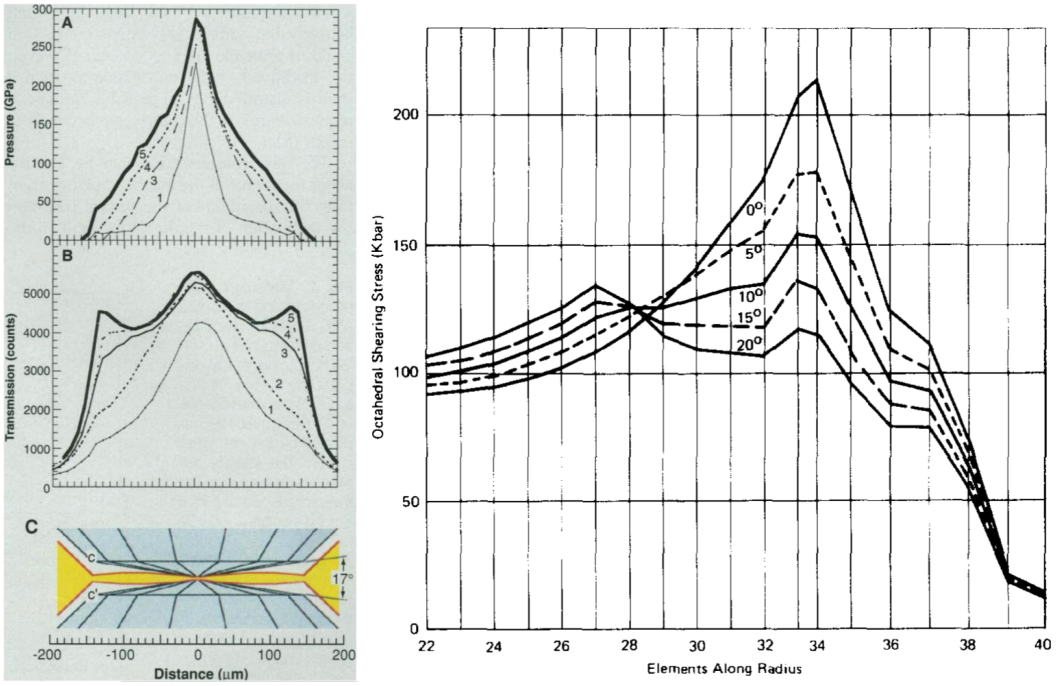

Figure 2.12 *(left) data from work of Hemley et al. [65] showing (A) pressure distribution along Re gasket as measured by diffraction equation of state, (B) gasket thickness profile, (C) cross section of DAC/gasket assembly before and during loading. (right) simulated stress profile in culet region from Bruno and Dunn [66] showing the effects of different bevel angles on shear stresses at approximately* 21 GPa.

FEA is used to numerically analyse stress patterns in objects with complex geometries under non-trivial loading scenarios. Decomposing the system into elements ('meshing') allows for a large yet finite number of stress and strain tensors to be evaluated fully, at any stage of the simulated experiment. Realistic modelling requires extensive material data, and the input of some poorly characterised parameters such as friction coefficients, limiting the accuracy of the results. To verify the models, and identify the ultimate cause for failure of the system, the calculated stress distributions must be compared with experimental data. Studying the process of pressure generation in a gasketed anvil cell complicates FEA for several reasons; **1)** the large pressures under the anvil quickly cause plastic deformation in the gasket, requiring longer computation times, and the use of simplified models of plasticity, since the properties of highly-deformed gasket materials at high pressure are generally unknown; **2)** the interaction between components requires often unknown contact parameters to be defined; **3)** the material properties of hard, brittle materials are poorly defined as measurements are highly dependent on less controllable parameters, such as surface finish or purity which alters the mechanical properties.

Some FEA studies in the literature have avoided some of these complications through artificially generating the pressure distribution from the gasket, instead of modelling the full anvil-gasket assembly. This type of model has helped in identifying the cause for large levels of basal tension in diamond anvils [68], leading to anvil seat optimisation [69]. However, it fails to distinguish the complex onset of support provided between the anvil and the gasket, and neglects the effects of gasket deformation on stresses in the culet. Existing FEA studies have been concerned with diamond anvil cells, using small culets and thin gaskets [66, 70–72]. The present study is unique in that it considers sapphire, a far more compressible anvil material, with much larger dimensions than those used for the DAC construction, and the gaskets used are thicker, and undergo significantly larger deformations.

Bruno and Dunn [66] considered the effects bevelling the face of a 300 µm diamond culet. The model assumed that the diamond was isotropic in hardness, and that the deformed gasket and anvil behave purely elastically. They found that octahedral shear stresses at the edge of the bevel were optimal for a bevel angle of $10^\circ - 15^\circ$, reducing the shear stresses in the anvil, see figure 2.12, whilst increasing the gradient of axial stress. The results of this study seem consistent with the experimental observations of Mao and Bell that bevelling the edge of the culet

extended the pressure range of the anvil [73]. Other attempts to optimise diamond anvils, to reach the highest possible pressures, have been reported by Novikov et al. [70], where many more parameters of the diamond anvil were varied, in an attempt to optimise the design. Their study uses a very detailed anisotropic model, considering the cleavage planes of diamond, to find optimal dimensions through regression analysis. Moss and Goettel [71] analysed the effect of bevelling the anvil on the cupping of $25 - 40\,\mu m$ diamond culets. The cupping of the diamond at extremely high pressures has been speculated to cause a bridging between the two anvils at the edge of the culet, and premature anvil failure. Here plastic deformation was modelled using non-linear equation of state models. This cupping of the anvil was later observed experimentally, using X-ray transmission data alongside further FEA results [65, 72]. This study used a more complicated material model for the diamond, assuming anisotropy, with pressure-dependent coefficients. Many of the studies mentioned above date from the 1980s and 1990s; advances in computation power and FEA techniques motivate returning to old problems with new tools.

Part I

High pressure techniques for neutron diffraction

Chapter 3

Developing a load cell for cryogenic neutron diffraction studies

This chapter presents the design of a 45 kN load cell for sub-1 K neutron diffraction measurements. The load cell is designed for use with an opposed anvil system to generate sample pressures up to 6 GPa using sapphire anvils, and higher using diamond anvils, the full details of which are discussed in Chapter 4. Unlike the Paris-Edinburgh neutron diffraction cell, this cell is driven using a novel stacked membrane (or 'bellows') unit; pressurised helium gas is used to expand the unit, apply load to the anvils and compress the sample contained in a gasket. The compact design of the cell makes it suitable for use with all standard 100 mm closed cycle refrigerators and cryostats, as used at the ISIS neutron facility, whilst the bellows unit allows the load to be varied in the cell without the need to warm the cell back to room temperature. At large scale facilities such as the ISIS neutron facility, the cost of operation makes it very competitive to secure time on the instruments. The ability to control pressure in-situ saves considerable time, allowing users to maximise the useful data collection time in their allocated window on the instrument.

3.1 Design motivation

Pressure cells for low temperature neutron diffraction are limited by two competing factors **a)** the sample volume needs to be large enough to produce

sufficient scattering data. Large samples require large absolute volume changes, and much greater support, to generate high pressure. This requires much higher loads, such that the cell needs to be large; **b)** the size of the cell determines the lowest temperature achievable and the time required to reach this temperature. The Paris-Edinburgh cell can reach temperatures down to 3.5 K using a specially developed liquid helium cryostat [74, 75]. At its most efficient the system is first quenched with liquid nitrogen, evacuated, and then the cryostat begins operation, taking approximately 7 hours to reach base temperature, at considerable cost in cryogen consumption. Klotz et al. [75] used a closed cycle refrigerator to reduce helium consumption, and reports that 80 K can be reached in approximately 2 hours with nitrogen pre-cooling, then reaching 4 K in approximately 12 hours, before then introducing liquid helium to the chamber to reach 1.5 K relatively quickly (approx. 15 minutes).

The main limitation with the Paris-Edinburgh cell at low temperatures is in changing the pressure of the sample. The most standard form of the cell is loaded pneumatically with hydraulic oil which freezes at 240 K, meaning that the cell must be warmed back to this temperature if the pressure is to be altered. In addition the density change of the oil upon cooling can result in a large load reduction after freezing, making it difficult to maintain the desired pressure. To avoid this, a mixture of organic solvents (pentanes) may be used to replace the oil, which remain liquid to 120 K, [76] where it faces the same problems. To maintain pressure control at lower temperatures, helium gas must be used. This is more difficult to seal in the cell, reducing the maximum pressure which can be reached, and is consequently more dangerous at the typical pressures required for pressure cell operation (200-1000 bar).

In addition to being difficult control the pressure at low temperatures, the large mass of the cell makes temperature stabilisation very challenging, creating large thermal gradients through the cell due to differing material properties and cooling rates. Some advances have been made recently whereby the anvils are only weakly thermally linked to the rest of the pressure cell, using a material with poor thermal conduction such as teflon. It has been estimated that two CCRs in this arrangement should have sufficient power to cool the anvils to approximately 20-30 K [9]. However, this has required a complete redesign of the original CCR system, and will likely still be unable to reach the temperatures often required for the study of weakly magnetic materials.

Furthermore the pressure in the sample volume must either be determined from

other loading curves, or through using a pressure marker such as Pb, such that the beam is required to determine the pressure accurately. The thermal inertia of the cell, coupled with the high loads required, make it very difficult to reach a specific region of pressure/temperature; this is particularly the case where the pressure required is less than 0.5 GPa, as simply sealing the sample in the gasket requires loads of approximately 50 kN.

Overall, whilst it is possible and not uncommon to perform low temperature studies using the Paris-Edinburgh cell, it is far from optimised for such work. The alternative pressure cells currently available for neutron studies are less affected by these issues but either don't offer the option for in-situ pressure control, or are severely limited in pressure range, or both. Furthermore, equipment to access the lowest temperatures with the Paris-Edinburgh cell remains very unique to each neutron source, each operating the cell in different geometries, using highly customised cryogenic assemblies. This is a severe disadvantage for the low temperature development of the cell, making it difficult to perform different studies using a variety of different neutron instruments, or to repeat the same experimental conditions on multiple instruments using the same cell.

For these reasons it is clear that a new pressure cell is required, optimised specifically for low temperature neutron diffraction to pressures comparable to the Paris-Edinburgh cell, which can be easily integrated into existing sample environment. Ideally the cell could reach temperatures below 1 K opening up a new range of achievable science with neutrons.

3.2 Previous designs

Opposed gem anvil cells for neutron experiments have been in development for some time; the earliest designs found in the literature refer to a project originating from the DISK diffractometer at the Kurchatov Institute (Moscow), with continued development at Dubna, and the Laboratoire Leon Brillouin in France. In addition to this, significant advances have been made by researchers using the Japanese neutron source (J-PARC), the Institute Laue-Langevin [77], and also by researchers at the SNS at Oak Ridge in collaboration with the Carnegie Institute. The development of gem anvil cells for neutrons began in a similar period to the development of the Paris-Edinburgh press, though have currently failed to become as widely used. This is largely due to the much longer

count times required for gem anvil cells due to the smaller sample volumes they can contain, the low neutron fluxes available, and more recently due to the high levels of tailoring required to optimise neutron instruments for use with such small samples. In addition the smaller sample sizes make assembly of the gem anvil cells a considerably more specialised technique, requiring more precision assembly. These early designs, and more recent developments will be summarised here.

3.2.1 Dubna anvil cells

The possibility of studying samples small enough for diamond anvil cell work was first realised at the Kurchatov Institute (Moscow) in the 1980s [78]. Glazkov et al. [78] found that samples of the order $\sim$ mg could provide sufficient scattering data in approximately 50 hour data collection times, using a medium- to low-flux reactor, through developing an annular detector coverage on the DISK diffractometer. The authors realised that whilst more intense neutron sources would improve matters, the quality of data and diffraction technique could equally be improved. The annular detector allowed for multiple powder reflections to be measured simultaneously, drastically reducing count times compared to single moveable-detector instruments. The main challenge in incorporating this many detectors on a single instrument was the electronics. Electronic processes to ensure that multiple detectors could be correctly identified and calibrated were still under development.

In addition to using a large detector coverage, the DISK team also used double incident beam monochromation to improve the signal to noise ratio through increasing the efficiency of Cd shielding, tight incident beam collimation (4 mm x 4 mm smallest beam size at sample), whilst each detector had 215 mm long, 5 mm x 50 mm wide collimators, reducing background scatter significantly.

A joint research program with the Laboratoire Léon Brillouin (LLB) would drive the development that followed, focussing on balancing the requirement for sample volume with the requirement to generate reasonably high pressures, whilst developing techniques to improve the diffraction techniques used. Much of this work was pioneered by I.N. Goncharenko, who contributed widely to the development of large volume sapphire and diamond anvil pressure cells for neutron diffraction [79–83], and techniques for improving data collection and quality through developing compact Ni-Ti neutron super mirrors (in collaboration with the Paul Scherrer Institut) to focus the incident neutrons, bring large flux

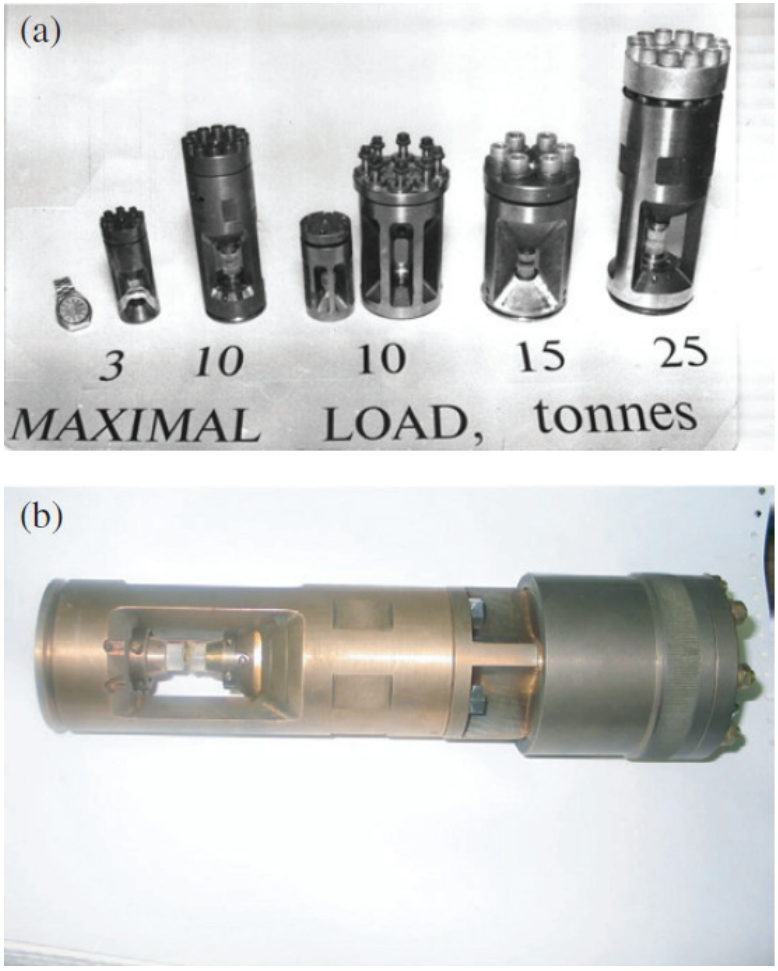

Figure 3.1 *Pressure cells from the Kurchatov Institute [85]. (a) mixture of stainless steel (for high temperature) and BeCu (for low temperature) sapphire and diamond anvil cells for generating large static forces. (b) sapphire anvil cell with pneumatic system to allow for in-situ pressure control at room temperature.*

gains at longer wavelengths [84].

Some years later, at a sister facility at the Joint Institute for Nuclear Research (Dubna) the instrument DN-12 was developed for time-of-flight high pressure measurements [86]. This has the added advantage that the fixed-angle geometry may be used, allowing the beam to be introduced through the back of the anvils, and tightly focussed on the sample volume, almost entirely removing the background scattering from the surrounding gasket material. The use of neutron super mirrors, and later reliance on the fixed 90° geometry, made high pressure studies on these instruments reliant on long neutron wavelengths, limiting the completeness of the data which could be collected. This made the instruments well suited to studying magnetic structures, but full structural refinements would

not always be possible.

Full details of each loading are not reported by Goncharenko, though his sapphire pressure cells were able to generate pressures up to 8 GPa on samples of sufficient size to collect sufficient data in approximately 4 hours on the MICRO (G6.1) high pressure diffractometer at the LLB (reported to be approximately 1 mm^3. Furthermore, pressures up to 40 GPa could be generated with diamond anvils, with 12 hour collection times. Figure 3.1 shows a few of the cells from the Kurchatov Institute with their respective load limits [85].

3.2.2 J-PARC cells

The PLANET instrument at the J-PARC facility in Japan was designed as a dedicated time-of-flight high pressure beamline [87–90]. Significant research has been performed to extend the high pressures achievable on the instrument through developing a variety of hybrid anvil assemblies [91–93]. In addition, there are several earlier studies motivating the use of sapphire anvil cells for neutron diffraction [94, 95].

PLANET is the first dedicated high pressure neutron diffractometer in Japan, incorporating many of the principles incorporated into the time-of-flight instrument DN-12 at JINR, Dubna but with significant increases in available flux. The incident beam is tightly controlled with slits close to the sample region, and a super mirror is used to focus the neutron beam to a small sample volume. In addition, very tight detector collimation is incorporated, leaving a very tightly defined region of sample space from which data can be obtained. This is essential to efficiently reduce the background from the pressure cell construction, and when coupled with the fixed 90° scattering geometry, the surrounding gasket material. A few gem anvil pressure cell designs from J-PARC are presented in figure 3.2.

3.2.3 SNAP diamond anvil cell

A recent and significant advance in high pressure neutron diffraction was reported from the SNAP diffractometer at the Spallation Neutron Source (SNS, Oak Ridge), whereby data from $2 \times 10^{-2} mm^3$ of sample were collected at 94 GPa. The cell, shown in figure 3.3, is capable of applying up to 12 t to a pair of diamond anvils with 1 mm culets [99]. The diamonds use conical backs [100] which are

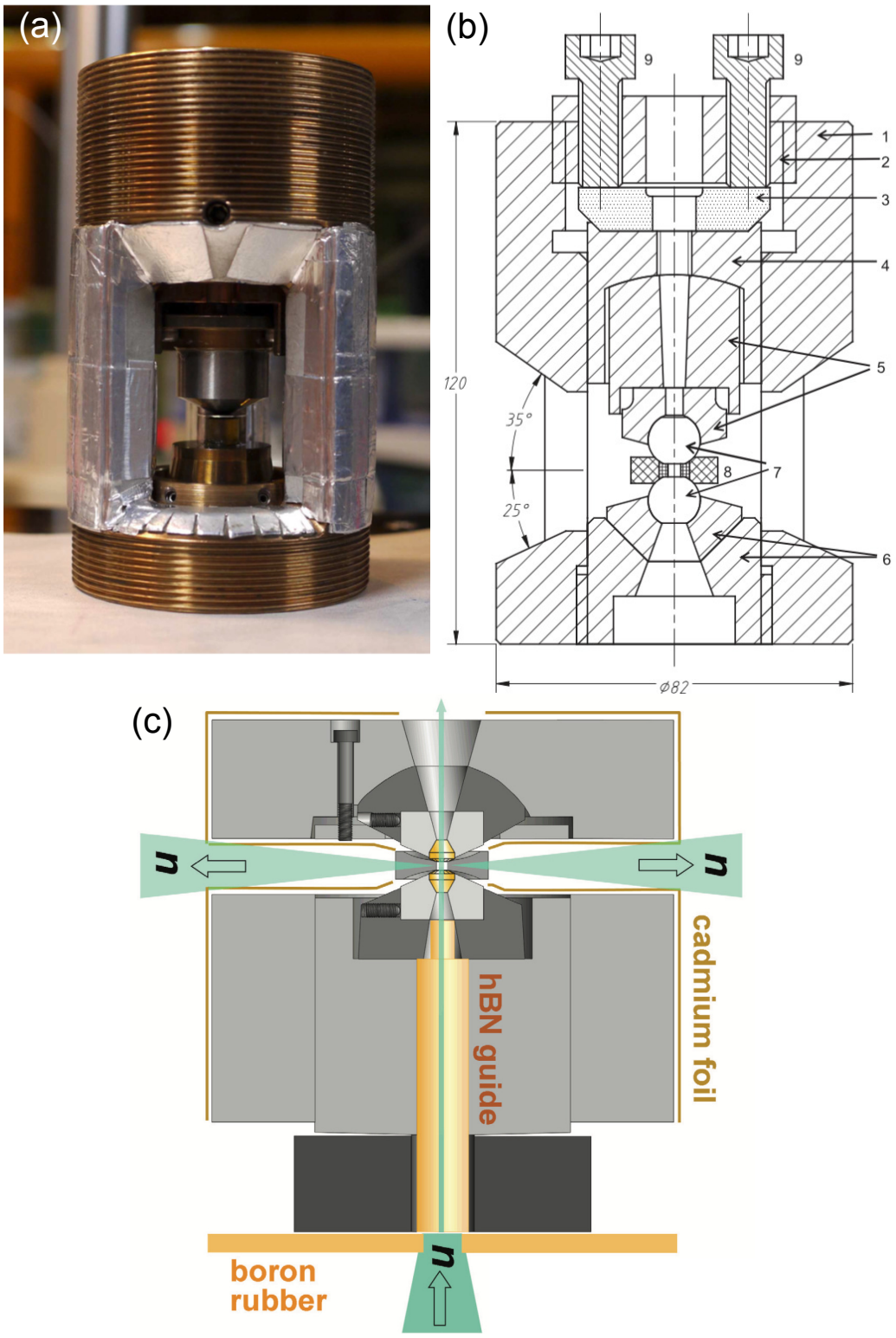

Figure 3.2 *Collection of gem anvil pressure cells for neutron diffraction (a) hybrid anvil cell with WC (top) and nano-polycrystalline diamond (NPD, bottom) anvils. Cell can generate* 6 t *via static compression with six M6 bolts,generating* 8 GPa *on* 0.3 mm^3 *of sample. [96] (b) large volume sapphire anvil cell for generating* 2 GPa *on* 10 mm^3 *of sample. Details in [97], (c) NPD anvil cell, capable of generating* 14 GPa *on* 0.7 mm^3 *of sample. [98]*

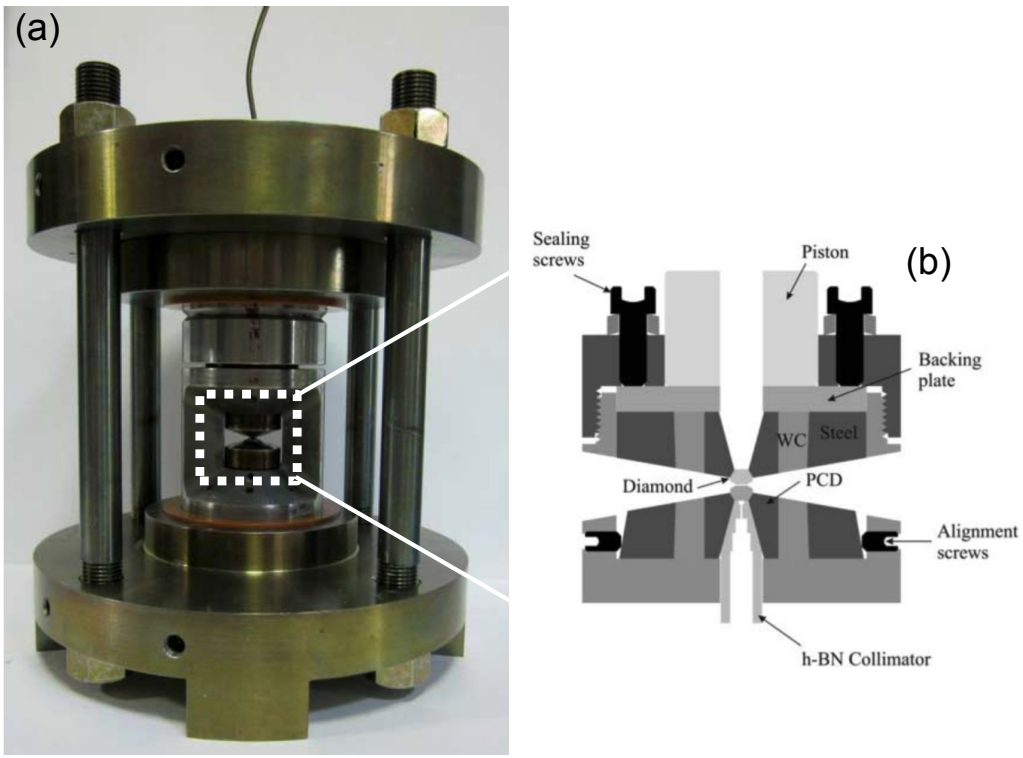

Figure 3.3 *Strongly supported diamond anvil cell (b) as demonstrated at SNAP diffractometer [99]. The cell is contained in a large two plate platform (a), held with four tie-rods. The load is then applied to the anvils using a steel membrane filled with gas or fluid, which provides linear force application of* $0.05\,\mathrm{t\,bar^{-1}}$.

reinforced with polycrystalline diamond supports, WC, and binding tool steel to prevent failure under these high loads.

Aside from the precision assembly required to generate these pressures, the SNAP diffractometer has also been optimised to study such small samples. A long parabolic mirror guide, with slits at each end, enable the beam to be focussed very finely, without considerable loss of flux. Slits at the detector side of the instrument, fixed at 90° scattering geometry, further reduce any parasitic scattering from the front and back of the cell.

3.3 Design parameters

3.3.1 Cryogenics at the ISIS neutron facility

The vast majority of cryogenic systems operated at the ISIS facility are Ø50 mm bore or Ø100 mm bore top loading Orange cryostats and Sumitomo CCRs (STFC, ISIS Sample Environment, 2016), see appendix A for schematic views of each. Whilst both 50 mm and 100 mm variants can reach the same base temperatures, there is a considerable difference in cooling time when operated with maximum sample volumes. Due to the extensive use of cryostats/CCRs at the ISIS neutron facility, the present pressure cell was designed to be easily incorporated into existing systems. As the main challenge in developing a new cell was achieving high pressures on sample volumes large enough to obtain neutron data, 100 mm systems were chosen for standard operation, as they allow for larger sample assemblies. This placed clear size constraints on the cell, requiring it to fit in a Ø100 mm bore, with the base of the cell and the sample position approximately 100 mm apart.

For dilution fridge operation, the only suitable equipment operated by the ISIS neutron facility is the E18 Vericold fridge (base temperature 20 mK), similar to that detailed by Batey et al. [101]. The dilution fridge has more relaxed geometry restraints (200 mm × 250 mm).

Orange cryostats and CCRs cool the sample volume though convective processes, with the sample in sub-atmospheric exchange gas, transferring heat from the sample to one or two heat exchanges coupled to the sample chamber. Radiation baffles are used to reduce radiative heating effects, but most importantly geometrically constrain the convective cooling loops in the cryostat/CCR. For this reason, at base temperature, there will be a considerable temperature gradient along the length of the stick, such that limited cooling power at base temperatures may be focussed on cooling only the sample region.

3.3.2 Neutron instrument considerations

The interaction of the neutron beam with the sample and surrounding pressure cell material needs to be considered. Where the geometry of the cell visually obstructs the neutron beam, it must be made from a material highly transparent

to neutrons. It is also beneficial for the diffracted beam to have approximately symmetric paths through any surrounding material, as this enables simple corrections for beam attenuation. There are multiple factors to consider depending on the geometry of the instrument being used, and its detector coverage, the type of source being run, and whether the sample being studied is a single crystal or polycrystalline material.

Neutrons can be produced either in a 'spallation' process (colliding medium energy protons with a heavy metal target) [102] or through the process of nuclear fission; both produce neutrons at a range of energies (or wavelengths). Spallation sources inherently have the advantage of time resolution, whereby the timing of the neutron generation allows for the neutron wavelength to be calculated and used to determine the wavelength of each detected neutron (known as 'time-of-flight' technique). This can be incorporated into continuous reactor sources with mechanical 'choppers' to create timed beam intervals, this has been shown to be effective in spectrometers [103, 104], though is rarely used for diffraction instruments [105].

The fission process is operated continuously and therefore the 'time-of-flight' information is lost. Instead, a monochromator must be used to select a single well defined wavelength of neutrons to use for diffraction. Spallation is significantly more efficient to run, producing more neutrons per proton event at lower equivalent energies. Currently reactor sources create higher fluxes on average [106]. It is possible to run a continuous source using the spallation process, such as at the Swiss spallation source SINQ.

Neutrons interacting with a crystalline sample diffract satisfying the Bragg condition (discussed in Section 2.1.7). In the case of a powder sample, the sample should ideally have an even distribution of randomly oriented crystallites, such that the diffraction condition is satisfied for all symmetry related reflections at some angle satisfying the Bragg condition. In the case where multiple known wavelengths are incident on the sample, these diffraction conditions may be met in a so called energy-dispersive manner, over a fixed angular range. For angle-dispersive measurements the detector coverage must be large enough to measure the full diffraction pattern, either as a fixed system or through moving a single detector.

For a single crystal sample, depending on the symmetry of the crystal, a combination of detector positions, and sample orientations are required to

access the full reciprocal space. For a time-of-flight instrument the number of orientations required may be fewer due to multiple wavelengths diffracting at each orientation, though this is dependent on detector coverage.

Energy dispersive time-of-flight measurements are popular for high pressure neutron diffraction measurements, where the scattering angle is fixed within a small range, and all the measured neutrons pass through a well defined region of the cell. Careful collimation of the incident beam, and masking regions of the pressure cell outside the window of interest results in a minimal background signal. However, this technique also has disadvantages; in a fixed geometry the instrument is heavily reliant on long wavelength neutron data to probe long d-spacings (such as for large unit cells, or for investigating nuclear/magnetic superstructures). The available flux at these wavelengths is considerably lower than that available at mid- and low-range wavelengths, such that count times increase considerably to obtain good diffraction statistics over a broad d-spacing range. Whilst this is improved by summing multiple detector banks together (which cannot be done where the diffraction angle differs between detectors) the total gains possible become limited by the free aperture of the pressure cell. Furthermore, this technique results in the incident beam being attenuated by both the anvil material (incident), and the gasket material (when diffracted).

The alternative introduces the beam between the two anvils radially, and the scattered beam is then measured radially over a much larger Q-range. Here the beam is attenuated mostly by the gasket material. If the neutron are produced from a reactor source, then the cell must be rotated to collect a full spectrum. If the neutrons are produced from a spallation source (time-of-flight), and the aperture of the cell is designed to match the detector coverage, then significantly larger data sets can be collected without needing to rotate the cell. The time-of-flight high pressure beam line at the ISIS neutron facility TS1, PEARL, routinely operates pressure cells in fixed $2\theta = 90°$. This angle is chosen to give a balance between resolution, scattering statistics, and the d-spacing range accessible. Conversely WISH at the ISIS neutron facility TS2, has a large position sensitive range of detectors, and is optimised for angle dispersive measurements.

3.3.3 The PEARL and WISH diffractometers

The ISIS neutron facility is a spallation neutron source with two tungsten targets used to generate neutrons from pulses of protons. PEARL and WISH are on

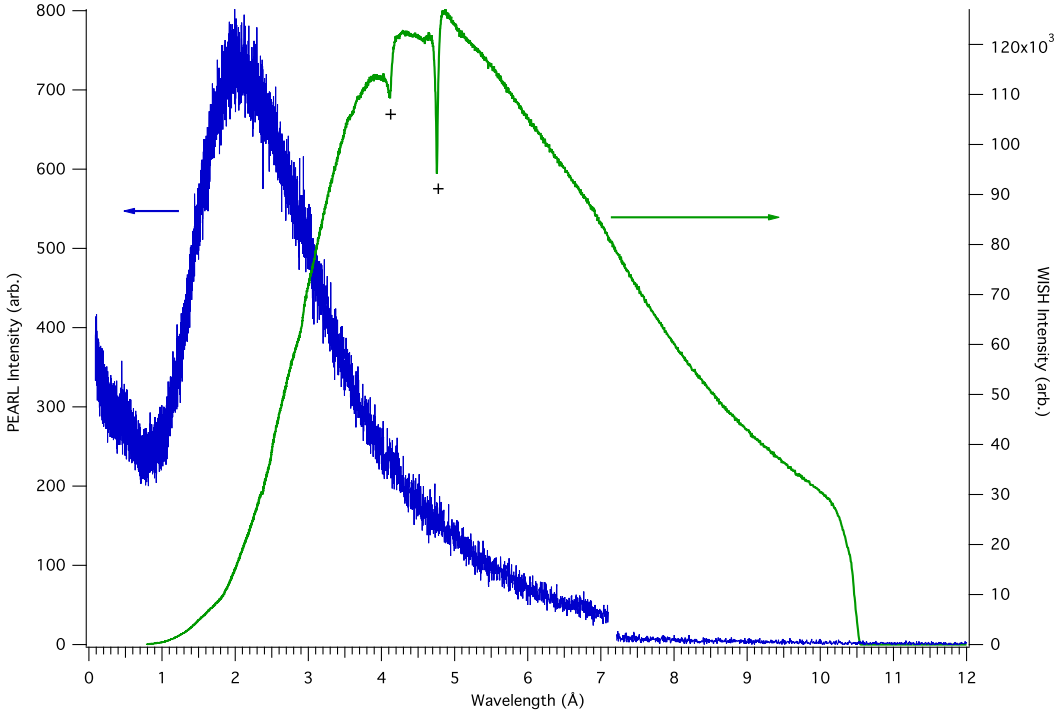

Figure 3.4 *Comparison of pulse profiles measured on the PEARL and WISH diffractometers at the ISIS neutron facility. Intensities are unnormalised, and hence plotted on separate axes. The step in the PEARL spectrum just above 7 Å is where the data have been cropped to remove the prompt pulse (see main text). The features in the WISH spectrum (+) are Bragg edges from the choppers on the instrument.*

different target stations (TS1 and TS2 respectively); PEARL uses 4 out of 5 pulses from the synchrotron, with WISH using the other 1 out of 5 pulses. WISH is therefore said to be a long pulse instrument, allowing for much longer wavelength neutrons to reach the sample position before the next pulse arrives at the target. In addition to this, WISH is equipped with a ballistic parabolic super mirror guide, [107] giving it a flux advantage at longer wavelengths over PEARL (see figure 3.4), which was designed to use the full beam spectrum available to maximise the d-spacing range available at $2\theta = 90°$. PEARL has the capability to continue measuring during the 'long pulse', where the final pulse is sent to the second target, enabling it to use these longer wavelength neutrons, but with significantly poorer statistics.

Another important feature of the two instruments is their positions from the targets; PEARL is significantly closer to the target (12.8 m) than WISH (40 m). This longer flight path gives WISH a considerable increase in resolution over PEARL ($\delta d/d = 0.3\,\%$ and $0.65\,\%$ respectively), but would ordinarily also give a reduction in flux at the sample position. This is countered by more efficient moderation of the neutrons, and advanced neutron guides, to give WISH a large integrated flux for a high resolution instrument (1.1×10^8 neutrons/cm^2/s in high flux mode, or 1.08×10^7 neutrons/cm^2/s in high resolution mode over the full bandwidth) [107]. PEARL on the other hand has an integrated flux of (2.6×10^6 neutrons/cm^2/s), limited to a narrower bandwidth. It is also worth noting that a large amount of this flux on PEARL is delivered through high energy neutrons, which are normally rejected due to difficulties in masking sources of background at high energy. If WISH and PEARL are compared over a similar bandwidth (0.5-6 Å see figure 3.5) then the integrated flux of WISH (9.8×10^7 neutrons/cm^2/s) greatly exceeds PEARL (3.4×10^5 neutrons/cm^2/s). [1]

PEARL has a fixed incident beam, which is then collimated using long BN and Gd slits (Ø3-6 mm) placed within approximately 5 mm from the sample, giving excellent control over the level of parasitic scattering from the pressure cell. Both instruments have a series of adjustable 'jaws', allowing the beam to be profiled at several different stages of the flight path. PEARL can vary the beam size at the sample position from 20 mm square down to 2 mm diameter, using additional 'scrapers' to give a very well defined beam at the sample position. The final

[1] Unpublished data - measured using nGEM 2D neutron detector May 2017. Beam size 5 mm × 5 mm at sample position, detector approximately 250 mm behind sample position.

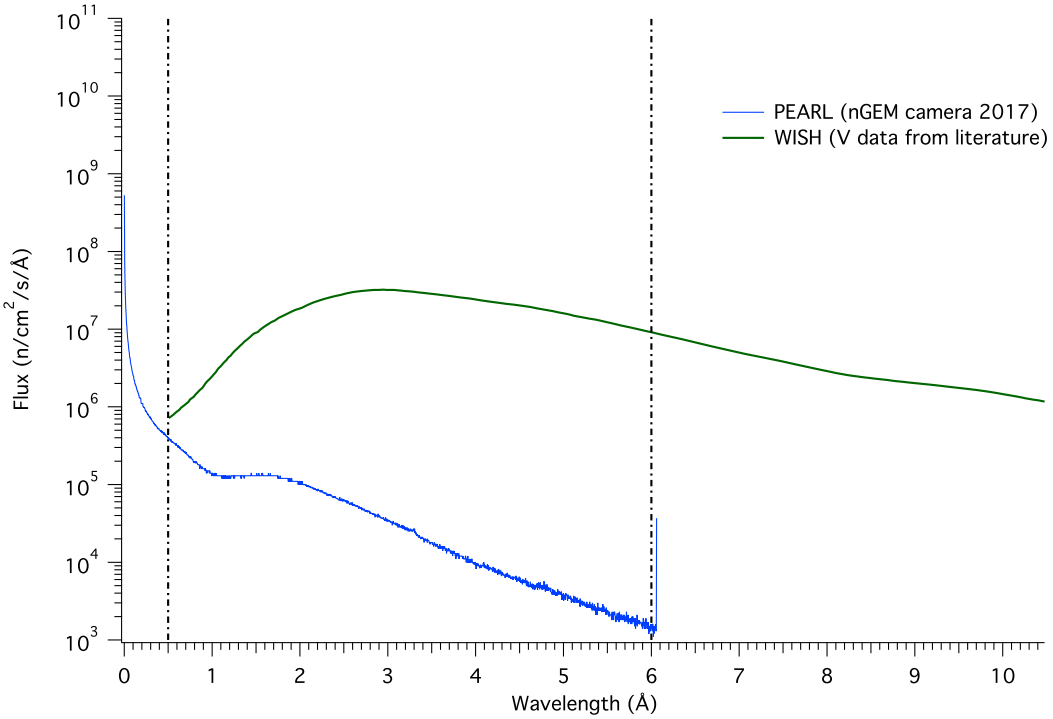

Figure 3.5 *Comparison of fully normalised flux data between WISH and PEARL diffractometers. The PEARL data was measured using a 2D energy sensitive neutron detector, the WISH data is from the literature [107]. The dashed separated region represents the normal operating bandwidth of PEARL. This demonstrates the large amount of high energy flux which is not routinely used for measurements due to strong background contributions.*

set of jaws on WISH are a considerable distance from the sample position, but can still provide a well defined profile at the sample. However if the beam is set to too small a profile, the divergence becomes considerable, such that the surrounding material is still immersed in the beam, resulting in a negligible decrease in parasitic scattering. WISH regularly operates with two beam profiles, 42 mm × 20 mm for powder samples, and 25 mm × 25 mm for single crystals. For this reason, masking, and slits incorporated in the pressure cell, close to the sample, are more important for WISH. Additional sample environment (cryostat shielding) limits the efficiency of this additional masking due to space constraints.

The magnitude of the flux provided is not the only important consideration, but also where the peak flux is in wavelength. Although signals become stronger with high flux, so do background contributions. Shielding and masking becomes less efficient the larger the incident flux at high energy. For this reason, and when coupled with the compelling science case of accessing significantly larger regions of Q-space, WISH becomes an attractive alternative instrument for performing high pressure diffraction measurements. Due to the layout of WISH (see figure 3.6), the fixed angle scattering geometry is an inefficient method of data collection, despite its potential advantages in terms of background reduction. The large in-plane detector coverage is well suited to radial-geometry scattering. An oscillating radial collimator reduces background from the instrument, and detected parasitic scattering from larger pieces of sample environment, such as cryostat shields, and vacuum tanks.

In the radial scattering geometry particular attention must to be given to the material chosen for the gasket. As will be discussed in detail the next chapter, there are many subtle mechanical constraints used to determine which materials are well suited as a gasket, many of which interplay with the material properties of the anvils used to compress them. Under sufficient force, the highest pressures can be generated in the strongest gasket materials, provided there is sufficient load applied, and so the challenge is in finding a strong, but deformable, material which is also highly transparent to neutrons.

3.3.4 Material selection

As discussed in chapter 2 there are multiple thermal, and thermo-mechanical properties to consider in addition to geometrical constraints and neutron scattering considerations. It is clear that the most neutron transparent high

Figure 3.6 *Pseudo-schematic showing the detector layout of WISH relative to the 'beam in' direction. The white grid represents the normal detector positions (some have been pulled back for maintenance). The sample is positioned at the centre of the ring within a vacuum tank. Between this and the detectors there is another tank filled with helium, which covers the full* 170° *in plane coverage either side and the* 30° *out of plane coverage.*

strength alloy is TiV4Al6. This is confirmed through transmission measurements performed on test pieces on the PEARL diffractometer at the ISIS neutron source, as compared against BeCu (see Appendix B for details). However, this alloy has very poor thermal diffusivity, approximately an order of magnitude lower than that of BeCu down to 50 K, whilst the iron content of the alloy can be a problem in magnetic studies at very low temperatures. Whilst the ultra pure ELI classification of this alloy is available, this form of the alloy is known to undergo a ductile-to-brittle transition at approximately 110 K.

Similarly Maraging and Inconel steels suffer from brittleness at low temperatures. This can lead to catastrophic failure of a highly stressed alloy, which may be stable at room temperature. As such BeCu is the most suitable structural material for the pressure cell. The poor neutron transmission of the material makes it very important that the amount of pressure cell material in the path of the beam is negligible. The largest benefit of using BeCu is in the high Cu content resulting in relatively high thermal diffusivity compared to steel. TiZr seems to offer the added benefit of being a null scattering material (contributing zero Bragg reflections), whilst also being relatively transmissive of neutrons. However, it has poor thermal diffusivity, and reduced tensile properties when compared with BeCu, which would result in the need for more material to support the same loads. TiZr is discussed further in Chapter 4.

3.4 Cell concept

The conventional way to apply load to clamped cells, and large opposed anvil cells is to use a hydraulic press to compress the sample assembly, and either a locking nut or set of bolts to then lock the cell. Hydraulics give good control over the loading of the cell, and using external hydraulics allows the overall dimensions of the cell to be reduced. Where extreme temperatures are used, or where very high loads are required, it is often unfeasible to incorporate the load frame into the instrument, the Paris-Edinburgh cell being a notable exception. Therefore to change the pressure the cell must be returned to ambient temperature, and allowed to radioactively decay. If long neutron data collections are performed the cell may become very active, remaining unsafe to handle for some time. BeCu activates particularly badly, often taking 24hrs to reach safe activity levels. For the current cell design a compact loading apparatus is incorporated into the cell body, allowing for in-situ pressure control.

Helium gas was chosen as the most suitable hydraulic fluid to transmit load to the sample at low temperatures. It remains fluid at a given pressure to lower temperatures than any other substance, allowing the pressure to be controlled most effectively. When the helium freezes, the isochoric pressure loss to absolute zero is lower than for any other solid, such that the reduction in load should be minimal. Additionally, the shear strength of solid helium is lower than any other substance at the same temperature. This ensures that pressure gradients in the solid are low, making it more efficient as a load transmitting medium. The pressure temperature melting curve of helium is included in the supplementary material in Appendix B.

The required volume of pressure fluid needn't be very large in order to transmit the load, whilst the required pressure depends on the internal dimensions of the cell and piston. Somenkov [85] report that the very largest opposed anvil pressure cells used at the Kurchatov Institute were capable of generating approximately 25 tonnes force, though the standard size cell was capable of 6 tonnes force. Goncharenko [82] reported that both of these cells could only be operated statically, due to space restraints in 100 mm cryostats. Okuchi et al. [96] report forces generated up to 5 tonnes, again only statically. Whilst a conventional diamond anvil cell is limited to approximately 1 tonne force, the diamond anvil cell used on the SNAP diffractometer applied forces up to 12 tonnes force using a double-membrane device with outer diameter slightly larger than 100 mm, too large for normal cryostat operation.

3.4.1 Mk1 design

Since the maximum sample volume which can be taken to a given pressure in the cell is limited by the maximum load, the initial design of the pressure cell attempted to incorporate the largest forces possible given the space restraints of the cryostat. An overview of the Mk1 design is shown in figure 3.7. It consists of a single cell body machined from BeCu, the larger, lower section of the cell contains the piston, and the hydraulic fluid to transmit the load to the sample. The sample region is visible through four equally spaced windows on the cell, where the anvil assembly is housed, such that neither the incident or diffracted neutron beam is attenuated by the cell. Each pillar blocks 20° of in plane detector coverage, designed to ensure that the 90° bank is clear. This was chosen as 90° gives a good balance between resolution, magnetic neutron diffraction signal, and

scattered intensity. The upper section of the cell is smaller in diameter, reducing the total mass of the cell and marginally improving the solid angle of the windows. The main challenge was the design of the hydraulic section of the cell. Two variants of the system were trialled, each having previously been implemented with some success in the Paris-Edinburgh load cell. The internal diameter of the hydraulic cross section is 65 mm; if frictional effects between the piston and the body of the cell are ignored, an ordinary 200 bar bottle pressure should be able to generate approximately 6 tonnes force; if the input pressure is increased to 1 kbar (achievable using an intensifier unit) the maximum force would be closer to 30 tonnes force. However, whilst finite element analysis (performed using ANSYS Workbench Static Structural Module) of the cell indicates that the lower chamber of the cell can easily cope with the stresses of 1 kbar, it also shows that the pillars of the cell would be expected to yield at 600 bar (see Appendix B), such that the cell can be safely operated up to approximately 300 bar with a safety factor of 2. This maximum working load was determined by calculating the load the cell would be expected to yield, and subsequently limiting the maximum working load to incorporate the safety factor.

The main disadvantage with using helium is that it's low viscosity also makes it more difficult to seal than other hydraulic fluids. In the frictional seal design, an indium seal is used to seal a relatively large cross section behind the piston. Indium is chosen as it is extremely malleable, filling the volume between the two sealing faces, however, this seal reduces the efficiency of the cell due to the friction in the seal hindering motion of the piston. The alternative seal used in the Paris-Edinburgh cell is the 'energised' seal. This is a teflon ring with a three sided square profile, loaded with a coiled spring. The concept of operation for most seals is that if the pressure is higher in the seal than in the vessel it is sealing, then it will hold. The energised progressively deforms, improving the seal with increased pressure. Both of these seal mechanisms were trialled, and both sealed successfully up to 200 bar at room temperature. Upon cooling in an orange cryostat, the frictional seal started to leak at 50 K and pressure was completely lost by 25 K. The energised seal was marginally more successful, maintaining a good seal down to 30 K, where is started to leak.

It was therefore decided to redesign the pressure cell to make a number of improvements; addressing the efficiency of the device, optimising the load performance and mass of the cell, and reconfiguring the angular positioning of the pillars relative to the instrument.

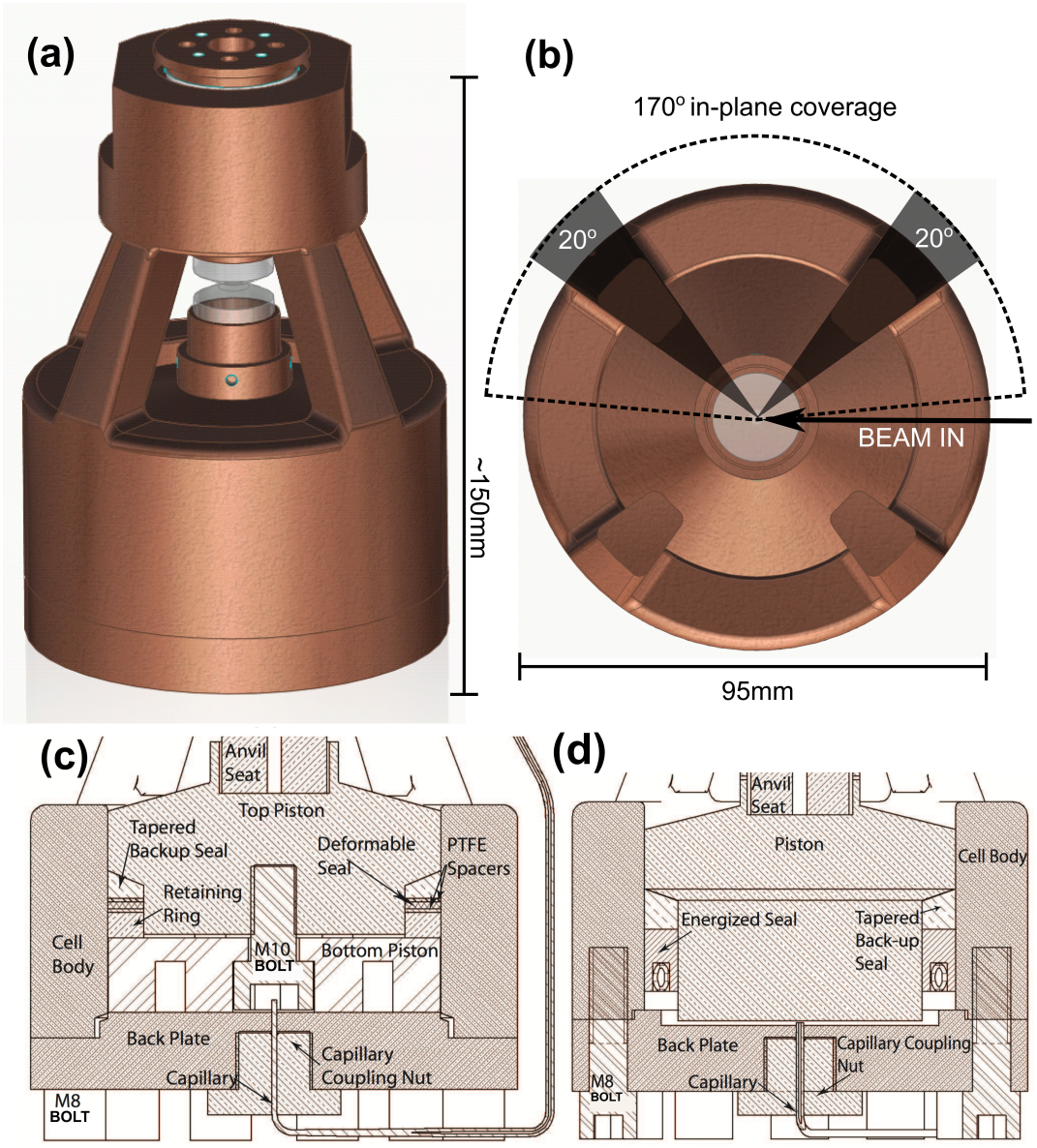

Figure 3.7 *(a) isometric CAD render of assembled Mk1 pressure cell; (b) top section view illustrating in-plane angular apertures, and pillar positions relative to the beam in position, and the detector coverage on WISH. Note that WISH has detector banks on both sides of the cell, ommited for clarity; (c) schematic section view of frictional indium 'deformable' seal variant; (d) schematic section view of energised seal variant.*

3.5 Cell redesign

3.5.1 The bellows unit

The key issue with the Mk1 design was the containment of the hydraulic helium at low temperatures; this was probably caused by the difference in thermal contraction between the cell body, and the material in the seal components. The solution was to use an enclosed membrane style system, as is popular with diamond anvil cells where much lower loads are required, and as was used with the SNAP diamond anvil cell. Most commercially available membrane systems are limited in load capacity. Details of other membrane systems reported in the literature are shown in table 3.1 [108–113]. All, apart from the large membrane used with the SNAP cell, which cannot be used with standard 100 mm cryostats, are limited to applying much less than 1 tonnes force.

Table 3.1 *Membrane specifications compiled from the literature as indicated. (n/a) - information not available.*

	Maximum Load (tonnes force)	Maximum extension (mm)	Dimensions of unit (length, diameter mm)
Feng et al. [108]	0.5	1	8, 21
Pfleiderer et al. [109]	0.3 (with amplification)	n/a	15, 20
Chen and Weinstein [110]	1 (four units stacked)	1.5	20 (each unit), 26
Webb et al. [111]	0.2	n/a	15, 45
Daniels and Ryschkewitsch [113]	8 (burst load)	< 0.25	2, 50
Boehler et al. [99]	12	< 1	n/a, 102

The traditional membrane structure is limited in either operable load, or in extension. Chen and Weinstein [110] overcame this limitation by stacking multiple units in series, mechanically coupling the units in parallel to ensure an additive total force. This complicates the design of the cell components, whilst increasing the total length of the system significantly. Daniels and Ryschkewitsch [113] simply welded two sheets of steel together, with a capillary connection, and reported large forces possible, though with extremely limited extension, such that

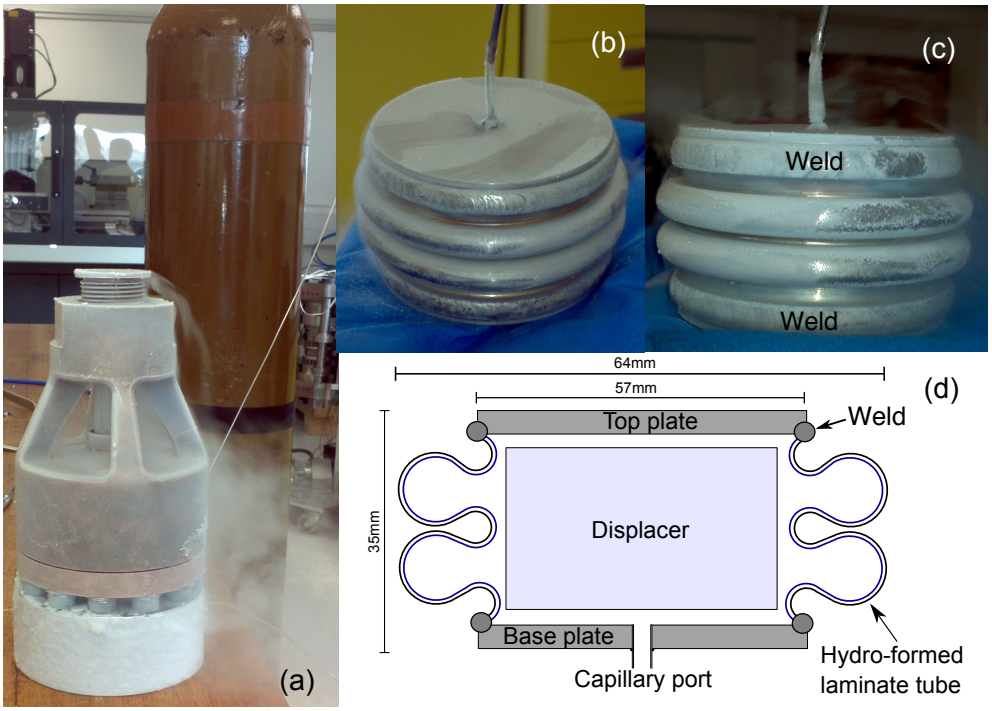

Figure 3.8 *(a) Assembled Mk1 cell with bellows unit for leak testing at liquid nitrogen temperatures; (b,c) bellows unit after first cool down test; (d) schematic of bellows design illustrating 'sprung' wall design. Only two concentric cylinders are shown for clarity.*

the device is only suitable for use with thin samples, where low deformations are required. High loads and large deformations enable high pressures to be generated on both small and larger samples where greater absolute volume reductions are required to generate the same pressure. This gives the cell versatility for use with a variety of different sample assemblies.

The limited deformation is due to the high stresses in the bending of the membrane foils, which are held together by a single weld; to overcome this, an alternative design was adopted. This device is known as a 'bellows', which is similar to a stacked membrane, but is reliant on a different mechanism of operation. Instead of relying on the bending of the upper and lower membrane foils to generate displacement, the extension is instead incorporated into the sides of the device. Instead of using the flexure of two foils to apply displacement and load, the top and bottom plates of the bellows remain rigid, and a spring profile in the wall between them deforms. In this case, eight concentrically stacked 0.25 mm tubes of stainless steel were hydro-formed together to create the laminated spring profile. 5 mm thick stainless steel top and bottom end plates were welded to either end of the profiled tube, ensuring rigidity under high loads. Figure 3.8 shows the

construction of the unit. The centre of the device is filled with a displacer, reducing the total volume of gas required to pressurise the device, which is filled via a 1.5 mm diameter capillary, with 0.2 mm inner diameter.

The bellows unit is proofed to 1 kbar, with an approximate linear load output of $0.0225\,\mathrm{t\,bar^{-1}}$ of inlet pressure. For standard bottle pressure (200 bar) the maximum load output is 4.5 tonne force, whilst the maximum extension of the device is 1-2 mm, depending on the initial compression of the device before loading.

Pressure control

The pressure in the bellows must be continuously monitored during cooling as the helium condenses. Initially the load on the cell was manually monitored using a regulator. This results in a fluctuating load on the sample, which can damage the anvils. To improve this an automated gas handling system was commissioned and assembled at the ISIS neutron facility. A solenoid driven regulator is operated in a feedback loop with the measured pressure of helium in the capillary leading to the bellows. The panel also includes a vacuum port, allowing the bellows unit to be evacuated prior to pressurisation, to avoid icing in the capillary, forming a blockage. A schematic of the system is shown in the Appendix B. Whilst this system substantially improves the low temperature performance of the bellows, it should be noted that the feedback loop relies on the pressure measured outside the cryostat at the top of the capillary. This assumes that there is a negligible pressure gradient formed in the capillary down to the bellows. The pressure gradients in small diameter tubes due to temperature gradients has been reported elsewhere [114]. As the diameter of the capillary in this case is much larger than the mean free path of helium over the full temperature range, the expected pressure drop is negligible.

Low temperature characterisation

One concern with the use of a gaseous membrane or bellows unit is that the load output from the device will vary with temperature, depending on the relative contraction of the cell material and the unit. This was not an issue with the Mk1 design, as the gas pressure was applied directly to the piston of the cell. To characterise the load output of the bellows, a quick series of strain gauge tests

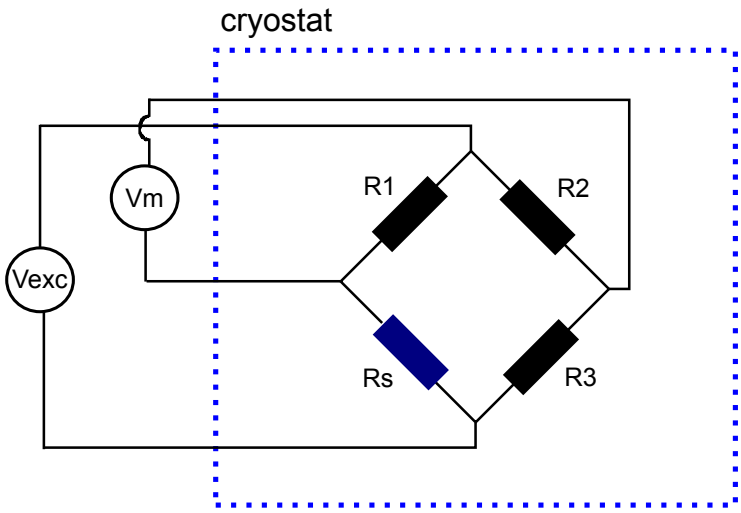

Figure 3.9 *Schematic of full strain gauge bridge circuit. The circuit is excited with a voltage V_{exc}, and whilst the ratio of resistances $R_s/R_1 = R_3/R_2$ the measured voltage, V_m, is zero.*

were performed. The sample assembly was replaced with a blank rod of BeCu, machined to known dimensions, and fixed with two strain gauges. One aligned with the axis of the rod, the other with placed along the diameter of the rod. The cell was then cooled from room temperature to base temperature in a CCR.

To remove the resistance of the long wires leading to the strain gauges through the centre stick to the cryostat, a full strain gauge bridge was used [115]. A bridge circuit measures a voltage change across the circuit only if there is an imbalance between the resistance of the strain gauges in the circuit (see figure 3.9). Instead of using external resistors to balance the strain gauge on the test piece, three additional identical strain gauges (R_1, R_2, R_3) were fixed to an unstrained reference sample of BeCu, which was installed close to the gauge on the strained test part. It was therefore assumed that any temperature differences between the strained and unstrained legs of the bridge were minimal. This technique results in no measured voltage change due to the thermal expansion of the BeCu test piece, or due to temperature induced changes in resistance of the strain gauges themselves, as these effects are assumed to be identical between all legs of the bridge. In other words, R_s will only become unbalanced due to axial strain effects on the test piece. A Keithley source-meter was used to excite the bridge with 6 V DC, and also to measure the resultant voltage due to strain differences between the four strain gauges. To reduce the voltage drop over the wires leading to the bridge (through the CCR), the compliance current was set to a minimum. To remove effects other than the output from the bellows, an

ambient pressure cooling run was performed first for background corrections. This measured voltage was subsequently subtracted from measurements with load applied from the bellows unit.

The measured voltage can be converted to strain using the simple relation that the resistance of a wire (R) can be related to it's resistivity (ρ), length (l) and cross sectional area (A):

$$R = \frac{\rho\, l}{A}$$

As such the relative change in resistance ($\Delta R/R$) is proportional to the relative change in length of the wire ($\Delta l/l$). The strain gauges used were calibrated by the supplier, providing a gauge factor (GF) or constant of proportionality, to account for minor changes in A and ρ under strain. The strain (ϵ) is related to the measured voltage [116]:

$$\epsilon = \frac{-4\,\frac{V_m}{V_{exc}}}{GF\,(1 + 2\,\frac{V_m}{V_{exc}})}$$

Figure 3.10 shows the processed data, showing that the load output drops by up to 8% at low temperatures, recovering a little at base temperature. This drop in load is not due to the difference in thermal expansion between the bellows and cell body, which is corrected for in the background measurements, but due to the change in mechanical properties of the bellows. As stainless steel is cooled, it's elastic modulus (E) stiffens. The gradient of E versus temperature is largest from room temperature down to approximately 100 K, then flattening. This would explain the change in behaviour at the temperature, though doesn't explain the recovered load at lower temperatures. The elastic modulus of stainless steel 316 is reported to increase by 7-8% from room temperature to 4 K, consistent with the measured drop in load.

The strain gauge data at room temperature was also used to determine the absolute value of the load output from the bellows as a function of pressure. The axial and hoop stresses in the BeCu test piece were compared against those predicted from finite element analysis. These results confirm the approximate $0.0225\,\mathrm{t\,bar^{-1}}$ performance, and are included in Appendix B.

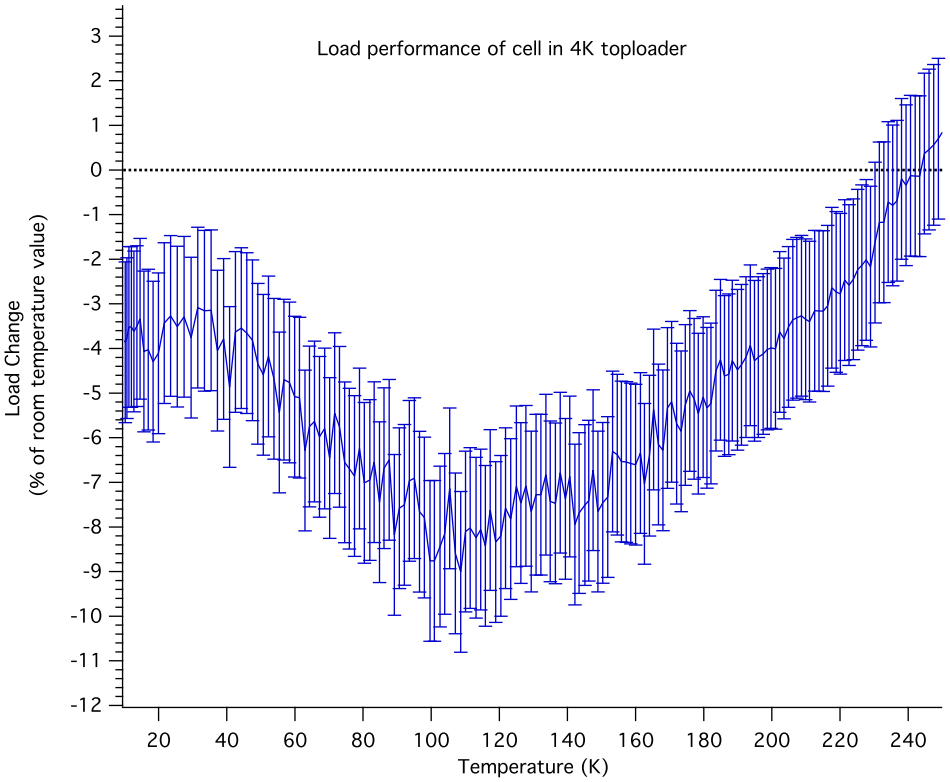

Figure 3.10 *Plot of experimentally determined load output of bellows unit as a function of temperature, as determined by strain gauge measurements. Calculated load drop determined from axial strain gauge on BeCu test piece. The errors are calculated as constants based on the uncertainty in the measured, and input voltage due to the Keithley source-meter.*

3.5.2 Mk2 design

An additional problem with the Mk1 design was that the size of the cell was disproportionate to its load capabilities. The base of the cell was strong enough to contain 1 kbar, yet the pillars of the cell could only safely support 600 bar. Furthermore, with the new bellows unit, there was no longer the need for such thick walls to contain the pressure fluid. Finite element analysis was performed to redesign the cell, improve its ease of use, and incorporate the bellows design more efficiently.

Aside from mass reduction, the position of the pillars on the Mk1 design were changed to optimise the aperture of the cell for use on WISH, and to improve the masking/shielding of the pressure cell to reduce background. The widows on the Mk1 give 70° clearance at equally spaced sections of the cell. The positioning of these pillars meant that no matter what angle the cell is rotated there is a pillar blocking some useful part of the detectors on the instrument (each blocking 20°). The main use for the cell is for low temperature magnetic studies under pressure, such that a mixture of high and low Q scattering data is required; low Q is needed as the magnetic form factor attenuates magnetic reflections at high Q. Conversely high Q, on a time-of-flight instrument, has improved resolution, and is needed for the study of more subtle crystallographic features. A mixture of scattering geometries allows peak instrument flux to be centred on the d-spacing region of interest in the sample. The geometry of the Mk1 cell also makes it difficult to effectively mask the incident beam to be incident only on the sample position. If one of the windows is blocked by a slit, then the useful aperture of the cell is reduced by 70°.

3.5.3 Cell FEA optimisation

The Mk2 design is shown in figure 3.11, with finite element analysis shown in figure 3.12. Additional FEA was performed on the anvil housing, the piston, and threaded parts of the cell, to ensure suitability for the loads required. The upper section of the cell was simplified, removing the tapered pillars, reducing the stresses in the top and bottom of the pillars, requiring less material to support the same load. In addition, the geometry of the pillars has been changed, concentrating the aperture of the cell around the $2\theta = 90°$ detectors, with $\pm 60°$ from this position. This provides a better balance of useful scattering angles

available to the cell. Contracting the four pillars to two with beam apertures allows the apertures to be used to easily and efficiently mask sections of the incident beam, without reducing the useful aperture of the cell.

The altered geometry of the cell brings additional benefits; the alignment of the anvil assembly is much easier, largely determined by the fit of the anvil seats to the cylindrical axis of the cell. It was also decided to make the anvil assembly a removable sub-assembly. This was done for two reasons: (a) it allows for the system to be assembled away from the load cell, under a microscope if required; (b) the smaller sub assembly can be used to gas load the anvil assembly in the future, bringing significant benefits to the hydrostaticity of the sample pressure. FEA of the anvil housing confirms that the anvil assembly is capable of holding up to 20 kN (within a safety factor of 2, calculated as previously), which is sufficient to lock and seal a gasket with an average face pressure of 2.8 GPa on a pair of 3 mm culets. If required, the thread on the anvil assembly is also capable of withstanding the torque required to generate this load.

The lower segment of the cell was significantly reduced in thickness (from 15 mm to 6 mm), as it was no longer required to withstand hydrostatic pressure when operated with the new bellows system. The length of the piston engagement was also significantly lengthened, reducing the frequent number of piston jams experienced with the Mk1 design.

The locking plate and bolts at the base of the cell was replaced with a single threaded base plate. The threads on both the upper and lower locking sections of the cell were changed to buttress (square) threads, designed to hold higher axial loads than a standard metric thread. This was verified via FEA, and allowed the dimensions of both to be reduced significantly. The cell was redesigned such that stresses reach a theoretical maximum at 600 bar; the base of the pillars are the weakest part of the cell. The cell is therefore safe to use routinely to 300 bar, or approximately 6.5 tonnes force. The overall mass of the cell, including the bellows, is 3.5 kg, reduced by over 20% from the original 4.5 kg. An interesting way to compare the efficiency of a load cell is to compare the ratio of load output per kg mass. The Mk1 maximum output was $3\,\mathrm{t\,kg^{-1}}$, the Mk2 has a maximum output of $3.9\,\mathrm{t\,kg^{-1}}$. The Paris-Edinburgh cell (all variants) which do not require a separate enclosure for the hydraulic fluid can output a maximum of $5\,\mathrm{t\,kg^{-1}}$. It is the mass, and dimensions of the bellows unit which reduces the efficiency of the cell presented here.

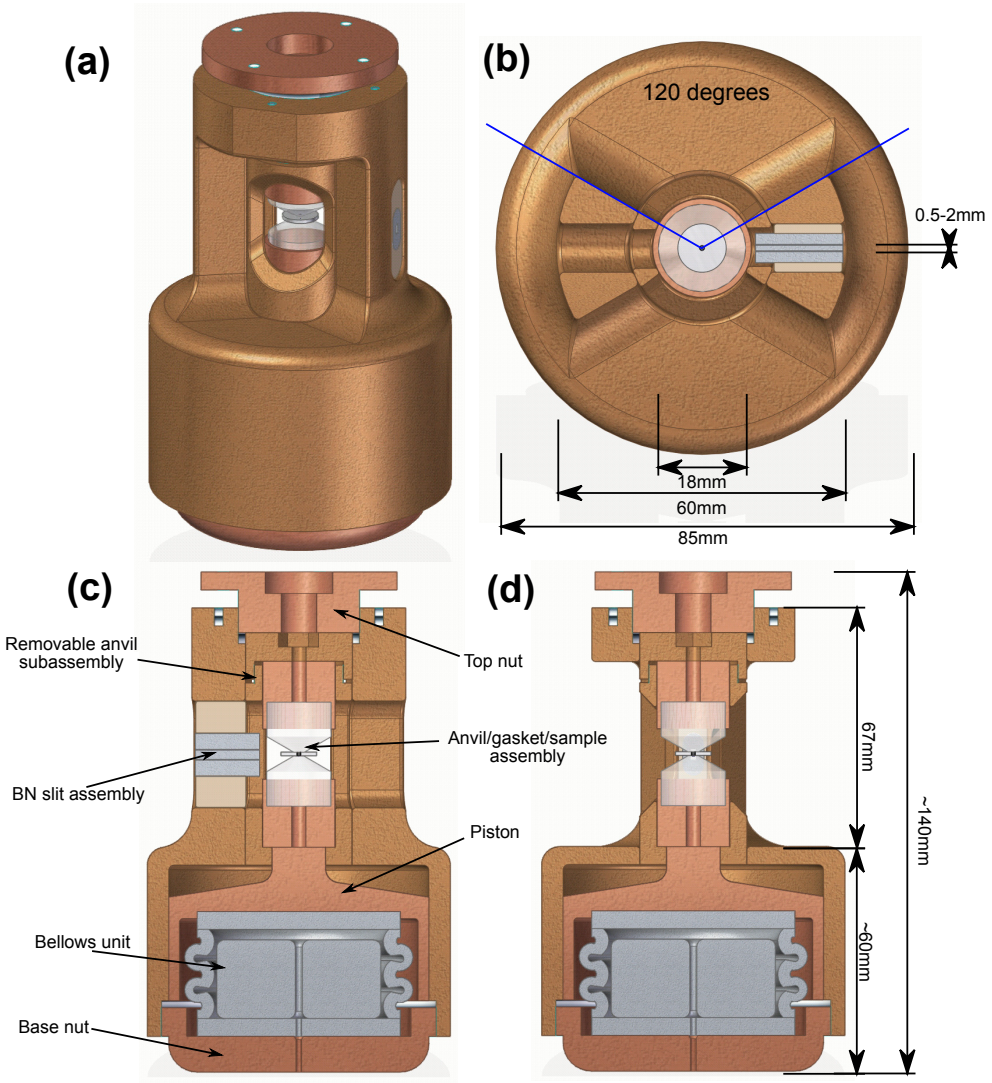

Figure 3.11 *(a) Overview of fully assembled Mk2 load cell; (b) section view taken through horizontal sample plane, illustrating free aperture for diffracted beam; (c) vertical section view showing pillar geometry used to house BN slit assembly. The anvil assembly is self contained, and can be assembled without the load cell; (d) vertical section of cell showing free out of plane aperture.*

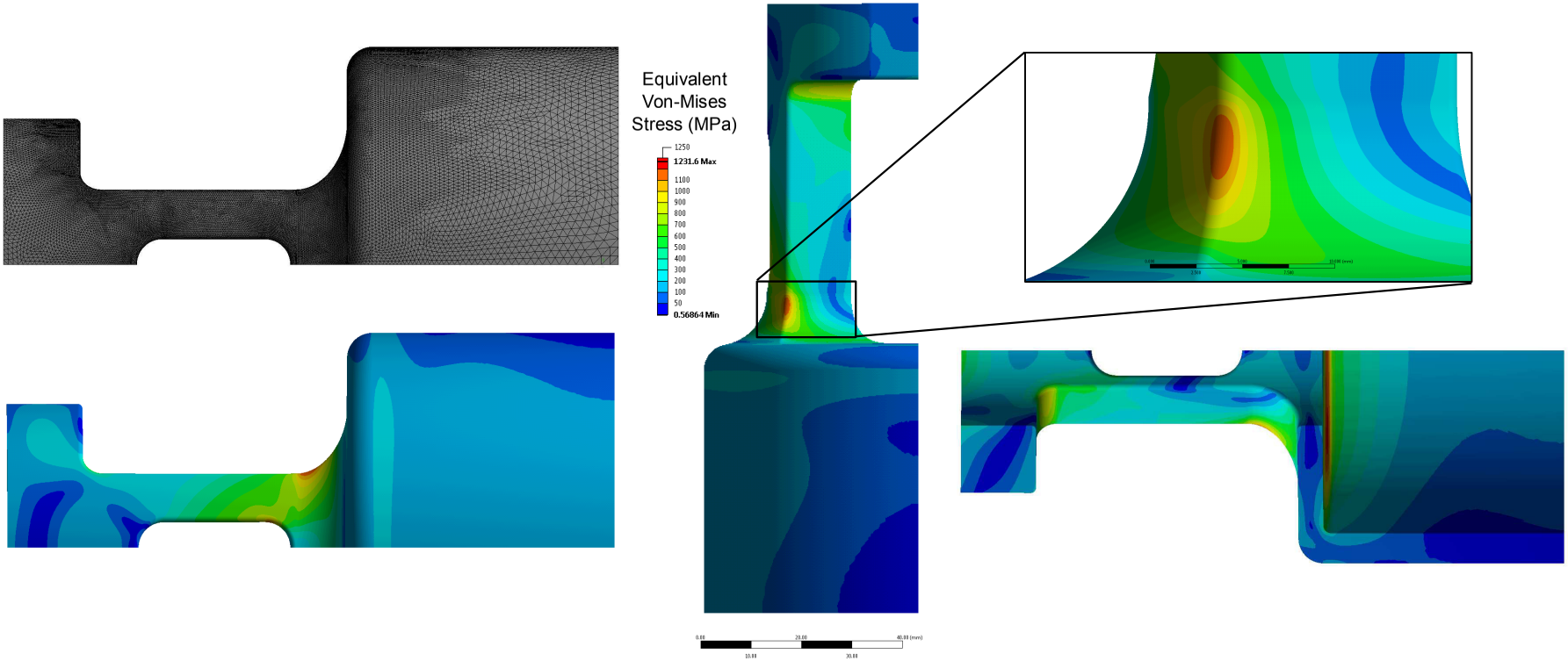

Figure 3.12 *FEA analysis performed on Mk2 design, showing mesh used, equivalent Von-Mises stress distribution, and points of maximum stress in the model. Calculations performed under force equivalent of* 600 bar *load. The maximum axial elongation of the cell was found to be approximately* 100 µm*. The yield strength of fully hardened BeCu is approximately* 1.3 GPa*. The symmetry of the cell was used to reduce the model to 1/4 the original number of elements. The lower section of the cell was restricted against axial movement, with the load applied to the upper surface of the cell. Weak supports were placed on one side of the cell to prevent rigid body motion.*

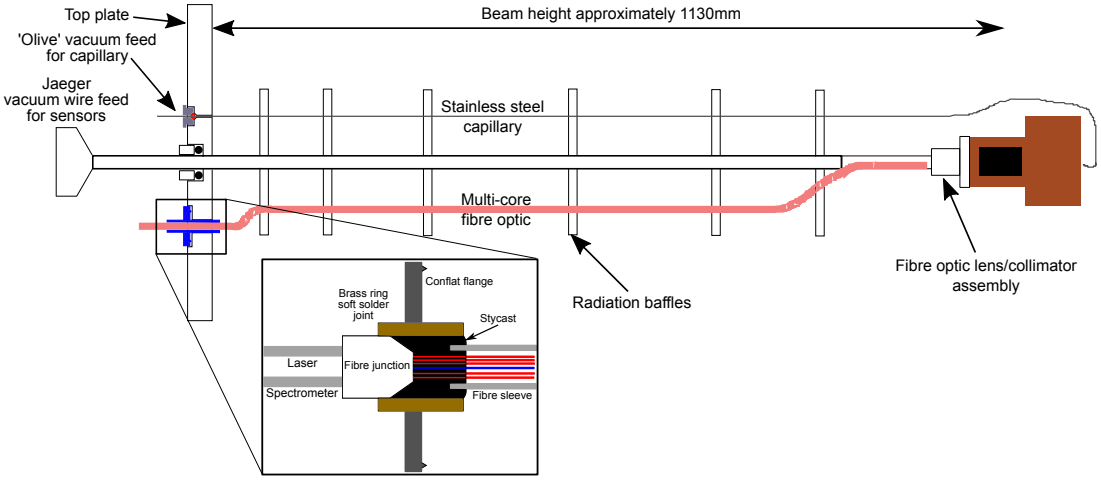

Figure 3.13 *Schematic of custom sample probe for pressure cell (shown horizontally, not in loaded orientation), incorporating vacuum feeds for the stainless steel capillary, and fibre optic cable. The stick itself is made from stainless steel. To sustain the weight of the cell, without increasing the cooling time of the stick, two different thickness tubes are used together, improving rigidity.*

Low temperature operation

To operate the cell at low temperatures in the cryostats and CCRs available, it was connected to a custom sample probe. The standard high pressure sample probe has a fixed probe temperature sensor, a floating sensor to attach to the sample, and connections for heating coils to aid sample temperature stabilisation. The Mk2 pressure cell requires additional connections; the capillary for the bellows unit, and a fibre-optic feed through to be used with the anvil assembly for in-situ sample pressure measurements. These additional connections need to operate under a vacuum to avoid icing in the cryostat/CCR. A schematic of the sample probe is shown in figure 3.13.

If the cell is inserted into the CCR with the CCR already cold, it can reach base temperatures in approximately 3 hours. However, if the cell is cooled with the CCR starting warm, it can take closer to 6 hours to reach base temperature. The same setup in the cryostat takes a varying amount of time to cool depending on how liberally the flow of liquid helium is set. At a modest flow rate of 20 mbar the cell will cool to approximately 2 K in 6 hours, which can be reduced to 3 hours if the flow rate is increased.

Loading the cell

Before loading the cell it is important that the approximate position of the anvil subassembly is set in the cell, such that the sample position is approximately centred on the incident window.

Initially the loading is performed using only the anvil sub-assembly, and is easiest to achieve under a microscope. Removing the top anvil, a pre-indented and drilled gasket is then positioned on the lower anvil. It can be helpful to fix the gasket in place for the loading procedure using a small piece of blu-tack, which can be removed after loading. If loading a powder, it is important to maximise the packing fraction of the sample in the hole, without excessively straining the sample. This can be done by progressively adding small quantities of powder to the hole region, and compressing lightly with the top anvil to encourage the powder to pack in the gasket hole. Excess sample material should be removed from around the sample region, either using a cotton bud, or through lightly spraying compressed air.

If a ruby chip is to be included in the sample region for in-situ pressure measurements, this is best fixed to the centre of the top anvil using a very small quantity of grease. This is done instead of placing the ruby in the sample region, as the introduction of pressure transmitting medium can often wash the ruby chip away, or out of sight from the spectrometer. The grease helps to ensure that the ruby chip doesn't fall off the anvil during the loading process.

Due to the very small volume of sample being loaded, including pressure medium is challenging. The most effective technique is to gently drop the medium over the sample hole in excess. The packing of the sample in the hole prevents it being washed away, whilst the medium can still fill the gaps in the sample volume. The excess medium on the surface of the gasket gives additional time to seal the cell before it all evaporates. With the medium included, the top anvil, with ruby chip fixed, should be slowly lowered onto the gasket, avoiding rotating the anvil as it makes contact with the sample, as this can cause the ruby chip to dislocate. The locking nut should then be tightened, again, avoiding torque on the sample.

The anvil insert must then be promptly transferred to the loading cell; a light force needs to then be applied to ensure that the pressure medium is sealed in the gasket. The exact force required will depend on the amount of pre-indentation performed on the gasket. If ruby is used, the best way to ensure sealing is to keep

increasing the load on the cell until the ruby signal starts to shift. This indicates pressure increase, and a sealed gasket.

3.6 Neutron diffraction testing

3.6.1 Masking & sample centering

One of the advantages of the Mk2 design is that it is easier to mask, and shape the incident beam. The small window between the pillars is used to house a number of different BN slits of different dimensions. These can be altered to match the required sample size, and further adapted using Cd or Gd foil.

The incident beam side of the cell (either can be chosen) should be faced off with Cd foil, to ensure that BeCu is absent from the measured data. Additional Cd can be used to face the larger windows on the cell, though the slits used should ensure that there is minimal BeCu contributed to the beam.

When used in the cryostat, the load axis of the cell is parallel to the axis of the stick, and it is very difficult to align the slit on the cell with the top flange, due to the length of the stick. A laser alignment tool, fixed to the top of the sample stick, is used to roughly align the slit within a 5° window of the nominal 'beam-in' position. The incident slit has a 5° acceptance angle. To centre this properly, a rotation stage is required on the cryostat/CCR to allow for finely controlled axial rotations in 1° steps over the 5° window of the nominal slit centre. Through comparing the intensity of the sample reflections as a function of angle, the actual centre position can be determined.

3.6.2 Searching for the missing phase of $SrTiO_3$

$SrTiO_3$ is paraelectric under ambient conditions, but undergoes an antiferrodistortive phase transition from cubic $Pm\bar{3}m$ to tetragonal I4/mcm at 105 K [117], which can be replicated at room temperature at a pressure of 9 GPa. The sample remains paraelectric at lower temperatures due to the presence of strong quantum fluctuations preventing the onset of ferroelectric order. There have been several indications that a further orthorhombic phase transition may exist in the material under ambient pressure at low temperatures [118, 119] and at

room temperature at high pressure (approximately 14 GPa) [120, 121], though the evidence has been largely speculative, without any definitive structural data. Although hydrostatic pressure usually suppresses ferroelectricity in insulating perovskites, this additional phase was thought to be the structure of the suppressed ferroelectric phase of $SrTiO_3$. A more recent combined structural and Raman single crystal study found no evidence of additional phases present up to 53 GPa at room temperature [122]. There are no reports of high pressure studies of $SrTiO_3$ at low temperatures, though it is possible that the distortive transition can be encouraged at low temperature at lower pressures, as is found with the cubic-tetragonal transition. The newly developed pressure cell was chosen to investigate the effect of pressure on the low temperature phase of $SrTiO_3$, and to determine the presence and structure of a new phase. Neutron diffraction was chosen to enable the more accurate determination of the orientation of the oxygen octahedra in the presence of the heavy Sr and Ti atoms.

Results

High purity (99%+ metals basis) $SrTiO_3$ was purchased from Alfa Aesar in powder form. Initially a portion of the sample was loaded into a thin vanadium can to verify the expected signal from the sample; the can was then cooled in an orange cryostat to 70 K to see the emergence of the tetragonal phase (see figure 3.14)

The pressure cell was loaded using sapphire anvils, and an aluminium gasket, using deuterated 4:1 methanol:ethanol as a pressure medium. Ruby fluorescence was used to determine the sample pressure in-situ, allowing the pressure of the sample to be monitored over the full temperature range of the experiment. The cell was loaded to 2.5 GPa and cooled to 230 K with data collected on cooling. The cell took 2 hours to reach this temperature, and a further 3 hours were required to reach 10 K where a 7 hour data collection was performed. The pressure in the cell was seen to increase marginally upon cooling to 2.6 GPa. The cell was then warmed back to 50 K and pressurised further to 3 GPa before being cooled back to 10 K.

Data from the cell were initially corrected to remove regions on the detectors masked by the pillars of the pressure cell, and single crystal reflections from the sapphires were digitally masked from the data. Data collected at 2.5 GPa and 10 K is shown in figure 3.15. The extracted crystallographic data is shown in

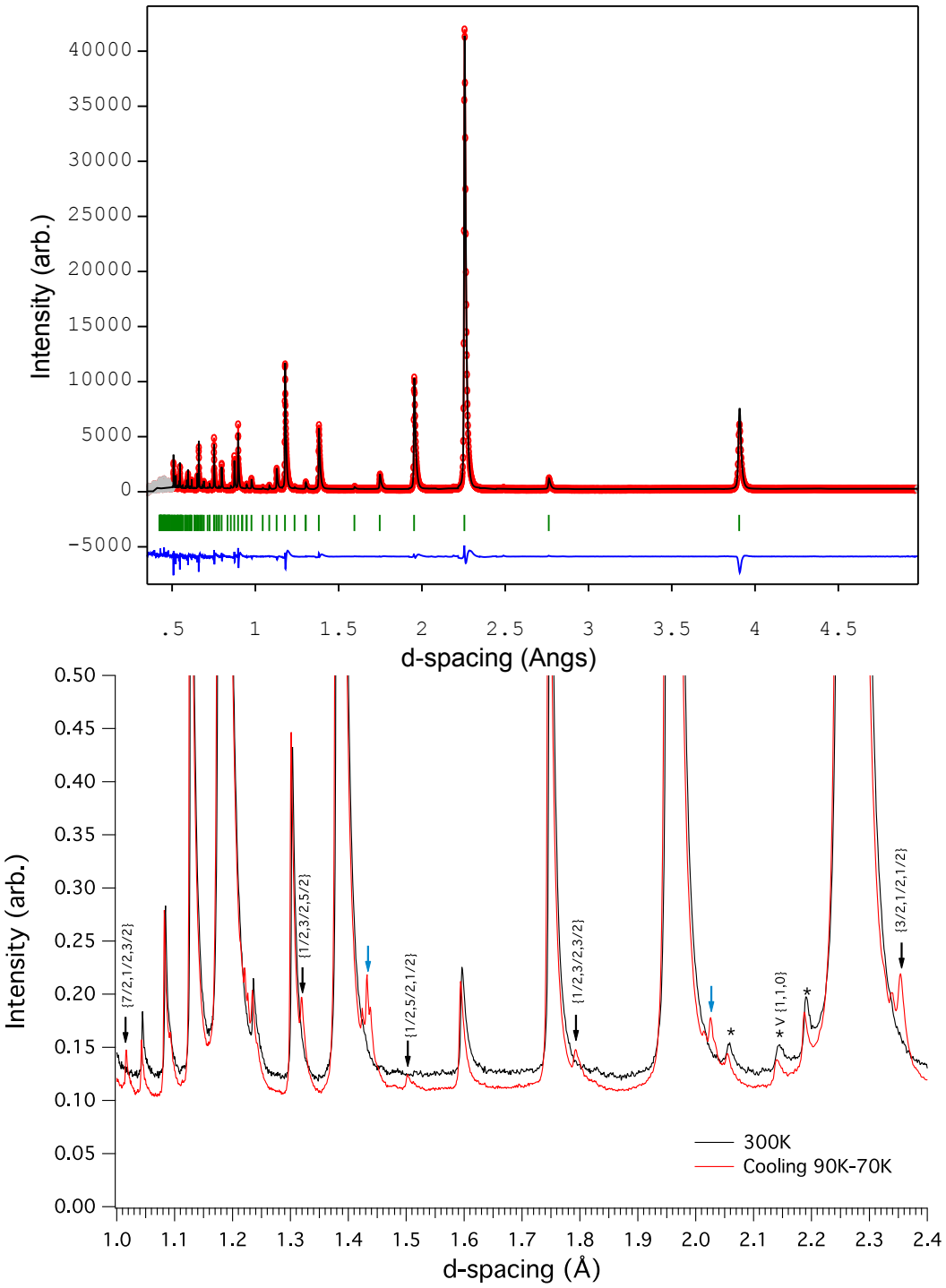

Figure 3.14 *(top)* 300 K *Reitveld refinement, confirming expected ambient structure,* $a = 3.906$ Å. *Data collected from backscattering detectors. (bottom)* 300 K *and* 90 K *data compared, showing the cubic to tetragonal transition. No splitting can be observed, but superlattice reflections appear (indexed in the cubic phase). The peaks marked* $(*)$ *are due to unidentified impurities in the sample, the peaks marked* ↓ *are reflections in the low temperature phase which cannot be indexed according to the tetragonal superlattice reflections, and may be due to an impurity phase.*

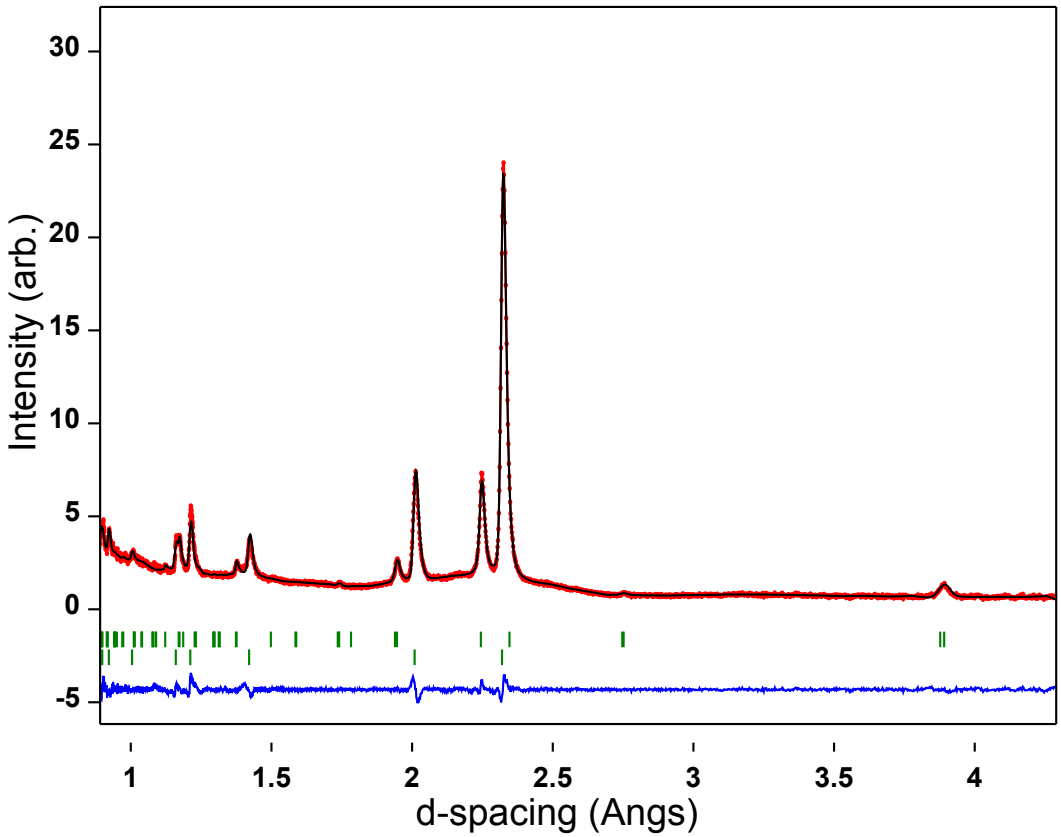

Figure 3.15 *$P = 2.5\,\mathrm{GPa}$, $T = 10\,\mathrm{K}$ data from bank 4 ($2\theta = 120°$), upper tick marks are from sample indexed in tetragonal phase, lower tick marks are from Al gasket. The Al peaks have a slightly distorted peak shape due to the high strain the gasket is under at this pressure.*

Table 3.2 *Atomic positions as refined from $P = 2.5\,\mathrm{GPa}$ dataset with $SrTiO_3$ in the tetragonal phase.*

Spacegroup I4/mcm	x	y	z
Sr	0	0.5	0.25
Ti	0	0	0
O1	0	0	0.25
O2	0.2324(27)	0.7325(19)	0
a		5.5059(8) Å	
c		7.757(2) Å	
R_{Bragg}		5.5%	
χ^2		2.325%	

table 3.2.

Discussion

The data collected from the vanadium can confirms that the cubic-tetragonal transition shows the appearance of superlattice reflections at $\left(\frac{h}{2}, \frac{k}{2}, \frac{l}{2}\right)$ (indexed in the cubic phase) where $h, k, l = 2n + 1$ $(h \neq k)$ due to the doubling of the unit cell caused by the oxygen octahedra distortion, consistent with a change of symmetry from $Pm\bar{3}m$ to $I4/mcm$ [123]. The intensities of the superlattice peaks are very weak compared to the lattice reflections, though it is expected that they will become more intense at lower temperatures, after a longer period of time. However, no peak splitting is measurable, even in backscattering, due to the extremely small expected tetragonal distortion ($\frac{c}{a} \approx 1.0006$). The peaks expected to split, such as the (100), or (110) are observed to sharpen due to the lower temperature, rather than broaden due to the splitting.

The levels of background in the pressure cell are significantly higher, with some parasitic peaks contributed from the gasket material, and many of the small superstructure peaks from the sample are not visible at all. A small amount of peak splitting is possibly observed, though the instrument is still resolution limited. Although the data is sufficient to refine, this test shows that observing weak superlattice reflections from more subtle phase transitions (weak tetragonal distortion) is beyond the capability of the cell.

3.7 Future development

The cell is more suitable for the study of magnetic phase transitions, where the levels of background from the cell are lowest. $BiNiO_3$ is antiferromagnetic below room temperature, and is known to transform into a metallic state under applied pressure. At low temperatures there are indications that an additional phase exists between the ambient and high pressure phase. The cell was chosen to investigate whether this intermediate phase retained the magnetic structure of the ambient phase, or not. Figure 3.16 shows some recently collected raw data from a sample of $BiNiO_3$ in the cell at ambient conditions, and under pressure. This sample is challenging due to the low symmetry (triclinic) of the ambient conditions phase, but the data show that the sample is clearly visible. The cell

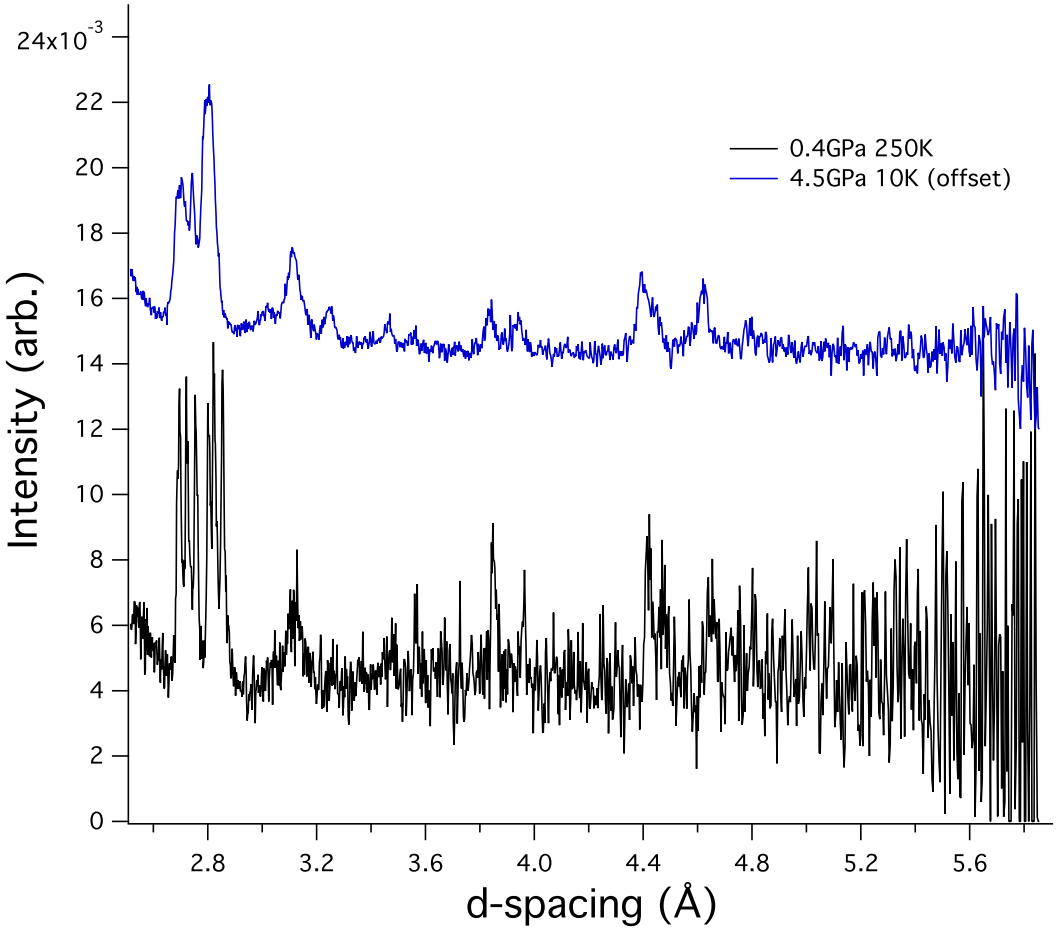

Figure 3.16 *$P = 4.5\,\mathrm{GPa}$, $T = 5\,\mathrm{K}$ data from bank 4 ($2\theta = 120°$). High pressure data is offset for clarity, the difference in statistics is due to the difference in counting times. All the peaks are from sample apart from a single contribution from a Pb pressure marker. cBN anvils were used, removing the need to mask any regions of the detectors, but preventing use of the ruby spectrometer.*

generated approximately 4.5 GPa pressure, and reached a base temperature of 5 K, provisionally there were no strong indications of any change to the signal from the sample; this will be investigated further. The complexity of the sample structure has prevented a full Rietveld refinement of the data, showing that there are clear limitations on the science which can be achieved with such small samples.

Currently the most substantial limitation with the cell is the pressure which can be applied to the bellows through the pressure control panel. With the current setup using 200 bar helium, the cell can output 4.5 tonnes force. The panel and cell are designed to hold 300 bar, but the panel isn't fitted with any form of pressure intensification. Due to the small volume of working gas held in the panel and bellows, a large buffer volume, connected to the intensifier will be required

to maintain the desired 300 bar, which could feasibly be maintained with a hand-driven intensifying unit.

In addition to upgrading the pressure output of the control panel, it is possible that the dimensions of the bellows unit itself can be optimised further; currently the mass of the bellows is 0.6 kg. Reducing the dimensions of the bellows would not only reduce it's mass, but would allow for additional optimisation of the load cell, leading to increased versatility in how fast the cell can be cooled and warmed.

In addition to small improvements to the operation of the cell for use in existing cryogenic equipment, it should be noted that if the cell were not reliant entirely on convective cooling, it could feasible reach base temperature in under an hour. For example, if a nitrogen pre-cooling loop were included 70 K could be reached very quickly, before switching to normal cryostat/CCR operation to continue cooling to base temperature.

Chapter 4

Developing an opposed anvil system for use with the cryogenic load cell

This chapter presents the design details of the opposed anvil system (anvils and gasket) used with the cryogenic load cell presented in Chapter 3. The details of the anvil system are discussed separately from the load cell design, as it presents a separate set of problems from those considered for the load cell. Furthermore, the load cell was designed to accommodate a number of different possible anvil sub-assemblies, the benefits and limitations of each will be discussed here. In addition, finite-element analyses of the opposed anvil system are presented, in an effort to understand the mechanics of large volume anvil cells, and their pressure limitations.

4.1 Introduction

Understanding large volume anvil systems is important for a number of different applications aside from neutron diffraction, the most industrially significant of which is the use of multi-anvil, and belt presses for high pressure material synthesis. One of the biggest markets for high pressure synthesis is in the growth of synthetic diamond, which is mostly used for abrasive purposes, but has many other emerging applications. Aside from industrial significance, high pressure synthesis is important scientifically, allowing the growth of other materials unstable under ambient conditions, which can be 'quenched' back to

room temperature. This is interesting for understanding numerous geophysical processes, but also for the synthesis of novel materials for electronic, magnetic and other applications.

Whilst the extreme hardness, and strength of diamond allows researchers to generate multi Mbar pressures on microscopic samples, scaling the system up is faced with a number of problems. Most crucially, larger gem quality diamonds are not readily available, or as reliable to operate due to the presence of natural flaws. The use of chemical vapour deposition (CVD), where a free carbon plasma is used to deposit high purity diamond on a seed surface, and nano poly-crystalline diamond (NPD) have helped increase the size of available diamond anvils (though they are not yet as readily available as alternative materials). However, scaling-up the anvil system (loads and dimensions) using an alternative anvil material doesn't necessarily reproduce the same pressure performance as for a conventional diamond anvil cell. To understand the limitations in scaling, and the mechanics of these systems, finite-element analysis is used, and the results are compared to those expected from theory.

4.2 Designing the anvil system

4.2.1 Anvil materials

The load cell can be used with a variety of different anvil materials, provided that they satisfy the geometric constraints of the load cell, outer diameter $\leq$ 18 mm and height $\leq$ 30 mm. A compilation of the physical properties of some common anvil materials is presented in table 4.1. This highlights the issues of balancing toughness, flexural strength and compressive strength. Whilst compressive strength is required to prevent deformation under high pressures, the anvil must also be tough to prevent the formation of cracks under stress. Aside from the physical hardness, and strength of the anvil materials, additional consideration must be given to the neutron properties of each.

In cases where the neutron beam is introduced in the axial geometry the beam is attenuated strongly by the anvil material. The intensity profile is altered, due to the presence of Bragg edges, such that the sample data needs to be carefully intensity corrected through careful background measurements. For a polycrystalline material Bragg edges form a saw tooth transmission profile as a

function of wavelength, due to diffraction from various crystallographic planes in the material. For a given *hkl* plane the Bragg angle increases as the wavelength increases until $2\theta = 180°$. Above this angle, no scattering can occur from that *hkl* plane, and as scattered intensity falls off in backscattering [62], this gives rise to a sharp increase in transmission. Conversely, for a single crystal material, only one wavelength will satisfy the Bragg condition for a given orientation of the crystal. This gives rise to a simplified transmission spectrum; essentially a level line with well defined dips. Further details may be found elsewhere [124].

In the radial scattering geometry, the anvil (whether single- or poly-crystalline) doesn't directly attenuate the sample signal through primary scattering processes, though may introduce small secondary scattering effects. Instead, the gasket material attenuates the incident neutron beam.

Natural diamond, and sapphire, have the added advantage of optical transparency, allowing the sample hole to be inspected during loading, and pressure to be measured during loading using ruby spectroscopy. Diamond and sapphire crystals have the advantage that their diffraction contributions can easily be disentangled from powder sample data, as sharp single crystal peaks which can be masked from the data. This is more so with diamond due to it's higher crystallographic symmetry when compared to sapphire. cBN is a strongly neutron absorbing material, which is advantageous where the cell is used in a radial geometry, effectively very tightly collimating the incident beam onto the sample volume.

The binder material used in some sintered ceramics can sometimes cause problems; either contributing a strong background signal (incoherent or coherent) or may be magnetic. For WC, Co and Ni are frequently used as binders. WC is a tough ceramic, capable of withstanding significant pressures and deformation before failure. The Co binder has several disadvantages, activating strongly under neutron irradiation, whilst also a room temperature ferromagnet ($\mu \sim 1.5\mu_B$), making it undesirable for low temperature studies. The Ni binder carbide is also ferromagnetic ($\mu \sim 0.5\mu_B$) at room temperature, and doesn't activate under neutron irradiation. However, it is significantly less susceptible to magnetic fields than Co, though this may be expected to change at very low temperatures. Tungsten carbide has further disadvantages; the quantity of binder used affects the carbides magnetic response, and it's mechanical properties. The diffraction signal from the WC, and any impurities in the binder, isn't particularly clean, such that it is advisable to avoid WC for low temperature studies where possible.

Sintered diamond anvils, whilst offering a lower incoherent background (binder dependent), also contribute strong powder reflections to the pattern, which cannot easily be removed from the data. For the above reasons, it is clear that single crystal anvils are preferable where powder samples are considered.

Sapphire anvil preparation

A considerable advantage of using sapphire over diamond is that it can be supplied to a very high purity in much larger dimensions, and at significantly lower cost. As sapphire is not as hard as diamond, it is easier to polish, and profile the anvil in the laboratory. Here is a brief summary of the polishing technique used during the work of this thesis.

There is a correlation between the quality of surface finish, and the flexural strength of sapphire [143], it is therefore important to maximise the quality of surface finish. The majority of the sapphires used were purchased pre-ground to approximately the desired profile. This significantly reduces the time required to finish the anvil, allowing more time to be spent on improving the final surface finish.

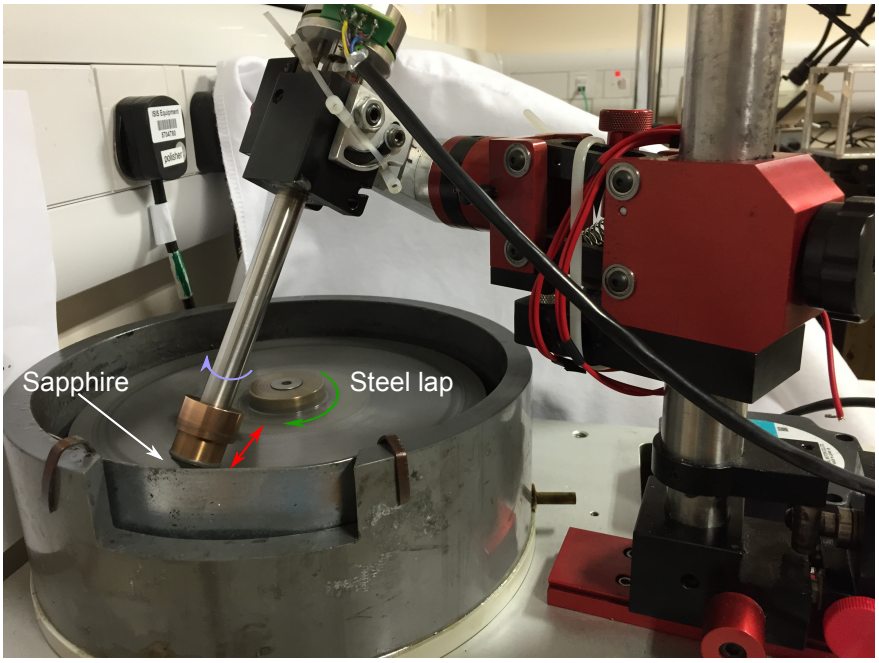

Figure 4.1 *Mechanical polisher, adapted to polish conical surfaces. The work piece is rotated, and ground over the surface of a steel disc which is also rotated, such that rate of wear should be even over the entire surface.*

Table 4.1 *Comparison of physical properties of various anvil materials where available from the literature. The range of values shown for WC include the deviation expected due to grain size.*

	Compressive strength	Tensile Strength	Fracture Toughness	Hardness	Flexural/Transverse Rupture Strength
Natural diamond	8-16 GPa [125], 10-30 GPa [126], 90-470 GPa $\|\|$*[111]*, 130-558 GPa $\|\|$*[110]*, 219-225 GPa $\|\|$*[100]* (theoretical) [127–129]	1-10 GPa [125], 2.8 GPa [130], 52.6 GPa $\|\|$*[111]*, 53.6 GPa $\|\|$*[110]*, 98.4 GPa $\|\|$*[100]* (theoretical) [128]	2 $MPa/m^{\frac{1}{2}}$ [131], $3.4 - 5\,MPa/m^{\frac{1}{2}}$ [130]	90-100 GPa Knoop	n/a
Sapphire (Al_2O_3)	2.4-3.4 GPa [132], 2-2.9 GPa [133], 2.4 GPa [134]	0.3 GPa $\|$a-axis, 0.45 GPa $\|$c-axis [132], 0.41 GPa [134]	4 $MPa/m^{\frac{1}{2}}$ [133]	2200-2300 Vickers [135]	0.69 GPa $\|$c-axis [136], 0.32 GPa [137], 0.42 GPa [138], 0.68 GPa [138, 139], 1.03 GPa $\|$c-axis, 1.54 GPa $\perp$c-axis [133]
WC [36]	6-7 GPa	2.3-2.5 GPa [140]	$8 - 10\,MPa/m^{\frac{1}{2}}$	1500-2000 Vickers	3.3-6 GPa (dependent on test volume) [140], 2-3 GPa [36]
cBN [36]	2.9 GPa	n/a	$6 - 7\,MPa/m^{\frac{1}{2}}$ [141], $10.5\,MPa/m^{\frac{1}{2}}$	28-30 GPa Knoop @10 N	0.55-0.72 GPa [142]
Sintered diamond (COMPAX) [36]	7.6-8.3 GPa	n/a	$9.5\,MPa/m^{\frac{1}{2}}$	36 GPa Knoop	1.5 GPa
Sintered diamond/SiC (ALMAX) [36]	4.7 GPa	n/a	$9.5\,MPa/m^{\frac{1}{2}}$	62 GPa Knoop	0.5 GPa

The anvils were initially polished mechanically, using a lapping-disc made from steel (figure 4.1), and a number of different diamond slurry grades. For rough profiling 10 µm grade slurry was used, which is then reduced in stages down to 0.5 µm grade for an optical finish. The rotational speed of the disc, and the pressure applied to the work piece, gave variable results on the quality of the polish. However, it was not clear whether this was due to the polishing process, or due to the mechanical tolerances on the polisher itself. To improve the finish, the anvil was finally hand polished using a fine lint-free cloth, and a very fine grade of Al_2O_3 paste. All sharp edges on the sapphire were 'broken' or rounded to prevent premature crack initiation. The main challenge with this polishing technique was in ensuring that the back and culet faces of the anvil remained strictly parallel.

To improve this, sapphire anvils were purchased with an optical grade chemical polish on the culet surface, with a specified tolerance on the parallelism of the two surface, and a pre-glaze finish on the pavilion which was then hand finished in the laboratory. The chemical polish of the culet was generally not found to improve the pressure performance of the anvil, indicating that there are more significant mechanical limitation to consider first.

4.2.2 Gasket considerations

Choice of gasket material depends on several parameters; the desired pressure range, the toughness of the anvil being used, and the background signal. Whilst the highest pressures can be reached with a gasket of higher yield strength if load is considered unlimited, in reality one must consider the load efficiency of the material, such that maximum pressures are attainable at the maximum load available.

For neutron diffraction there are a number of potential gasket materials; though in the radial scattering geometry, with such small samples, the reduction of beam intensity on the sample caused by the gasket, and the levels of coherent and incoherent background are critical.

To determine the effects of gasket attenuation on the measured signal, a series of test measurements were performed without the pressure cell. Empty gaskets, with dimensions typical of those used for pressure tests, were made from Al, BeCu and TiZr, and fixed to the end of a centre stick at the correct beam height. In

each case the gasket was orientated as it would be in the pressure cell, with the axis of the disc approximately perpendicular to the incident beam direction.

Time-of-flight sensitive monitors are positioned on the instrument immediately before, and after, the sample position, and were used to compare the transmission spectrum of each gasket. The results are presented in figure 4.2. To account for different monitor efficiencies the ratios of the results were compared (see figure 4.3). Apart from the Bragg edges from the choppers (used to tune the incident range of wavelengths), it was clear that there were no measurable additional edges introduced by the gasket material. Ideally the ratio in figure 4.3 would be 1 for all wavelengths, but importantly seems essentially linear. Comparing the peak intensities of the downstream monitors for each gasket material confirmed that Al was the most neutron transparent, and TiZr the least, matching the level of incoherent scattering. The result is important, showing that Bragg edges from the gasket affect the signal negligibly, such that involved attenuation corrections are not required.

4.2.3 Neutron diffraction testing

The diffraction signal from a number of gasket materials is considered in figure 4.4. The data was collected during the gasket attenuation tests performed on the WISH diffractometer. The gasket was fixed to a centre stick using a small amount of Al tape. It is clear that TiZr contributes no peaks over this q-range, and V only contributes a weak peak at approximately 2.15 Å. However, the nominally pure V contributes some spurious peaks at the longer d-spacing range, which is potentially important for the study of magnetic structures. In addition, the level of incoherent background for the V is probably too high. Interestingly, despite TiZr contributing a strong incoherent signal at lower d-spacings, this is found to drop to a level comparable with Al above 4 Å. Subsequent tests including the pressure cell, and anvils, have shown this result to be anomalous, and probably caused by imperfect mounting of the gasket, or poor statistics for the test. Figure 4.5 shows a comparison between the two gasket materials when held correctly in the pressure cell; showing no visible dip in background above 4 Å.

BeCu has two very broad peaks around 2 Å, which become more textured under applied load, making it very difficult to fit sample data in this region. Whilst all the gaskets chosen were specifically non-magnetic, some alloying content in stainless steels can result in magnetism at low temperatures, which may result

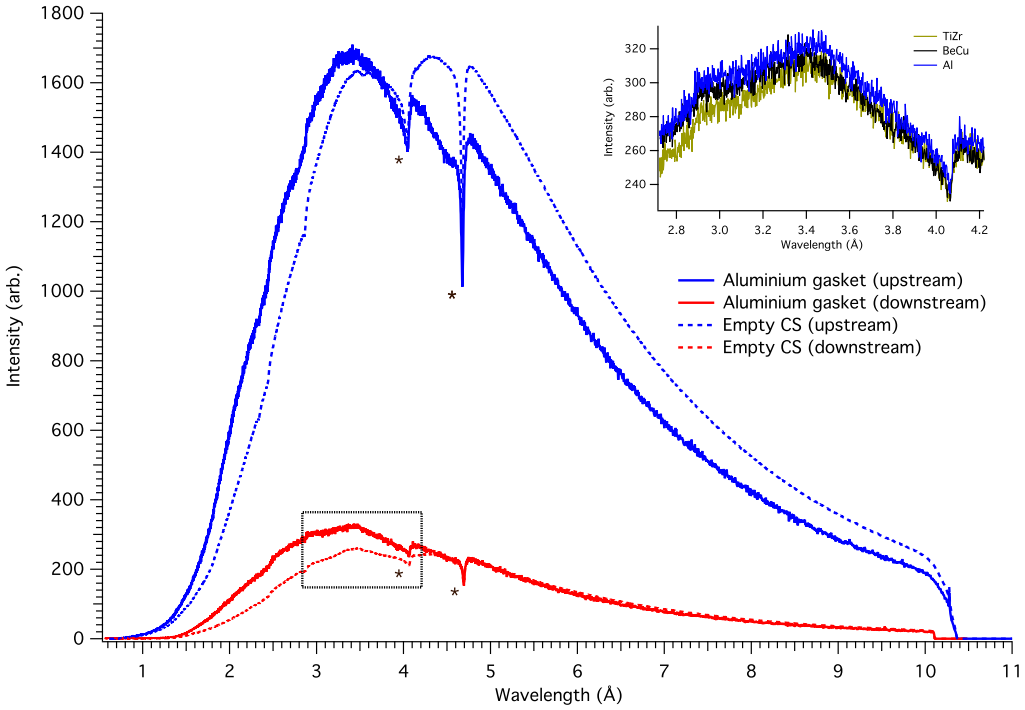

Figure 4.2 *Attenuation measurements from gasket material on WISH neutron diffractometer. The plot shows the measured intensity upstream and downstream from the sample position, compared to that from the empty instrument. The lower measured intensity of the downstream data is due to differences in monitor efficiency. The peaks marked (∗) are Bragg edges measured from the choppers on the instrument. Inset; downstream monitor data compared between three different gasket materials at peak flux. The skew between empty instrument and sample is due to different chopper settings.*

in additional peaks appearing at longer d. The nominally pure vanadium sample shows additional impurity peaks between 3.5 Å and 4.5 Å, which have not been characterise.

An additional consideration is the 1/e length for each of these materials. Al has a transparency approximately an order of magnitude larger than TiZr, and is therefore preferable in cases where the sample volume need be very small, or is a much weaker scatterer of neutrons.

4.3 Load testing

A number of different gasket/anvil configurations have been tested, using the Mk2 load cell, offline. These tests were performed using ruby spectroscopy to

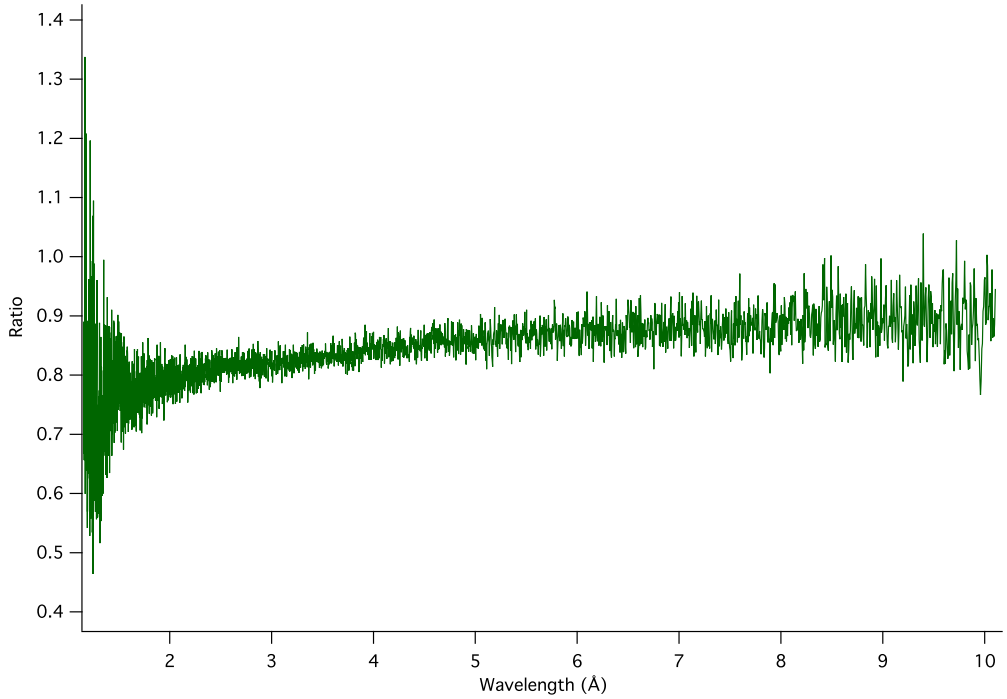

Figure 4.3 *To account for different efficiencies, the ratio of the upstream monitor to downstream monitor is compared with and without the sample. Perfect transmission would result in a ratio of 1.*

determine the sample pressure, such that only load curves for sapphires and diamonds are available. It is not expected that the load curves should differ much for alternative anvil materials of the same profile and dimensions, used with the same gasket configuration.

The samples used for the loading curve were in some cases real samples, and in other cases would be NaCl. To ensure a good packing of sample, the sample would be compacted into the sample hole using the WC anvils, though not to excess. In each case methanol:ethanol pressure fluid was included with the sample; a pool of pressure fluid was included in the sample region immediately prior to locking the two anvils together.

4.3.1 Sapphire anvils

The sapphires were polished to a simple conical profile, with a culet diameter of 3-4 mm, outer diameter of 18 mm, and taper angle of 30°. This taper angle was chosen to give a balance between the amount of support provided to the anvil, and the pressure-load efficiency of the anvil (discussed further in section 4.4.4).

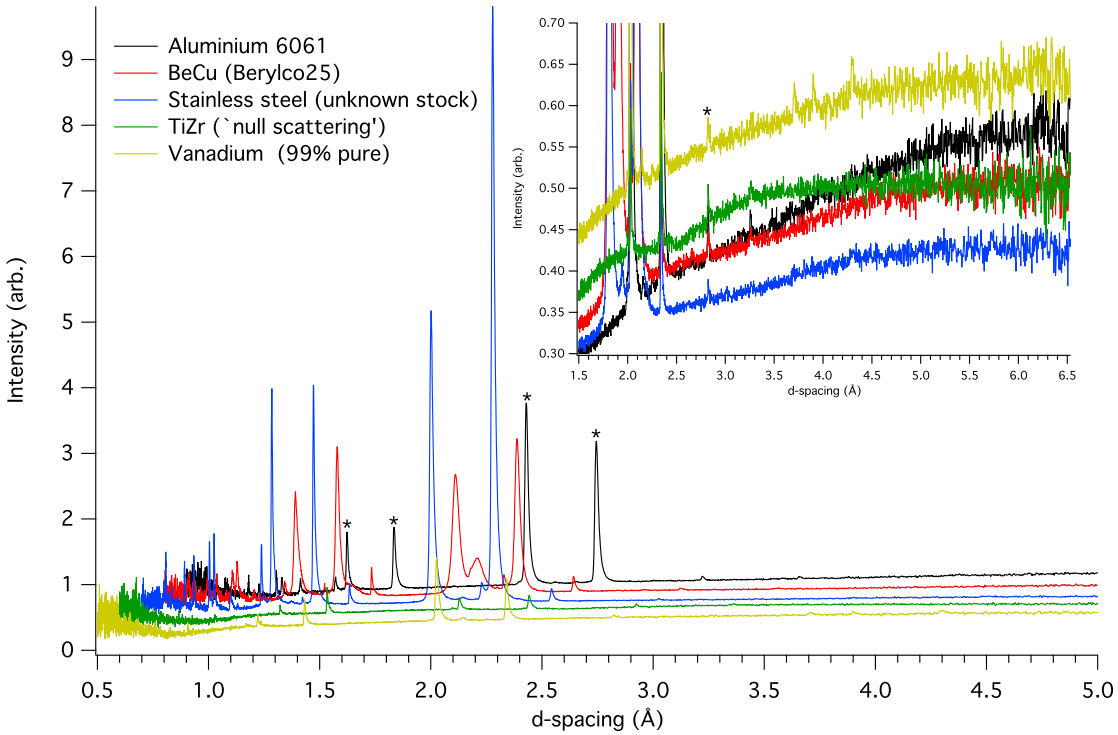

Figure 4.4 *Waterfall plot of diffraction signals measured on the* $75° < 2\theta < 105°$ *detector banks from various potential gasket materials, intensities normalised by current. The gaskets were fixed to a centre stick using a small amount of Al tape, hence the aluminium peaks are visible to some extent in each histogram (marked* $*$*). Inset, true scale (not offset) comparison of the incoherent background signal from each measurement.*

Pre-indentation of the gasket is done to provide massive support to the anvil and to the sample region upon loading. However, sapphires invariably seem to fail during the pre-indentation process, and are particularly vulnerable where the gasket is relatively hard. To avoid this issue, tougher WC anvils, polished to the same profile and dimensions as the sapphires, were used for the pre-indentation. It has been reported elsewhere that TiZr sticks to the surface of the sapphires, and that sputter coating is required to avoid this. No evidence of excessive gasket/anvil bonding was found during these tests. The sample holes were drilled to approximately 50-60% the diameter of the culet in each case. Figure 4.6 shows a typical loading curve for an aluminium and TiZr gasket.

The loading curves for the two gasket materials reflects their differing plastic mechanical properties. TiZr has approximately double the yield strength of the Al 6061 alloy, and shows different work hardening properties. During tensile tests TiZr shows 9-10% elongation at break, whereas Al 6061 shows 12-17% elongation

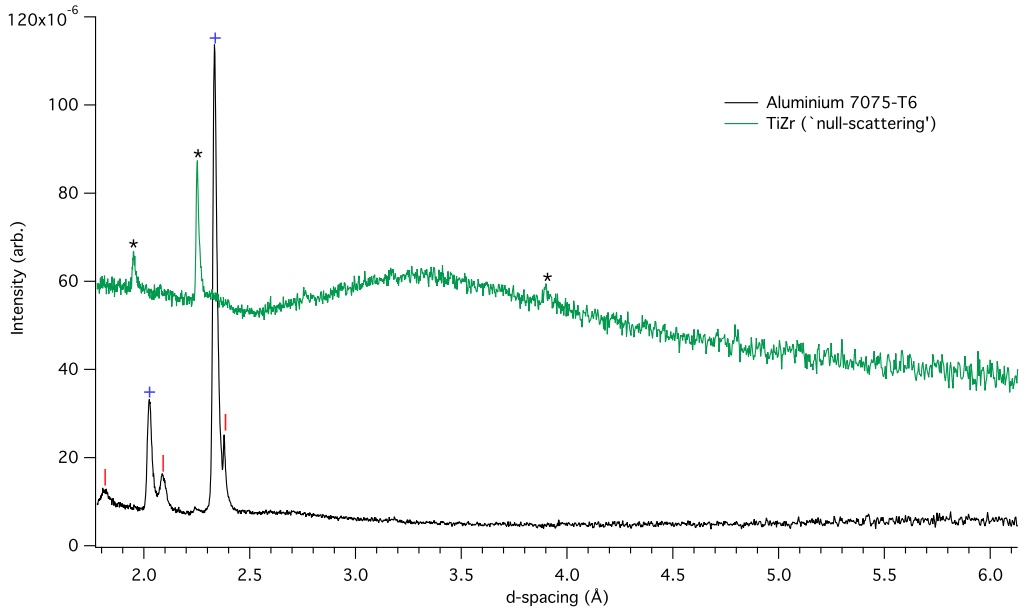

Figure 4.5 *True scale measurements of TiZr and Al gaskets mounted in the pressure cell, showing a consistent level of incoherent background from both. Peaks marked ∗ are sample contributions, those marked + are Al peaks, and those marked | are unmasked contributions from the anvils.*

at break. Metals under compression can show different material properties to those measured in tensile tests, due to the failure mechanism varying between the two. Figure 4.7 shows how the relative thickness of a blank Al and TiZr gasket (without sample hole) varies as a function of applied load. This was measured in steps, taking the gasket up to a given load, downloading, and measuring the thickness with callipers, and subsequently reloading. The results do not, therefore, account for elastic thickness changes, only plastic deformation.

4.3.2 Diamond anvils

Test measurements using smaller sample volumes than achievable with sapphire anvils have shown promising results on WISH. Provisional neutron data taken with diamond anvils in the Mk2 load cell with 10^{-2}mm^3 of sample, show that sample peaks are visible after 45 minutes of data collection. At this scale the level of incoherent background becomes critical. The cell is being further developed to incorporate < 0.5 mm wide slits on the pressure cell, which could improve the signal to noise significantly. However, this presents new difficulties in accurate alignment of the pressure cell. This is discussed further in section 4.5.

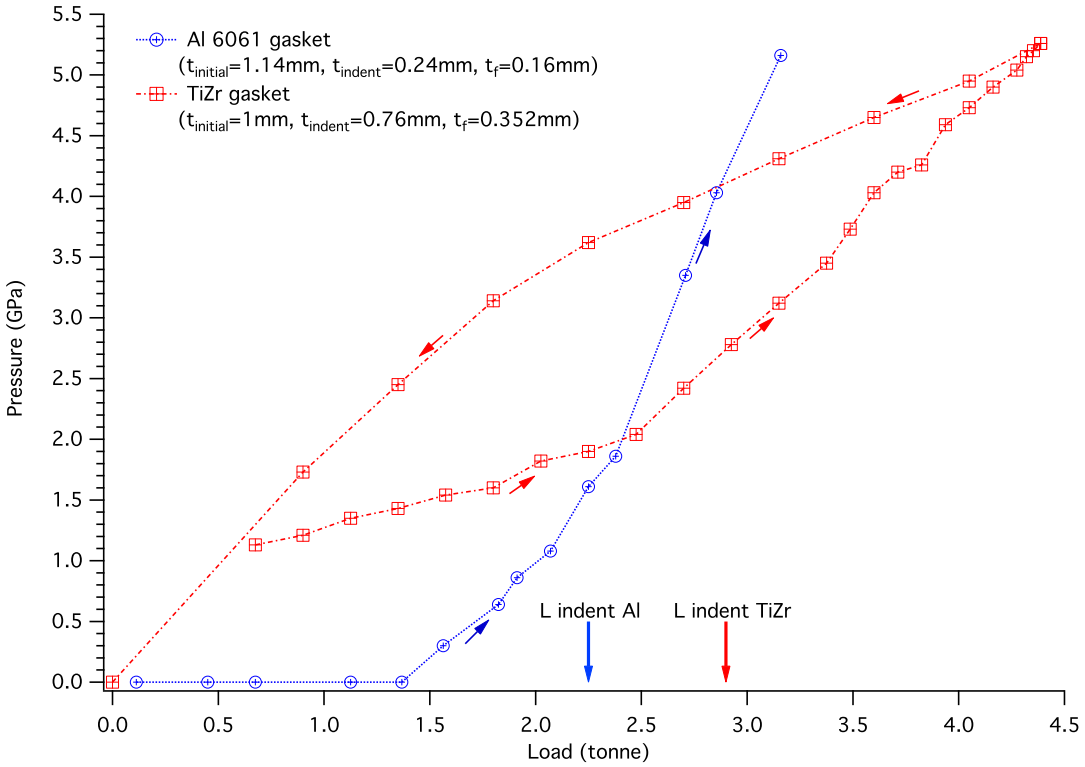

Figure 4.6 *Pressure/load curve measured using ruby spectroscopy for sapphire anvils. The sample hole was initially* 1 mm *for the TiZr, and* 1.2 mm *for the Al loading. 4:1 Meth:Eth used as pressure medium, with NaCl sample for TiZr, and $SrTiO_3$ sample for Al gasket.*

The advantage of working with much smaller samples is that significantly higher pressures can be generated (approximately 20 GPa), whilst diamond is also a much more reliable anvil material, less prone to unpredictable damage during routine loading. Figure 4.8 shows the first loading curve for the diamond anvils in the Mk2 load cell. Conical seated diamonds (so called 'Boehler' style [100]) with culets of 1.2 mm (girdle diameter 2.5 mm, with a 6° bevel up to 1.3 mm diameter, and a 12° bevel up to 1.4 mm diameter, 30° aperture, 40° pavilion angle) were used with WC seats.

Promising pressures were reached at relatively low loads. However, the pressure became unstable above 6 GPa and started to drop on increased load. After unloading it was clear that the sample hole had started to drift off-centre, however, the size of the sample hole remained stable. This suggests that this was an anvil alignment issue, and not a limitation of the gasket material. This test result contradicts the findings of Boehler et al. [99], who found that 1.5 mm culet diamond anvils, without a steel support ring around the WC seat, would fail at 1 tonne force, for a sample pressure of 2-3 GPa. No damage was caused to the

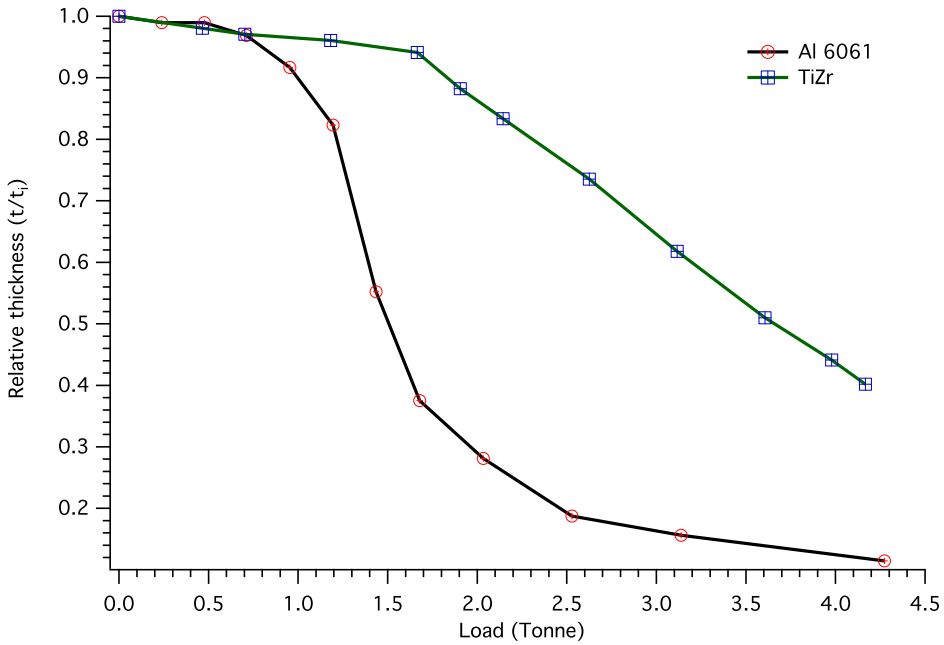

Figure 4.7 *Comparing the compressive properties of Al 6061 and TiZr gaskets between two WC anvils with* 3 mm *culets. The gaskets had the same outer diameter (*12 mm*) and both had starting thicknesses of approximately* 1 mm.

anvils or WC seats in this case.

4.4 FEA optimisation of sapphire anvils

Sapphire anvils are far less reliable than tougher alternative composites (tungsten carbide etc.), though it offers attractive advantages in terms of background contributions, and optical transparency. It has been found through extensive testing of sapphire anvils that they're not very resilient to any extent of gasket deformation, and almost always suffer some form of minor surface damage during a typical loading. Furthermore, the quality of surface finish is observed to be very important where fluid pressure media are used. Methanol-ethanol pressurised on a poorly polished face of sapphire likely propagates into surface cracks, resulting in premature failure (usually around 2.5 GPa) unless the sapphire is coated with some secondary material. To understand the limitations of using sapphire as an anvil material, and explore possibilities for improving their reliability, an extended finite element analysis was performed.

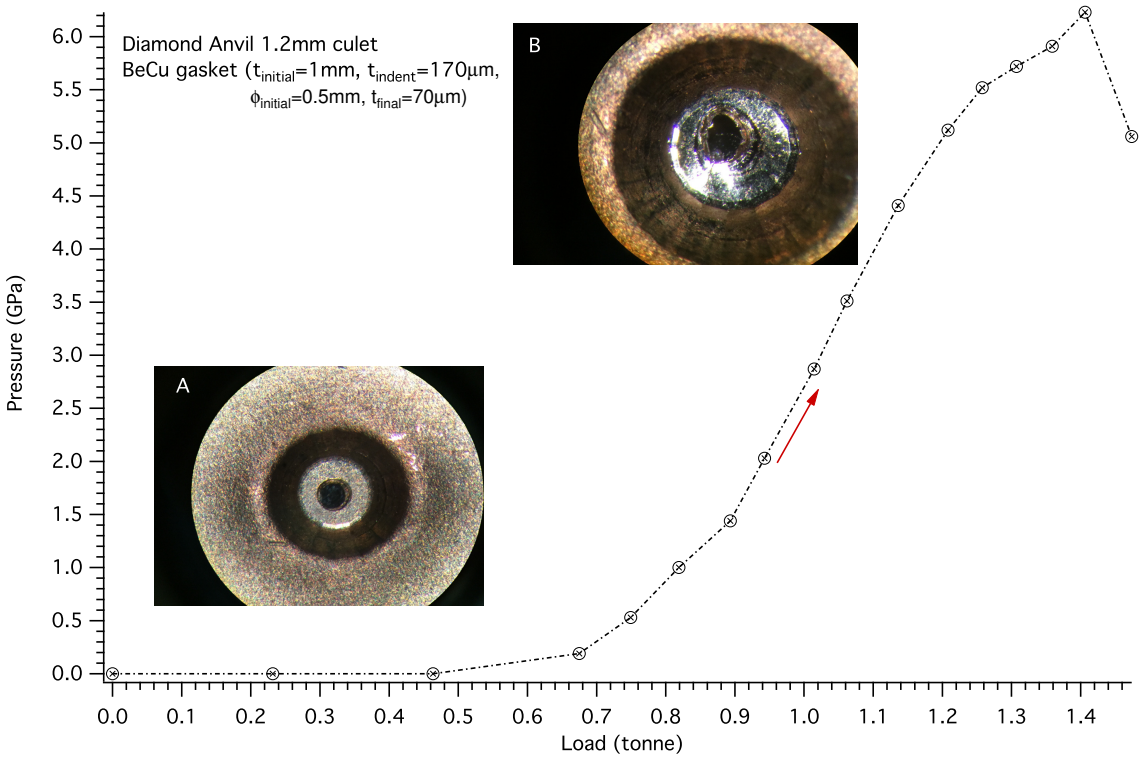

Figure 4.8 *Loading curve for diamond anvil test with BeCu gasket. Meth:Eth pressure medium. (A) sample hole prior to loading, (B) sample hole after reaching maximum pressure, showing that the hole had drifted away from the culet centre due to a misalignment.*

4.4.1 Modelling methods

The analysis was performed using the ANSYS Workbench Static Structural Module. The basic premise of the model is that the geometry (or part) is meshed into many elements, defined by a larger number of nodes. Artificial loads and supports are applied to the mesh which assumes material-like behaviour as imposed by a number of different mechanical models. As the load is increased the mesh deforms, and stresses generate. The finite-element algorithm aims to allow the mesh to deform whilst fully accounting for the forces involved. Once the model has fully converged the calculated stresses can be overlaid onto the mesh. Further details may be found elsewhere [144].

The models used for this study assume certain symmetry constraints, which reduce the model to 1/8th of the original through plane symmetry, and then further reduces the model to 2D assuming axial symmetry along the axis of the sapphire, reducing the number of computational processes significantly. Despite single crystal sapphire being an anisotropic material, useful information can be

inferred from these models. This is justified through comparing results from an anisotropic 3D model and 2D isotropic model in Section 4.4.9.

4.4.2 Material data & model assumptions

The anvil is designed to operate in the elastic regime, such that the required material properties are only the elastic moduli, poisson ratio, and density. Due to the large temperature ranges being considered, these properties will be expected to change. However, it is found that the fracture toughness of sapphire increases at lower temperatures [136, 145]. Whether this trend continues to extremely low temperatures or not is not discussed. In the absence of material data, it is therefore assumed that room temperature is the worst case scenario, and is therefore the focus of these simulations.

The gasket is designed to deform both plastically and elastically, which complicates the simulation. In the simplest case, the material can be assumed to simply yield at a given stress, providing no additional support. However, ductile materials tend to undergo extensive plastic deformation before actual fracture/breakage of the material. Where stresses beyond the yield strength are endured prior to failure, the material is said to 'work harden'. For opposed anvil experiments it is usual to pre-indent the gasket before drilling the sample hole. This has multiple effects, as will be discussed in this chapter, but adds additional complication to the model. Pre-indenting the gasket means that the gasket has a non-zero stress state prior to loading with the sample. The models assume that the gasket has no prior stress state, which adds an offset to the behaviour of the gasket.

To approximate the work hardening in the models, a bilinear model can be used, which assumes that beyond a specified yield strength, the stresses in the gasket grow linearly obeying a reduced modulus, or 'plastic modulus'. The plastic modulus must be determined through material testing; tensile testing can be used to verify the elastic modulus, and to measure the yield strength of the material, whilst a linear fit to the plastic region of the stress-strain graph can be used to provide an initial value for the modulus. However, the tensile behaviour of a material, and its behaviour in compression as a gasket may be very different. This is due to the effects of friction or differences in the yielding mechanism. Thickness/load profiles were measured for the gasket (without sample hole), averaged over several loadings, and compared to those predicted from the models.

Fixing the yield strength and elastic modulus, the plastic modulus was tuned to best fit the measured profile. This technique is similar to that reported by Fang et al. [146] for the finite element analyses performed for toroidal anvils used with the Paris-Edinburgh cell. The coefficient of friction was fixed to $\mu = 0.3$, though it was not found to dramatically influence the behaviour of the gasket between $\mu = 0.1$, and $\mu = 0.5$, consistent with the theoretical work of Dunstan [54].

4.4.3 Yielding criteria

The yielding criterion is typically identified as a critical stress state in the system where plastic deformation is initiated (the limit of elastic yielding in the test material). There are multiple methods for determining the nature of this stress state, it being highly dependent on the material being studied, and the nature of the loading. For example, for ductile metals under simple tension, the level of deviatoric strain in the material (represented by an equivalent Von-Mises stress) gives an accurate indication of the maximum loads it may support, in strong agreement with experimental performance. Deviatoric strain is the resultant strain in the sample when hydrostatic strain is neglected. It may be considered as a measure of distortion in the sample, neglecting uniform changes in volume. For brittle materials, which behave very differently in compression and tension, and may have multiple modes of yielding due to auxiliary effects such as geometry or surface finish, there is no single accurate metric for failure. Brittle materials show very little plastic deformation prior to ultimate failure. For this reason, in this analysis, 'yielding' and 'failure' will be used synonymously.

This is reflected by the range in reported strengths of sapphire reported in the literature (see table 4.1), as the strength is strongly dependent on multiple factors, including how the strength is measured (three or four point flexural tests [147]), such that the intrinsic strength may be within a wide range of values. However, the disparity between different axis alignments, and sapphire's weakness in tension suggest that regions of high tension may initiate failure. This has been verified by Shipway and Hutchings [148], who found that the high axial tensile stress in a sapphire sphere under compression between two platens, was the likely cause of failure. It was also found that for large contact areas surface tension (rather than bulk tensions) becomes more dominant, and may lead to premature failure due to surface imperfections. The conclusion that compressive failure is initiated through tensile fracture is also supported elsewhere [149]. However, the

data for flexural strength and shear strength indicate that shearing may also be important in the initiation of failure. Shear is a measure of angular distortion between orthogonal axes in a material. Principal shear stresses may be calculated as the difference between the principal stresses in the system ($\tau_{max} = |\sigma_1 - \sigma_3|/2$) [150]. If a region of the anvil is found to be under both very high tensile and compressive stresses then this will show as region of high shear, where brittle materials are prone to failure. This is supported by Bruno and Dunn [66] who suggested that large shear at the edge of the culet area leads to chipping of the culet, motivating the use of additional bevel angles.

In a complex loading scenario tension can most easily be identified through considering the maximum, middle and minimum principal stresses in the system (σ_1, σ_2 and σ_3 respectively, ordered as $\sigma_1 > \sigma_2 > \sigma_3$)). The maximum principal *s*train (ϵ_1) of the system may be derived from the principal stresses as $\epsilon_1 = \frac{1}{E}(\sigma_1 - \nu(\sigma_2 + \sigma_3))$, where E is the isotropic modulus of elasticity. Where $\epsilon_1 > 0$ the system is under some form of tensile deformation, this may be achieved with different stress states, depending on the sign of the principal stresses. In a simple tensile test $\sigma_{2,3}$ are generally small, so when $\sigma_1 > 0$ the system is under uniaxial strain. In a more complex compressive loading, it is possible that $\sigma_{1,2,3} < 0$, whilst $\epsilon_1 > 0$. This equivalent to considering a gradient of compression as a form of internal tension. For this reason this study considers the strains of the system rather than the stresses. Figure 4.9 depicts a typical principal stress field compared to the principal strain field for an anvil under high levels of compression. The principal stresses in the system indicate that the system is under pure compression around the culet region, while the system is strained under tension. Since tensile deformation is a weakness in brittle materials, and as the stresses mislead the extent of this in this case, strains were considered during these analyses.

4.4.4 Simple anvil analysis

The gasket/anvil assembly is deceptively simple; in reality the balance between many variables leads to large variations in stresses, and achievable sample pressures, the limits of which are difficult to predict experimentally. For example, Bundy [7] motivated that a crucial geometric parameter to determine the maximum stresses sustainable by a tapered anvil is the level of gasket pre-indentation (i.e the amount of support along the conical section of the part).

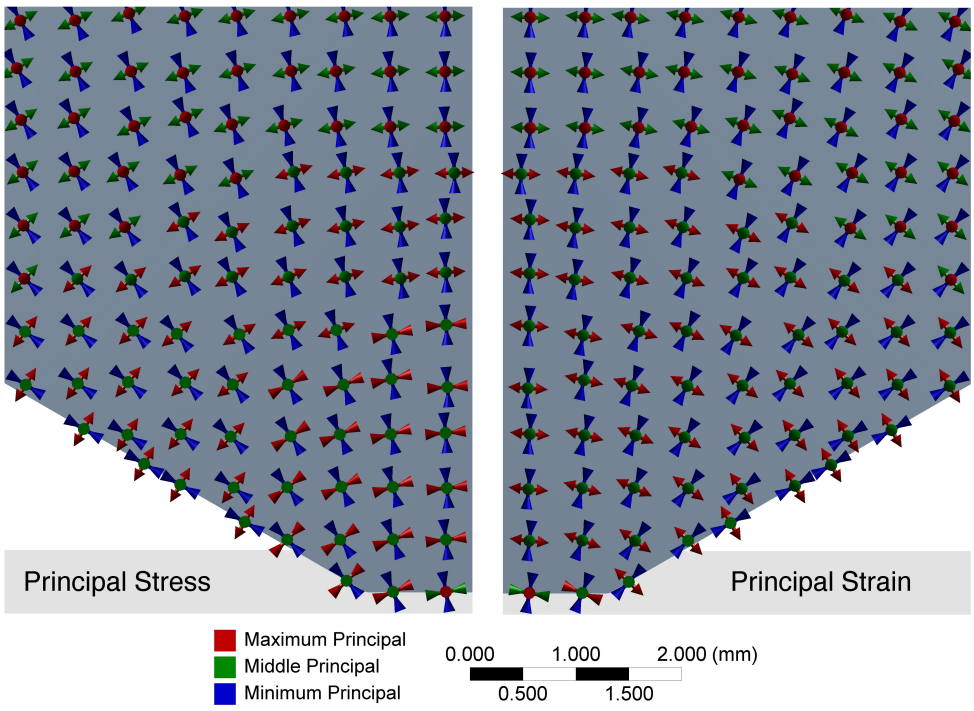

Figure 4.9 *(left) Principal stress field, (right) principal strain field for a typical anvil simulation. The form of these fields is typical of all the simulation performed for this chapter.*

Implementing this theory with a real gasket requires that other coupled variables be controlled. If the ratio of indented gasket thickness to initial thickness is kept constant for a number of different absolute starting thicknesses, the ratio of culet diameter to indented thickness is varied, which has a strong effect on the stresses in the anvil. This is discussed further in section 4.4.5. This section looks at a simplified model of the assembly, whereby the anvil is considered separately. The effects of applying pressure along the pavilion to support the culet are investigated.

The result from Bundy [7] shows that applying an external pressure to the flanks of a conical anvil allows it to sustain face pressures higher than critical stresses; however, the derivation doesn't provide insight into how this is the case, or how it may be further exploited. FEA has been used to investigate this further through calculating the expected pressure distribution along the flank of the culet for a given taper angle (from [7]), and simulating full stress distributions in the anvil. To remove ambiguity over the value of S (see p24), the ratio of $P(x)/P_0$ was considered to calculate the pressure distribution along the flank. Figure 4.10 shows how varying t_0 (and therefore x_1) varies the tensile strain in the culet region of the anvil, the shear stress profile has an identical form,

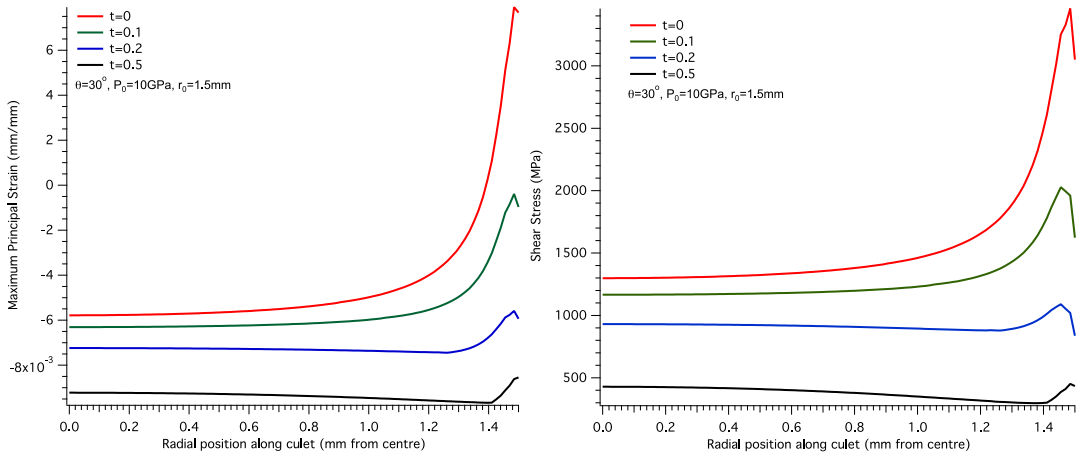

Figure 4.10 *Effect of varying level of gasket support along flank of anvil on tensile strain, and shear stress behind culet region. Model considers anvil only. The taper angle, and face pressure were fixed.* t *refers to the axial support length along the flank of the anvil (see figure on p25).*

and shows a similar trend. Applying pressure along the flank loads the anvil multiaxially, around the central axis and culet, instead of uniaxially on the culet only. Increasing t_0 increases the volume of anvil that is compressed multiaxially, allowing higher pressures to be reached before failure. Massive support can therefore be summarised as the use of auxiliary material to reduce the distortion of ancillary material.

Furthermore, in this simplified loading scenario, with a constant face pressure, and logarithmic pressure profile on the flanks of the anvil, the results of Bundy [7] can be verified. Data for the shear strength of brittle materials is not readily available, though it can be estimated to a first approximation as the tensile strength of the material. Without massive support, Bundy estimates that the anvil should be able to withstand a pressure $P_0 = S$. From the FEA, $P_0 = 1.5\,\mathrm{GPa}$ generates a maximum shear stress, and tensile stress of approximately $0.5\,\mathrm{GPa}$. If massive support is included (equivalent to indenting the gasket to half the original thickness), the pressure can be increased to approximately $P_0 = 3\,\mathrm{GPa}$ before these values are reached. The region of maximum stress shifts up away from the culet to a region above the gasket.

4.4.5 Anvil & gasket model: anvil analysis

Although accurate within its own approximations, the model discussed in the previous section is oversimplified for the analysis of a diamond anvil style assembly. The main difference between the two is that the face pressure is not expected to be constant over the face of the culet, being strongly centred over the sample region, and then falling steeply off over the gasket region. Similarly, the pressure applied to the flanks of the anvil is unlikely to be as high as estimated in the previous simulations. To further understand the assembly, the gasket needs to be included.

Experimental loadings of sapphire anvils show that there are two main failure modes for sapphire anvils during loading (type 1 and type 2), even in cases where the gasket remains stable, and at pressures lower than expected from theory (see Appendix D). Both types result in fracture of the anvil. Type 1 failure is more common (approximately 3/4 of failures) than type 2 failure, consisting of localised damage to the culet. The formation of the crack appears to indicate shear fracture under compression. Type 2 failure is more extensive, usually splitting the anvil cleanly into two pieces. Due to the c-axis orientation of the anvils being parallel to the load axis, the failure is possibly consistent with prismatic or pyramidal slip in the sapphire. Pyramidal slip is usually associated with tension along the c-axis [0001] direction, [151] which suggests that pyramidal slip is more likely. Furthermore, compression along the c-axis could lead to rhombohedral twinning [132], which is thought to be the cause for weakened sapphire at elevated temperatures. The nature of failure in brittle materials makes it difficult to locate the root cause for failure through inspection of the recovered component, making it difficult to know for sure if twinning is playing a direct role. However, the final cause for fracture in each case is likely still due to bulk tension or shear. Observations from these load tests [4], and from other sources [36], suggest several causes for the limited pressure performance of sapphire, which are further investigated with FEA.

Since it is expected that the cause for failure is either bulk or surface tension in the anvil, this study focusses on three key regions of interest in the anvil; the central portion of the anvil (bulk region), the culet surface region, and the surface of the conical face (pavilion) of the anvil. To compare the form of tensile strains between each model, paths are taken through each of these three regions as indicated in figure 4.11.

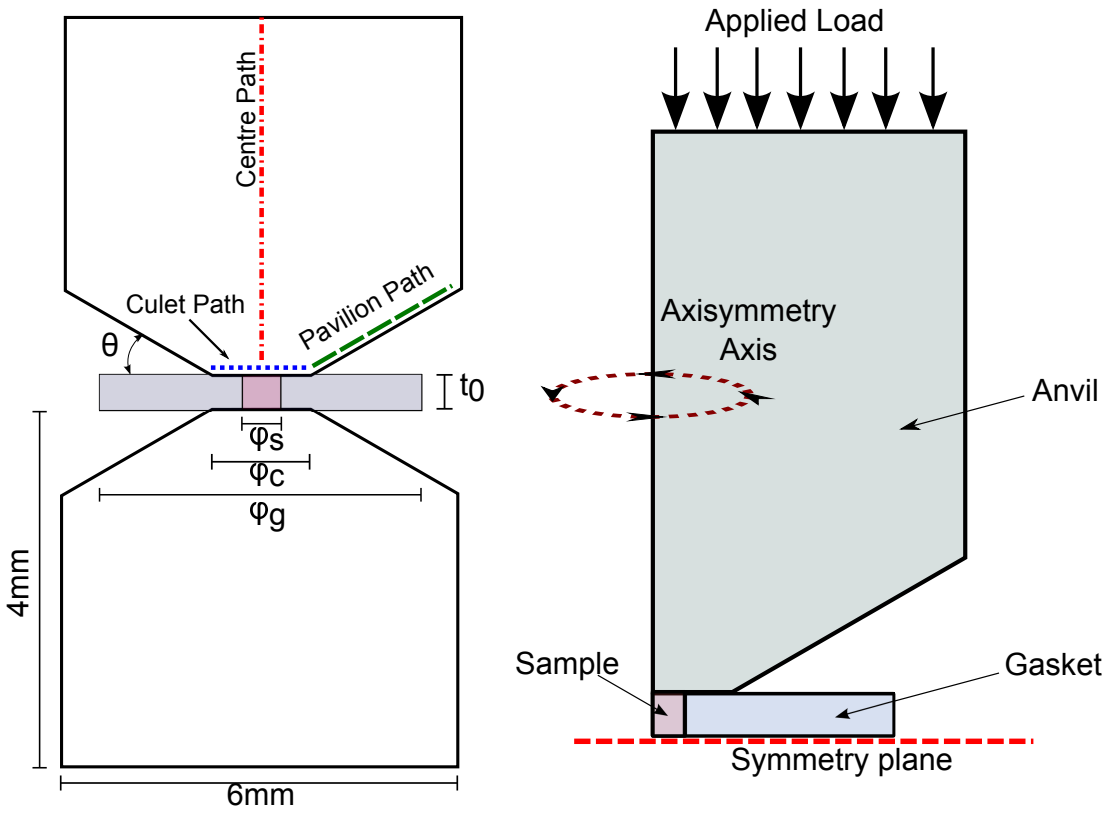

Figure 4.11 *(left) schematic of actual assembly, (right) FEA model used, with symmetry constraints, and applied load.*

Effects of scaling

The initial motivation of using sapphire anvils is that they can be grown to much larger dimensions than diamonds, perhaps leading to the opportunity to reach similar pressures with much larger samples. However, this works on the assumption that the system will behave in the same way when scaled up to larger absolute dimensions. If all the dimensions of the system are scaled in proportion, and the applied load is scaled up as the square of this factor, then the form of the stress distribution should be unchanged. However, the extent of the distribution scales with dimension. From Weibull statistics [152], the cumulative probability of failure of a brittle material scales with the volume as

$$P_{fail}(\sigma) = 1 - \exp[-V \times \lambda(\sigma)]$$

where V is the volume of material under stress σ, and $\lambda(\sigma)$ is the density of critical flaws/dislocations in the crystal. The larger the stressed volume, the larger the cumulative probability of failure at a given stress [133, 152].

Gasket hardness

Initially the effects of gasket hardness were considered. This used the anvil parameters as described by Furuno et al. [94], whilst the material properties of the gasket were varied as noted in table 4.2. The parameters which determine material hardness (defined as resistance to plastic deformation by indentation) are the yield strength and the tangent modulus of the bilinear model, but are dominated by the former, such that the gasket materials are listed in approximate order of increasing hardness.

Table 4.2 *Material properties used in finite element analysis. Values from literature are referenced where applicable, other values were determined in the present study using tensile testing, and calibration with load testing.*

	$E_{elastic}$	σ_{yield} : $E_{plastic}$	Density
Sapphire (isotropic) [133]	350 GPa	n/a	3.98 gcm^{-3}
NaCl Sample (Powder)	35 GPa	150 MPa : 500 MPa	2.17 gcm^{-3}
Cu alloy	110 GPa	280 MPa : 1.15 GPa	8.30 gcm^{-3}
Aluminium 6061 (I)	75 GPa	350 MPa : 500 MPa	2.84 gcm^{-3}
Aluminium 7075 (II)	75 GPa	500 MPa : 500 MPa	2.84 gcm^{-3}
TiZr	95 GPa	0.9 GPa : 1.1 GPa	5.23 gcm^{-3}
BeCu25 (H) (I)	123 GPa	800 MPa : 1 GPa	8.24 gcm^{-3}
BeCu25 (AT) (II)	123 GPa	1 GPa : 2 GPa	8.24 gcm^{-3}
BeCu25 (HT) (III)	123 GPa	1.4 GPa : 2 GPa	8.24 gcm^{-3}

Figure 4.12 shows a compilation of the results obtained from the models, all taken at a normalised sample pressure (determined as the average of normal stresses in the sample) of 9.5 GPa, the applied load required to reach this pressure was typically 10 kN on a 1 mm diameter culet. This pressure was chosen as it is achievable experimentally with sapphire anvils, and is below the observed failure pressure. For comparison, the calculated strain distributions for an anvil with a compressibility similar to diamond (E$\approx$ 1220 GPa) are shown for the hardest gasket material (BeCu III) considered.

The data from the culet region indicate that a harder gasket material increases the tension and shear within the anvil at the edge of the sample hole, whilst reducing tensile strain at the edge of the culet which gains more support. A similar trend is seen along the path of the pavilion, showing that the critical region is the point where the anvil and gasket depart from contact. A harder gasket material results in a large transition from compression to tension resulting in large shear strains.

If the path through the central region of the anvil is considered, it is found that neither the maximum shear nor the maximum tensile strain is increased with increased gasket hardness, but their distributions are broadened, suggesting that the anvil is more evenly strained. This is consistent with the expectation that the pressure distribution along the culet is also broadened for a harder gasket material.

4.4.6 Preindentation & anvil/gasket relative dimensions

There are several aspects of the anvil profile which can be studied with FEA, furthermore the effects of gasket geometry can also be investigated. Figure 4.13 compares stress distributions between anvils with different taper angles. The sample and gasket dimensions were kept constant, as were the outer dimensions of the anvil. As the taper angle is varied, the load performance of the anvil greatly changes, as a result the load was normalised between simulations so as to generate a sample pressure of 10 GPa in each case. This was determined through averaging the directional stresses in the sample region, $P \approx \frac{1}{3} \mid \sigma_x + \sigma_y + \sigma_z \mid$. Altering the taper angle effectively varies the level of flank support that the anvil receives. The results show that a smaller taper angle reduces the levels of tension behind the vulnerable culet region, but at low taper angles, tension starts to build at the base of the anvil to significantly larger levels. As such a value between the two brings a balance. 30° gives a good balance between support to the culet, pressure/load efficiency, and minimal strain at the base of the anvil.

4.4.7 Relative dimensions

A further geometric consideration is what effect the relative dimensions of the assembly have on the stress distribution. For example, the ratio of culet diameter to absolute or relative indented thickness. This was motivated by the observation that if the gasket undergoes significant deformation that the sapphire frequently undergoes type 2 failure. Furthermore, if the anvil is indented too much, type 1 failure is inevitable. To understand this a comparative study was performed using an aluminium (Al II) gasket of 1 mm unindented thickness. The culet diameter and indented thickness were varied. The load was scaled to ensure the same average face pressure in each case. Figures 4.14–4.16 show the pressure distribution between the gasket and the anvil, the maximum principle strain,

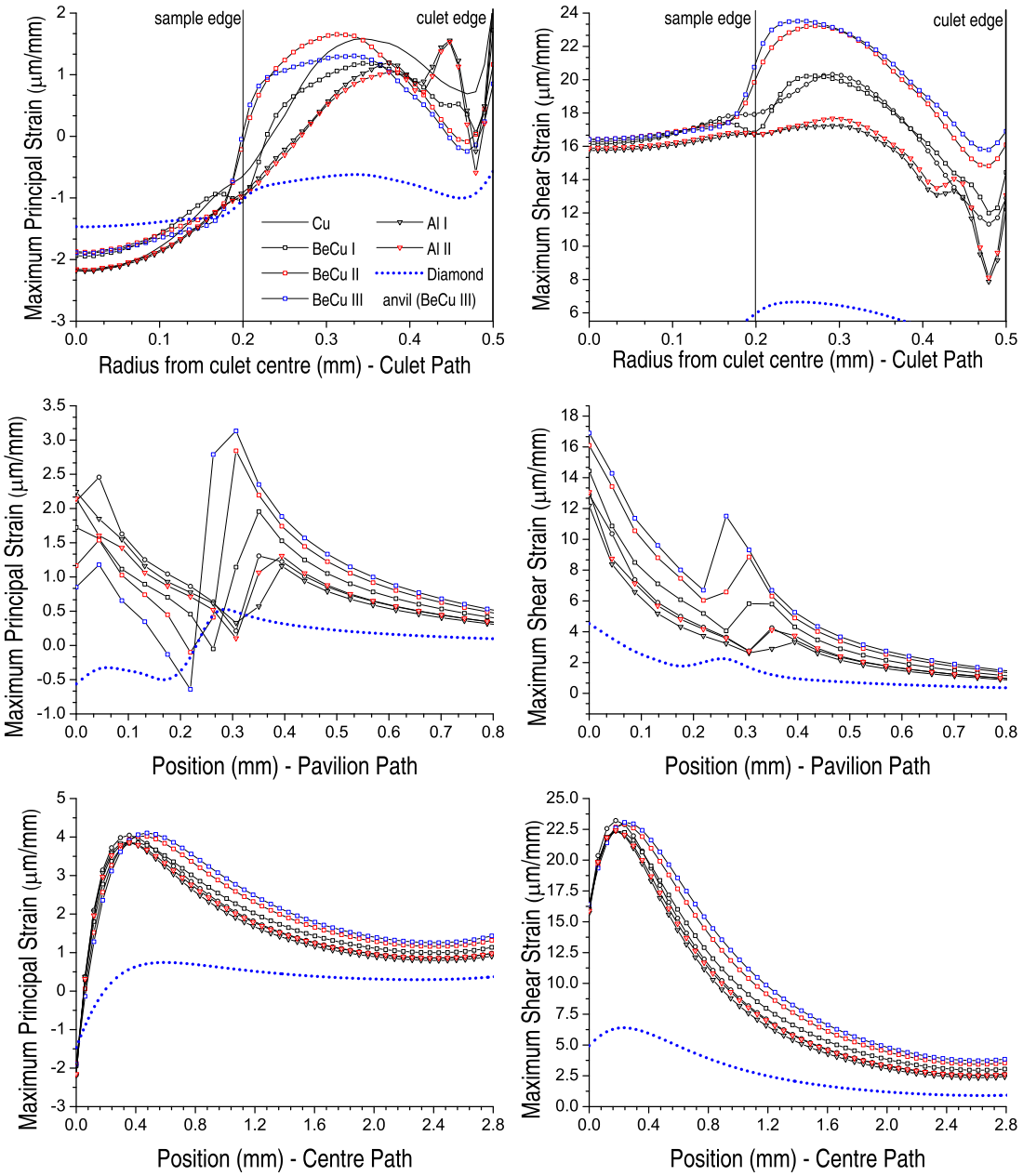

Figure 4.12 *Strain distributions along the three paths considered for different gasket hardnesses. (left) maximum principal strain, (right) maximum shear strain. (top) culet path, (middle) pavilion path, (bottom) centre path. The blue dotted line in each plot is the strain distribution for a diamond anvil in the same loading scenario with the BeCu III gasket. The model parameters used for this comparison are* $\phi_c = 1\,\mathrm{mm}$, $\phi_s = 0.4\,\mathrm{mm}$, $t_0 = 0.3\,\mathrm{mm}$, $\phi_g = 3\,\mathrm{mm}$, *and* $\theta = 18°$.

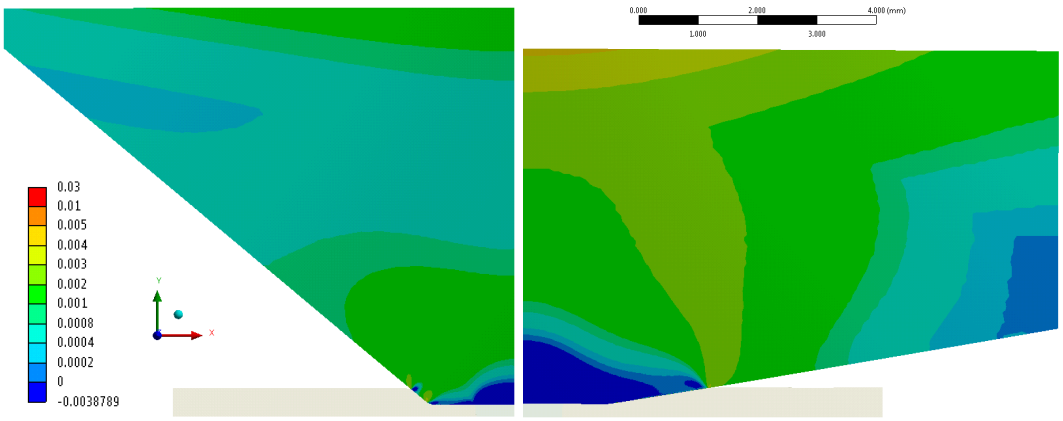

Figure 4.13 *Side by side comparison of maximum principle strain contour plot for* 40° *and* 10° *tapered sapphire anvils; the load is scaled in each case to generate a sample pressure of* 10 GPa.

.

and maximum shear strain simulated in the culet region, respectively.

Considering the pressure distributions, the point of maximum pressure shifts towards the edge of the culet when the gasket is more preindented. The sample and gasket material at the centre of the culet is squeezed towards the edge of the culet, at this point the gasket material is more strongly supported by the surrounding gasket material. As such the pressure initially builds faster outside the sample region. This is how gaskets are able to seal fluids up to such high pressures, as the pressure in the gasket (or seal) is higher than that in the sample region [153]. Where the gasket is less preindented, the pressure builds faster at the centre of the gasket, as material at the edge is less supported. As the culet is reduced in size relative to the dimensions of the gasket, the effect is less pronounced. Despite the load being scaled between the different culet dimensions, there is a shift in the values of the pressures generated. This is due to the aspect ratio of culet diameter to indented thickness ($\frac{\phi_{culet}}{t_{indent}}$) being different in each case. This determines whether the gasket behaves in the thick or thin regime. In the thick regime, the pressure is increased purely by thickness reduction, with a large proportion of the gasket volume being extruded outwards; in the thin regime, the material at the centre of the culet is supported by the surrounding material, such that pressure increases without significant thickness reduction [153], this is discussed further in section 4.4.8.

The maximum shear and maximum principle strain profiles show that a thick gasket results in high shear and pure compression at the *c*entre of the culet, whereas a thin gasket results in tension and shear at the *e*dge of the culet, but at

lower absolute values. This observation is consistent with test observations that even with high levels of pre-indentation, type 1 failure is caused by shear and tension at the edge of the culet. Where the gasket is initially thick, and type 2 failure is common, the data suggest that failure is driven by a combination of the anvil being under high compression along the c-axis, whilst under bulk shear.

4.4.8 Anvil & gasket model: gasket analysis

Aside from characterising the stresses in the anvil material, FEA can be used to provide insight into the gasket mechanics. If one considers a disk, of thickness t, with radial coordinate r, which is compressed between two rigid anvils providing frictional force f to the faces of the disk, then through balancing the forces, the radial stress gradient is found as

$$\frac{\partial \sigma_r}{\partial r} = -\frac{2\mathrm{f}}{\mathrm{t}}$$

The Von-Mises criteria predicts yielding where non-hydrostatic stress conditions exceed measured uniaxial critical levels. Dunstan [54] integrated this expression, with suitable boundary conditions, using this criteria for failure, and subsequently provided extensive analysis of the gasket deformation. Through applying the theory of massive support to the gasket, as outlined by Bundy [7] in the case of the anvil, Dunstan was able to quantify the effect it has on gasket performance.

One major limitation in this analysis of the gasket, is that the effects of plastic deformation, and work hardening are neglected. Here FEA is used to quantify the effects of plastic material behaviour in the gasket, to verify the applicability of Bundy's massive support analysis to the gasket, and to subsequently compare the results with the theories of Dunstan.

As these simulations are not concerned with non-ideal cases where cupping of the culet at high pressure may play an important role in gasket behaviour, the anvil is assumed to be perfectly rigid. The gasket is modelled as TiZr, with material properties as outlined in table 4.2.

To directly compare the effects of work hardening on gasket stability, the thickness of the gasket can be considered. Dunstan derived an expression for the maximum stable thickness, t_{max}, of the gasket for a given pressure, P, where the culet radius

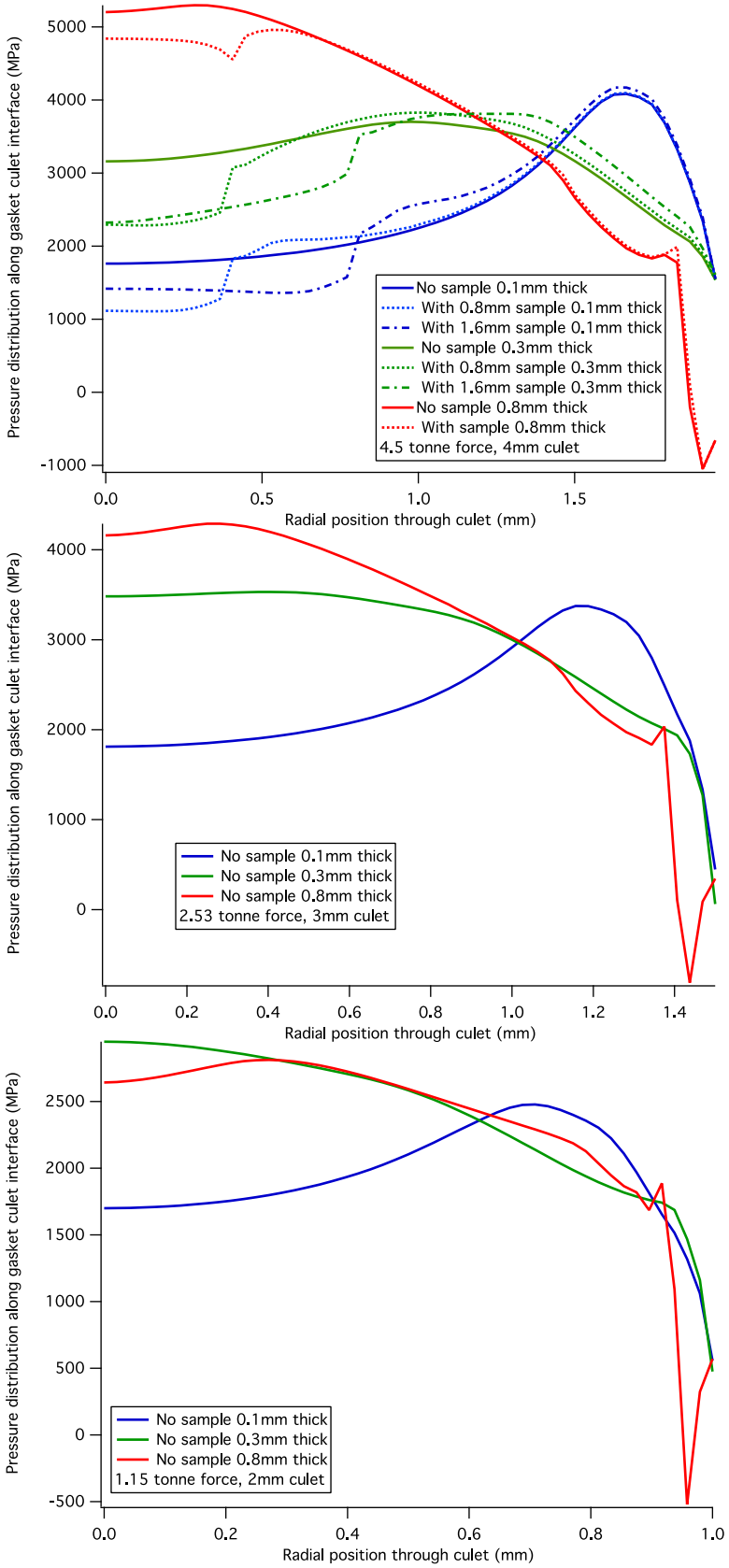

Figure 4.14 *Pressure distribution calculated between the gasket and anvil under different levels of preindentation for a* 4 mm *culet (top),* 3 mm *culet (middle), and* 2 mm *culet (bottom).*

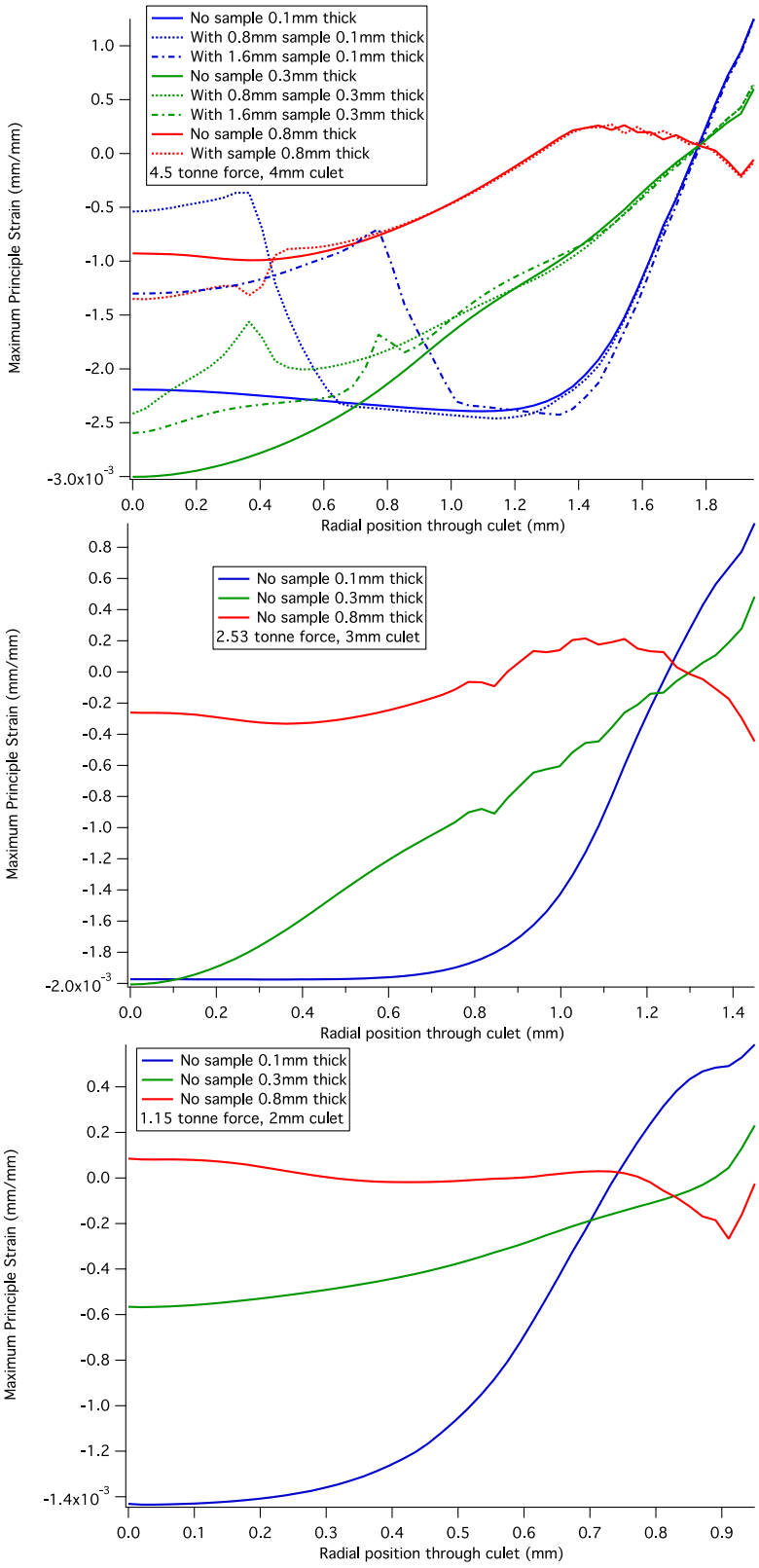

Figure 4.15 *Maximum principle strain distribution calculated in the culet region of the anvil under different levels of preindentation for a* 4 mm *culet (top),* 3 mm *culet (middle), and* 2 mm *culet (bottom).*

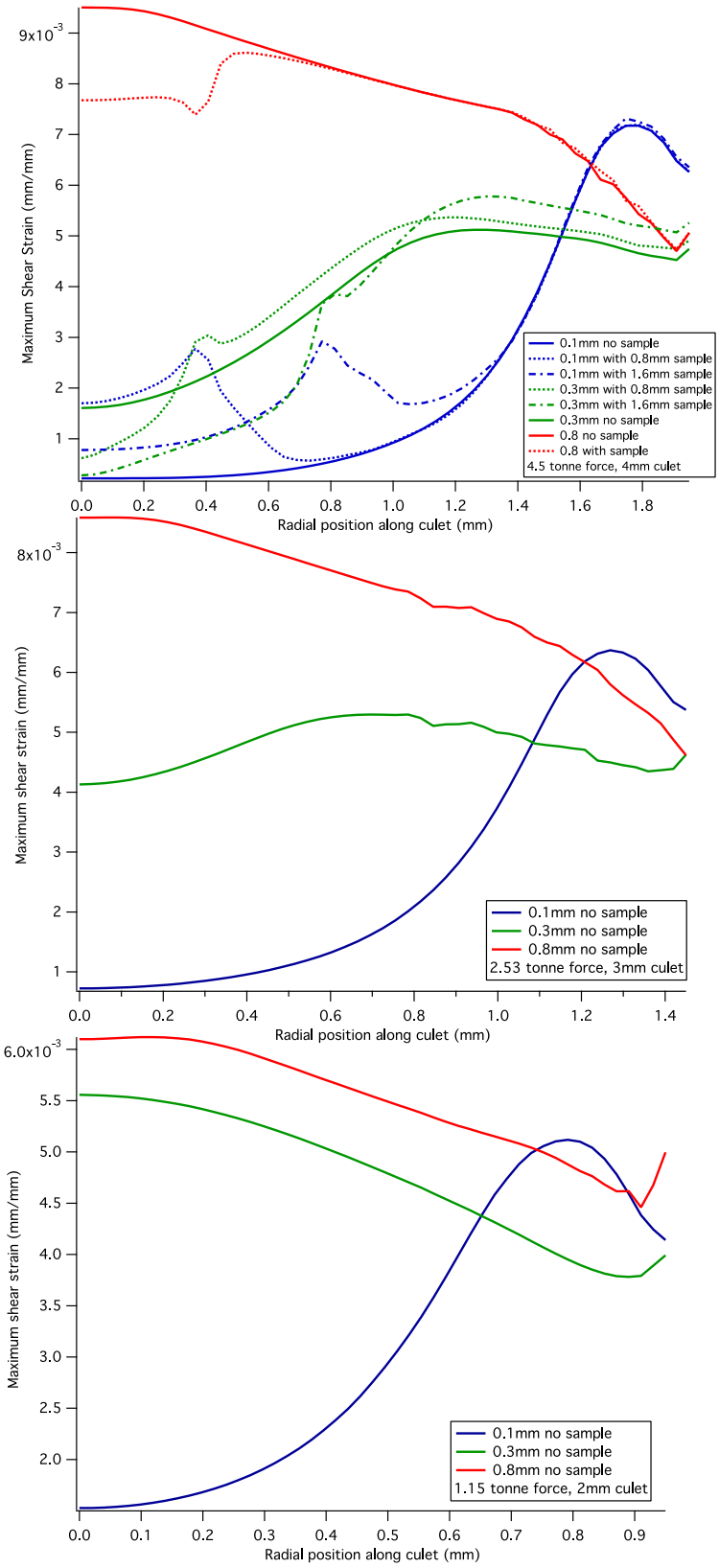

Figure 4.16 *Maximum shear strain distribution calculated in the culet region of the anvil under different levels of preindentation for a* 4 mm *culet (top),* 3 mm *culet (middle), and* 2 mm *culet (bottom).*

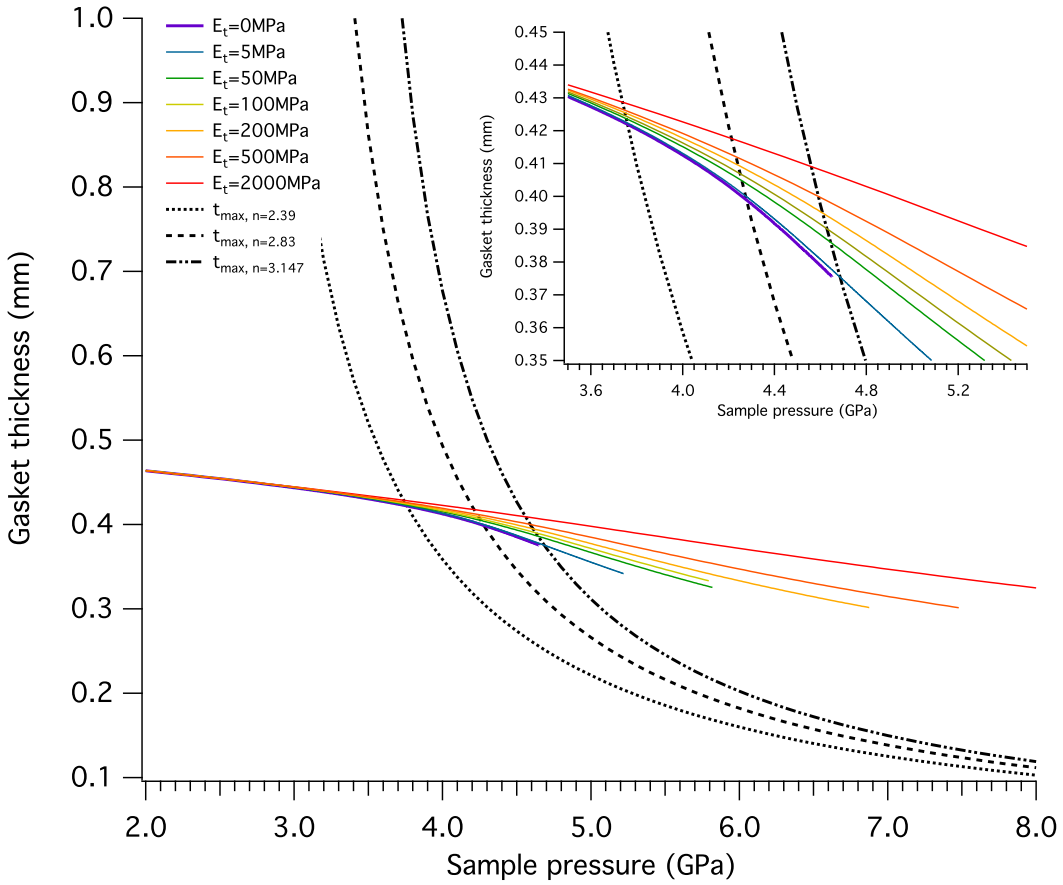

Figure 4.17 *Plot of gasket thickness versus sample pressure for a number of different tangent modulii. The dashed lines are the predicted maximum thicknesses for the gasket according to equation 4.2*

.

is r_0, and the sample hole is r_g, for given level of preindentation, n:

$$\mathrm{n} = 2\ln\left(\frac{t_0}{t}\right) + 1 \tag{4.1}$$

$$t_{max} = \frac{\sigma_y}{\sqrt{3}(\mathrm{P} - \mathrm{n}\,\sigma_y)}(\phi_c - \phi_s) \tag{4.2}$$

Figure 4.17 shows a plot of gasket thickness versus sample pressure for a number of different tangent modulii, compared against the maximum thickness predicted by equation 4.2. It is clear that even with small work hardening contributions (low E_t), the gasket can maintain its thickness beyond that expected without plastic behaviour. As the tangent modulus is reduced to zero, it is expected that the curves should match. The simulations suggest that this is the case, though the full loading curve cannot be simulated, as the lack of stress/strain information beyond σ_y cause the simulation to diverge.

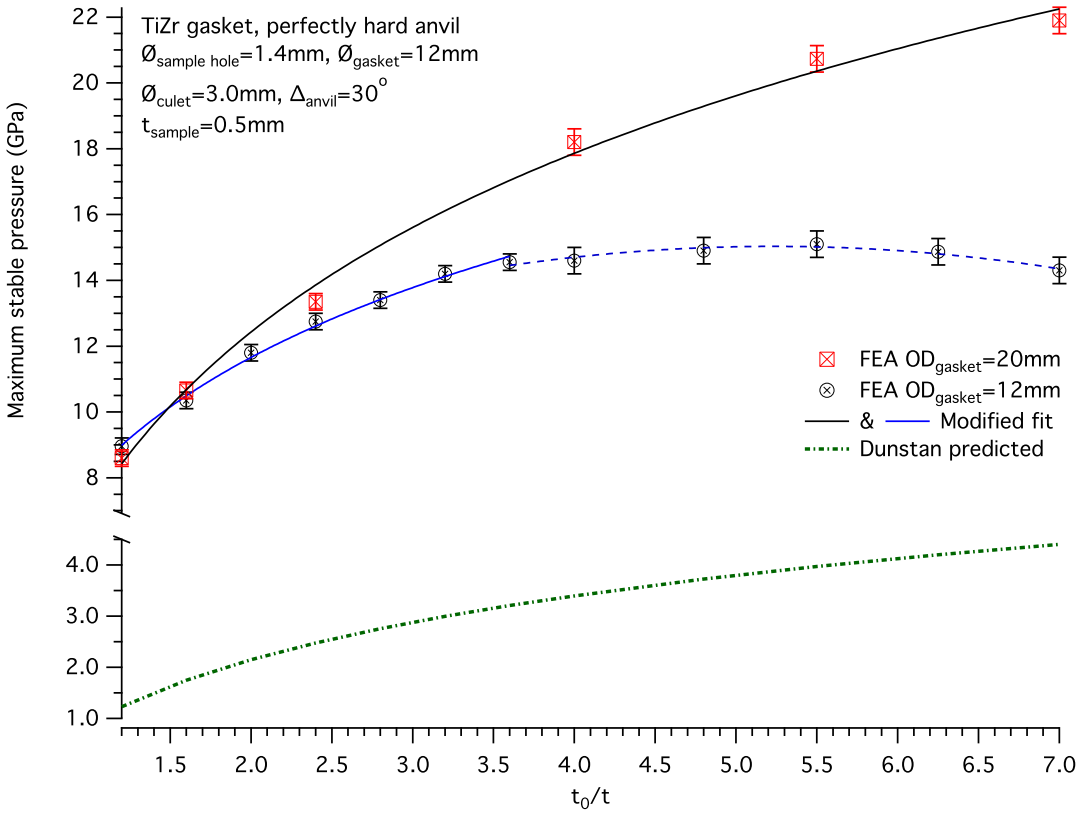

Figure 4.18 *Plot of maximum stable sample pressure versus level of preindentation as simulated from FEA (parameters indicated), compared with prediction from Bundy [7] and Dunstan [54].*

.

To further quantify the effects of work hardening, equation 4.1 can be used to estimate the maximum stable pressure in the sample region for a given level of pre-indentation. Since $P = n\,\sigma_y$, a logarithmic behaviour is expected. Figure 4.18 is a plot of maximum stable sample pressure versus preindentation for two different gasket geometries. The maximum stable sample pressure was calculated as the point where the gasket hole begins to extrude outwards in the models. The results show a number of interesting effects. Primarily, although the logarithmic form of the trend is as predicted, the magnitude is strongly offset due to the effects of work hardening. A scaled logarithmic curve is used to fit the FEA results. For the upper curve this alters the original expression in two ways; it states that without preindentation, the gasket may still be stable to pressures approximately 8 times the yield strength of the material, whilst with preindentation the effect is approximately 4 times that predicted without work hardening.

Also, the effect of the ratio of culet diameter to the outer diameter of the gasket is seen. If the gasket has insufficient outer diameter, then the effects of

preindentation saturate, and even starts to decrease. Beyond the departure from logarithmic behaviour, this is tentatively fit using a polynomial. This is as the volume of only elastically stressed material around the anvil decreases relative to the plastically deformed region. Increasing the outer diameter restores the expected logarithmic increase in maximum stable pressure. It should be noted, that the load required to reach these pressures also increases, such that there is an optimum region to work in for a restricted load. Figure 4.19 shows a plot of maximum stable pressure versus load required to generate the pressure. The Mk2 load cell is capable of outputting 45 kN from 200 bar input gas pressure. From figure 4.19 this can generate a stable output pressure of 13.5 GPa for a TiZr gasket with 0.5 mm thick sample. From figure 4.18 this would suggest that preindenting the gasket to beyond 40-50% of the original value is counter productive. It also suggests that there is no significant benefit to increasing the outer diameter of the gasket for this level of preindentation.

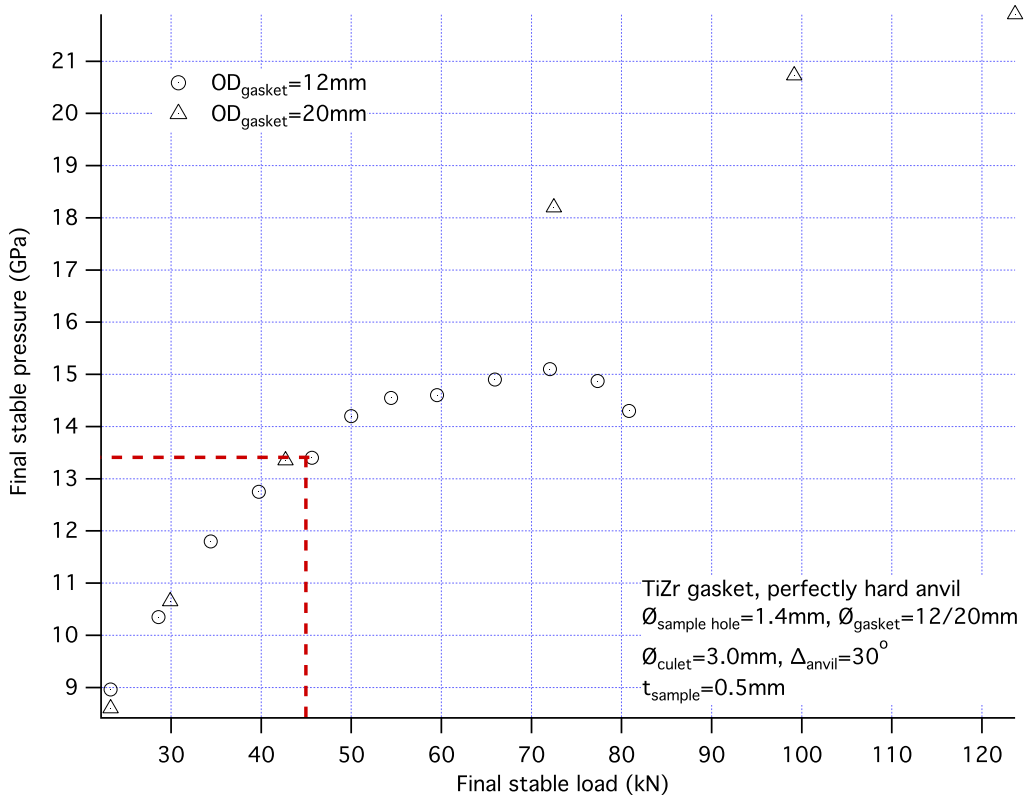

Figure 4.19 *Plot of maximum pressure achievable versus load required to generate it.*

.

4.4.9 Anisotropy

To test the effects of an anisotropic anvil material the model must be extended to three dimensions. This significantly increases the required computation time. To quantify the effect, two 3D simulations were performed, one with isotropic properties, and one with the elastic constants detailed in table 4.3. As the elastic stiffness matrix must relate the stress to the strain (both of which are rank two tensors in three dimensions), the elasticity matrix is a rank 4 tensor. The symmetry of sapphire reduces the 36 components of this matrix to 6 independent coefficients [11]. Figure 4.20 shows the maximum principle strain for the isotropic and anisotropic case of a sapphire loaded along the c-axis with 32 kN. The gasket (not shown in the figure) was assumed to be isotropic bilinear beryllium copper in both cases. Although the anisotropic model has a different stress distribution in the ac-plane, the bc-plane looks much the same as with the isotropic model, the key feature being a large region of tensile strain arching behind the compressed region of the culet. Interestingly, the ac-plane is placed under significantly lower amounts of tension in this loading geometry, though has much larger compressive stresses building at the edge of the culet volume.

Table 4.3 *Anisotropic elasticity coefficients (all values in* MPa*), from Tarumi et al. [11], taken at* 280 K*. The z-axis (C_{33} coefficient) corresponds to the c-axis of the crystal.*

C_{11}	C_{33}	C_{44}	C_{12}	C_{13}	C_{14}
497.3	501.1	147.2	162.8	117.0	22.7

4.5 Conclusions and future development

This chapter has outlined the importance of balancing the mechanical, neutronic, and thermal properties of the materials used for the low temperature, high pressure anvil assembly. Several optimal anvil and gasket materials have been identified, and their diffraction signal and beam attenuation compared. To optimise the pressure performance of the pressure cell, balance this with the benefits of increased sample volume, and to understand the cause for failure of sapphire anvils, an extended finite element analysis has been performed. This has helped to clarify and characterise the nature of 'massive support' in high pressure systems, and has quantified the effects of gasket work hardening compared to the

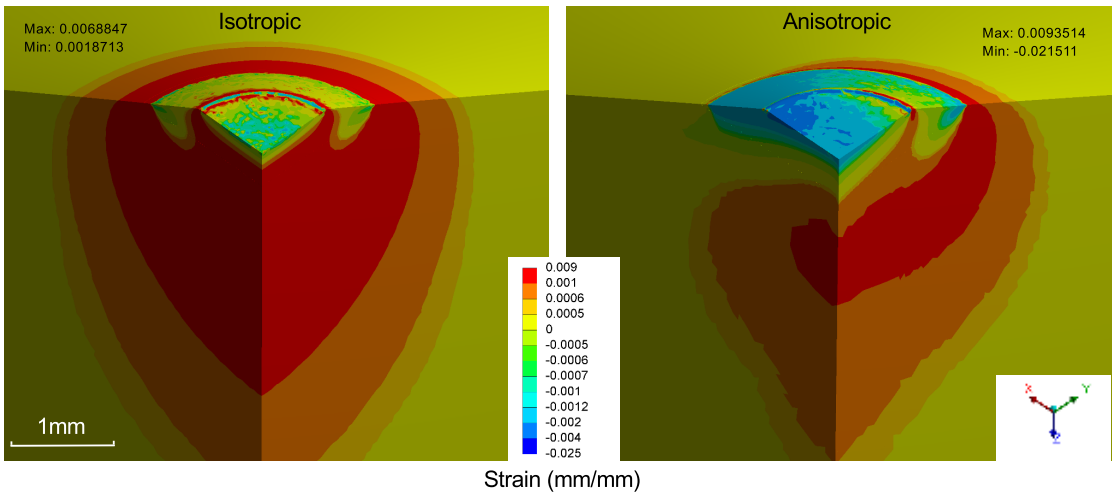

Figure 4.20 *Comparison of maximum principal strain for isotropic and anisotropic model of sapphire loaded along the c-axis.*

.

performance expected from a simple elastic gasket analysis, whilst also studying the effects of relative dimensions of the culet and gasket on stresses in the anvil.

There are many more possibilities for studies using FEA to optimise the anvil assembly. One obvious area for further study is the optimisation of taper angle, and the effects of bevelling the culet. However, this style of simulation is more well suited to isotropic materials, where additional failure modes such as slip planes and twinning are not present, and the effects of surface finish are less critical. To retrieve a more quantitative analysis of sapphire anvils, a more sophisticated level of simulation may be required, and further experimental data may be required. These techniques could be used further in the study of sintered anvil materials, such as cBN or WC, looking at applications in large volume pressure cells, such as multi-anvil, or belt-press systems, crucial for high pressure synthesis. Through varying the tangent modulus and yield strength of the gasket material, the effects of work hardening could be taken further to adapt the current theory of gasket mechanics to include plastic behaviour. Furthermore, more sophisticated models of plasticity could be incorporated.

Chapter 5

Design and construction of a miniature collimator system for high pressure neutron diffraction studies

5.1 Introduction

Currently achievable levels of flux for neutron diffraction are orders of magnitude lower than those achievable with X-rays, meaning that sample sizes need to be larger to achieve sufficient diffraction statistics in a reasonable time-frame. However, the high penetrability of neutrons makes them uniquely well suited for the study of bulk material properties, whilst their intrinsic spin allows them to be used to characterise magnetic structures.

Although there is a significant amount of science that is possible with neutrons within these sample limitations, it is not always feasible to use or produce large samples. For example, sample volume limits the achievable pressures due to pressure cell limitations [36]. This indirectly limits other external parameters applicable such as the temperature or magnetic field. Some samples may be challenging to synthesise in large quantities as a powder, or may not form sufficiently large single crystals (as is the case with zeolites [154]). Single crystal diffraction contains information that powder samples lose due to orientation averaging.

Improvements in neutron detection, and in the production of neutrons at large

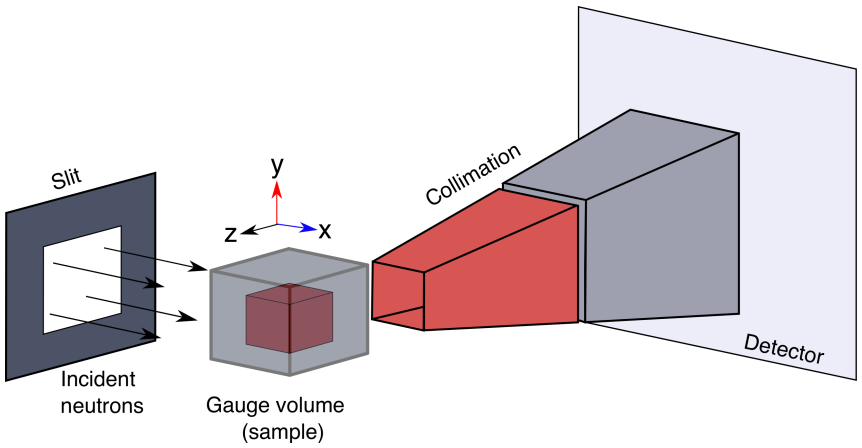

Figure 5.1 *Schematic showing the gauge volume defined using a slit to narrow the incident beam, and a collimator to narrow the diffracted path. As shown, the size of the gauge volume can be reduced if the collimator is longer, or closer to the sample. The gauge volume can be reduced further if additional vertical foils are inserted within the collimator. In reality the gauge volume is not sharply defined as in the figure, but has a gaussian intensity profile in 3D.*

facilities, makes it sometimes possible to secure data from samples of a few mg with certain instruments. To distinguish the sample data above the background it is important to mask as many sources of background from the instrument and auxiliary equipment as possible. This is typically achieved using 'beam scrapers' or slits to narrow the incident beam, and collimators to focus the detectors on a reduced volume of space in the sample area. For example, this principle is used extensively on the instrument Engin-X at the ISIS Facility [155], allowing the volume of space visible to the detectors (gauge volume) to be reduced to 0.5x0.5x0.5 mm^3, so that detailed strain profiles within large samples can be obtained. Conventional collimators are limited in how small the gauge volume can be by the length of the collimator, the minimum possible proximity to the sample, the maximum number of slits that can be accommodated, and the space available within the instrument (see figure 5.1). Instruments also need versatility with collimation, to allow for different types of measurement, sample sizes, and sample environments. The collimators used to vary the gauge volume on Engin-X are bulky, and difficult to align, such that most instruments tend to use collimation with larger gauge volumes which remain fixed in place, or which oscillate about a fixed point to reduce shadowing effects.

Conventional neutron collimators use thin foils, typically made from mylar, aluminium or stainless steel, coated in an absorbing material, such as gadolinium or enriched boron, to absorb divergent incident neutrons, or those scattered

from unwanted sources. The foils are held together, and tensioned to ensure uniformity, using bolted frames. The unit for gripping and tensioning the foils limits how closely they may be placed together, their angular separation, their proximity to the sample, and therefore the efficiency of the collimator. Modelling software, in combination with ray tracing simulations, show that there are designs which can greatly improve the performance of the collimator, but are not possible to implement using conventional assembly or machining techniques. Here we present the design and construction of a 3D rapid prototyped (printed) collimator, free from many of these constraints. The scale, and prospect for customisation, of the device means that the techniques presented can be applied to a broad range of applications. These include the design of interchangeable collimators for a particular neutron instrument, allowing a broader range of possible measurements, or for use in developing small scale pressure cells for neutron diffraction, which are currently hampered by high background [99].

5.2 Existing collimator designs

For collimation of incident radiation, one of the simplest devices is an extended slit. The length and cross-section of the slit reduces beam divergence, improving the resolution of the instrument, but this must be balanced with the loss in flux. If used at the detector side of the sample, the slit can be tapered to match the geometry of the detector. A more efficient device, known as a Soller, consists of tightly spaced coated foils or sandwiches of absorbing and transmitting foils which are stacked parallel either vertically or horizontally, reducing the intensity loss whilst controlling the divergence of the beam [156]. A honeycomb pattern of foils may be used to control the divergence of the beam in two dimensions [157]. An alternative design uses micro-channel plates (MCP) made through drawing and fusing many cladded glass tubes together, and dissolving the glass leaving a grid of channels [158, 159]. Honeycomb and MCP collimators offer much improved flux transmission, and allow for consistent collimation of larger beam sizes. The diameter of the MCP channels means that they need only be a fraction of the length of a honeycomb collimator to achieve the same collimation.

For the diffracted beam, depending on the detector and scattering geometry, collimators are usually radial type. A radial collimator consists either of a housing of angularly spaced foils, or a collection of Soller units angled around the sample. The former have fewer foils, so offer the best transmission to detector, but are

consequently more limited in gauge volume. Sollers offer tighter collimation, at the expense of lost detector coverage due to the frame of the each Soller. Thin MCP collimators [160] may be installed close to the detectors, such as for imaging or transmission experiments, but require curvature to be effective for angular-dispersive diffraction. Whilst it is possible to introduce curvature to MCPs through 'slumping', there are few examples of this being implemented, possibly due to difficulties in manufacture. Honeycomb collimators are made from joined die-pressed foils, which currently cannot be manufactured with radial angular separation. 3D printing can overcome the limits of these conventional designs; Zhong et al. [161] present an elongated slit design, made from 3D printed W-Ni, for the collimation of hard X-rays in a modulation telescope. The device is large and uses broadly spaced 3 mm thick walls which would be inefficient for neutron scattering measurements. Here we present the design of a 3D printed near-sample radial collimator, with significantly thinner 0.1 mm wall sections, providing a compact method to reduce the gauge volume without the need to remove existing collimation from the neutron instrument.

5.3 3D direct metal laser-sintering

Direct metal laser sintering (DMLS) is an additive rapid-prototyping process whereby fine metallic powder is layered and sintered together in high precision using a laser source. The process takes a computer aided design, which is then sliced into multiple layers/planes. The powder is then sintered to match each layer, gradually building the full model. The finished part can be treated much like parts constructed using traditional techniques, being machined, ground, coated, and polished. Further information on the process, and a review of its development can be found elsewhere [162, 163].

The advantages of this technique are that there is virtually zero material wasted, powder that is not sintered in the layer may be removed and reused, and that more complex geometries can be made without concerns due to tooling access. Curved profiles, thin wall sections, and tightly spaced components can be printed without added complexity. The precision of the printing can be as good as ± 0.05 mm, whilst the materials offered are varied; maraging, or stainless steels, aluminium and copper are commonly used. The minimum wall thickness achievable depends on length of the feature, and the material it is made from. The minimum resolution typically offered commercially is 0.1 mm. Another advantage of laser

sintering, unlike other plastic printing techniques, is the more consistent material properties of the finished part.

5.4 Collimator design

The main objective of this work was to improve the signal-to-noise ratio from a sample volume of approximately 0.5 mm^3 housed in an opposed sapphire anvil pressure cell similar to that reported in the work of Jacobsen et al. [4]. In this cell the sample signal is very weak compared to the signal from the anvils, the gasket (used to contain the sample between the anvils), and the pressure cell itself. It is not possible to mask the sapphires or gasket without obscuring the sample. Due to the cryogenic purpose of this cell there were additional design constraints that needed to be met; firstly any additional material had to be of minimal mass so as to have as little effect on cooling times as possible; secondly that the device must fit within a 100 mm cryostat bore. Initially miniature conventional collimators were considered, but were either impossible to construct so close to the sample, and in such a confined space, or did not offer a fine enough collimation to offer improvement to the signal.

3D laser sintering offered the possibility to remove the need for tensioning systems, and also opened up the possibility of manufacturing a 2D radial collimator (curved in two planes radially), with angled foils positioned both vertically and horizontally. This may offer a considerable advantage over conventional 1D radial (curved in one plane) collimators, which do not discriminate signal from points along the axis of the collimator, and can be easily formed and angled in complex geometries unlike 2D MCP collimators. The main benefit of rapid-prototyping is that the specific shape and dimensions of the collimator can be easily customised to fit the pressure cell in question in the computer aided design stage.

5.4.1 Simulation

To verify the feasibility of using such fine near sample collimation with limited collimator length, several simulations were performed using custom JAVA ray tracing code to visualise the gauge volume, [164] and Monte Carlo neutron ray tracing was performed using McStas [165, 166] to estimate the possible improvement in sample signal.

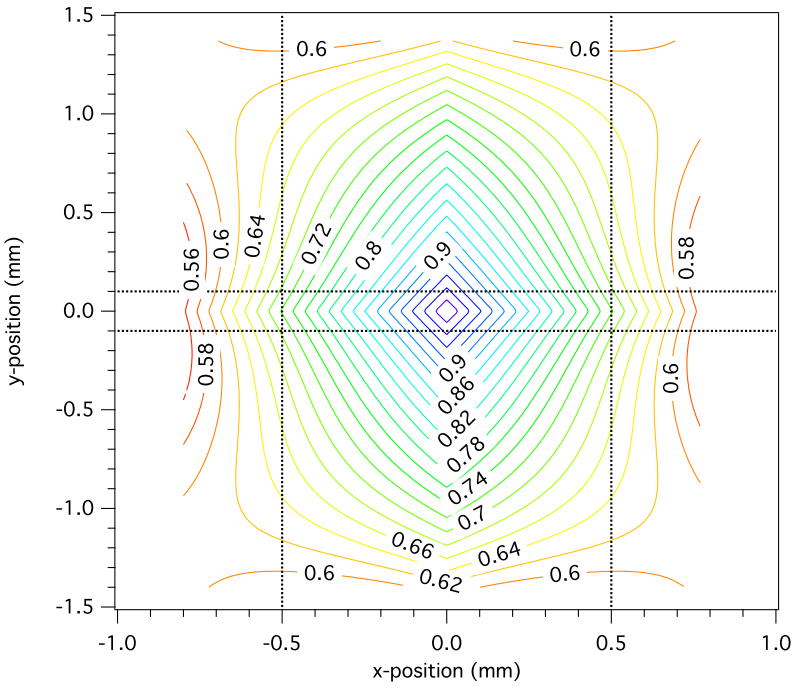

Figure 5.2 *Gauge volume profile in xy-plane (as defined in figure 5.1) of sample region as defined by two dimensional radial collimation. The sample region is defined by the dashed lines in the figure. The contour scale is relative to maximum solid angle at the central position of the collimator. The opening parameters were chosen to have a* 4° *horizontal separation, and a* 6° *vertical separation. The JAVA simulation assumes zero wall thickness.*

The design of the pressure cell meant that the collimator can be no closer than 15 mm to the sample, and to ensure that the device would fit safely into the bore of the cryostat the length of the collimator should not exceed 30 mm. With these two parameters fixed JAVA ray tracing was used to determine the effect of number of collimator slits, and their angular spacing, on the gauge volume in the sample region. This was achieved through calculation of the visible solid angle at each point in the sample region using vector analysis and assuming zero wall thickness. If the material in the beam is assumed to be an isotropic scatterer, the solid angle may be thought of as a measure of the signal contribution. The simulation radially stacks a number of collimators similar in geometry to that shown in figure 5.1 summing the solid angle contributions from each at a given position in the sample volume. Figure 5.2 shows the calculated gauge volume profile chosen for the design of the collimator, with both vertical and horizontal collimation. The vertical collimation was designed to be broader than the horizontal collimation to allow for variations in the vertical position of the sample between the anvils. Integrating the drop in solid angle over the sample region shows that it falls to 86 % of the uncollimated value horizontally, and 95 % vertically. If the parameters of the collimator slits are altered to reduce the loss in solid angle in the sample volume, then there is a proportional increase in background signal from surrounding. Vertically this is less important, as this region can be effectively masked through narrowing the incident beam, this is less effective horizontally as the beam is directed straight through the gasket.

The effects of wall thickness have been calculated by Wang et al. [167], who found that the effect is non-negligible but small, reducing the maximum transmission of the collimator by as much as 15 %. The most efficient collimator will have a wall thickness just sufficient to ensure structural stability, and no larger. This can be verified using the CAD model with other computational techniques such as finite-element analysis, prior to manufacture.

To make a quantified estimate for the level of reduction in background signal from the gasket, Monte Carlo ray tracing was performed using a simple McStas instrument. The instrument was modelled consisting of a source, cylindrical detector bank, and a beam stop behind the sample position. The sample was modelled as a cylinder of Ni powder 1 mm thick with 1 mm diameter, and the gasket as a hollow cylinder of Al powder with the same thickness but an outer diameter of 10 mm. The powder pattern was compared with just sample, sample with the gasket included, and sample with gasket and collimation included. The

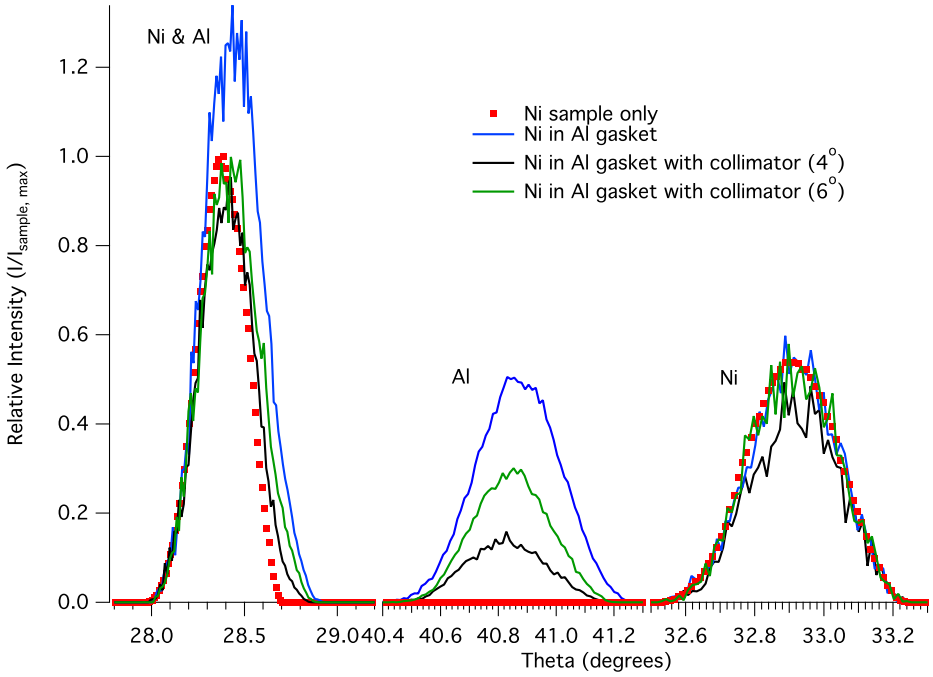

Figure 5.3 *McStas simulation results. The three peaks are (from left to right) sample with overlapping peak from gasket, gasket peak, sample peak without gasket contribution. Whilst the* 4° *collimator offers a reduction of gasket contribution to* 20 % *it also reduces the sample intensity. The* 6° *collimator reduces the gasket peak intensity by* 50 % *and negligibly reduces the sample intensity.*

collimator was simulated with two different foil separations 4° or 6°, with an inner diameter of 30 mm and outer diameter of 92 mm. Incoherent scattering was neglected in these simulations to ease data comparison. The results are shown in figure 5.3.

5.4.2 Prototype construction and coating

3D printing does not guarantee that a part can be built successfully. The direction of the build in rapid prototyping will influence the likelihood of a successful build, and should be chosen so as to provide maximum support to the part as it is assembled. Long sections of thin wall segments may not build correctly as the material may not fuse together fully, or the laser may simply burn away excess material. Due to the potential length of the thin collimator walls it could not be predicted if construction would be possible. To find the minimum possible wall thickness that could be successfully printed, three test parts were trialled with wall lengths typical of the expected final design (approximately 5 mm) see

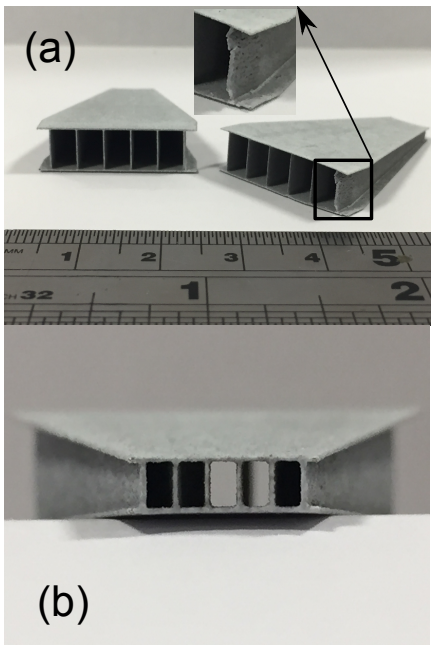

Figure 5.4 *Two of the stainless steel 316L printed test pieces painted with Gd-paint post thermal cycling (a) left,* 0.2 mm *wall thickness, right,* 0.1 mm *showing wall damage. (b) close view of sample side of* 0.2 mm *collimator.*

figure 5.4. Printing of the parts was done with CRDM Ltd. Stainless steel 316L was chosen due to the improved strength over aluminium, which would be preferred for cryogenic applications. The 0.3 mm and 0.2 mm thick parts were built successfully, whereas the 0.1 mm thick part had some minor perforations on the wall section.

These prototypes were also used to test the coating process for the collimator. Due to the thin wall sections, and the desire to keep their thickness minimal, Gd-paint was chosen as the coating material. The parts were spray-coated with an approximate thickness of $\approx$ 25 µm by Euro Collimators Ltd. The coated test pieces were also used for thermal testing, as the collimator will eventually be cooled to sub-5 K temperatures in a cryostat, to ensure secure adhesion of the coating, and that the thermal stress on the system doesn't result in a structural failure. This was done through sudden and repeated immersion in liquid nitrogen. The parts were thermally cycled several times from ambient to nitrogen temperatures with no indication of the paint coming loose, or damage to the parts.

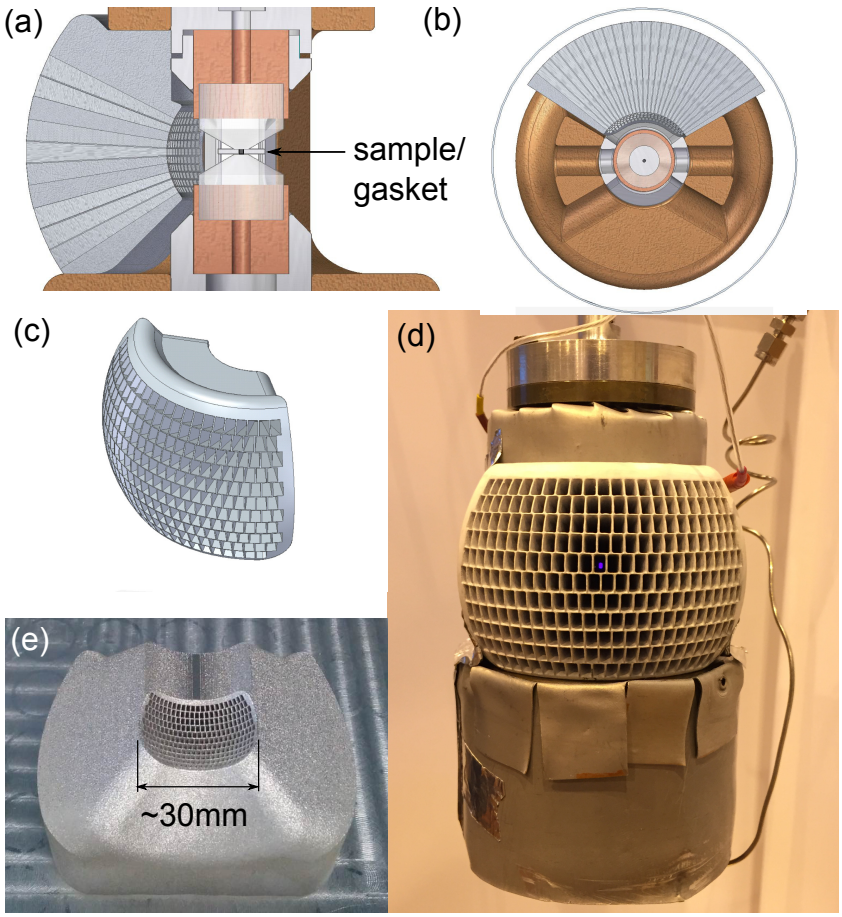

Figure 5.5 *(a) Vertical and (b) horizontal sections of pressure cell with collimator design, the sample sits between the two sapphire anvils, (b) shows the wall of the* 100 mm *bore cryostat, (c) CAD model of radial collimator, (d) detector side of printed collimator, coated in* Gd_2O_3 *paint, and fitted to pressure cell. The sample region can be seen through the collimator illuminated by the laser used for manometry. (e) Sample side view of printed collimator.*

5.4.3 Final design

The test builds identified the optimal wall thickness to be not less than 0.2 mm. Two dimensional collimation was chosen for the first full build of the collimator, as this provides a theoretical advantage over conventional collimator units which cannot angle foils simultaneously in vertical and horizontal planes, and gives the device a more rigid 'comb' structure. It is more common to use a 1D radial collimator with a slit to narrow the incident beam, but 2D collimation has the advantage that secondary scattering events are also effectively collimated. The shape of the device was chosen to be spherical to ensure that the length of each of the channels was identical, to ensure even collimation. The final design is

pictured in figure 5.5.

5.5 Online testing

The collimator unit was tested using the WISH instrument at the ISIS neutron facility. The gasket was made from aluminium, and the sample used for testing was a powder of the perovskite $SrTiO_3$, available from Alfa Aesar. The sample and gasket were placed between two sapphire anvils within the pressure cell, and aligned to be in the vertical plane of the collimator. The sample volume used in the test was approximately $0.25\,\mathrm{mm}^3$, and the count time for the test was 45 minutes. The tests used the symmetry of the cell, and detector layout of WISH to compare data with and without the collimator simultaneously. The raw data from the detector, and the focussed data, with Bragg peaks masked, are shown in figure 5.6. Some anvil materials used with the pressure cell are not single crystal, and so peak masking is not always possible.

5.6 Discussion

The raw data show a clear reduction in the intensity and number of parasitic Bragg peaks contributed from the single crystal sapphire anvils. The focussed data show a large reduction in the incoherent background present in the data, and a reduction in the intensity of the powder peaks of the gasket and sample. Comparing the integrated intensities of the sample and gasket peaks shows that the sample signal becomes approximately 10 times more intense relative to the gasket, with an approximately 96% reduction in aluminium intensity. Analysis of the background signal also shows an increase of signal to noise of approximately 76%. In addition, a number of the weaker parasitic reflections at longer wavelengths are removed from the data completely.

The sample peak intensities, relative to the background in each case, reduce to $\approx 40\,\%$ of the uncollimated levels, which is larger than expected from the simulations. This is partly due to the effects of finite wall thickness, as the foils block the signal over sections of the detectors interrupting the powder rings and reducing the integrated intensities. The angular interruption due to the foil thickness is estimated to be 4° over the 30° out of plane coverage available on

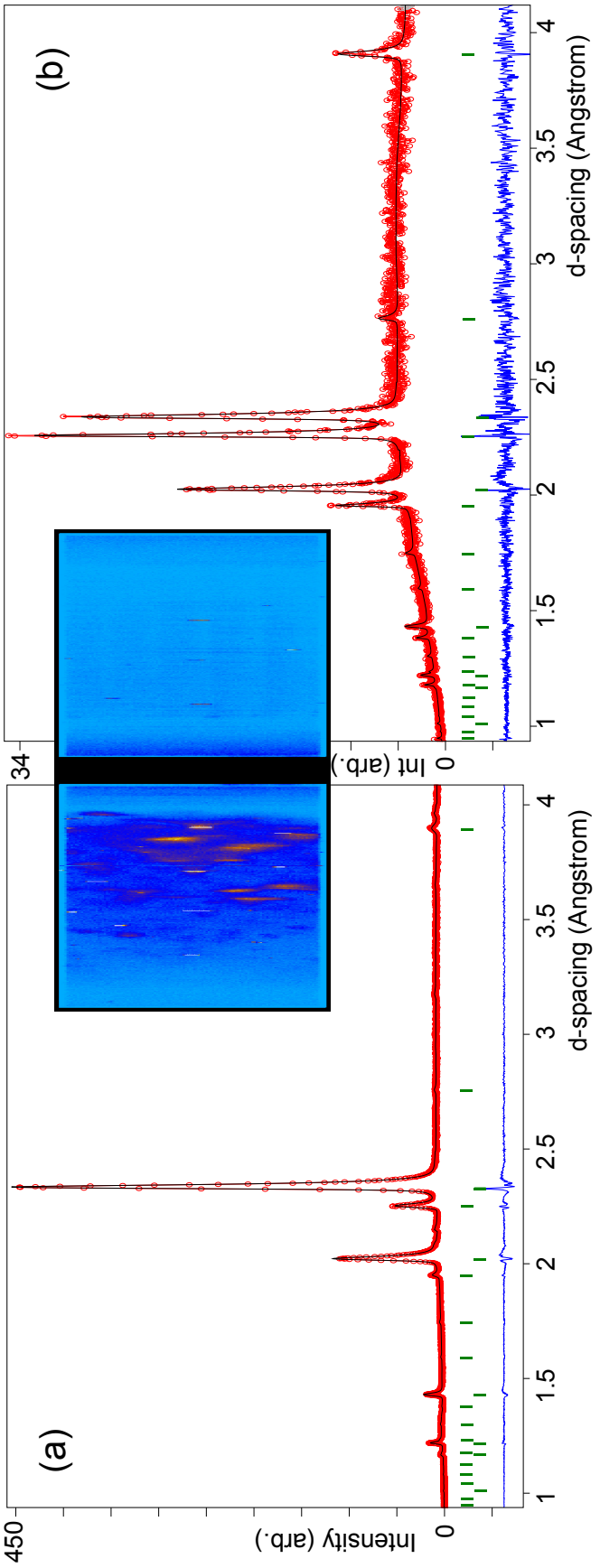

Figure 5.6 *Focussed diffraction data, with sapphire Bragg peaks masked, taken from the two $2\theta = 90°$ detector banks on WISH at the ISIS facility (a) without collimation, (b) with collimation. The data has been LeBail fit showing the reflections from the $SrTiO_3$ sample (upper ticks) and the Al gasket (lower ticks). Inset, raw unmasked data from detectors, left hand side without collimation, right hand side with collimation. Masking the Bragg peaks is significantly less time consuming with the use of collimation.*

WISH, and 20° over the in plane 110° windows on the pressure cell. The reduction in sample peak intensity relative to background is approximately uniform across the detectors, with no peaks completely disappearing, indicating that this loss in sample signal may mostly be due to the inclusion of the vertical collimation. The 2D design presented may therefore be more suitable for use with single crystal samples, where a maximum reduction in powder signal contribution is desired. Another possibility is that the collimator was slightly misaligned when attached to the cell. Due to the need for tight collimation, a misalignment of the focus of the collimator by 0.5 mm could lead to a reduction in intensity of by approximately 40%.

The foils also cast a shadow over the detectors, where parts of the sample are masked slightly at certain angles, beyond the effects of wall thickness. This problem is caused by the foils being angled to a point at the centre of the sample. In cases where the sample is surrounded by mostly empty space, the collimator can be adjusted to minimise this shadowing by increasing the inside diameter of the collimator relative to the diameter of the sample. In the case of pressure cells, reducing the shadowing effect in this way results in a large increase in background from surrounding material. Oscillating the collimator about its axis would average out the effects of shadowing, but would require a rotational mechanism difficult to implement in a cryogenic environment. Another possibility, only suitable for powder analysis, uses the symmetry of the scattering geometry of the pressure cell. A secondary collimator could be installed on the opposite side of the cell to the primary collimator, with a slightly different spatial layout of channels. The data from both sides of the instrument could then be summed, again averaging out the effects of shadowing certain reflections more than others.

Aside from 2D radial collimation, there are many other collimator concepts which could possibly be manufactured using 3D rapid prototyping. Due to the geometry of the Debye-Scherrer cones formed from powder samples, collimators made from vertical foils are intrinsically less efficient in forward and backscattering angles, being most transmissive at $2\theta = 90°$. This is unfortunate, as the resolution is maximised in backscattering. Using 3D printing it may be possible to incorporate a conical form to a radial collimator, where the vertical foils become increasingly curved from the vertical at angles away from 90°. This would dramatically improve the efficiency of the transmission of the collimator in forward and backscattering regions.

Whilst it is possible to simulate a perfect collimator, where the geometry of the collimator is only limited by the ability of the software to incorporate it, the manufacture of such devices is severely limited by machining and assembly capabilities. 3D rapid prototyping is a step towards lifting this limitation, allowing for increasingly complex designs to be manufactured relatively inexpensively.

5.7 Conclusion

A 3D laser-sintered collimator has been shown to effectively reduce neutron incoherent background, and coherent contributions from the material immediately surrounding the sample. The use of such collimators is very promising for increasing the efficiency of data collection from small samples for neutron scattering experiments, or for improving the data quality collected where sample volume is constrained by the sample environment. Online testing at the ISIS neutron facility has shown that the collimator drastically reduces levels of background signal generated by material directly surrounding the sample. The tests have shown that the sample signal is reduced more than expected due to foils shadowing regions of the sample to the detector. The next iteration of the design will use 1D collimation, attempting to reduce the wall thickness to 0.1 mm in order to reduce sample losses to the collimator, and will use a larger angular separation to reduce shadowing effects. In addition, neutron transmission measurements will be performed to further characterise the efficiency of the collimator.

Achieving efficient collimation is challenging, with there being a need to tailor specific collimators to individual measurements; for example the optimal geometry differs between single crystal and powder samples or for the incorporated sample environment, different sample volumes, or different detector layouts. The demonstrated effectiveness of 3D rapid prototyping in collimator manufacture is promising for the development of individual collimation units for experiments without the need to alter the existing setup of the instrument. Compact devices can be incorporated in existing sample environment, such as being installed in the jacketing of cryostats, or within larger existing collimators, which many instruments are already able to accommodate.

Chapter 6

An improved low-temperature piston-cylinder cell for neutron diffraction with in-situ electrical measurement

6.1 Introduction & design motivation

Clamped piston-cylinder style pressure cells are used extensively at large neutron facilities such as the ISIS neutron and muon facility, and the Institute Laue Langevin (ILL), as a very versatile device suitable for use on many different instruments. The devices may be compact, such that they fit into dilution fridge inserts allowing sub-Kelvin temperatures to be reached; whilst the axial symmetry of the cell means that samples may be rotated easily, meaning that both single crystals and powders can be studied, whilst the background from the cell should remain approximately isotropic. However, these clamped systems are limited by requiring a large hydraulic press to load, and vary the sample pressure. Once the cell is loaded to a given pressure, the pressure must be measured on the instrument through monitoring a pressure standard in the cell (such as NaCl or Pb). Depending on the design of the seal, cycling the load is not always possible, so overshooting can cause problems. Furthermore, particularly where BeCu is used, there are concerns with handling the active cell, such that it can be very time consuming to reach the correct pressure. In addition, where low temperature

studies are performed, thermal contraction of the cell can cause a drop in sample pressure, and quantifying this before measurement could save time.

The work of this chapter is a result from a collaboration with the sample environment group at the ILL, with the aim to adapt an existing, and well used, piston-cylinder pressure cell to support in-situ pressure determination through electrical measurement. In addition to alleviating the above problems, introducing wires to the pressure cells allows many other studies to be performed with the cell, in combination with neutron diffraction, which go beyond resistivity measurements of the sample.

Here a clamped piston-cylinder cell is presented with in-situ pressure measurement, capable of generating 1.4 GPa in volumes suitable for neutron diffraction studies. To demonstrate the additional measurements possible with the cell, in addition to neutron measurements, a high pressure ultrasonic study of the compound UGe_2 is presented.

6.2 Existing & modified cell design

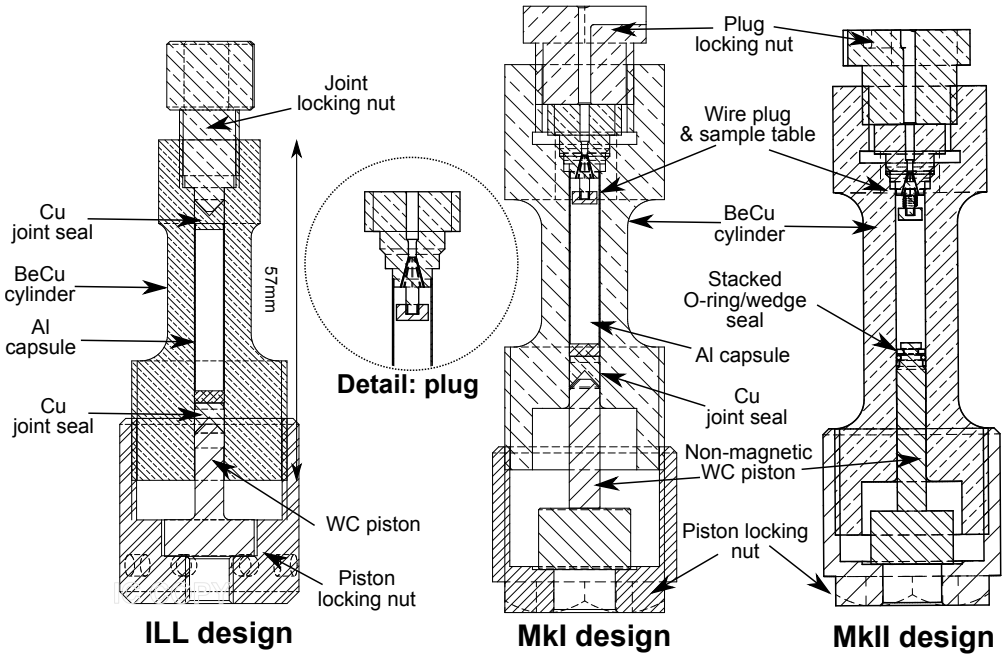

Figure 6.1 *Cross-sectional view of original clamped cell as designed by the ILL, the redesigned MkI cell incorporating a wire plug (detailed), and the redesigned MkII cell, incorporating the plug, and removing the need for an aluminium sample capsule.*

Cross-sectional views of the existing and modified (MkI & MkII) clamped piston-cylinder cells are shown in figure 6.1. The original design contains the sample in an aluminium capsule, each end of the cell is then sealed using a conical Cu joint, which is deformed to seal against the wall of the cylinder by a conical plug and piston. The MkI design replaced the fixed Cu joint with a wire plug, sealed with a deformable Cu ring. The piston end of the MkI was left as designed by the ILL. The MkII design removed the need for the Cu joint seal, and the aluminium capsule, through incorporating a stacked seal on the end of the piston. The plug design of the MkII is identical to that of the MkI.

6.2.1 Plug design & assembly

There are several reported techniques for feeding wires into a pressure cell, some of which are discussed by Eremets [17]. In the simplest case a series of wires may be introduced through a hole in a plug at one end of the cell, which is filled with a hard curing adhesive. This technique relies on several things: that the adhesive is impermeable to the pressure fluid used; that the adhesive forms a strong bond to the walls of the hole; that the ratio of length to diameter of the hole is relatively large, such that the internal friction (shear strength) of the adhesive can balance the force generated by the pressure medium on the adhesive.

Reported values for the shear strength of Stycast epoxy range from $\tau = 3{-}15\,\mathrm{MPa}$ [168, 169], with the 2850 FT type being the strongest variety for low temperature adhesion [170]. A simple pressure $= \frac{\text{force}}{\text{area}}$ calculation allows the estimation of the required ratio of length (ℓ) to diameter ($\varnothing$) of the adhesive filled channels to withstand a given pressure (p). The maximum force that can be held by the adhesive is proportional to the inner surface are of the channel, and this must balance the force exerted on the upper surface area exposed to high pressure:

$$\frac{\ell}{\varnothing} = \frac{p}{4.\tau}$$

The proofed pressure range of the ILL clamp cell is 1.2 GPa, taking $\tau = 15\,\mathrm{MPa}$, the estimated $\frac{\ell}{\varnothing} = 25$. As such, a $\varnothing$1 mm hole would need to be 25 mm long to support the pressures required, assuming a perfect bond to the pressure cell, and ignoring thermal effects. Whilst the shear strength of Stycast increases to approximately $\tau = 69.7\,\mathrm{MPa}$ at 77 K [168], the linear thermal contraction of BeCu from 293 K to 77 K (for example) is 0.3% [55], whilst Stycast 2850 FT contracts

by 0.8% over the same temperature range [170]. This results in internal strain within the plug, which at lower temperatures, or after several temperature cycles, can cause the adhesive to start to de-bond with the plug. To reduce the chances of the seal popping out during warming of the cell, a conical hole can be included at the high pressure side of the plug.

Machining small diameter holes over long distances is challenging, and is no guarantee of success over many loadings; an alternative approach is to introduce a conical lead-through. This fills the conical hole of the plug with a smaller plug, around which is a layer of adhesive housing the wires. This layer of adhesive acts as a gasket; with increasing pressure in the cell, the small plug is pushed harder against the conical face of the larger conical hole, forming a progressively tighter seal. One disadvantage of this technique is that if the adhesive layer is misjudged, the wires can be guillotined under pressure. Another is that the dual plug design increases the dimensions of the assembly.

To overcome this, an adapted design based on the dual plug concept was used, as originally developed by Jiří Kamarád (Institute of Physics, Prague, Czech Republic) [171]. Narrow channels are included along the length of the outer surface of the plug to securely guide the wires, and reduce the chance of damage upon loading. The channels are only just larger than each individual wire, increasing the $\frac{\ell}{\varnothing}$ ratio without the need to drill longer, narrower holes. An added advantage of this design is that a pillar and table can be included with the plug, around which the manganin pressure sensor can be wound, and on which the sample can be accurately positioned and mounted. An overview of the plug assembly is shown in figure 6.2.

The adhesive chose for the plug was Stycast 2850 FT with catalyst 24LV [170]. Walker [172] reports that adding a small amount of fine mesh alumina or diamond powder significantly improves the hardness of the cured adhesive, and improves its thermal properties accordingly. However, it was found that due to the small dimensions of the channels used, and the low viscosity of mixed Stycast, adding additional components made it very difficult to ensure that the Stycast filled the full length of the channel.

The plug was assembled sat within a rubber bung inserted into a conical flask with a side-arm. The side-arm was used to connect a vacuum pump, used to pull the Stycast through the narrow channels. To ensure a good mating between the conical insert and the conical hole the two were fine ground together with 1 µm

diamond grit. Before assembly all parts were ultrasonically washed in acetone to remove residue from the grinding and machining processes. The conical plug was first pressed into the hole with the aid of a pin held on a clamp stand, and the ø100 µm enamelled Cu wire from Advent Research Materials Ltd. was then fed through the channels. Stycast was then slowly applied with a pin head evenly around the top of the channels, with vacuum used after each application. After 30 min, the Stycast begins to cure, and application was stopped. The adhesive was then left to fully cure over 24 h.

A manganin coil was included in the cell as a manometer, the resistance of the wire as a function of pressure is well characterised [173]. The coil was wound around the shaft of a drill bit, and held together with dilute GE varnish. The coils were cycled between 350 K and 70 K through immersion in liquid nitrogen and warming on a hot plate to remove residual stresses in the wound coil introduced during preparation and during the thermal contraction of the coil.

6.2.2 MkII design motivation

The original and MkI design of the cell uses an aluminium sample container as an essential part of the sealing mechanism. The close fit of the container with the walls of the cylinder, helps it to partially resist axial deformation, giving enough support for the Cu joint seals to deform against the cylinder wall. The concept works effectively in the original design, though was unreliable in the MkI design, which was much more difficult to seal at the piston end. This was probably due to the quality of fit between the aluminium containers (which were machined at the ILL) and the cylinder (machined at Edinburgh) providing insufficient support to the container, and therefore insufficient resistance to allow the Cu joint seal to start deforming. It was found that the inclusion of a 0.5 mm thick oversized teflon cap underneath the Cu joint at the piston end provided enough support to seal the cell. Furthermore, the deformable aluminium capsule had the potential to interfere with the delicate wire assembly on the table of the plug, particularly during removal from the cell.

The multiple attempts to improve the sealing on the MkI design led to the MkII design, which saw a change in seal design to a two stage mobile seal. Whilst the machining of tungsten carbide components has historically made it prohibitively costly to make parts beyond a simple rod, modern tooling has made it far more cost effective, allowing the inexpensive manufacture of the stepped WC piston

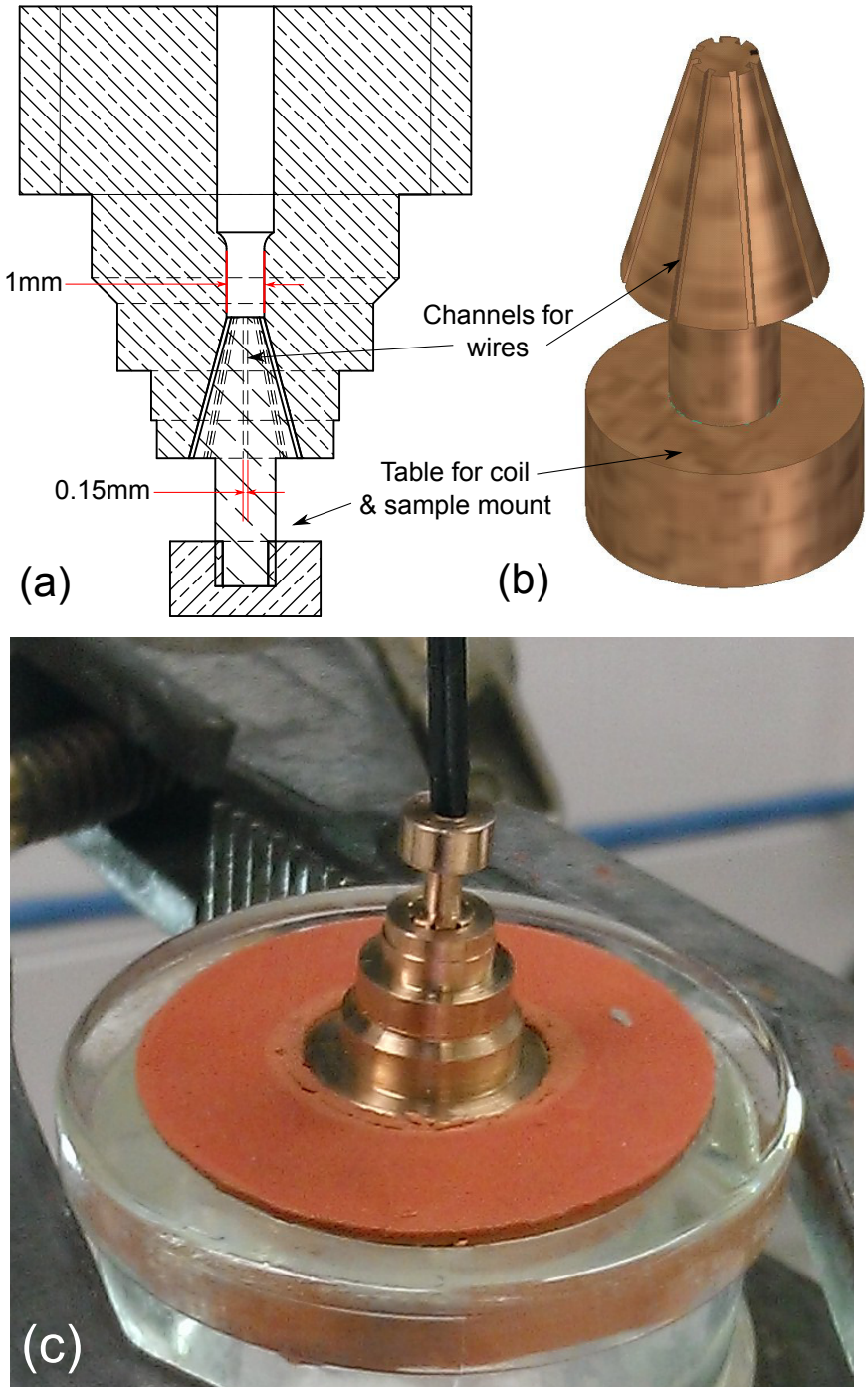

Figure 6.2 *(a) Cross-section view of conical dual plug assembly, with dimensions of the channels and hole shown to scale. (b) Isometric view of smaller conical insert only, showing the* 0.15 mm *wide/deep channels included to filled with wires and adhesive. (c) Assembly of the plug, the conical insert is held in place with a pin, the wires are then fed through the channels. Vacuum is then applied to the underside of the rubber bung, to encourage the Stycast into the channels.*

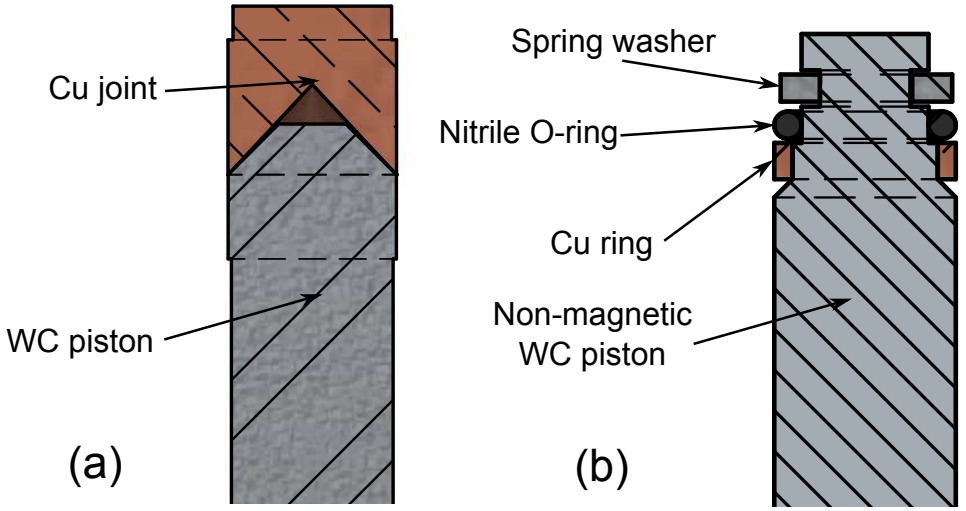

Figure 6.3 *Schematic showing (a) old seal design with Cu joint and (b) MkII piston design with two stage O-ring/Cu wedge seal.*

shown in figure 6.3. At low pressures, an O-ring is used to seal against a gland on the piston, and against the walls of the cell, at higher pressures the O-ring starts to extrude up the piston, pushing against a Cu ring, which then forms a wedge seal. A spring washer is included at the end of the piston to encourage the entire seal assembly to come out with the piston on unloading, leaving the bore of the cylinder clear.

This seal design is significantly easier to assemble than the original concept, with all components being commercially available at low cost, and independent of parts machined to tight tolerances and fine surface finish. In addition, the removal of the Al sample capsule is beneficial for neutron diffraction measurements. Although Al is very transparent to neutrons, it will still contribute a powder rings to the diffraction pattern in addition to the BeCu. The MkII reduces the sources of background.

6.3 Load testing

The plug should be assembled first. First the plug should be cleaned, removing any remnant sample or pressure fluid, a light soak in dilute ethanol is sufficient, and shouldn't affect the Stycast. Once clean, the Cu ring seal should be attached to the diameter around the plug, and the manganin coil attached to the pillar, the table can then be attached via the thread. Four of the wires included should

then be soldered to the coil, two at each end, as current and voltage leads for four-terminal sensing. The remaining four wires can then either be left redundant, or used for other measurements on the sample (discussed in later section). All bare connections to the wires should be covered in varnish to prevent short-circuits during loading. If a single crystal, the sample can be aligned and mounted on the table, if not the sample is included after the plug is sealed in the cell.

To seal the plug in the cell, the cell should first be held in a vice via the flats on the cell. The plug can then be gently lowered into the bore of the cell, and push fit to ensure that the plug has engaged the cylinder correctly. The wires from the plug must then be fed through the locking nut, which should then be spanner tightened until the Cu ring seal has deformed. The cell can then be removed from the vice, and turned over. If loading a powder the sample should now be inserted, ensuring that 10 mm of bore is left clear. For all samples, the pressure medium should now be added. Either Fluorinert, Daphne oil, or a light mineral oil may be used depending on the experiment, again ensuring that there is a clear length in the bore. The cell can be lightly tapped to encourage air bubbles to be released, as these will reduce load efficiency.

The piston is then assembled, and loaded into the open end of the cell, the piston locking nut used to hold the piston in place. The O-ring should prevent any leaking before loading, so the cell may now be freely handled. To load, the cell should be stood on end, with the wires guided through the groove on the plug locking nut. The WC pusher is then inserted and load is applied directly to the back of the piston. A Keithley source-meter (or similar) can be used to monitor the resistance of the manganin gauge. Note that the coil requires pressure annealing, and so the value of the resistance will fluctuate slightly during the first few loadings. Care must be taken not to overload the cell during this period.

6.4 Calibrating the manganin coil

To fully calibrate the manganin coil, the resistance of the coil over the full temperature range at zero pressure must first be measured $R_0 = R(P = 0, T)$. Dmowski and Litwin-Staszewska [173] report that the following constant can be derived from manganin at a given temperature:

$$\alpha(T) = \frac{1}{R_0}\frac{dR(P,T)}{dP}$$

Where $\alpha(T = 298\,\mathrm{K}) = 2.34 \times 10^{-2}\mathrm{GPa}^{-1}$. Furthermore the constant α has a linear temperature dependence such that

$$\beta = \frac{1}{\alpha_0}\frac{d\alpha}{dT}$$

where $\beta = -3.80 \times 10^{-4}\mathrm{K}^{-1}$ below $T = 110\,\mathrm{K}$ and $\beta = 2.56 \times 10^{-4}\mathrm{K}^{-1}$ above $T = 110\,\mathrm{K}$. Therefore, with a known $R(P = 0, T)$ the pressure at any temperature can be evaluated. The ambient, and high pressure, voltage drop curves for a typical loading are shown in figure 6.4. The change in difference in the two curves indicates a pressure drop on cooling of approximately 7-8% down to 120 K, below which the pressure is stable. This is caused by differences in thermal contraction within the cell.

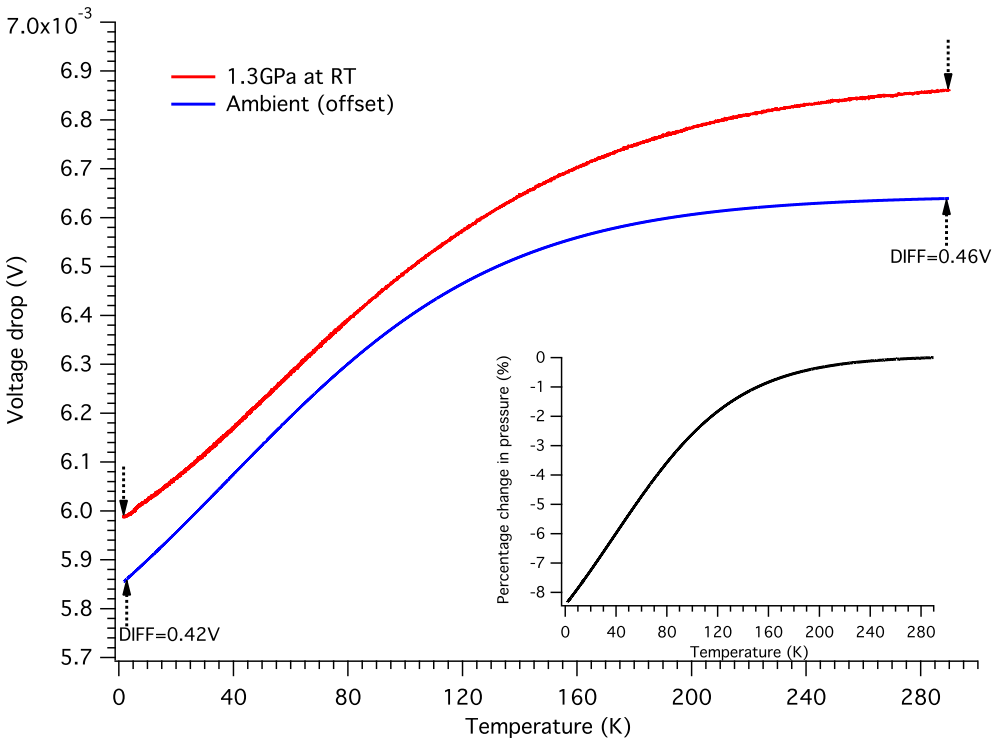

Figure 6.4 *Measured voltage drop over the Manganin coil, from room temperature to* 2 K, *at ambient pressure and* 1.3 GPa. *(inset) percentage drop in sample pressure as a function of temperature.*

6.5 Ultrasonic study of UGe_2 single crystal

Ultrasound ($\nu > 20\,\mathrm{kHz}$) is well established tool for studying the elastic properties of materials; measuring the speed of sound within a material can be used to

determine elements of the elasticity tensor, and discontinuities in this can reveal the onset of a variety of phase transitions [20, 174]. In addition to this, at the higher frequency end of the spectrum, ultrasound can be used to excite and measure oscillations in the Fermi surface. Through monitoring the ultrasonic response of the Fermi surface, and its orientational dependence, topological information can be inferred.

Ultrasonic measurements under pressure have been reported previously in Paris-Edinburgh, diamond anvil, and piston cylinder cells [175–177], though these were concerned with simulating geological processes on temperature scales too high to perform Fermi surface measurements, or the interplay between ferromagnetism and superconductivity.

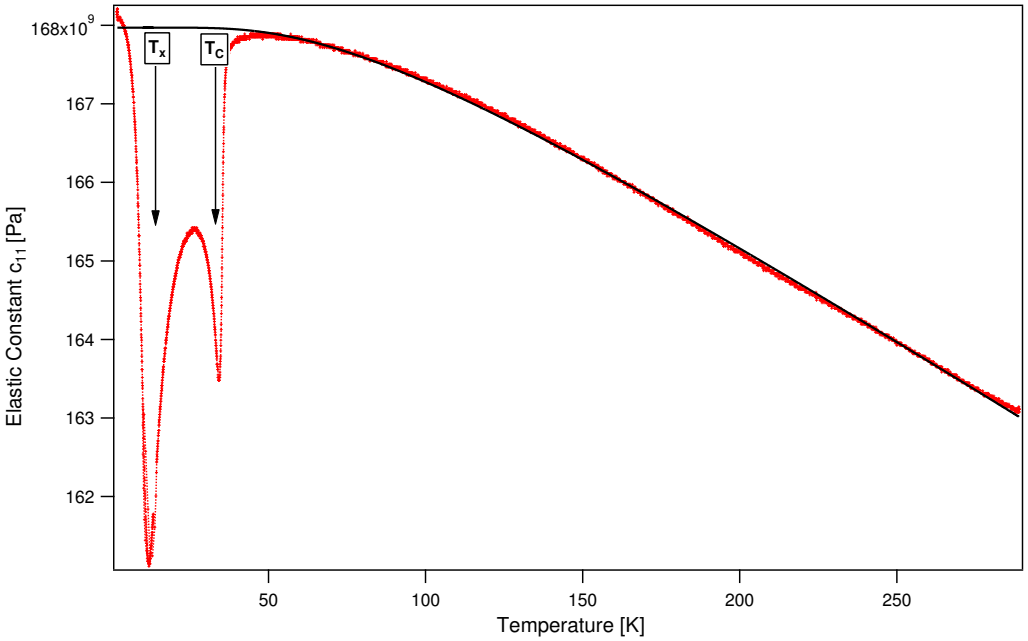

Figure 6.5 *Temperature dependence of elastic constant c_{11} of UGe_2 at* 1.1 GPa*, as determined through ultrasonic measurements of propagation velocity. Clear deviations are visible at the Curie temperature (T_C), with the onset of ferromagnetism, and T_x, the transition from FM1 to FM2.*

The compound UGe_2 is an unconventional ferromagnetic superconductor with a well established pressure-temperature phase diagram [178]. Superconductivity is only observed in the ferromagnetic phase below 1 K in the pressure range 0.8-1.6 GPa. The transition from paramagnetic (PM) and ferromagnetic (FM) states is fully suppressed at 1.6 GPa. The superconducting transition temperature is maximised at $P_x = 1.2$ GPa which is also associated with a metamagnetic transition from a low spin (FM1) to high spin (FM2) phase (see phase diagram

in figure 6.6). It is believed that magnetic fluctuations associated with this transition may play a key role in superconducting pairing mechanism in UGe_2 [179]. Previous elastic studies on UGe_2 were limited to ambient pressure only [180]. Previous ultrasonic studies under pressure have attached the transducer (to transmit and detect the returned ultrasonic signal) to the outside of the pressure cell. The ultrasound must travel through the anvil/piston/cylinder wall to reach the sample, and then return. This adds considerable background reflections to the measured signal, limiting the usefulness of the data, and introducing sources of systematic error. To demonstrate the versatility of the new piston cylinder cell for in-situ measurements, a small piezoelectric transducer was fixed directly to the surface of the crystal, and included inside the pressure cell. This technique has the added advantage that the crystal can be extremely precisely oriented, such that the error on the measured elastic constants is considerably smaller. Figure 6.5 shows a plot of the measured c_{11} elastic constant as a function of temperature, under a pressure of 1.1 GPa, close to P_x. The full details of this work can be found in [6]. The cell was prepared and loaded by Chris Ridley, the crystals were prepared, and ultrasonic data processed by Michal Kepa.

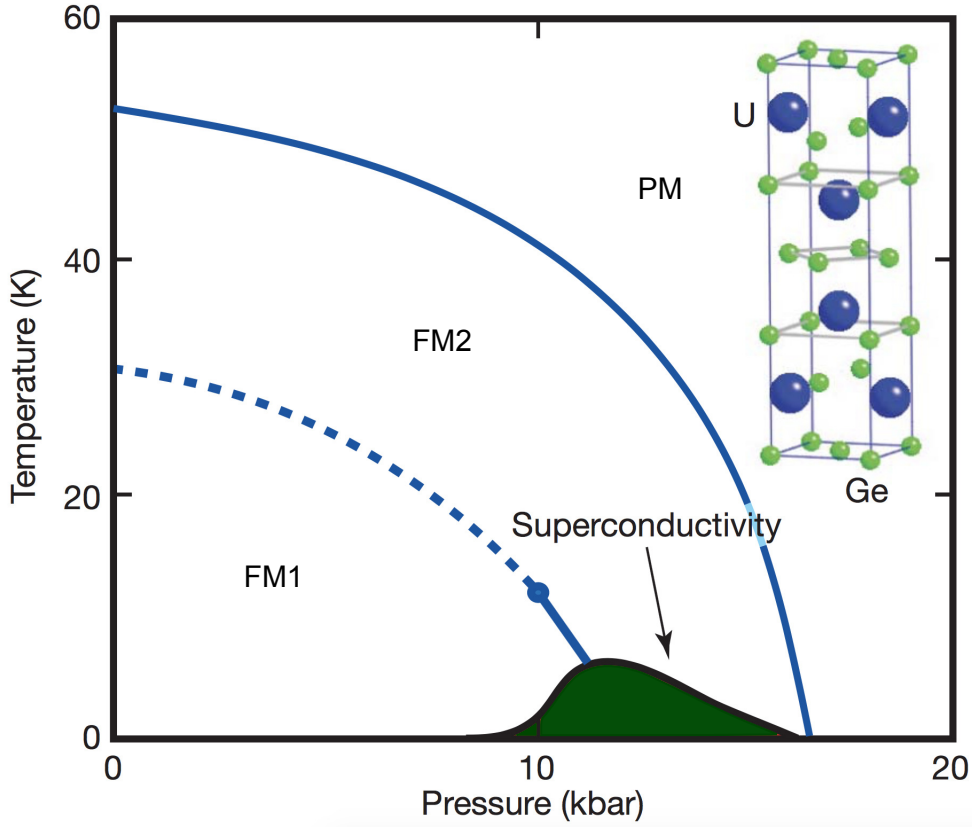

Figure 6.6 *Magnetic and superconducting PT phase diagram of UGe_2 adapted from [181].*

6.6 Conclusions & future work

A clamped pressure cell has been developed to incorporate a wire plug, allowing in-situ pressure measurement, and electrical measurements of the sample or sample environment within the pressure cell. In addition, an improved piston/sealing mechanism has been developed for the cell, removing the need for the sample encapsulation, simplifying the assembly. It has been shown that the cell can be used to perform ultrasound measurements of a single crystal of UG_2, with a table for maintaining sample alignment during pressurisation. The cell has great potential for future studies combining multiple measurement techniques. For example, the cell could incorporate a set of wound coils which could be used to apply magnetic field to the sample inside the pressure cell. This would give very fine control over the applied field to the sample, as attenuation from the cell material would be minimised.

Part II

Magnetic characterisation under high pressure

Chapter 7

Design of a clamped piston-cylinder cell for high magnetic field measurements at sub-Kelvin temperatures

7.1 Introduction

Applied magnetic fields can be used to display many interesting phenomena in condensed matter: the field may induce exotic magnetic structures, which may then be characterised using magnetometry, resistivity or neutron diffraction measurements; they can be used to quantify the static and dynamic magnetic properties of a material; in addition, the field can be used to perturb strongly correlated materials such as superconductors. As applied field is a vector quantity, these perturbations can be used to reveal information about the topology of the electronic structure. Research in this field is important to the development of our understanding of the physics of condensed matter, and also to the development of materials important to industry.

Depending on the energy scale of the desired measurement, or if there are other competing effects in the material, it may be necessary to perform measurements at sub-Kelvin temperatures; this reduces the thermal contributions, which may mask underlying effects, or completely remove them. This is the case for quantum

oscillation measurements, where fluctuations in the Hall resistance in an applied magnetic field reveal information about the Fermi surface of the system. The Fermi surface defines the electrical, thermal and magnetic properties of a material; for superconducting materials, mapping the Fermi surface helps to understand the links between the structure of the material and the properties of it's electrons. Specifically this helps to develop theories for the mechanism of the formation of Cooper-pairs.

As already motivated, pressure is a thermodynamic parameter which can be used concurrently with temperature to observe the behaviour of a material at different energy scales. In the study of magnetism, pressure is used to vary the interactions between neighbouring moments, altering the structure, electronic behaviour, or leading to magnetic frustration. Coupling applied pressure with magnetic field allows for further characterisation. The critical temperature required for superconductivity (T_C) is generally strongly pressure dependent, either increasing or decreasing the temperature; high field measurements under pressure can be used to better understand this process, and eventually engineer it to our advantage.

This chapter presents a 1.5 GPa piston-cylinder pressure cell designed for electronic measurements in high magnetic fields at low temperatures. As the cell was primarily developed for the study of superconducting materials, and the mapping of Fermi surfaces, it was designed so as to be suitable for use on a multi-axis rotation stage, allowing the field to be applied in any orientation with respect to the sample alignment.

7.2 Pressure cell design

7.2.1 Overview & design challenges

A cross-sectional schematic of the newly deisgned pressure cell is presented in figure 7.1 (top). The design is based on one previously reported in [182], shown in figure 7.1 (bottom), with a few key modifications designed to improve the loading technique, and increase the available sample volume. The pressure cell is a clamped piston-cylinder design, consisting of a press-fit cylinder with one closed end, and a locking mechanism consisting of a spherical shell which houses the cylinder assembly, and doubly acts as the piston and wire feed-through plug.

The outer diameter of the fully assembly spherical pressure cell is 20 mm making it suitable for use in the majority of dilution refrigerators, and cryostats/CCRs, and suitably sized to be included in various rotation devices.

Resistivity measurements are commonly performed in both opposed-anvil and piston-cylinder type pressure cells [183–185]. To remove the effects of changing resistivity in the leads, a four-wire measurement is essential. However, there are many potential sources of error in the setup of such experiments. Since the measured resistance value is an extensive quantity, from which the resistivity may be calculated, the size of the sample is important; generally the longer the length of the current path over with the resistance is measured, the more accurately the resistivity can be calculated. In addition, four-wire measurements have geometric considerations. In the case of measurements in a DAC, the sample may be only microns in dimensions. These restrictions on sample size mean that the Van der Pauw four wire measurement technique is required [186], allowing accurate resistivity measurements from irregularly shaped samples. This technique makes the assumption that the ohmic contacts to the sample are perfect, on the exact edge of the sample, infinitely small, and that the sample is homogeneous and uniform in thickness. In reality this introduces potentially large sources of error. Aside from this, assembling the DAC for electrical measurements is technically very challenging. To generate the large pressures routinely achieved in the DAC, the sample is contained in a metallic gasket, which must be properly insulated against the wires leading to the sample. Ensuring that the wires do not 'short-circuit' during the deformation of the gasket, and that the insulation does not reduce the stability of the gasket, requires precision, and novel assembly. By comparison, piston cylinder cells can load samples orders of magnitude larger, and due to the extra space in the cell and on the surface of the sample, the wiring can be optimised to reduce induced currents (using twisted pairs up to the contact), and the contacts can be made more reliably to the sample.

In the case of dilution fridge measurements there are additional complications in using a piston cylinder design due to size constraints in the fridge. This places an upper limit on the size of the sample which can be loaded to a given pressure at low temperatures. This is further reduced, in some cases, by the requirement to be able to rotate the sample in the dilution fridge. A cross-section of the rotation mechanism is shown in appendix F, showing that the maximum volume for included sample environment is a sphere with 20 mm diameter.

Studying larger sample volumes under pressure also brings complications when

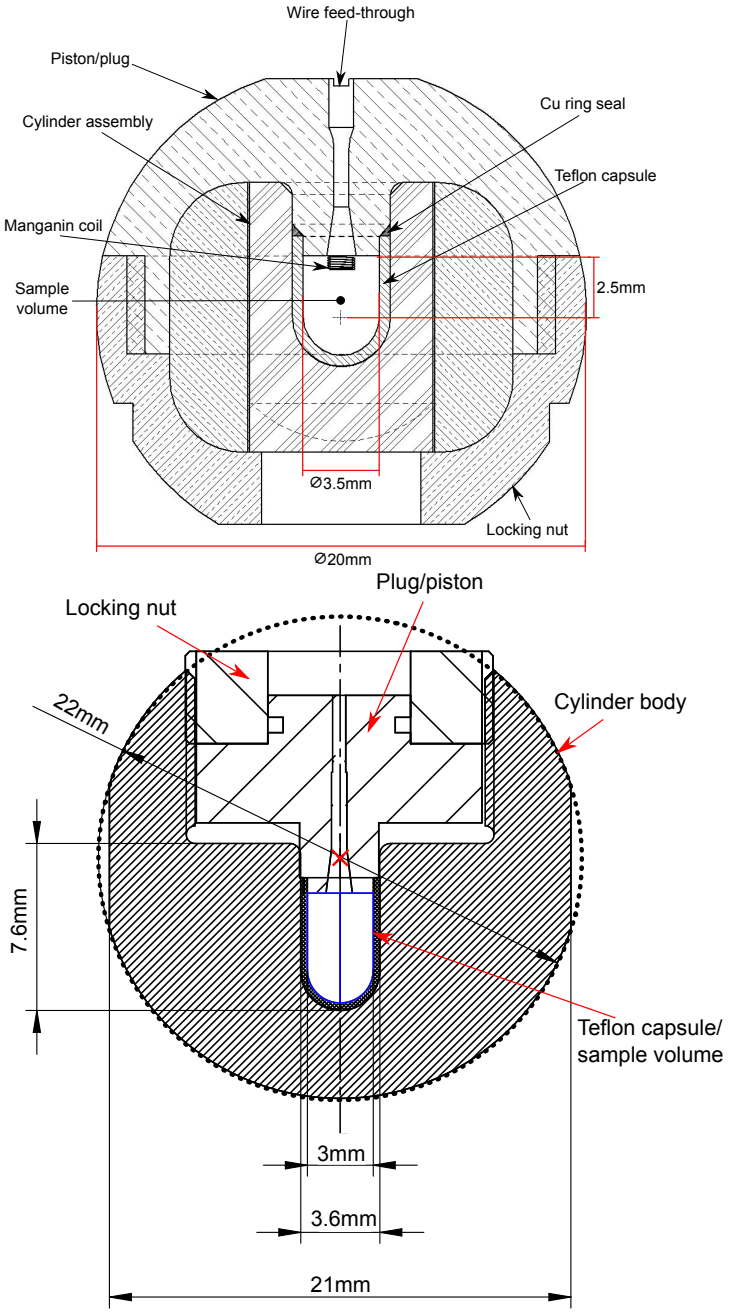

Figure 7.1 *(top) Cross-sectional view of present design of spherical pressure cell in fully locked position; the key dimensions are the overall* 20 mm *diameter of the cell, and the* 20 mm *diameter by* 4.5 mm *length of the sample volume. Loading apparatus not shown. (•) indicates centre of sphere. (bottom) Schematic showing the design of the cell published in [182], used as the basis of the improved design presented here. The cell is constructed from NiCrAl 'Russian Alloy' extending it's working pressure range to* 2 GPa. *(X) indicates centre of sphere.*

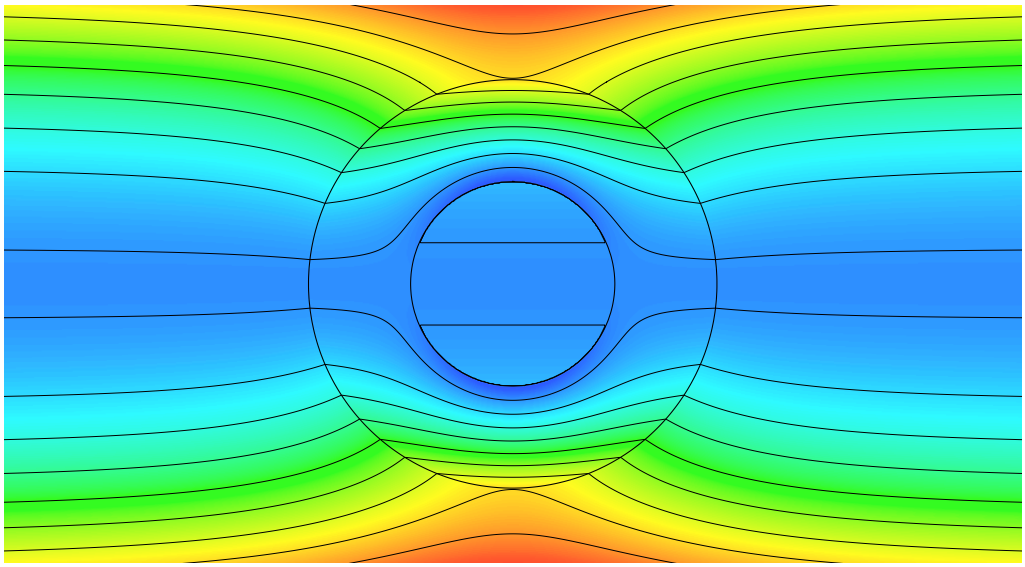

Figure 7.2 *Illustration of solution to magnetic scalar potential around a ferromagnetic ($\mu_r = 6$) spherical cross-section in applied B-field ($\vec{B_0} = 10\,\mathrm{T} \parallel$ to the horizontal). As the material of the cross-section has non-zero permeability it distorts the field within it, but the symmetry of the body results in a uniform, yet reduced, magnetic field within the cavity. If $\mu_r = 1$ then the field is completely undistorted.*

magnetic field is applied due to contributions from the pressure cell, which is typically also larger. The permeability of a material, μ, is used as a metric to determine how well a material can support the formation of a magnetic field in its bulk. $\mu_0 = 1.256\,637\,06 \times 10^{-6}\,\mathrm{H\,m^{-1}}$ is the permeability of free space, such that is often more convenient to consider the relative permeability $\mu_r = \frac{\mu}{\mu_0}$. If the relative permeability has a value other than 1, then it will distort or shield an applied magnetic field [187]. This can either result in the direction of the applied field being less well defined, it becoming less uniform, or it becoming more or less intense, or in some cases the cell may shield the sample from the applied field completely (e.g. if the cell material becomes diamagnet below a certain temperature, or the walls are sufficiently thick). Some superconducting materials have critical temperatures below 0.1 K, with very low critical fields. If it is difficult to control the applied field to a high precision, or know with high certainty that the field applied to the sample is the same as the field output by the magnet, then it becomes more difficult to collect reliable data. For this reason the magnetic characteristics of the materials used to construct the pressure cell must be known over the full temperature range of interest, and the geometry of the cell must be carefully considered to avoid systematic error.

The diamonds used in a DAC are typically only a few mm in dimensions, with the flat surface used to compress the sample only a fraction of a mm. As such the DAC construction need only be very small to generate significant pressures, meaning that field distortion is low. The magnetic susceptibility of diamond is small but negative, due to small diamagnetic contributions [188], such that it has a small effect to expel the applied field, which due to the limited symmetry of the DAC will be orientation dependent. The sample is also contained in a gasket material which must be chosen to fulfil a series of mechanical criteria to generate pressure, and also be non-magnetic. In the pressure cell presented here (figure 7.1) spherical geometry gives an advantage over a cell of lower symmetry made from the same material, due to the symmetric distortion of the field. If we consider a spherical shell in 2D, and apply a uniform external magnetic field in the plane of the shell, then Laplace's formula (with suitable boundary conditions) can be used to calculate the magnetic scalar potential. See figure 7.2 for an illustrated solution assuming a weakly ferromagnetic shell material, with no prior magnetisation. It is clear that although the field is distorted through the shell, resulting in a shielding effect in the central cavity, the field is still uniform within the cavity. With $\mu_r = 6$ (austenitic stainless steel) the field strength is reduced by approximately 50% within the cavity, if increased to $\mu_r = 100$ (Ni) this value increases to 95%.

7.2.2 Material selection

An overview of several suitable materials is reported elsewhere [112, 189], and will be briefly discussed here. One of the most commonly used materials is Cu with a 1-2% addition of Be, with a relative permeability close to 1. Small Fe impurities in BeCu, introduced in production of the alloy, can lead to erratic magnetic behaviour [190]. The appearance of a secondary phase in the presence of Fe can be controlled, using a small addition of Ni or Co to stabilise the magnetic properties. Aside from the magnetic properties of the cell, it is also important that it has sufficient strength to hold the loads required, whilst also being quick to cool to base temperatures and thermally stabilise. Several common materials are compared in table 7.1; from the available data, BeCu has the most favourable combination of high thermal diffusivity (allowing for fast and stable cooling) and yield strength. MP35N is also suitable, offering a considerably larger yield strength, at the cost of very poor thermal properties. CrNiAl offers improved magnetic permeability, and a higher yield strength. Due to the better

machinability of BeCu this was chosen for initial testing, with the option to make an additional cell in NiCrAl if required.

Table 7.1 *Compilation of material data for high strength alloys used in magnetic studies. Values for thermal conductivity λ, specific heat C_p, yield stress σ_{yield}, ductility, and relative permeability μ_r are all as measured at room temperature unless otherwise indicated. There is only limited material data currently available for CrNiAl.*

	λ ($\mathrm{W\,m^{-1}\,K^{-1}}$)	C_p ($\mathrm{J\,kg^{-1}\,K^{-1}}$)	σ_{yield} (MPa)	Ductility	μ_r
BeCu-25	95	418	1300-1450 @ RT, 1500 @ 20 K	4% @ RT, 10% @ 20 K	1.0018
CrNiAl (40HNU-VI)	-	-	2000 @ RT	7% @ RT	1.0003
CuTi (Cu-3Ti)	54	460	470-950 @ RT	22%-3%	1.0000
Al (7075-T6)	150	960	500 @ RT, 690 @ 33 K	15%	1.0000 (super-conductive $T <$ 1 K)
Elgiloy	12.5	-	965-1965	10% - 1%	1.0004
Al bronze (C64200)	45	377	620	9-12%	< 1.05
Hastelloy (C22HS)	11.8	412	360-760	40-62%	1.002
MP35N (Co-Ni Alloy)	11.3	502	1840@ RT, 2320 @ 20 K	11% @ RT, 9.2% @ 20 K	1.001

7.2.3 Finite element analysis & optimisation

Whilst the spherical shape of the pressure cell gives clear advantages in terms of efficient use of the available volume, and magnetic field attenuation, the added space restrictions complicate the design principle of the cell. The original cell design, as reported in [182], is shown in figure 7.1 (bottom). The main improvements to the design of Kornilov and Pudalov [182] are the reduced overall

size of the cell, an approximate 20-30% increase in sample volume, a more central sample position, and a relocation of the locking nut to the perimeter of the cell instead of above the plug. This gives the cell several advantages: increased sample volume provides more room for the inclusion of additional measurement wires, reducing the risk of 'shorting' during loading; the sample being at the centre of the sphere means that the field is more uniform in all orientations, the original design centred the cell on a position in the plug (as indicated in the figure by +); relocating the locking nut to the perimeter increases the maximum loads that can be supported by the thread due to an increase in contact surface area; the separation of the cylinder from the main body of the cell, coupled with the mating diameter of the plug/piston makes it easier to initially engage the plug with the cylinder, reducing the risk of knocking wires/contacts on the sample.

The required dimensions of the cylinder were initially estimated through calculation using the Lamé equations (as detailed in [17]). Through projecting the forces acting an a small segment of a cylinder in terms of three principal stresses (σ_θ, hoop stress, σ_r, radial stress, σ_z, axial stress), and calculating the incremental strain on the element, an expression for each stress component can be derived. The Lamé equations predict the elastic limit of a loaded cylinder; higher pressures can be generated through press-fitting the cylinder within another cylinder, or by autofrettage [49]. Autofrettage induces plastic deformation in the cylinder, which after unloading, leaves the cylinder compressively strained, allowing higher pressures to be generated before further plastic deformation [191].

The Lamé equations predict that, for a cylinder with outer diameter (OD) 14 mm and inner diameter (ID) 4 mm, the maximum pressure that can be generated without plastic deformation is approximately 53% of the yield strength of the material; in this case approximately 0.715 GPa, far short of the required 1.5 GPa. As the important parameter is the ratio of the two diameters, not their absolute values, it is found that in the limit of an infinite ratio of $\frac{OD}{ID}$ the maximum pressure achievable in the elastic limit, without press fitting or autofrettage, is 57.7% the yield strength of the cylinder material (see chapter 2). Kamarád et al. [191] reported pressure/strain data from loading a BeCu cylinder beyond it's yield point; this caused it to autofrettage, allowing it to hold pressures approximately 50% beyond it's yield strength, resulting in permanent deformation of the cell. This behaviour can be included in the FEA using either bi- or multi-linear approximations to the stress strain curve.

The elastic modulus for BeCu was set at $E_0 = 127$ GPa, a result derived from

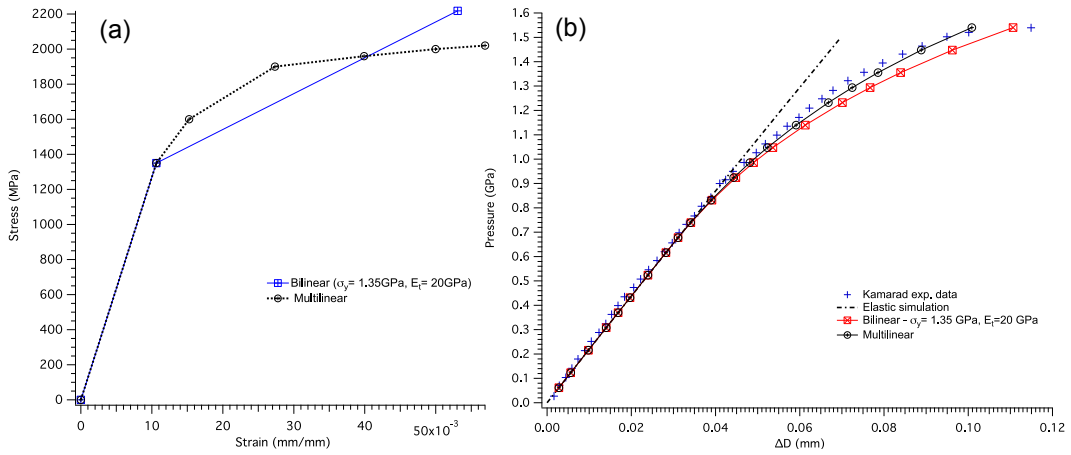

Figure 7.3 *(a) Stress-strain curve showing bilinear, and multilinear material models; (b) Deformation of external diameter of pressure cylinder as function of pressure as reported by [191] (+), as simulated with bilinear model (⊠), and as simulated with multilinear model (⊕). Dashed line shows simulated elastic response of cylinder.*

the results of Kamarád et al. [191], and within 2% of the value published by the manufacturer [192]. The yield strength was taken as 1.4 GPa in agreement with the hardness testing results by Kamarád et al., and the reported values for fully age-hardened BeCu from the manufacturer. The pressure/strain data was then used to compare against the data calculated in the FEA to tune the material data used in the simulations. For this a simple 2D model of a cylinder, with the correct dimensions, was used; using the axis-symmetry of a cylinder to reduce the computation time. Two different material models were used to find the best fit to the data: a bilinear model where the stress-strain behaviour post yielding is assumed linear with a lower modulus; a multilinear model which approximates the true non-linear post yield curve more accurately. Figure 7.3 shows how the two models compare, and how the simulation compares with measured data in each case. It is clear that the bilinear model, whilst showing the same form, overestimates the increase in the outer diameter of the cylinder at 1.4 GPa by approximately 20%. The multilinear model is a much better fit, though still overestimates the deformation by 2-4%. However, if one considers the error in the strain measurements from Kamarád et al., and uncertainty in the exact cylinder dimensions and material data, the fit is optimal.

With non-linear material data the effects of autofrettage and press fitting the cylinder within another cylinder can be considered with the FEA. As outlined in chapter 2 the optimal ratio of radii (internal radius, a; external radius, b; interference radius, c) for press-fitting two cylinders is given by $c = \sqrt{a.b}$, with

the optimal interference (pressure, P; elastic modulus, E; interference on radius, δ) on the diameter estimated by:

$$\delta = \frac{P\sqrt{a.b}}{E}$$

With the OD 14 mm and ID 4 mm, this gives an optimal value for $c = 3.74$ mm, and $\delta = 0.05$ mm. The cylinder assembly can then be partially autofrettaged, allowing the external cylinder to deform plastically, providing further support to the inner cylinder.

In order to determine the stability of the cylinder under pressure a failure criterion must be chosen. From chapter 2 there two options widely used for this type of problem, the Tresca (maximum shear) criterion, and the Von-Mises (maximum distortion) criterion. Whilst these two criteria are used to determine elastic failure of a material, where the pressure vessel is deliberately deformed beyond this limit, a condition for ultimate failure of the cell is required. The most appropriate failure criterion is that which matches observed cylinder failure most accurately; this was compared against the experimental data of Kamarád et al., where a single crack along the length of the cell indicated failure at $P > 1.5$ GPa, suggesting that hoop stress is critical. Figure 7.4 compares different failure criteria from the simulated results. As expected, the Von-Mises (VM) and Tresca criteria suggest that the cell is beyond elastic failure at this pressure. The trend suggests that the build in hoop stress in the cylinder wall may finally initiate failure. The VM stress shows a distinct boundary at approximately $R = 2.6$ mm where the cylinder ceases to be plastically deformed, remaining in the elastic regime. At this boundary the hoop stresses are also maximum in agreement with literature solutions [48]. As the pressure increases, the position of this boundary shifts towards the outer diameter of the cylinder. As the elastic region becomes very narrow, the hoop stresses grow. Thus the position of the plastic-elastic boundary can also be used as an indication of failure.

Simulating the press-fit cylinder, using the same material data as before, the hoop stress, and Von-Mises stress can be compared before and after loading the cylinder (figure 7.5). The value of the hoop stress reaches a maximum value of approximately 1000 MPa, approximately 28% below the expected failure point of the cell. The peak value of hoop stress is also still far from the outer diameter of the cylinder, indicating that the elastic region is still large. Interestingly, the VM stress at the inside diameter of the cylinder is at value close to the elastic yield

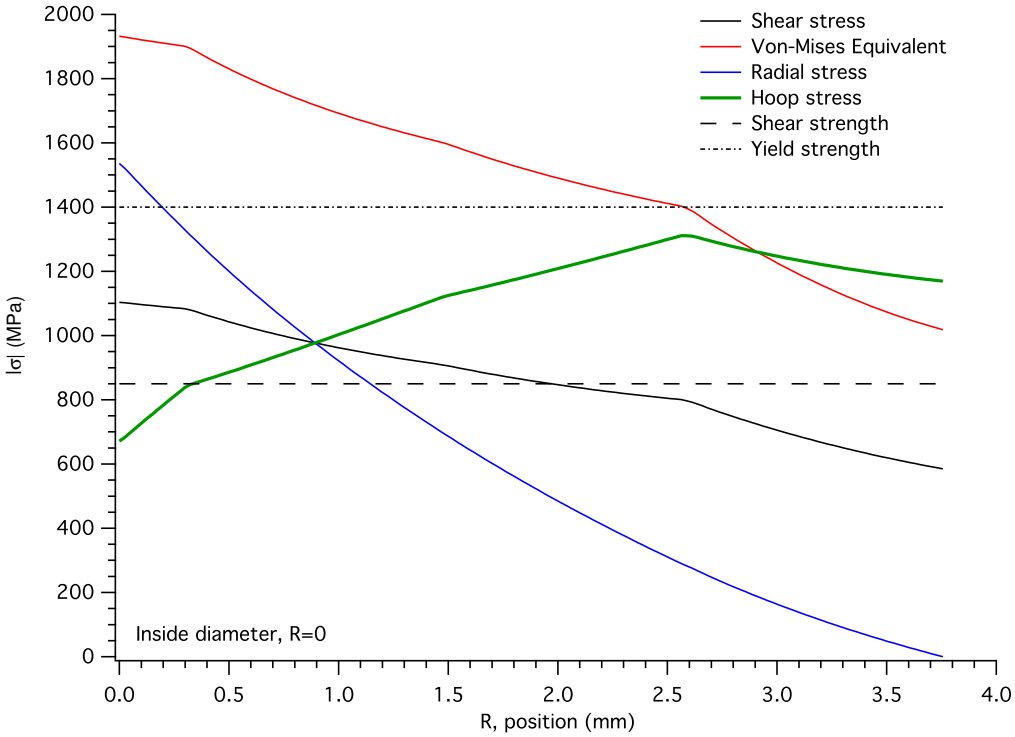

Figure 7.4 *Results from FEA showing principal, maximum shear, and Von-Mises equivalent stress during plastic yielding, at pressure just below the reported failure, in cylinder as calibrated against [191]. The elastic yield strength and expected shear strength of BeCu are also marked on the graph. With the data shown, and the known failure mode, the hoop stress seems to determine the point of failure in the cylinder.*

strength after the pre-stress, indicating that any further pre-stress would cause inward plastic deformation, and that the chosen parameters are indeed optimal.

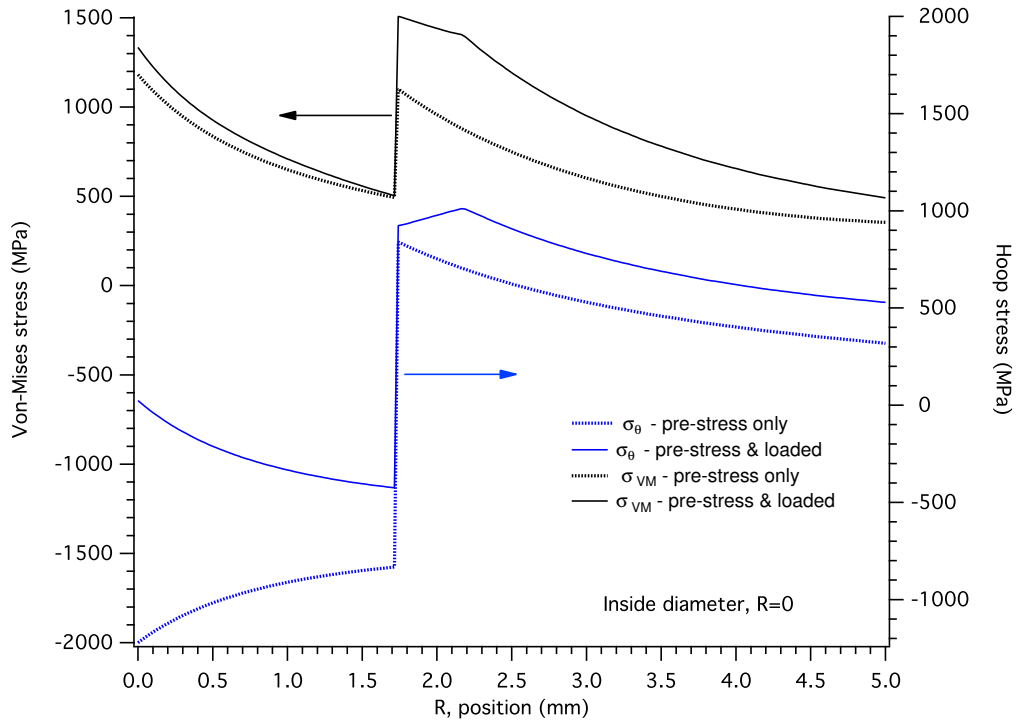

Figure 7.5 *FEA results for Von-Mises and hoop stresses in a press fit cylinder with* $c = 3.74\,\text{mm}$*, and* $\delta = 0.05\,\text{mm}$*, showing that critical hoop stress is 28% lower than expected failure stress.*

With the parameters of the cylinder fixed, the cell body was then optimised, using the same material properties as for the cylinder. The main purpose of this simulation was to check the stresses in the piston, the rigidity of the cell body, and the strength of the thread. Whilst a thread with a small pitch provides a more rigid frame, it is also unable to hold as high axial loads. After several iterations, a thread with $p = 1\,\text{mm}$ was chosen. Figure 7.6 shows the results of the simulations. The piston is shown to deform a maximum of 60 µm under maximum load, and whilst stresses are high in the piston, they remain in the elastic limit of the material.

7.2.4 Plug assembly & pressure measurement

Wires are included in the cell to allow for electrical measurements of the sample, and pressure determination. Twelve 100 µm ø enamelled Cu wires were included, 4 for resistivity measurements of the sample, 4 for resistivity measurements of

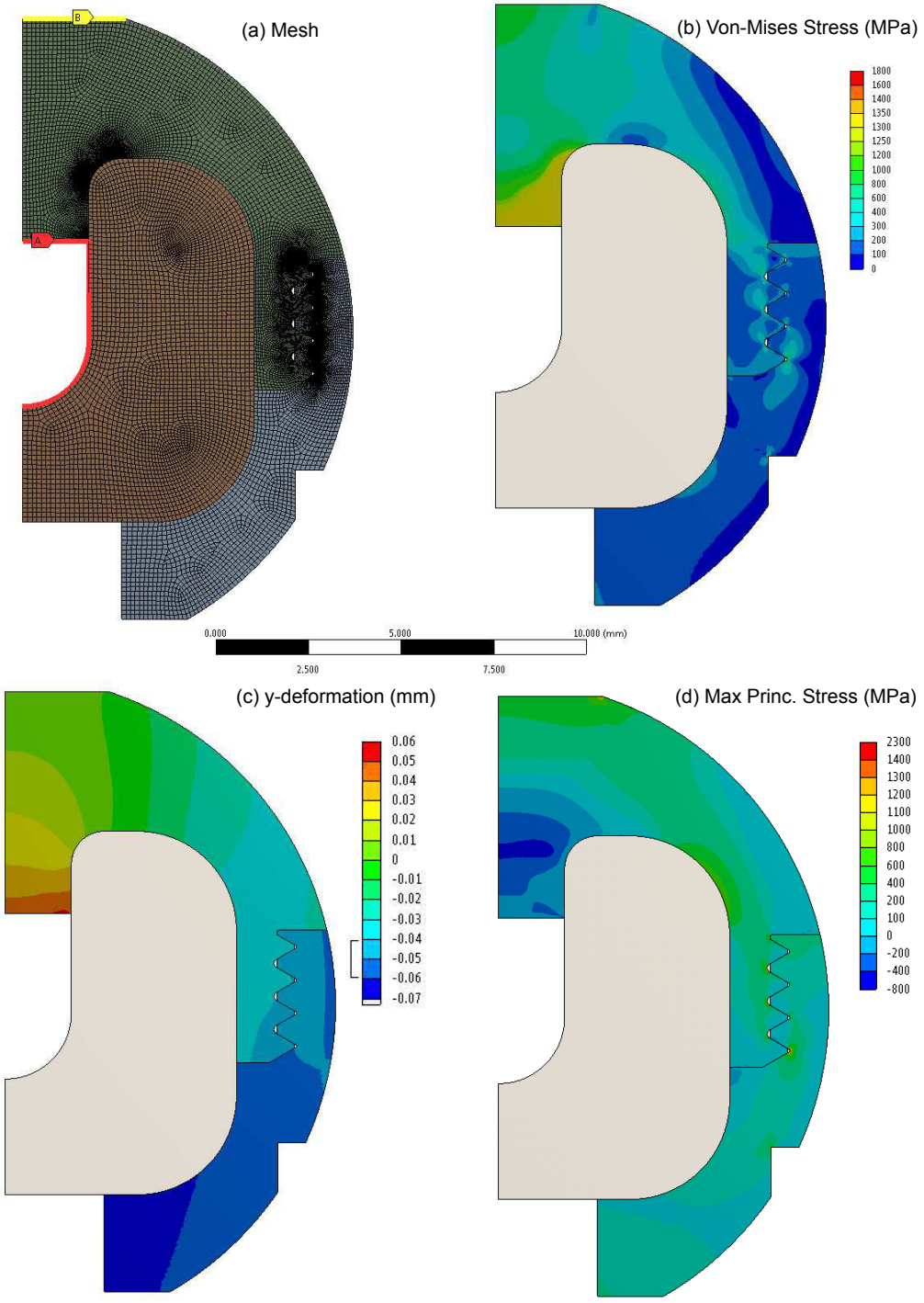

Figure 7.6 *Finite element analysis of the spherical cell body. The model is assumed to be symmetric about the central axis of the cell, and the materials used are assumed perfectly isotropic, allowing the model to be reduced to a 2D approximation. All contacts between bodies are assumed frictional with coefficient* $\nu = 0.3$*. (a) the mesh input to the solver, showing the region where* 1.5 GPa *pressure is applied (A), and the frictionless vertical constraint on the system to prevent rigid body motion (B). (b) the calculated equivalent Von-Mises stress in the system* (MPa)*. (c) resulting deformation in the y-direction* (mm)*. (d) the maximum principal stress* (MPa)

the pressure manometer, and 4 spares. Before assembling the wires in the cell, they were both thoroughly cleaned and de-greased through ultrasonic washing in ethanol, and acetone, to ensure that the sealing epoxy forms a good bond to the cell and the wires. Stycast 2850FT with catalyst 24LV was chosen as the most suitable epoxy [170], offering low thermal contraction and high thermal conductivity, whilst being highly electrically insulating. To improve the properties a small quantity of diamond or alumina powder can be added to the epoxy, further reducing the thermal expansion, increasing thermal conductivity, and increasing the hardness of the cured epoxy [172]. Ideally the thermal contraction of the epoxy, and the plug would be matched, preventing interfacial strain between the two, resulting in de-bonding. The easiest way to avoid this is to simply minimise the thermal contraction of both parts during material selection.

The base of the epoxy (without catalyst) was first thoroughly mixed, whilst being warmed to approximately 60 °C, as the epoxy tends to settle over time, and can partially crystallise during long periods of storage. Mixing the epoxy introduces large amounts of air bubbles, which if not removed can make the cured epoxy brittle, and porous. To degas, the required mass of epoxy was measured out and mixed with a small percentage of fine alumina powder (<50 µm size) and placed under a rough vacuum ($\sim$ mbar). This caused the epoxy to foam as the bubbles were removed. After some time, the bubbles subsided, indicating that the majority of the trapped air had been removed.

To apply the epoxy to the plug the cell had to be seated such that a light vacuum could be applied to the back of the plug to encourage the epoxy to fill the space between the wires and the walls of the cell. This was achieved through sitting the cell in a hollow rubber bung, sealed in a conical flask with a side-arm for a vacuum pump. Before adding the catalyst (at a ratio 7.5:100 parts by mass) the wires were inserted through the hole in the plug, and carefully bent to lay in the grooves in the top of the cell. The base of the hole was then covered with a small strip of adhesive tape, to ensure that the wires didn't fall through the hole, and to prevent the epoxy from flowing straight through into the conical flask. With the cell assembled, the catalyst was gently stirred into the epoxy base, minimising folding any air into the mixture. After mixing for 2-3 minutes, the epoxy should only be worked for a further 45 minutes, before being left to cure for 24 hours. The Stycast was applied to the plug using a pin head, encouraging flow to the back of the plug with the vacuum. After the plug was full, the vacuum was left on to allow for removal of any added bubbles, before being switched off to allow

curing. Photographs of the plug, and the assembled cell are shown in figure 7.7.

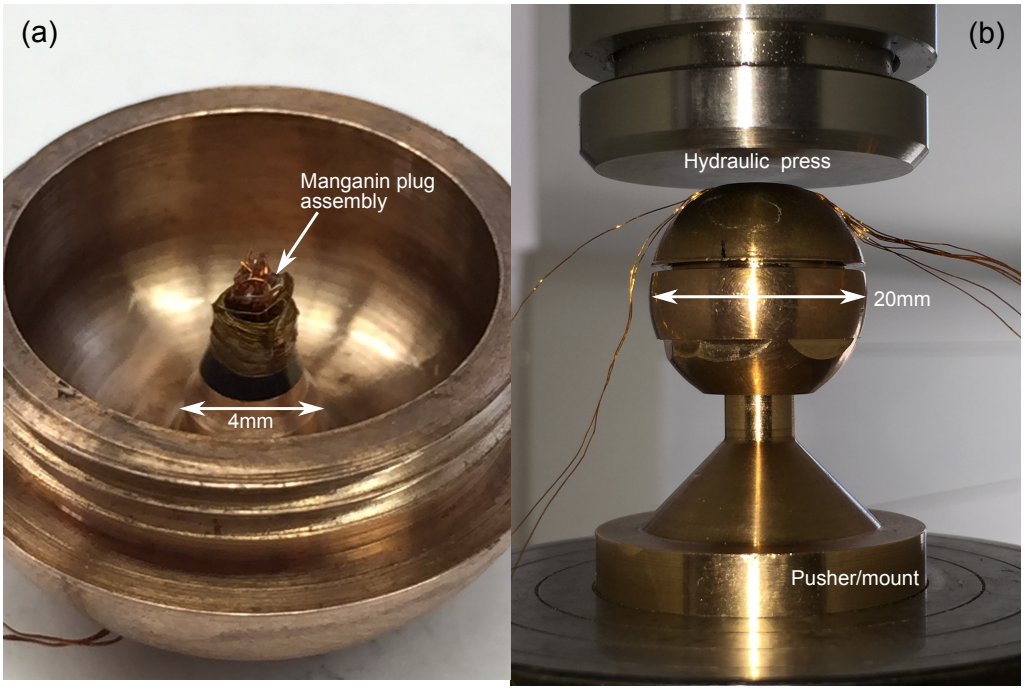

Figure 7.7 *Photographs of (a) the Stycast sealed and cured plug, assembled with 12 Cu wires and manganin coil, (b) the assembled pressure cell during the loading procedure. The removable pusher/mount is used to displace the cylinder assembly onto the plug/piston, which is then locked in place using the locking nut.*

As described in chapter 2, there are a variety of techniques to determine the pressure inside a pressure cell, either using optical access to measure ruby fluorescence, or the change in lattice parameter in a pressure marker as measured by diffraction. However, in this case there is no optical access to the sample volume, and no diffraction. It is possible to estimate the pressure based on the known diameter of the piston, and the applied load to the cell, though this doesn't account for friction in the cell and the seal. The most accurate technique uses the pressure dependence of the resistance of a coil of manganin wire in the sample volume. Manganin is a CuMnNi alloy with an extremely linear pressure coefficient, which itself has linear temperature dependence. This allows the pressure to be determined over the full PT range of interest [173], to an accuracy only limited by the accuracy with which the resistance of the manganin wire can be measured.

The manganin coil was prepared through coiling a length of enamelled 50 µm ø wire around the shaft of a 500 µm ø drill bit. The length of wire needn't be known exactly, though sufficient wire should be used to ensure that an accurate ΔR can

be measured above noise. For the purposes of testing the length of the wire was chosen to give a measurable resistance of approximately 100 Ω. The coil was then 'sealed' using a dilute mixture of GE-varnish. To ensure that the coil could be removed from the drill bit after the varnish was dry, a thin piece of paper was included between the two.

7.2.5 Seal mechanism

The cell seals in two stages; initially the teflon capsule contains the pressure medium, forming a seal through the fit it forms between the cylinder and the lip on the plug/piston; after the teflon capsule has densified, a Cu ring prevents extrusion of the teflon and forms a wedge seal between the piston/plug and the wall of the cylinder. The teflon capsule forms a relatively frictionless seal, resulting in a linear loading curve, though is not as reliable. The Cu wedge seal is highly frictional, but forms a very stable close fit, sealing the cell.

The Cu ring seal has a thickness of 0.5 mm, with diameters matching the recess on the piston/plug. The teflon capsule is machined to match the dimensions of the cylinder, with a wall thickness of approximately 0.4 mm.

7.3 Assembly & load testing

The cell is loaded using the piston/plug as a base. As space in the cell is still constrained, the wires on the inside of the plug should be shortened to a minimum. To save space, the copper wires can be fed through the manganin coil, allowing the coil to sit on the base of the plug, ensuring that it remains clear of the sealing faces. Before making any connections, the copper ring seal should be fitted to the plug; as the fit is tight, positioning the seal can sometimes knock connections. The sample can then be included, and either soldered or attached to the wires using silver-paint. If positioning the sample is essential, a coil of teflon can be used to prop or support the sample in place, though it should be positioned with care to avoid interference with the wiring.

The teflon capsule is then pushed into the cylinder assembly, to the base, and filled with pressure medium (Daphne or light mineral oil). The cylinder assembly is then seated into the locking nut, ensuring that the cylinder can turn freely.

The plug is then lowered onto the cylinder, and gently push fit. The thread can be lightly tightened prior to loading to keep the cell assembled.

The cell is then seated on the loading pusher, and the external wires are connected to a multimeter. The cell should be slowly loaded in a press, pausing at approximately 200 MPa intervals, allowing the resistance measurement to settle, and then tightening the locking nut before continuing. Locking the cell at intervals prevents sudden depressurisation of the cell in the event of the hydraulic press failing. A typical loading curve for the cell is shown in figure 7.8.

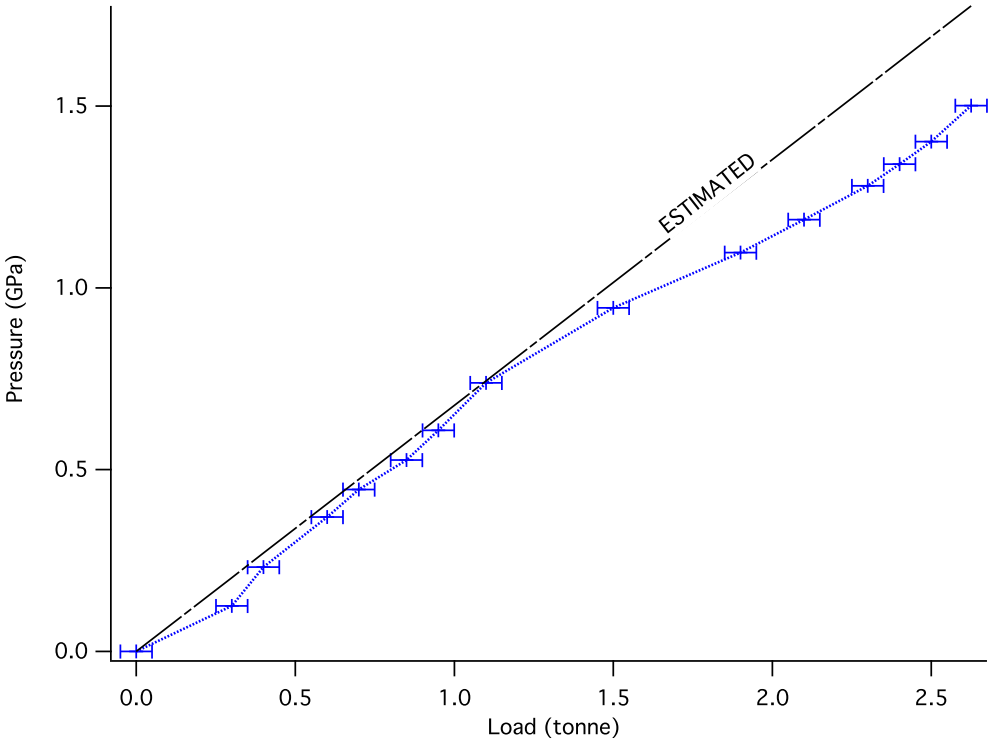

Figure 7.8 *Typical room temperature loading curve for pressure cell. Dashed line shows the estimated pressure load curve using the known diameter of the piston, and the measured load. The resistance of the manganin coil was measured using a four-wire measurement on a Keithley source-meter. The pressure was calculated from the measured resistance. There is a clear step at approximately* 1.5 t *indicating the deformation of the Cu seal, reducing the pressure load performance compared to the teflon capsule.*

As the volume of fluid contained in the cell is still relatively small, any mechanical play in the pressure cell results in a drop in pressure. This is seen when the load from the hydraulic press is slowly released from the cell, and the load is taken up by the thread on the cell. If only hand tightened, the cell can completely depressurise. It is very important that the cell is locked with a spanner to reduce

this effect as much as possible, though it has still been seen to drop by as much as 0.3 GPa.

7.4 Resistivity measurement of U_6Fe under pressure

U_6Fe has the highest superconducting temperature of any of the uranium superconductors (T_s = 3.8 K), [193, 194], and is primarily of interest due to it being on the verge of magnetic instability. The interplay of magnetism and superconductivity has been extensively studied, but still isn't fully understood, though magnetic interactions are strongly involved in the formation of the superconducting state. For a conventional superconductor, the superconducting state is entered through the formation of Cooper pairs of electrons (of opposite spin and momentum), due to distortions of the underlying ionic lattice. An applied magnetic field acts as a pair breaking operation, where the energy states of each electron is altered differently by the Zeeman effect. It has been observed that where the material is weakly ferromagnetic, the pairing of the electron can be mediated differently [178].

Pressure can be used to tune the magnetic, and therefore superconducting properties of these unconventional superconductors, where transport measurements in applied field provide insight into the pairing mechanism. An oriented single crystal sample of U_6Fe was loaded into the pressure cell, and pressurised to 1.45 GPa. Figure 7.9 shows four-point resistivity data along the [100] direction under pressure in zero field, showing a shift in T_s. The next stages of this experiment are to apply field, and measure the dependence of the resistivity, and T_s, on applied field direction. This will initially be measured in a cryostat ($T_{base} \approx 1.5$ K), in a two axis rotator developed by Michal Kepa (figure 7.10), before it is tested in the dilution fridge. It is clearly advantageous that the cell can be used with both systems. The cell was prepared and loaded by Chris Ridley, the rotation stage was designed by Michal Kepa and Chris Ridley, the sample was prepared by Michal Kepa.

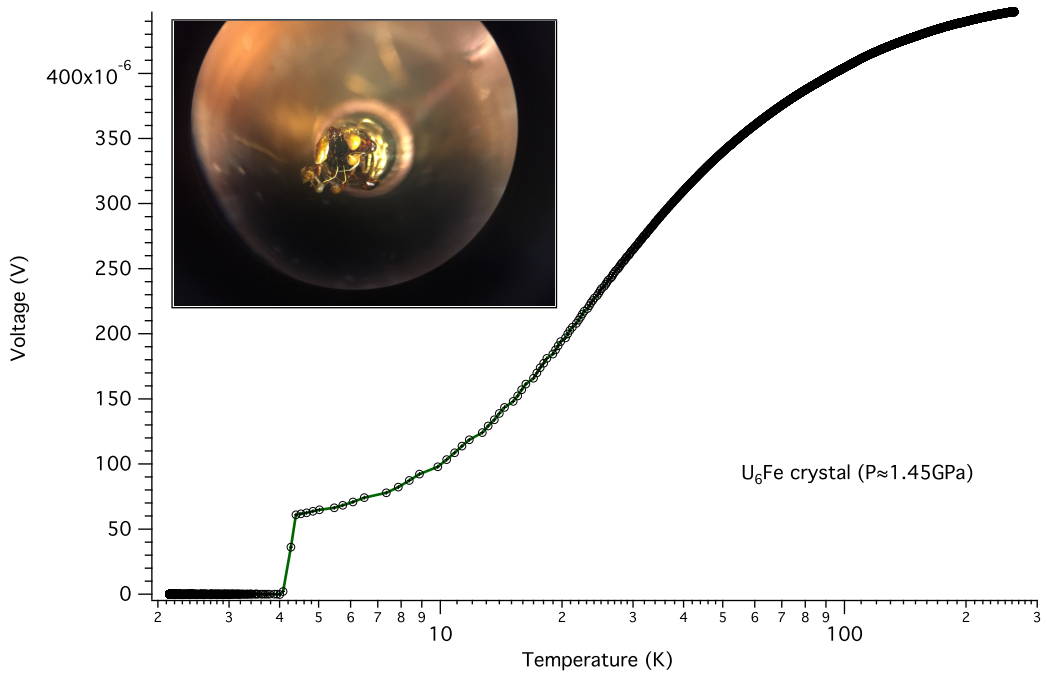

Figure 7.9 *Plot of voltage along [100] direction of U_6Fe at* 1.45 GPa *versus temperature. Inset: crystal mounted on plug/piston of pressure cell, with 6 spot welded Au wires, manganin coil is beneath the sample.*

7.5 Conclusions & future development

A miniature spherical pressure cell for electrical measurements at pressures up to 1.5 GPa has been designed, machined, and successfully load tested. The cell is suitable for measurements in high magnetic field, offering clear advantages over conventional cylindrical pressure vessels due to geometric considerations. Careful use of existing data for the material chosen has allowed a thorough finite-element analysis of the system to be performed, allowing the sample volume to be maximised within the limitations of the overall size of the pressure cell, demonstrating a true advantage of FEA.

Magnetoresistance measurements of the pressurised U_6Fe sample are currently being performed, to determine the anisotropy in the critical field dependence. Further measurements on the same loading are to be performed to perform quantum Hall measurements. The number of wires contained in the cell allowed for the sample to be wired up in multiple orientations, optimised for each measurement.

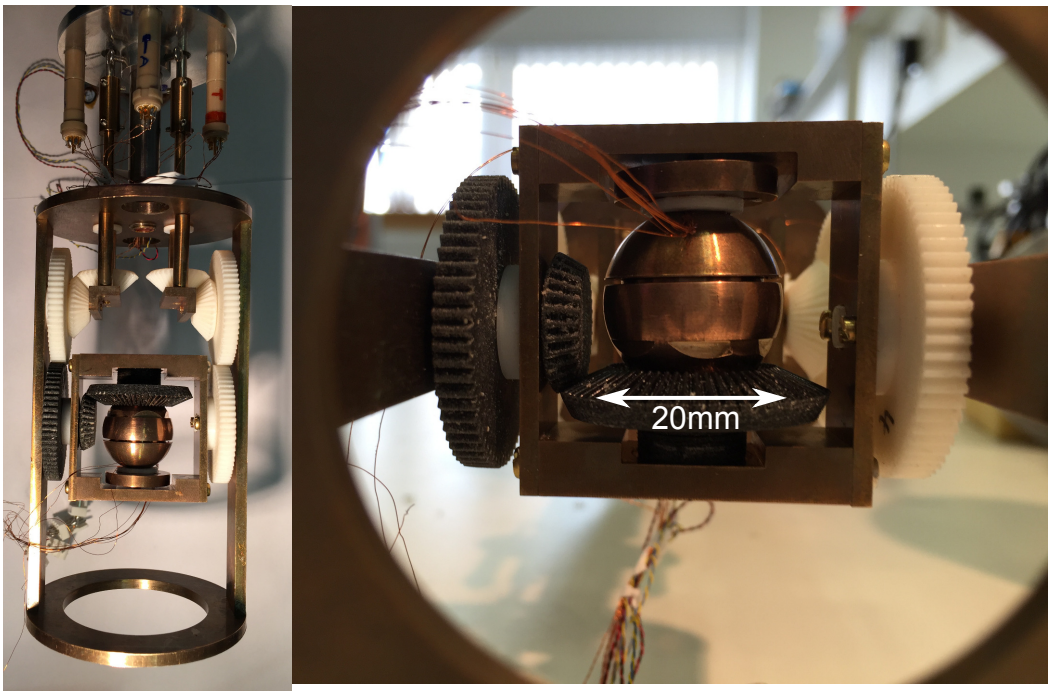

Figure 7.10 *Spherical cell mounted on two axis rotation stage designed by Michal Kepa. The gears are printed from plastic, reducing the level of field distortion due to the rotator. The two axes are partly coupled, but rotations about a single axis can be achieved through compensation.*

Chapter 8

A study of the high pressure Invar behaviour of Pd_3Fe

8.1 Introduction to Invar behaviour

Charles Guillaume discovered 'Invar' behaviour in the Fe-Ni alloy with approximately 36% Ni, leading to him awarded the Nobel prize in 1920. Figure 8.1 shows how the thermal expansion coefficient varies with Ni content. The low cost, and stability of the material over a large temperature range continues to make the material technologically important. Since the discovery in the Fe-Ni, Invar behaviour has been observed in many other binary and ternary alloys, such as Fe-Co, Fe-Ni-Co, and Ni-Co-Mn. Interest in Invar alloys was accelerated with the discovery that the Invar state could be induced at different Fe-Ni compositions through the application of pressure [195]. A similar effect is seen in Fe-Pd alloys, reported to be Invar-like at Pd 30% [196], with a pressure induced state at Pd 75% under applied pressure [1].

van Schilfgaarde et al. [198] explained the mechanism of Invar behaviour as being associated with a ferromagnetic high-spin to frustrated (non-collinear) configuration. This results in a volume reduction which counteracts the expansion caused through thermal changes. Dubrovinsky et al. [195] explained that increasing the Ni concentration (in the case of Fe-Ni alloys) stabilises the high spin ferromagnetic state; the application of pressure induces the frustrated magnetic state through altering the volume of the system. An alternative theory (known

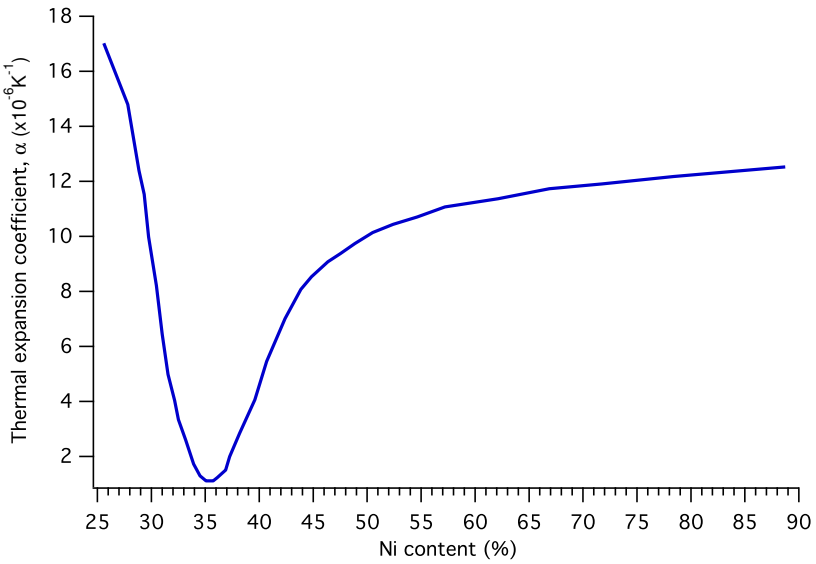

Figure 8.1 *Effect of Ni content on coefficient of thermal expansion in Fe-Ni alloys [197].*

as the Weiss 2 state model) explains the Invar anomaly being driven by a high spin to low spin transition resulting in a volume collapse, again counteracting the effects of thermal expansion. Both are outlined in [199]. The Weiss model fails to explain the low temperature behaviour observed [200] whereas the noncollinearity hasn't been observed in Fe-Ni alloys via polarised neutron measurements [201].

8.2 Introduction to Pd-Fe alloys

Pd-Fe alloys are of interest due to a large number of unusual properties caused by the interplay between mechanical, thermal, and magnetic effects. For example magnetic shape memory is observed in Fe-rich alloys [202], and Invar behaviour (zero thermal expansion) is observed in alloys with approximately 30% Pd [196] at room temperature. More recently a pressure induced Invar state was reported in powder samples of 75% Pd alloys [1]. The diverse mechanical properties of these compounds lend themselves to a broad range of engineering problems, with potential applications such as collapsible stents for bio-medical applications, and intelligent jet engine design to reduce air-traffic noise. In addition to direct applications, these alloys provide an excellent platform for comparison with physical models of transition metal systems, 3d-electronic structures, and magnetism in binary compounds.

The use of pressure to tune the Invar transition provides a unique tool to understand the transition, and subsequently the mechanism for zero thermal expansion in these materials. As highlighted in Section 8.1 there are two competing theories for the formation of an Invar state [199]; the first ascribes the effect to a collapse of local magnetic moments, and weak exchange between low moment sites, resulting in a large volume reduction with increased temperature, counteracting the effects of thermal expansion. The second describes Invar materials as high magnetic-moment structures, driven to local moment (order-disorder) orientation through strong exchange between Fe sites, which drives the volumetric collapse [203].

This chapter presents a study of the palladium rich, ferromagnetic Pd_3Fe alloy ($T_c \approx 530\,K$ [204]), reported to display high pressure Invar behaviour at room temperature. It undergoes a large volume collapse at 12 GPa, with an apparent collapse of long range magnetic order, observed through Mössbauer spectroscopy [1]. Zero thermal expansion over the range $300 - 523\,K$ is also reported, before the Curie temperature is reached. Density functional calculations of this pressure induced Invar behaviour have been performed for various possible structures, fitting both of the two proposed mechanisms, though none have provided a conclusive indication for the magnetic state of the sample post-collapse [205]. More recent theoretical studies have suggested that the alloy forms a triple-Q state where the moments on the lattice alternate pointing toward and away from the centre of the lattice [206]. This would support the theory of spin frustration (non-collinear magnetism), and it is speculated that a pressure-driven reduction of the Curie temperature could trigger this order-disorder transition, which in turn drives the Invar behaviour of Pd_3Fe.

The objectives of this study were to synthesise single crystal samples of Pd_3Fe, and perform high pressure neutron diffraction studies to understand the magnetic changes in the sample through the Invar transition, to see if any of these theories are supported.

8.3 Synthesis

Previous samples used for high pressure studies were polycrystalline, synthesised through arc-melting. Powder diffraction can be limiting, if the system becomes geometrically frustrated it will only be possible to confirm this with a single

crystal sample. Furthermore, the compression of a 3D data set to 1D can make it impossible to distinguish contributions from different planes due to peak overlap, whilst any residual strain or preferred orientation in the powder sample will lead to inaccurate peak intensities. For this reason, single crystal samples were synthesised.

8.3.1 Precursor preparation & Czochralski growth

The samples were synthesised from Fe powder (99.998% purity) and Pd powder (99.995% purity) from Alfa Aesar. The starter materials were measured into the correct stoichiometry, and pressed into pellets. The pellets were then treated in an ultra high vacuum furnace in a tantalum foil pocket to 1120 K for 2 weeks to remove hydride impurities from the Pd and other trace impurities from the Fe and Pd. Between treatments, the pellets were stored in high vacuum containers to prevent oxidation, or reformation of hydrides. No addition steps were taken to purify the Fe starter material. Small changes in the mass of the pellets during annealing were corrected for prior to melting the pellets.

The pellets were loaded into a Cu crucible in a Czochralski furnace; the components of the furnace were scoured and cleaned thoroughly with acetone and washed in ultrasound prior to melting the sample. The pellets were observed to melt together at approximately 1100 K, consistent with the phase diagram of Fe-Pd [207]. After the first melt, the sample was analysed via powder X-ray diffraction to verify the structure, and provisional composition of the sample.

Before pulling the crystals from the melt, the sample was etched in a dilute HF acid to remove surface oxides and impurities [208]. This was carefully monitored to prevent excessive preferential etching, which could change the composition of the melt. The sample was washed in acetone, and ethanol post etch. The tungsten pin, used to pull the crystal, was also etched in a more concentrated acidic wash prior to the crystal growth.

After reloading the sample into the furnace for the second melt, it was not observed to melt until a much higher temperature (approximately 1500 K), thought possibly to be due to the stability of the newly formed compound. The sample also violently outgassed an additional small amount of impurity to the crucible. The sample was cooled, and the crucible cleaned for the final melt and growth. The mass of the sample after the first melt was 4.990 g, after the second

melt this was reduced by approximately 79 mg to 4.911 g. This mass change may be expected to change the stoichiometry of the sample by no more than 1% either side of the ideal 75% Pd content, within error. The outgassed material was most probably the remaining traces of iron oxide in the sample; to prevent further outgassing and possible stoichiometry change the growth was performed under an Ar atmosphere. Pictures of the growth are shown in figure 8.2.

8.3.2 Cutting & orientation

X-ray Laue diffraction (in backscattering geometry) was used to determine the orientation of the crystals. As X-rays provide only a surface technique, there is no lab based technique to verify that the crystal is the same through the bulk of the growth. To help overcome this the growth was first cut in half, and then the two halves were analysed separately, rotating to verify consistency on both sides of each half. Figure 8.3 shows a Laue map for the two halves of the growth. This followed a technique used by Whitley et al. [209], however, the automated mapping did not work well for this sample, due to strong X-ray absorption.

From this it was possible to isolate regions of the sample approximately 2 mm in diameter, and 1 mm of a known orientation. This was done through orienting and cutting the sample in stages using a goniometer, and wire spark eroder.

$L1_2$ (Strukturbericht designation, space group $Pm\bar{3}m$) long range order was achieved in the samples through annealing under UHV at 875 K for 215 hours, as reported by Stetsenko and Avksentev [210]. The annealing procedure reported by Winterrose et al. [1] was found to be insufficient to achieve complete ordering in the sample. Ordering was verified by the presence of the (100) reflection in the diffraction pattern from the sample, indicating F- or P- centering.

8.3.3 Characterisation

Aside from Laue scanning the full surface of the final sample, ensuring a consistent orientation, and lattice parameter, unused parts of the original growth were ground using SiC paper into a powder in an attempt to verify the composition. This verified the structure of the sample, and that there were no unexpected phases in the sample (oxides etc), but the addition of SiC to the pattern, and the straining of the sample made it difficult to refine the data. X-ray fluorescence

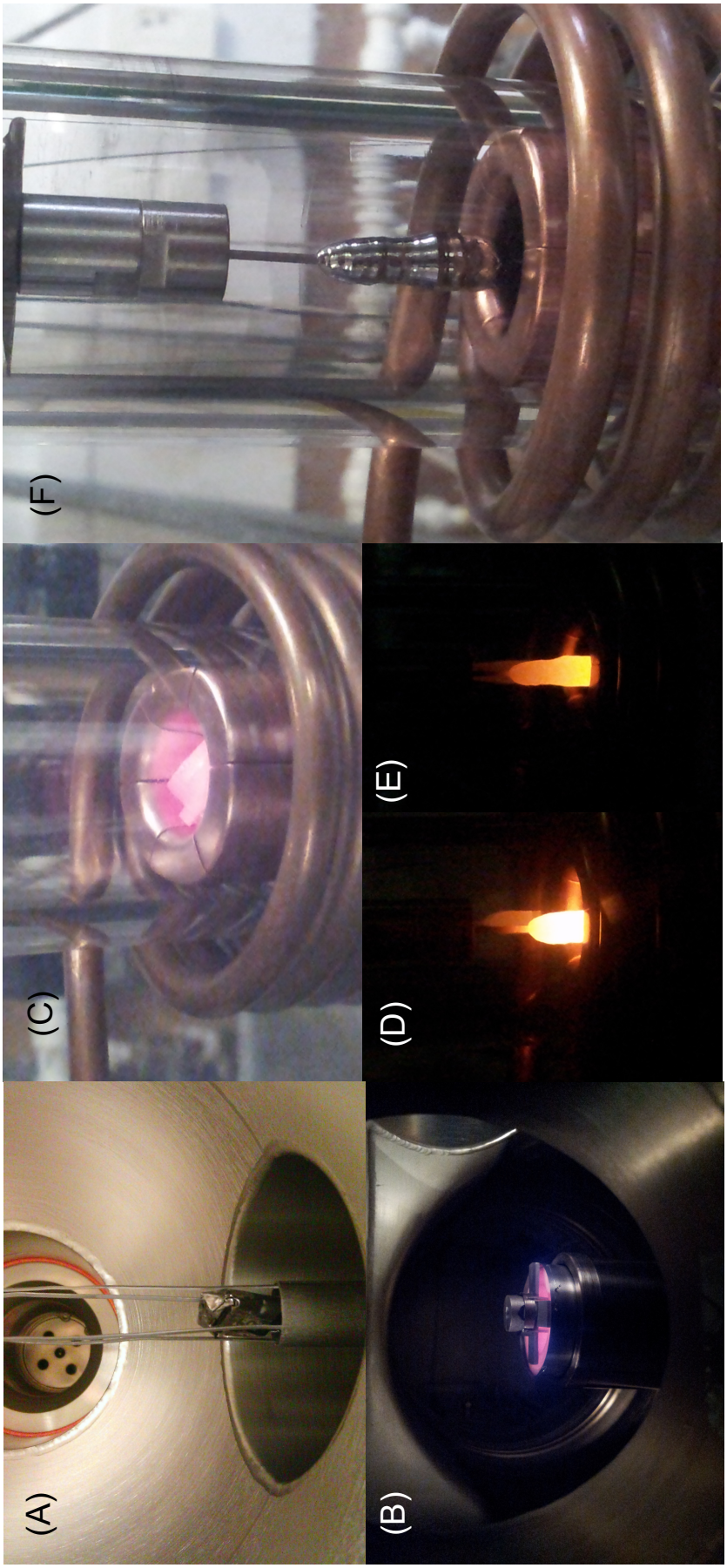

Figure 8.2 *(A) pellets loaded into UHV furnace in Ta foil, (B) during heat treatment, (C) first inductive melt of pellets in Cu crucible in UHV, (D-F) various stages of growth from melt in Ar atmosphere.*

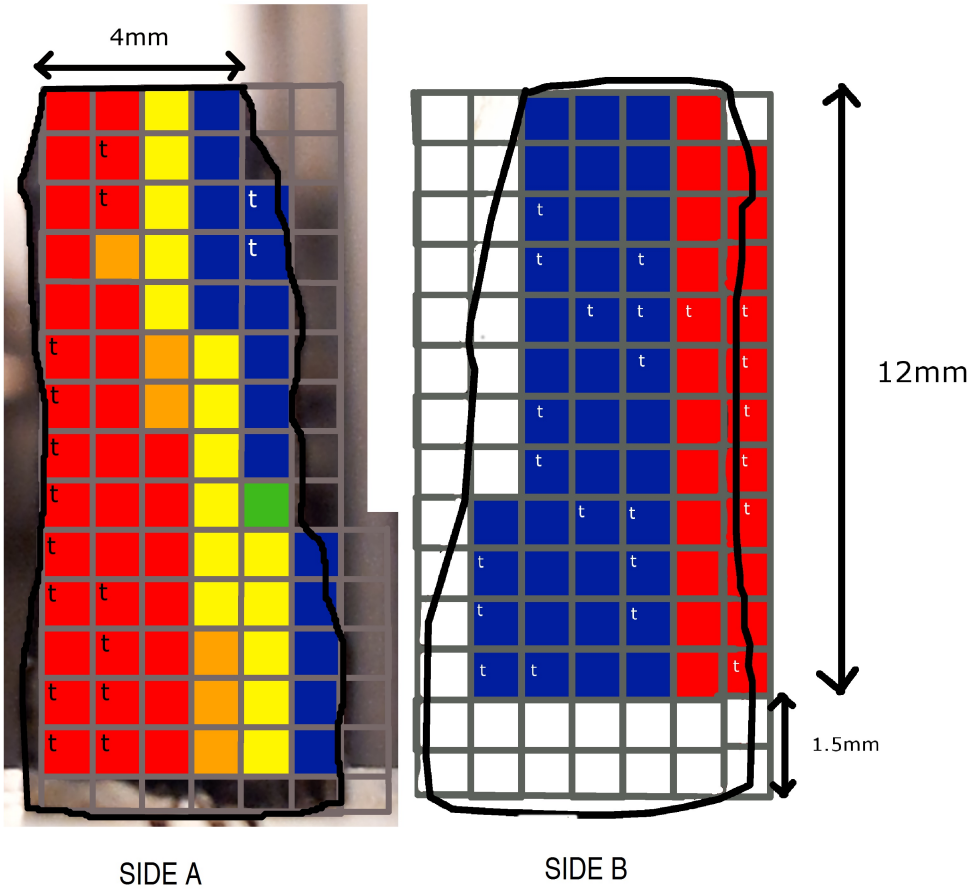

Figure 8.3 *Grain map for Pd_3Fe growth, cut in half. The different colours indicate different orientations of the sample, the subscript* t *indicates a region where the sample is strained, or partially twinned.*

measurements (using a PANalytical Epsilon3 XL) were taken on multiple cuts, and different sections of the original growth. This suggested that the composition was between 73% and 77% Pd, however repeated measurements caused this value to fluctuate around the nominal composition of the sample.

It is well documented that the Fe-Pd alloys have a strong Curie temperature dependence on chemical composition [211–214], providing an excellent method for verifying the composition of the sample. A SQUID-VSM (Quantum Design) with furnace attachment was used to measure the magnetic response from a 7 mg single crystal cut such that field was applied along the *(100)* plane.

Initially an MH scan was performed at room temperature, to verify the expected magnetic moment per atom, this is shown in figure 8.5. The extracted value is compared against other published results in table 8.1. It should be noted that Pickart and Nathans [215] reported difficulties due to preferred orientation, affecting the absolute values of the measurement. Furthermore,

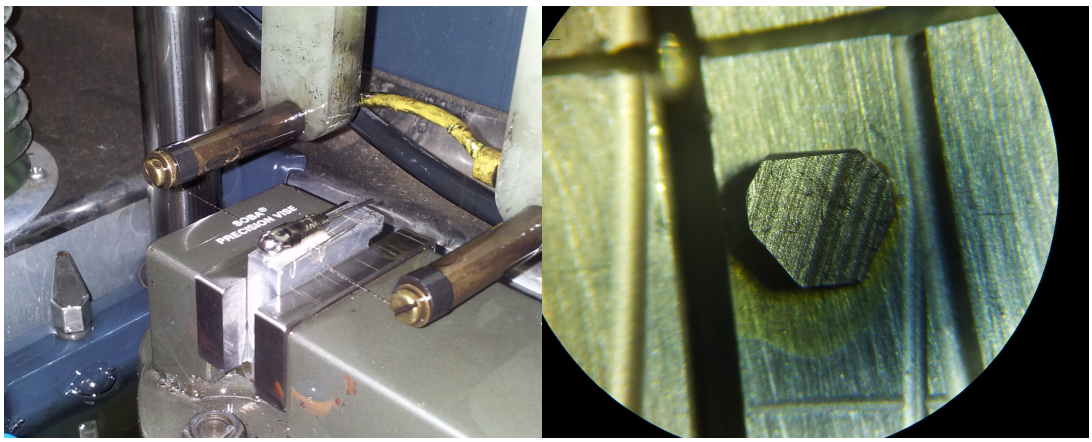

Figure 8.4 *(left) sample mounted on goniometer in paraffin bath of wire spark eroder (*50 µm *Cu wire) (right) one of the final samples oriented with (100) perpendicular to the plane within* ±1°.

assumptions had to be made regarding the magnetic form factor for the Pd sites. This perhaps explains the large discrepancy between this result and some of the values previously measured by neutron diffraction. Obtaining moments from Mössbauer spectroscopy is notably much less accurate than using a magnetometer, unfortunately the error on the result from Men'shikov and Tsurin [216] & Tsurin [217] could not be found.

Table 8.1 *Comparing measured room temperature magnetic moment to previously reported literature values.*

	$\mu_B/atom$	% agreement	Measurement method
This work	0.98590(71)	-	SQUID VSM
Crangle [214]	0.970(7)	1.5%	Ring balance
Pickart and Nathans [215]	1.065(20)	7.4%	Neutron
Cable et al. [219]	1.00(3)	1.4%	Ballistic & neutron
Men'shikov and Tsurin [216] & Tsurin [217]	1.1025(-)	10.5%	Mössbauer

The sample was then cooled in zero field to base temperature, a series of MH scans were then performed at temperature steps back to room temperature (in 5000 Oe field), before then performing an MT scan from 400 K up to 600 K, again in 5000 Oe field. Both of these plots are shown in figure 8.6, the high temperature data clearly shows the Curie transition, which has been fit using $M \propto (1 - \frac{T}{T_c})^{\gamma}$ below the Curie transition, and $\chi^{-1} \propto (T - T_c)$ above the Curie transition. This data suggests that $T_c \approx 540$ K, consistent with the previous reports for a 25% Fe content [220]. The transition displayed a slight smoothing effect, rather than

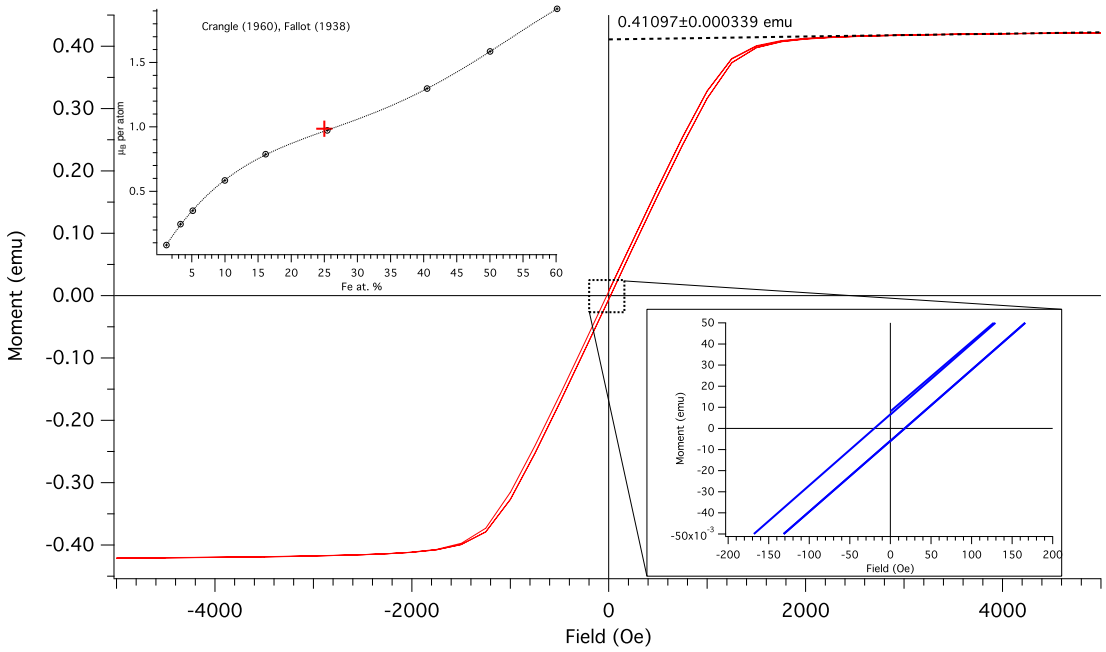

Figure 8.5 *MH curve for* 7 mg *sample at room temperature. The value of the saturated moment, M_s, is extracted through linearly extrapolating the high field measurement back to the y-axis (0.41097 emu). Expanded section shows small hysteresis effects expected from a weak ferromagnet. (Inset) μ_B per atom as measured by Crangle [214] and Fallot [218], + indicates measured value.*

a sharp transition. This was due to the high field used in the measurement, but may additionally have been due to small inhomogeneities in the sample. Neutron diffraction from the crystal showed that it had become polycrystalline after the furnace experiment despite remaining well below the expected melting temperature. It is possible that the relatively low vacuum of the SQUID was not sufficient to prevent oxidation of the crystal after prolonged measurement at high temperature.

8.4 High pressure analysis

8.4.1 Single crystal compression on the WISH diffractometer

The long wavelength range, and large detector coverage of WISH makes it a powerful instrument for the study of magnetic samples. Originally designed as a powder diffractometer, it is highly versatile, and suitable for many single crystal measurements. Initially the objective was to observe the large volume collapse,

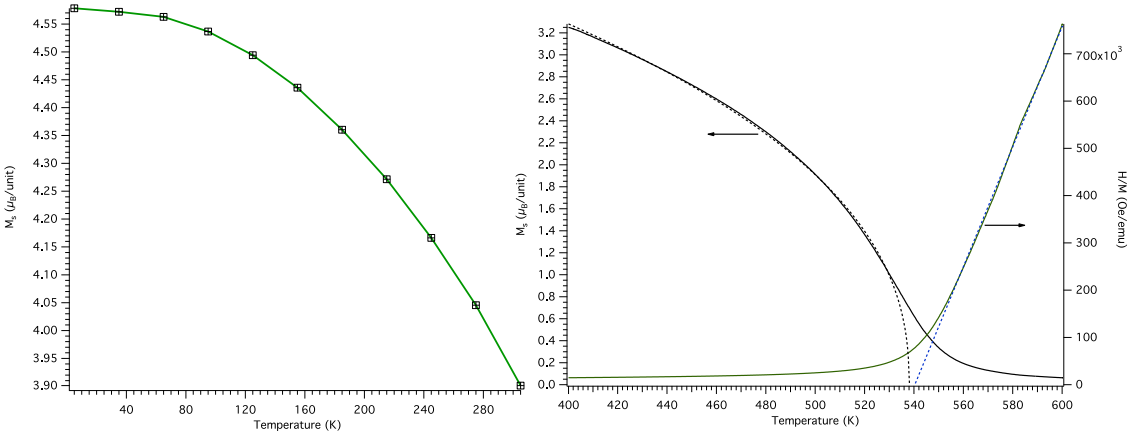

Figure 8.6 *MT curve for zero field cooled* 7 mg *sample in 5000 Oe field. (left) low temperature data, confirming no secondary transitions due to impurities in the sample. (right) furnace data, confirming Curie transition at approximately* 540 K*.*

and verify whether this is accompanied by a loss of magnetic order in the sample. As the previously reported large volume collapse occurred at room temperature, but at a pressure $10 - 14$ GPa, the Paris-Edinburgh cell was chosen to pressurise the sample, using double toroidal sintered diamond anvils, similar to the single crystal loading reported by Bull et al. [221]. A small pellet of Pb was included with the sample as a pressure marker, and deuterated 4:1 methanol:ethanol was used as a pressure transmitting medium.

The sample was cut with *(100)* perpendicular to the axis of the instrument, and oriented so that the {100} reflections were measurable on the $2\theta = 90°$ detector banks, giving a balance between resolution, and strength of magnetic signal (due to form factor). Due to the limited aperture of the Paris-Edinburgh cell, caused by the shallow angle of the anvils, which gets smaller as the load is increased, and the high symmetry of the sample, only this set of reflections was visible. The sample was stepped up in load to determine the compressibility of the sample. In addition, through comparing the relative intensities of the *(100)*, *(200)*, and *(400)* peaks (the *(300)* was too weak to observe) the magnetic contribution to the signal can be compared as a function of pressure, again due to the magnetic form factor dictating stronger scattering for low $\vec{Q}$.

The data from these measurements is shown in figure 8.7 alongside the data reported by Winterrose et al. [1]. The compressibility of the sample, and the sample pressure, was fit using a Rydberg-Vinet EOS (details outlined in [222]).

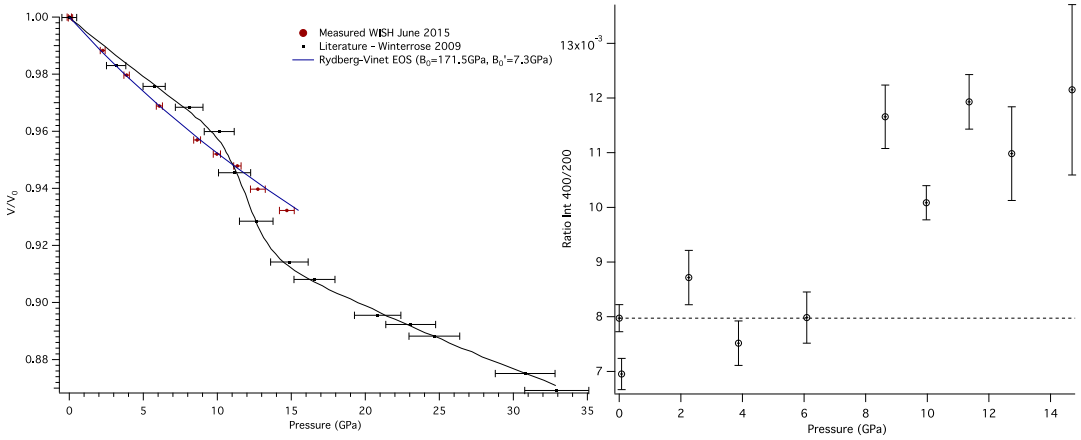

Figure 8.7 *(left) Compressibility of singe crystal sample as measured from the* $\{100\}$ *reflections, overlaid with data from [1]. The equation of state has been fit using Rydberg-Vinet EOS, with* $B_0 \approx 171.5\,\mathrm{GPa}$, $B' \approx 7.3\,\mathrm{GPa}$ *(right) Ratio of integrated intensities of* (400) *and* (200) *peaks as function of pressure.*

8.4.2 Powder analysis on the PEARL diffractometer

To further verify the results from WISH, and to investigate the apparent discrepancy between the measured bulk modulus of the sample with that reported by Winterrose et al. [1], additional high pressure powder measurements were performed on the PEARL diffractometer, using a standard single toroid set of anvils made from zirconia toughened alumina (ZTA). The ZTA anvils cannot achieve the same pressure range as sintered diamond, but offer significantly lower levels of background. Furthermore, powder measurements are more suitable for performing measurements of bulk modulus, giving greater certainty of the lattice parameter at each pressure.

The powder sample was obtained from the polycrystalline section of the grown sample towards the base of the sample. This showed some levels of preferred orientation, but it was still possible to Reitveld refine and accurately determine the lattice parameter as a function of pressure. This experiment was performed with two different pressure media, initially in deuterated 4:1 methanol:ethanol, and then in a mixture of fluorinerts 1:1 FC84:FC87. The measured bulk moduli are shown in figure 8.8.

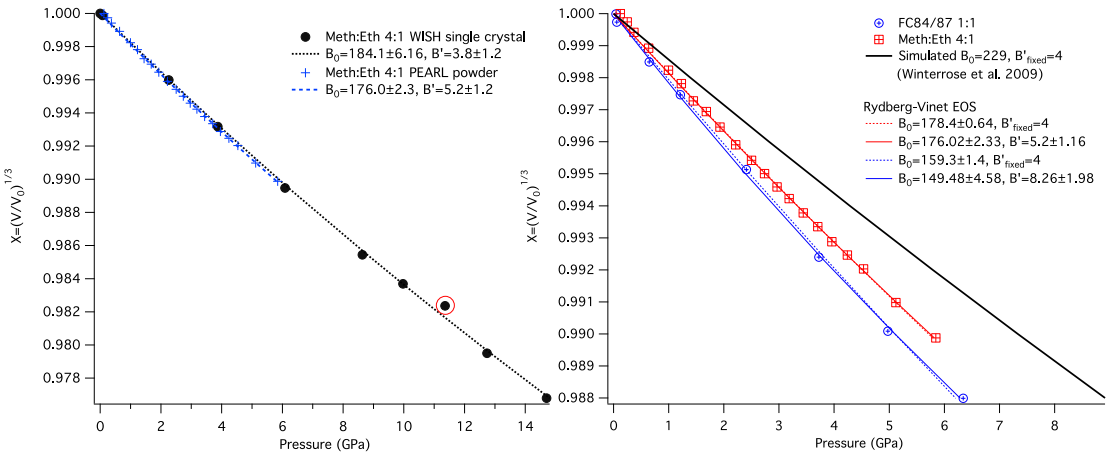

Figure 8.8 *(left) reduced compressibility of sample versus measured pressure compared between WISH and PEARL measurements. B_0 differs with data point marked treated as an outlier (right) PEARL measurements for methanol:ethanol, and fluorinert data compared with expected low pressure compressibility from literature. All fits use a Rydberg-Vinet formulation. The error bars are not visible over the markers.*

8.5 Discussion

No large volume collapse was observed up to 15 GPa from the single crystal data collected on WISH. Magnetically, the integrated data suggests that the sample transitions from ferromagnetic to paramagnetic at approximately 8 GPa, which isn't accompanied by any measurable drop in volume. This small change in intensity is consistent with the small moments measured at room temperature in zero field on the SQUID. Most noticeably, the bulk modulus measured is approximately 20-25% lower than that measured previously. The measurements from PEARL show that in methanol:ethanol both measurements are consistent within the error of the fits to the EOS. Also, there appears to be a non-negligible dependence on the measured value of B_0 depending on the pressure medium used [223].

The measurement from Winterrose et al. [1] using energy dispersive X-ray diffraction in a diamond anvil cell. However, there are some potential issues with the preparation of their sample which may explain the differences seen here. The powder sample was cold rolled from an ingot to a 25 µm thick sheet to fit it into the gasket. This may have work hardened the sample, effectively altering it's compressibility. Although some metals can be restored through heat treatment, it is possible that the annealing procedure reported was not hot or long enough

to affect the relaxation of the sample. The samples grown for the present study are absent of such effects.

The pressure medium used for this experiment was silicon oil, probably to reduce the background signal. However, there are conflicting sources of information as to what the hydrostatic limit of silicon oil is. Angel et al. [38] report that it is $< 1\,\mathrm{GPa}$, confirmed by unusual observations reported by Klotz et al. [39]. However others report that it may be superior to methanol ethanol [224].

The exact effect of the hydrostaticity on the measured physical properties of the sample are difficult to quantify. On a structurally stable sample, non-hydrostatic effects tend to simply broaden diffraction peaks. There are previous reports where the compressibility of a sample is measured as 18% more compressible in Ar than in silicone oil [225], though no detailed explanation was offered. More recent studies of the compressibility of silicone oil suggest that the complex interactions between the long chain molecules in the oil play an important role, causing some higher values of B_0 for the oil itself.

8.6 Conclusions and future work

The original objective of this work was to investigate the unusual room temperature pressure tuned Invar behaviour displayed by Pd_3Fe. A single crystal sample was successfully grown, and characterised through a number of X-ray techniques, SQUID magnetometry, and neutron diffraction. Attempts to reproduce the volume collapse observed by Winterrose et al. [1] were unsuccessful, suggesting that the sample is approximately 20% more compressible than previously reported. This may be due to differences in preparation of the sample, or due to compressibility of the pressure medium used. Either way the results from this present study offer an important contribution; if the volume collapse is only visible under partially uni-axial pressure this poses a number of unanswered questions as to the mechanism for the onset of Invar behaviour.

Before further tests are performed, additional characterisation of the present samples will be performed to verify the composition more precisely. This will be done using either X-ray spectroscopy or electron probe microanalysis. In addition, a high pressure SQUID study will be performed using a diamond anvil cell to verify the ferromagnetic/paramagnetic transition observed at approximately

8 GPa.

This work highlights the issues with high pressure studies regarding the hydrostaticity of the pressure medium significantly altering the physics observed.

Chapter 9

Summary

This thesis has presented novel high pressure equipment, and neutron scattering techniques. Primarily, **a compact opposed anvil pressure cell** has been optimised for low temperature operations, allowing pressure to be measured and controlled without the need to warm the cell above base temperature. This is significant, and beneficial for several reasons: many hours of experimental time are saved, improving the efficiency of performing high pressure experiments at costly large scale neutron facilities; the design of the cell can be used to reach pressures beyond what can be achieved using cells of a similar size (such as gas cells and piston cylinder cells), opening up a new realm of accessible science; there are no longer safety concerns in the handling of active pressure cells, as it remains contained in the cryostat for the duration of the experiment. This class of pressure cell will be of increasing importance to the neutron scattering community, as the demand for high pressures at cryogenic temperatures becomes larger.

In addition to developing an efficient load cell, **finite element analysis has been used to provide insight into the operation of opposed anvil systems**, and the principle of massive support, allowing the sample volume to be optimised for a given pressure limit. FEA has also been used to explain the observed modes of failure in sapphire anvils in this setup. Beyond the use of FEA, extensive work has been performed to characterise various gaskets suitable for high pressure studies in the radial geometry, and to compare this against the mechanical, thermal, and thermo-mechanical properties of the material. This is significant, and will be useful for other low temperature systems beyond

anvil/gasket assemblies.

Measuring decent sample statistics from a system where the sample is only 5% of the material in the beam is challenging, and not unique to high pressure experiments. This thesis has presented a **new technique for constructing collimators**, allowing scattering from micro-samples to be measured above the background of the surrounding material. 3D printing is quick, inexpensive, and easily customisable to any instrument, removing the geometric constraints imposed by conventional manufacturing techniques, making it a powerful technique for improving the quality of neutron data.

A piston-cylinder cell for neutron scattering has been adapted to incorporate in-situ pressure measurement, and the ability to perform multiple measurements on the sample simultaneously, through including an electrical plug, and new sealing mechanism. The use of the cell has been demonstrated through the ultrasonic study of UGe_2, though the ability to perform simultaneous measurements on a single loading, with neutron scattering offers powerfully consistent data, without additional systematic error.

Further to the work developing cells specifically for neutron scattering, **a spherical pressure cell has been developed** for performing transport measurements at dilution fridge temperatures, in high magnetic field. The cell has been tested, measuring the superconducting transition in the alloy U_6Fe. The high symmetry of the cell gives it a significant advantage over typical piston-cylinder cells for high field measurements, minimising field attenuation and distortion on the sample.

Finally, the **INVAR alloy Pd_3Fe has been studied under high pressure using neutron diffraction** to investigate the nature of the observed large volume collapse, and subsequent zero thermal expansion. A single crystal sample was successfully grown and cut, and extensively characterised. However, no large volume collapse was observed, and the only magnetic transition observed was due to the suppression of the Curie temperature. Compressibility measurements suggest that the sample is significantly softer than suggested from the literature, though this has been shown to be highly dependent on the pressure medium used. This suggests that the INVAR transition may not be achievable in purely hydrostatic conditions, but requires some level of uniaxial compression. Further characterisation of the sample to verify the composition to within 0.1% may provide further insight.

Chapter 10

Conclusions and future development

This thesis, and the work of others [99], has shown that it is starting to become possible to obtain neutron diffraction data from extremely small samples in environments contributing large amounts of background to the signal, over timescales previously unachievable due to incident flux limitations [78]. This opens a new realm of physics which can be investigated with neutrons. However, the key limitation with this technique now remains the instrument side of the experiment, with the crucial difficulty becoming sample alignment and beam focussing. Although it is becoming more common to study extremely small samples with neutrons, these are rarely enclosed in any form of sample environment, whilst the majority of samples studied are large, both only requiring only approximate positioning within the incident beam. For this reason most instruments are poorly equipped for dealing with precision alignment of pressure cells. Whilst there are iterative methods for aligning cells, such as the technique discussed where the cell is rotated and the sample intensity is mapped, this is time consuming, and currently limited to rotation only, whilst height can currently only be adjusted manually, and imprecisely. A major future development of neutron instruments will be the move towards higher sample positioning precision, analogous with the techniques used at synchrotron sources.

Aside from instrument upgrades, developments are bringing researchers extremely close to being able to perform combined X-ray and neutron studies on single sample [226], loaded in the same cell. This is exciting, as currently it is extremely challenging to ensure that the sample is in precisely the same state between data reduction. Furthermore, the quirks of high pressure instrumentation mean that

some effects may not be visible in all pressure cells alike; for example where a material may be extremely sensitive to uniaxial strains, these effects will always be significantly greater in opposed anvil cells than in large volume gas cells. Combined neutron and X-ray diffraction offers the best of both worlds, where the limitations of one are balanced by the advantages of the other, catering to the solution of a wide range of structure complexities and sizes.

Returning to the subject of pressure media; it is by far the most important consideration for high pressure studies, directly affecting the state of the material being compressed. Now that high pressure is becoming a more mainstream technique, the effects of pressure media should face increased scrutiny. Whilst many studies have been performed aiming to assess the hydrostatic limit of various media, it should be remembered that whilst our understanding of the high pressure behaviour of these chemically 'simple' materials (He, Ar, etc.) remains incomplete, there will always be uncertainty as to the thermodynamic state of a sample contained within them.

In addition to moving in new directions with neutron diffraction, there are many pressure cell designs which work extremely well for their purpose, it not always being necessary to generate megabar pressures. However, these cells have not been adapted or upgraded for some time, and there is a great deal which can now be done to improve the sample signal, and pressure range of these large volume cells. This has been shown with the use of 3D printing, where customised equipment with unusual features can be constructed relatively inexpensively. This could be applied not only to collimation, but also to mirrors to focus the incident neutron beam to a smaller spot size.

Aside from improving collimation and beam focussing, there are many new material possibilities which could be of interest, some of which already exist, and some of which could be developed for the future. For example, amorphous, or 'glassy', alloys offer the distinct advantage that they have only local structure, without long-range ordering. This has been shown to be promising for pressure cell work [227], but holds potential for further development to reduce the levels of incoherent background further. Additionally, foams are extremely promising for high pressure work. Although their porous nature precludes them from direct containment of pressurised fluids, they are still promising for providing outer structural support, at a fraction of the density of a solid, drastically reducing neutron attenuation. A final example is the use of composite alloys, such as aluminium-diamond, which could be interesting to use as a liner material

in a piston-cylinder arrangement, offering excellent neutron transmission (bar the Bragg edges from the diamond), and a high compressive strength perhaps exceeding tungsten carbide.

Improving current measurement techniques is important, but developing new capabilities is equally so. The ability to combine measurements, such as X-rays and neutrons, should naturally be extended to include electrical measurements, such as ultrasonic studies or resistivity measurements. Although these techniques work on different time-scales to that of a diffraction measurement, they offer the considerable advantage that the state of the sample is the same for all measurements. The strength of information collected in this way should not be understated.

Appendix A

Schematics of cryostat/CCR for neutron pressure cell

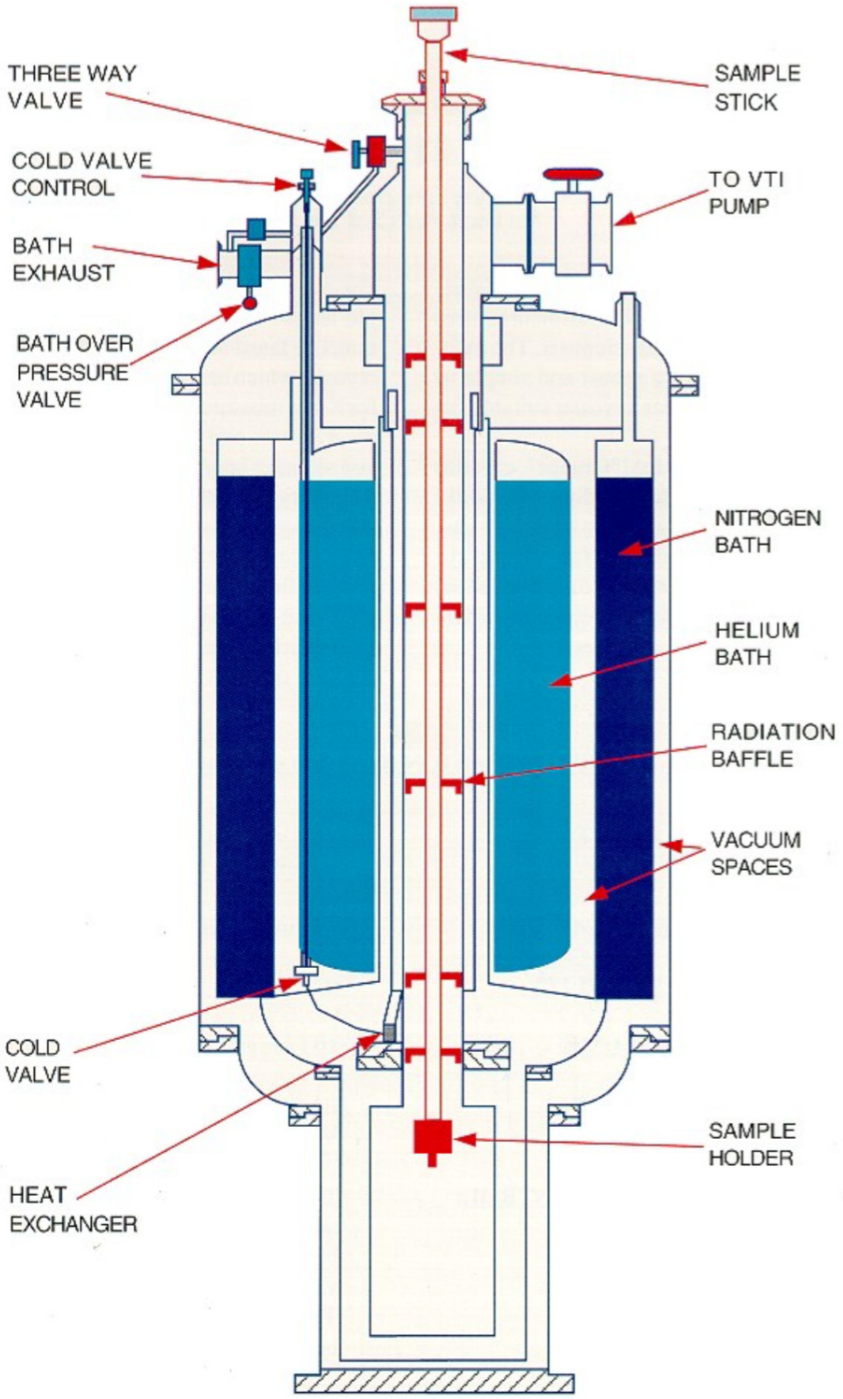

Figure A.1 *Schematic of ILL Orange Cryostat (figure from [8]).*

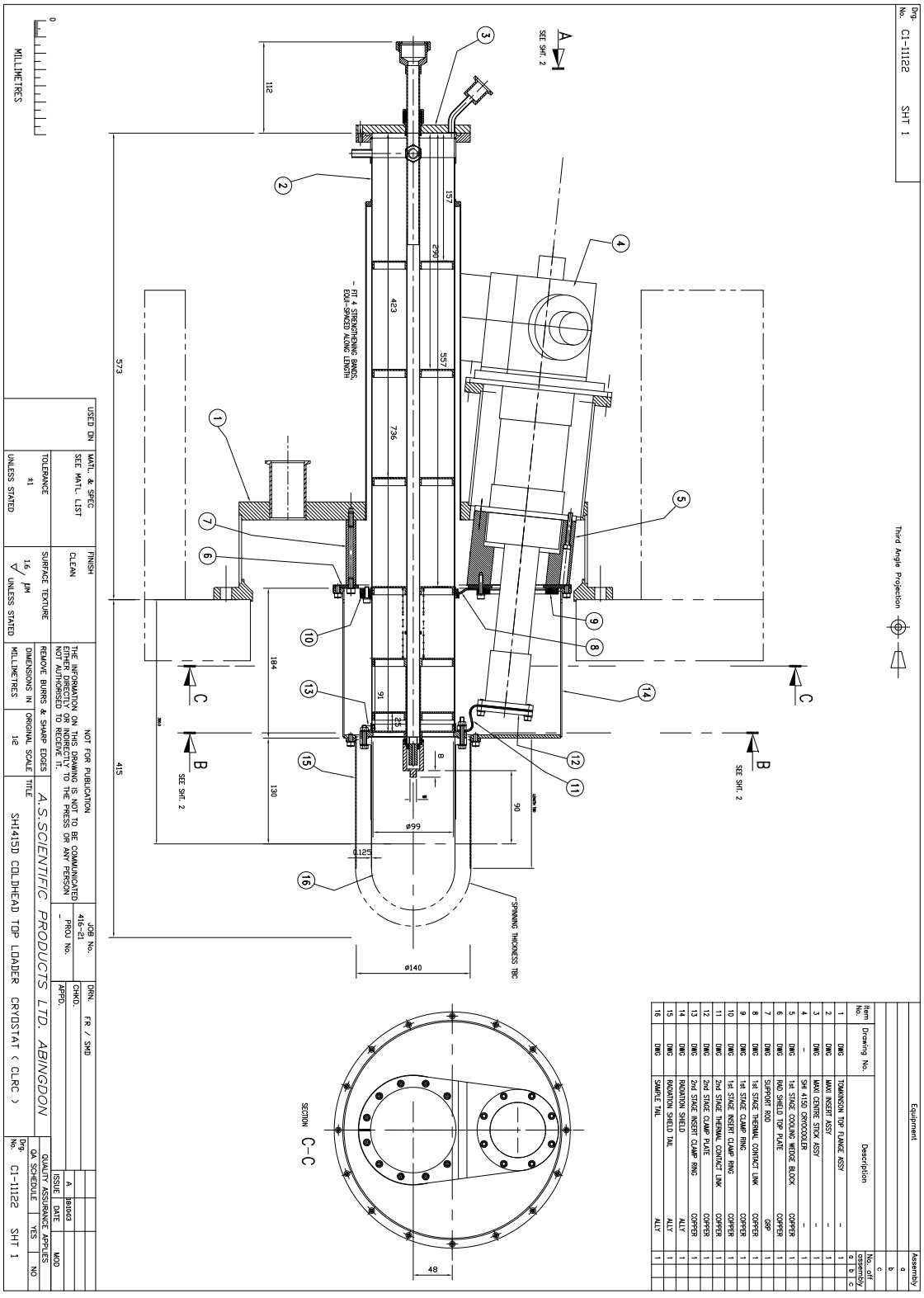

Figure A.2 *Technical drawings for top loading CCR assembly, with Sumitomo 415D cold head. Figure [9].*

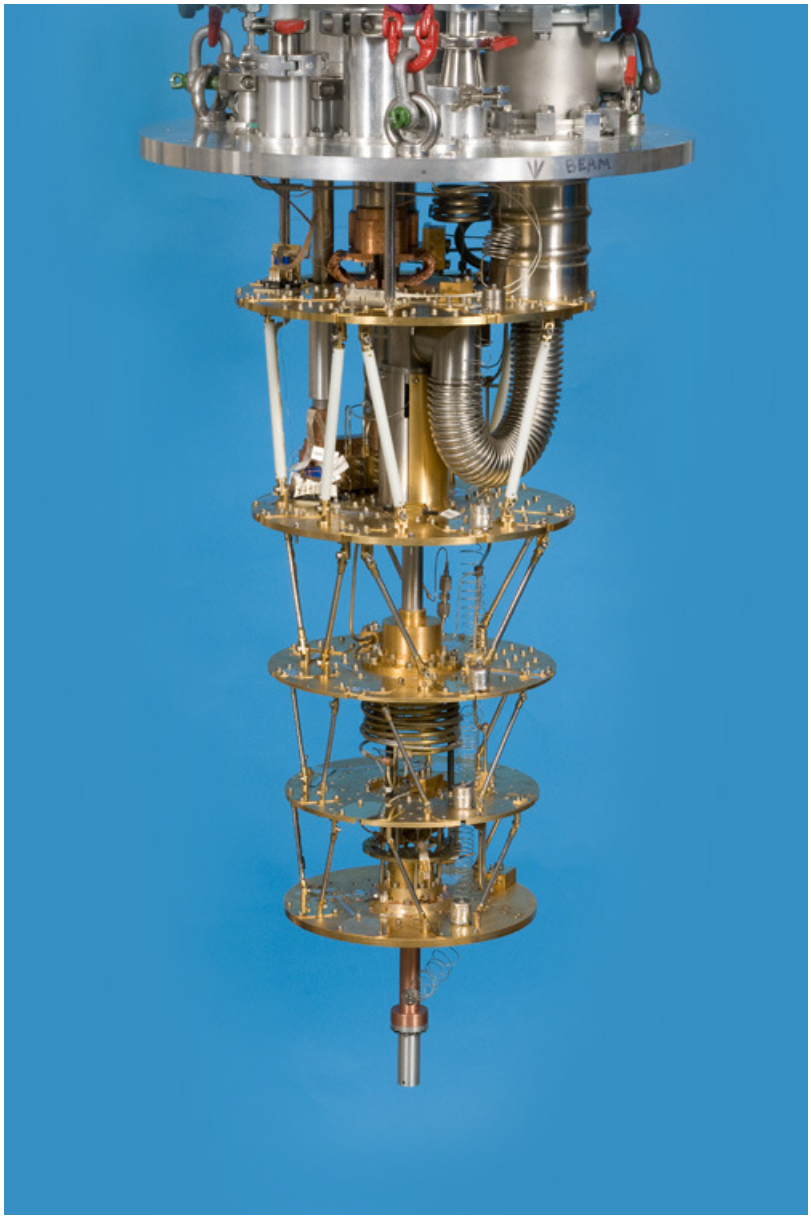

Figure A.3 *E18 Vericold dilution fridge (radiation shields removed). The structure is formed from OFHC Cu coated in Au. Figure from [10].*

Appendix B

Supplementary material for Chapter 3

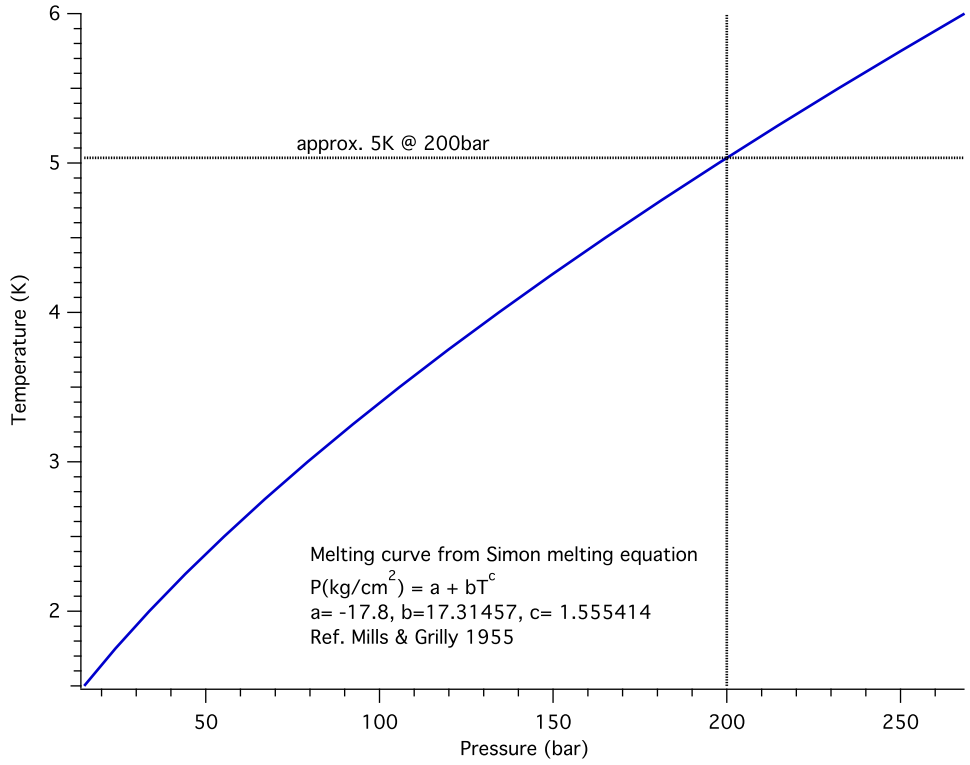

Figure B.1 *Helium-4 melting curve for temperature/pressure range of pressure cell. The maximum normal operating pressure of the bellows is* 200 bar*, at which helium will solidify at approximately* 5 K*. [228]*

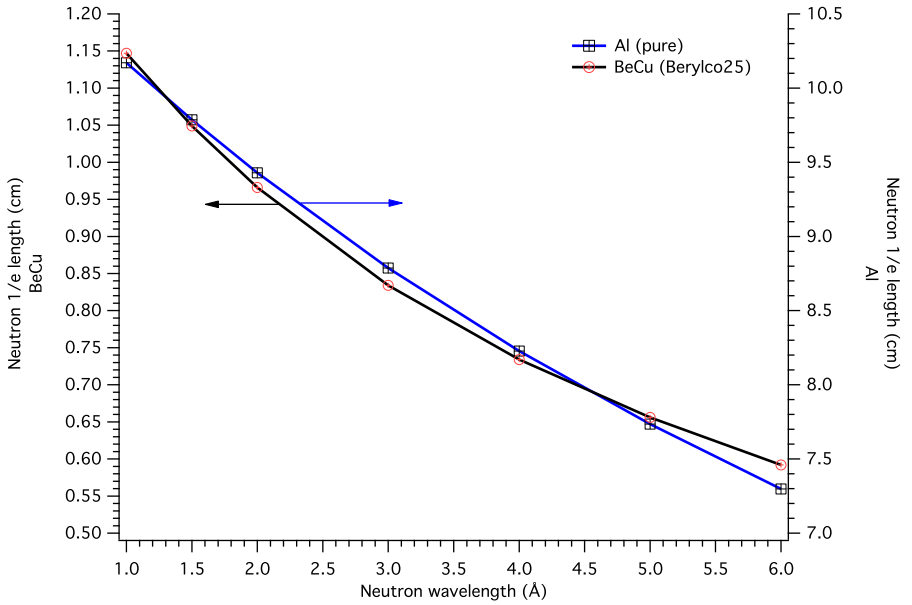

Figure B.2 *Plot showing wavelength dependence on 1/e length for BeCu and pure Al. A similar trend may be seen for most materials. Note: this data only indicates average behaviour of the sample, the presence of Bragg edges in transmission data is expected at particular wavelengths. Data compiled from [63, 64].*

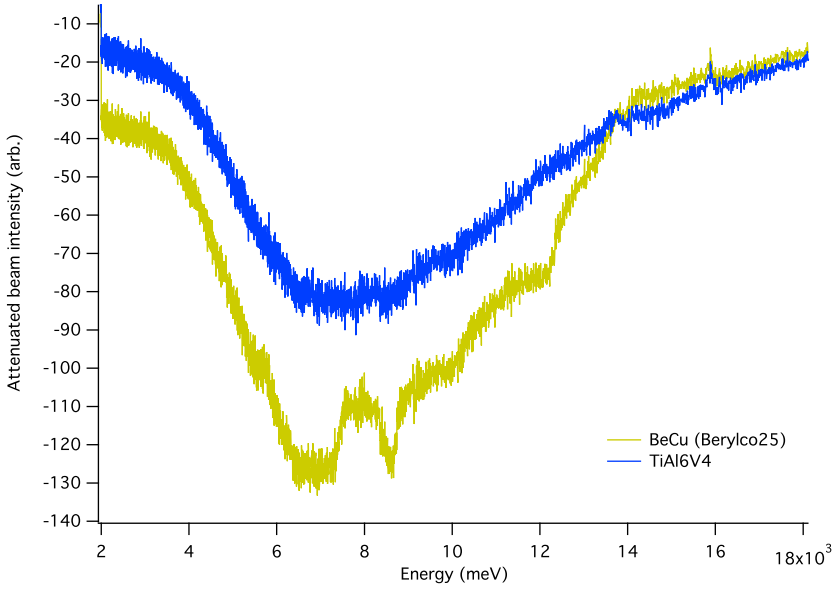

Figure B.3 *Beam attenuation measurements for TiAl6V4 and BeCu performed on PEARL diffractometer at ISIS neutron facility. The transmission measurements were performed in a V can, and normalised against the empty can. The samples were identically cut with* 4.85 mm *diameter and* 40 mm *length.*

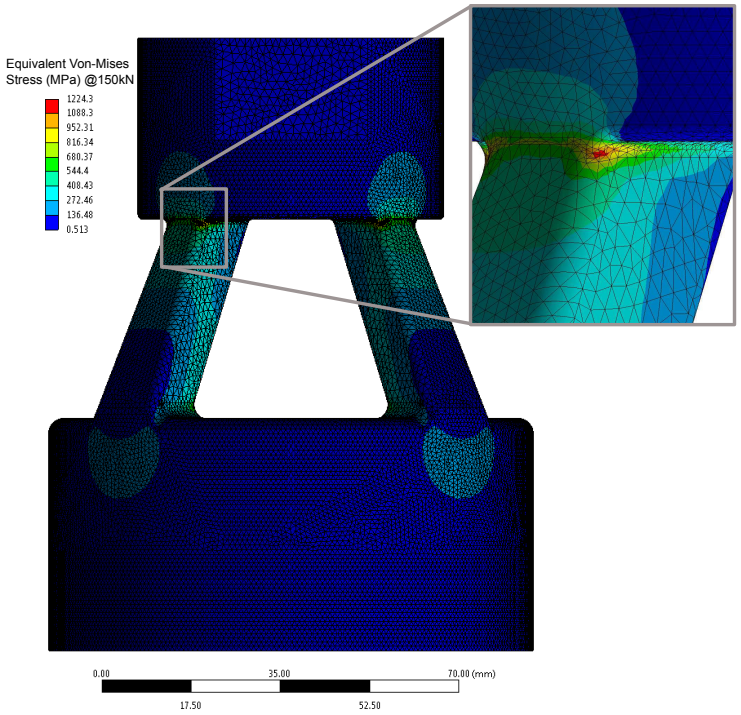

Figure B.4 *Finite element analysis from Mk1 cell body under* 150 kN *tensile force, Von-Mises equivalent stress displayed. At this force, equivalent to* 600 bar *internal gas pressure, the stresses at the top of the pillars of the cell become significant, and close to the ultimate tensile strength of BeCu (approximately* 1.3 GPa*).*

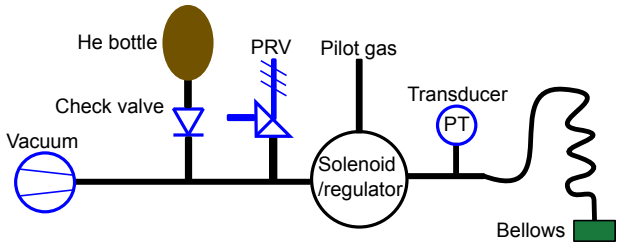

Figure B.5 *Schematic of gas panel used to monitor and control the bellows pressure.*

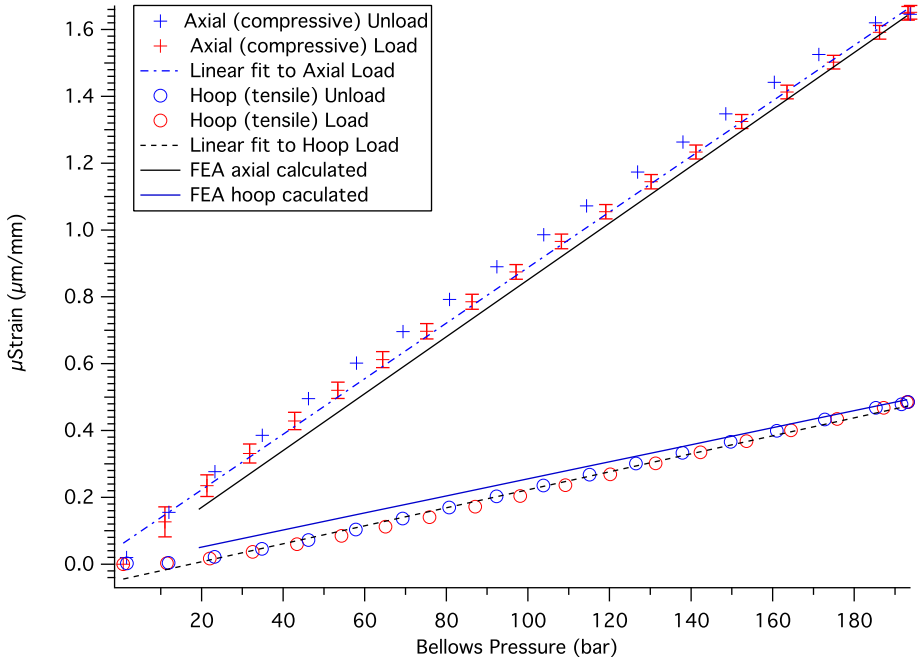

Figure B.6 *Axial and hoop strain, measured with strain gauges compared with simulated using FEA. The offset between the simulated and measured results is due deviation from a linear loading curve at low pressures, due to the pre-compression of the bellows, and non-perfect alignment of the strain gauges.*

Appendix C

Technical drawings for Mk2 load cell

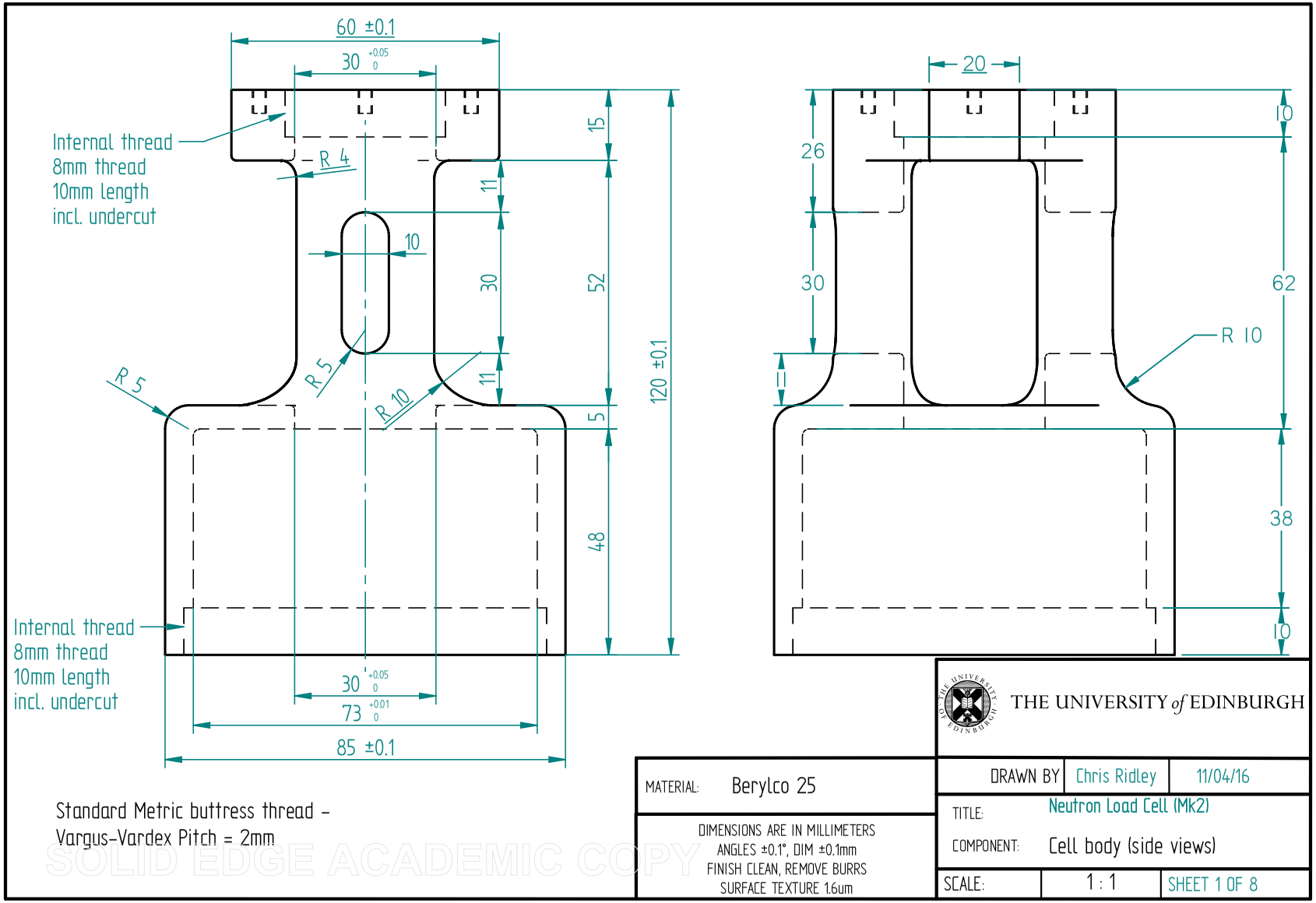

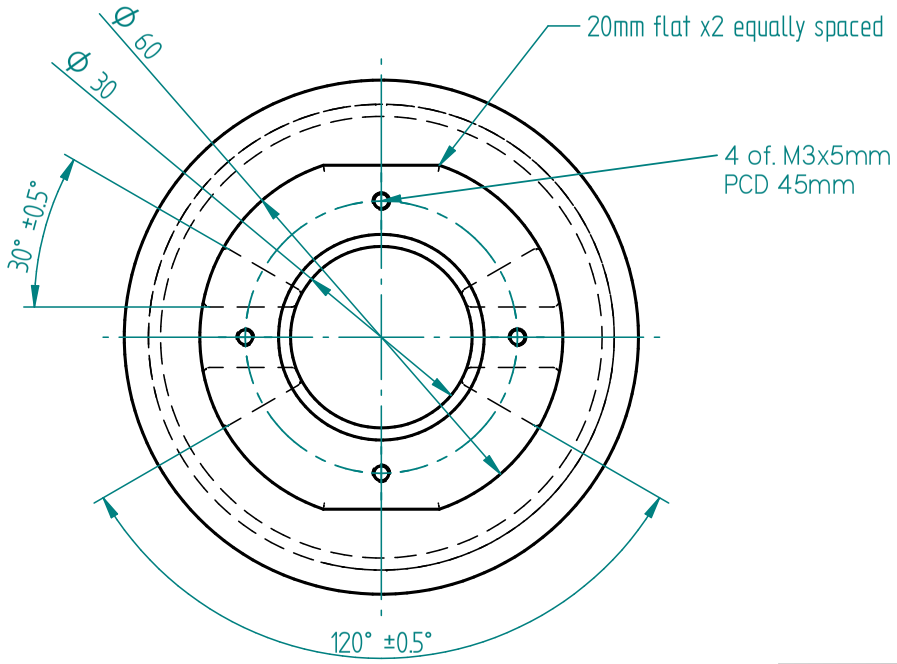

THE UNIVERSITY of EDINBURGH

MATERIAL:	Berylco 25	DRAWN BY	Chris Ridley 11/04/16
DIMENSIONS ARE IN MILLIMETERS ANGLES ±0.1°, DIM ±0.1mm FINISH CLEAN, REMOVE BURRS SURFACE TEXTURE 1.6um		TITLE:	Neutron Load Cell (Mk2)
		COMPONENT:	Cell body (Top view)
		SCALE:	1 : 1 SHEET 2 OF 8

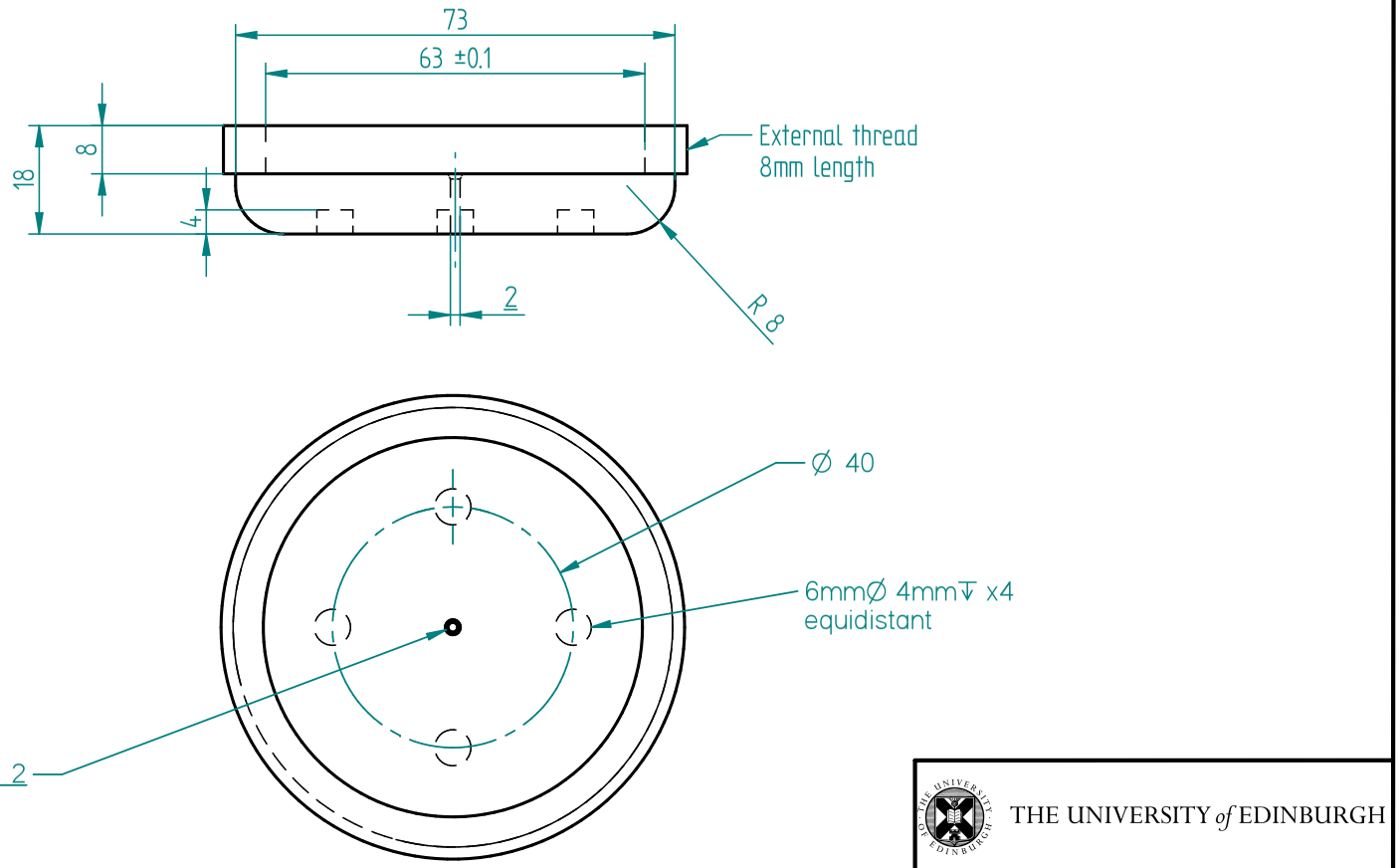

Standard Metric buttress thread –
Vargus-Vardex Pitch = 2mm

MATERIAL:	Berylco 25	DRAWN BY	Chris Ridley 11/04/16
DIMENSIONS ARE IN MILLIMETERS ANGLES ±0.1°, DIM ±0.1mm FINISH CLEAN, REMOVE BURRS SURFACE TEXTURE 1.6um		TITLE:	Neutron Load Cell (Mk2)
		COMPONENT:	Base plate
		SCALE:	1 : 1 SHEET 3 OF 8

THE UNIVERSITY of EDINBURGH

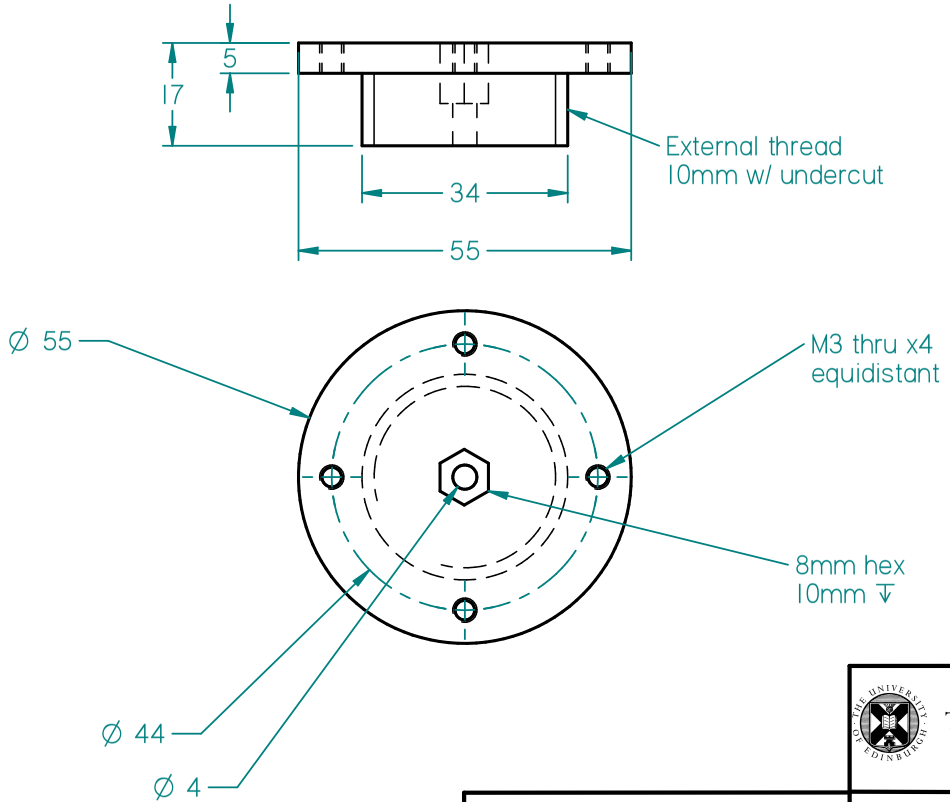

Standard Metric buttress thread -
Vargus-Vardex Pitch = 2mm

MATERIAL: Berylco 25		
DIMENSIONS ARE IN MILLIMETERS ANGLES ±0.1°, DIM ±0.1mm FINISH CLEAN, REMOVE BURRS SURFACE TEXTURE 1.6um		
THE UNIVERSITY of EDINBURGH		
DRAWN BY	Chris Ridley	11/04/16
TITLE:	Neutron Load Cell (Mk2)	
COMPONENT:	Top plate	
SCALE:	1 : 1	SHEET 4 OF 8

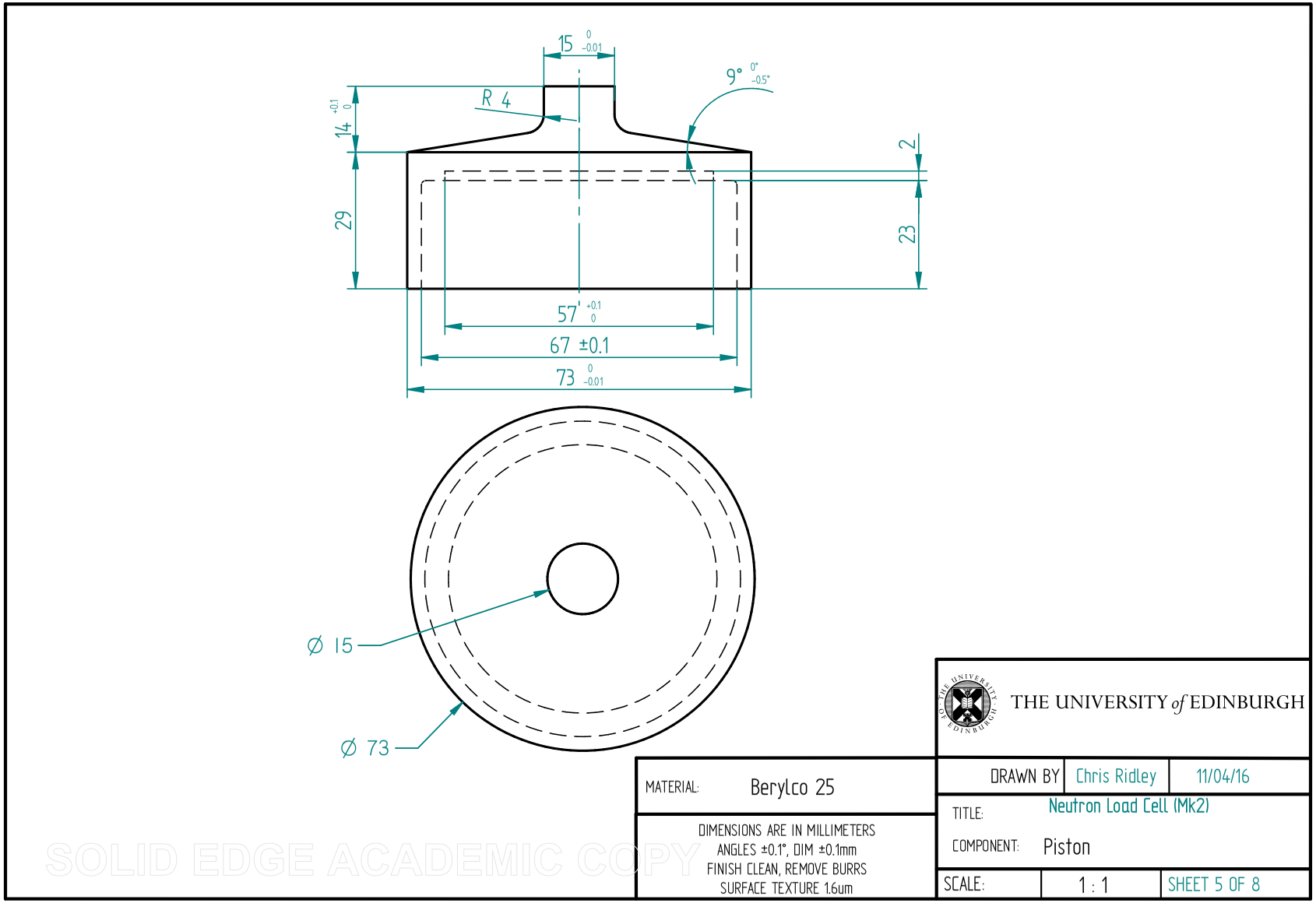
15 0 -0.01
9° 0° -0.5°
R 4
14 +0.1 0
29
2
23
57 +0.1 0
67 ±0.1
73 0 -0.01
Ø 15
Ø 73
THE UNIVERSITY of EDINBURGH
MATERIAL: Berylco 25
DRAWN BY Chris Ridley 11/04/16
TITLE: Neutron Load Cell (Mk2)
COMPONENT: Piston
SCALE: 1 : 1
SHEET 5 OF 8
DIMENSIONS ARE IN MILLIMETERS
ANGLES ±0.1°, DIM ±0.1mm
FINISH CLEAN, REMOVE BURRS
SURFACE TEXTURE 1.6um
SOLID EDGE ACADEMIC COPY

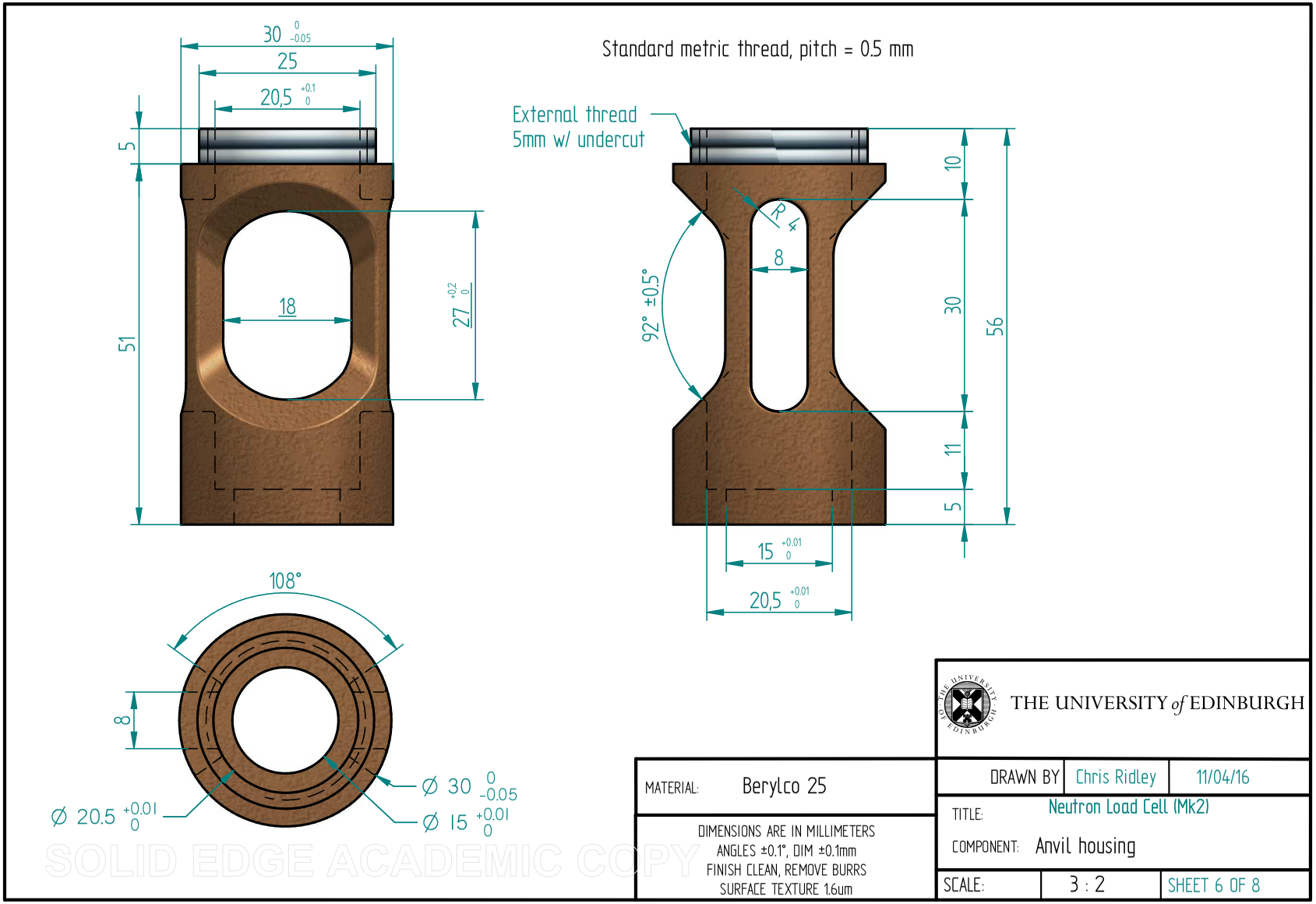

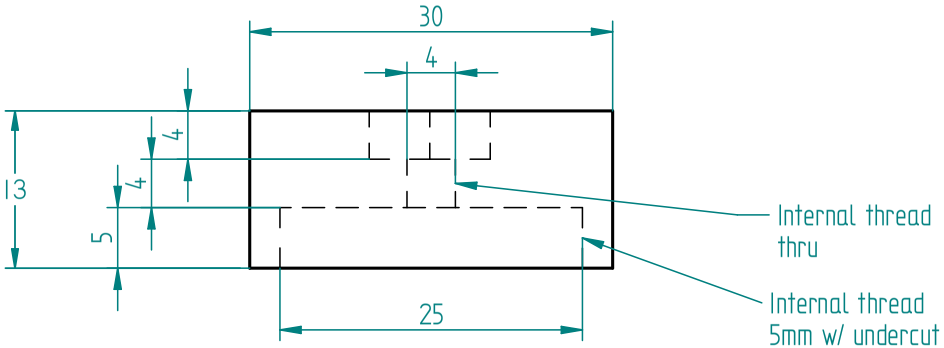

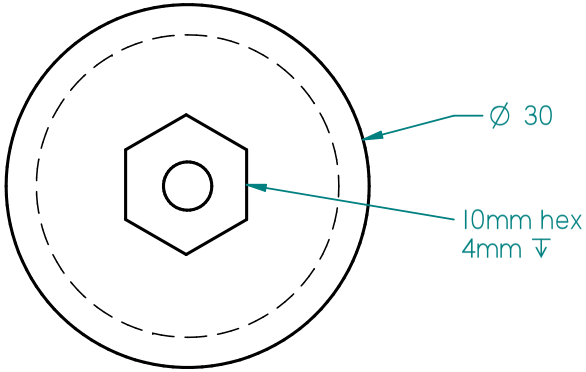

Standard thread, pitch = 0.5 mm

MATERIAL: Berylco 25		DRAWN BY	Chris Ridley	11/04/16
DIMENSIONS ARE IN MILLIMETERS ANGLES ±0.1°, DIM ±0.1mm FINISH CLEAN, REMOVE BURRS SURFACE TEXTURE 1.6um		TITLE:	Neutron Load Cell (Mk2)	
		COMPONENT:	Anvil housing – top plate	
		SCALE:	2 : 1	SHEET 7 OF 8

THE UNIVERSITY of EDINBURGH

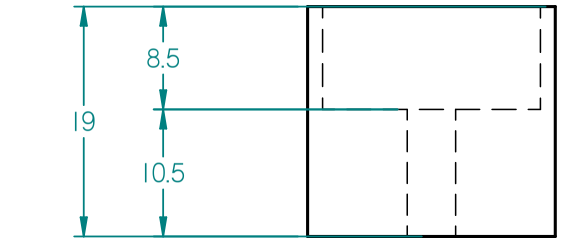

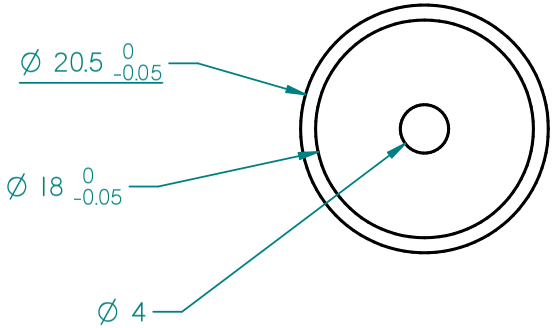

THE UNIVERSITY of EDINBURGH

MATERIAL:	Berylco 25	DRAWN BY	Chris Ridley 11/04/16
DIMENSIONS ARE IN MILLIMETERS ANGLES ±0.1°, DIM ±0.1mm FINISH CLEAN, REMOVE BURRS SURFACE TEXTURE 1.6um		TITLE:	Neutron Load Cell (Mk2)
		COMPONENT:	Anvil housing
		SCALE: 2 : 1	SHEET 8 OF 8

Appendix D

Failure modes observed in sapphire anvils

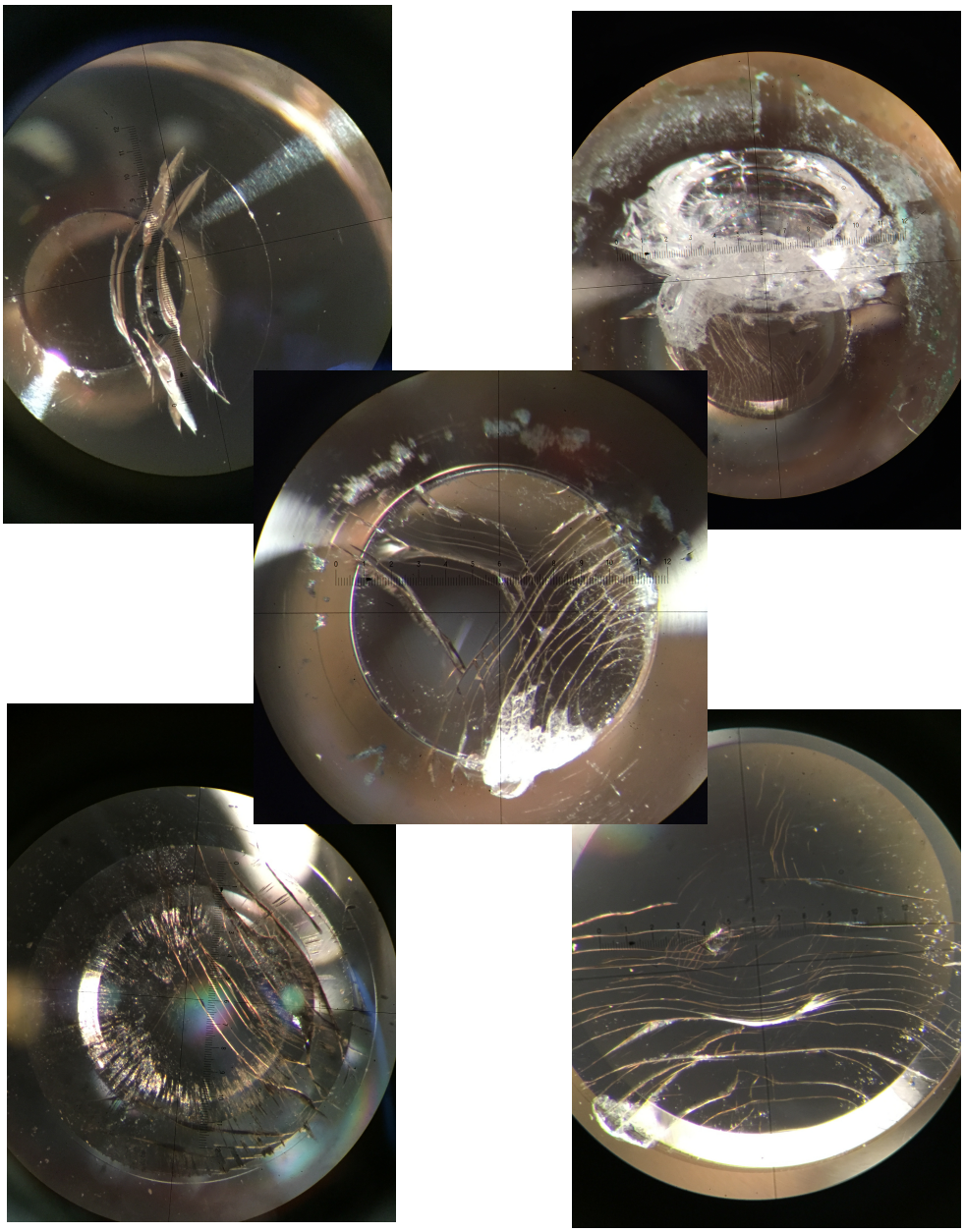

Figure D.1 *Type 1 failure observed in sapphire anvils. Damage localised to culet region. All anvils have a* 3 mm *culet,* 18 mm *outer diameter, and* 30° *taper angle, and were loaded parallel to the c-axis. This form of failure is seen with all anvil materials tried (TiZr, Al, soft BeCu, hard BeCu) to some extent.*

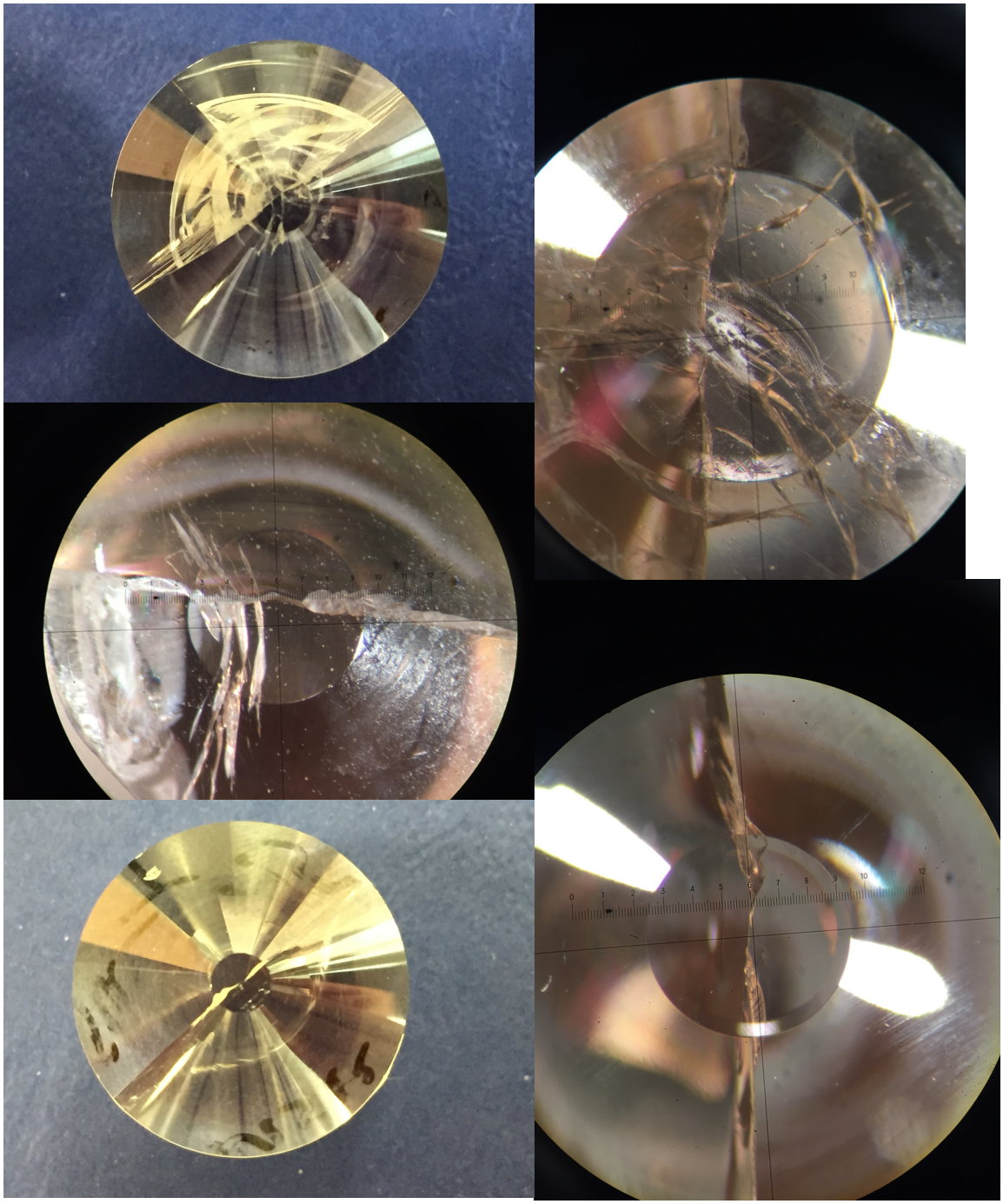

Figure D.2 *Type 2 failure observed in sapphire anvils. Extensive damage to bulk of anvil. All anvils have a* 3 mm *culet,* 18 mm *outer diameter, and* 30° *taper angle, and were loaded parallel to the c-axis. Less common mode of failure, usually occurs during extensive deformation of harder gasket materials.*

Appendix E

Technical drawings for neutron piston-cylinder cell

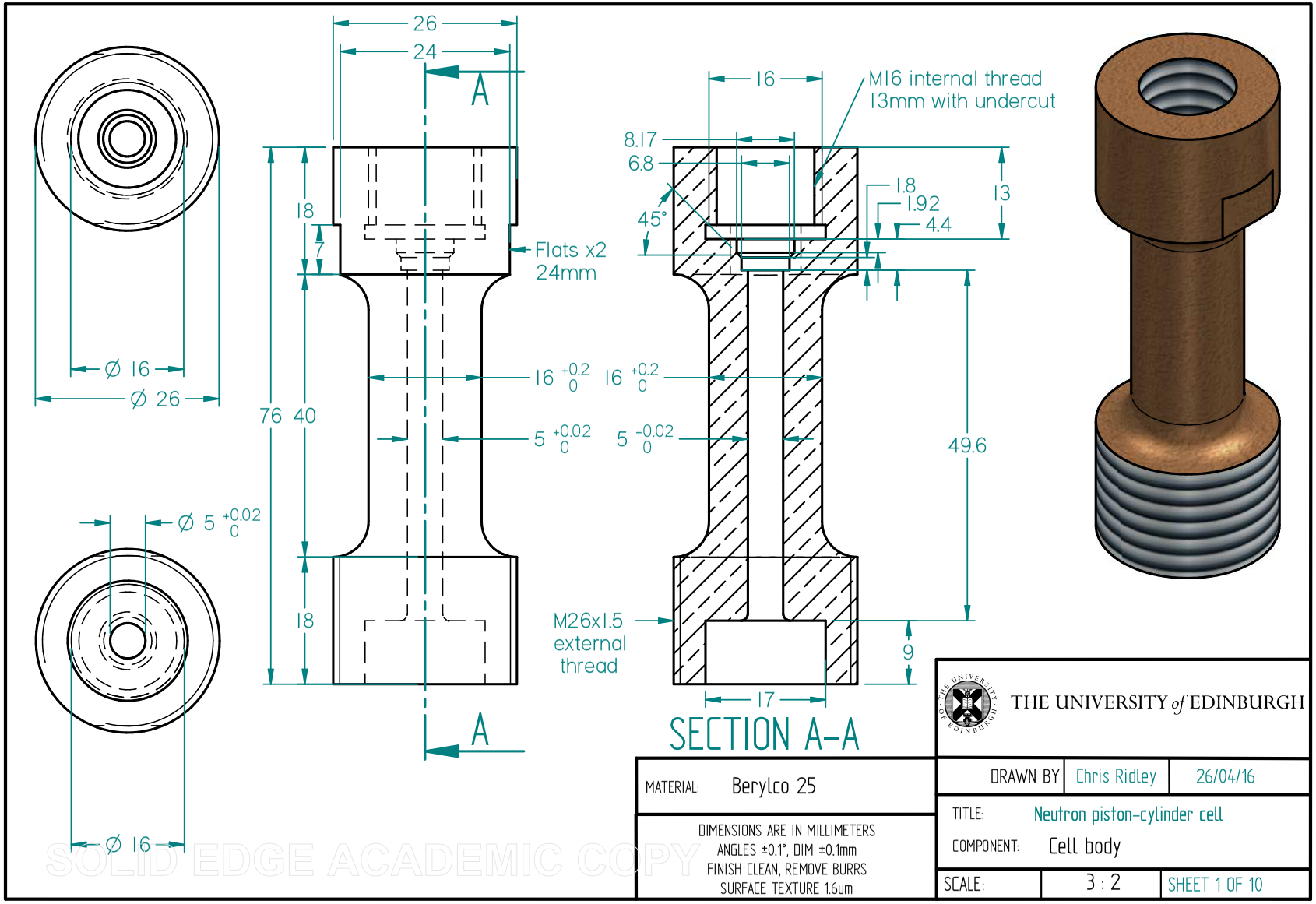

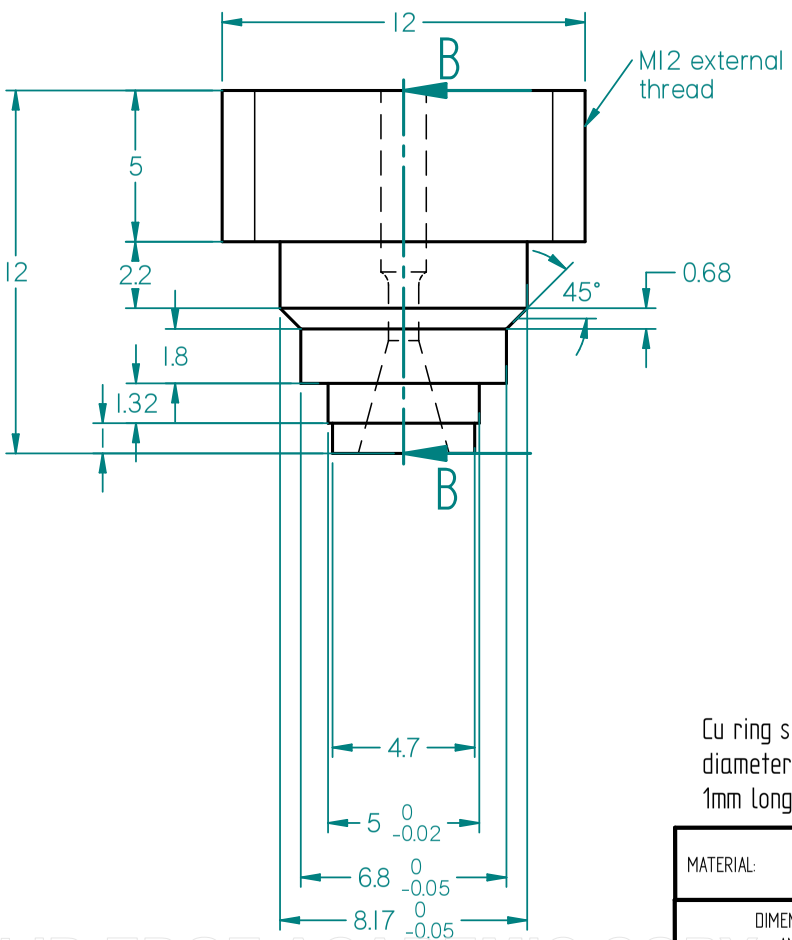

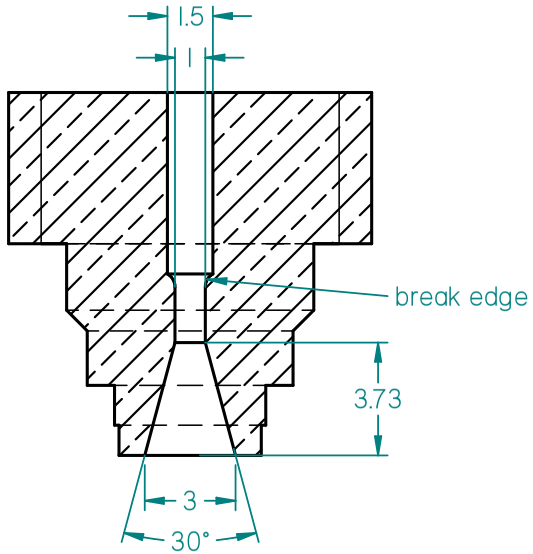

SECTION B–B

Cu ring seal, 8mm outer diameter, 0.6mm wall thickness, 1mm long (BES Ltd.)

THE UNIVERSITY of EDINBURGH

MATERIAL: Berylco 25	DRAWN BY	Chris Ridley 26/04/16
DIMENSIONS ARE IN MILLIMETERS ANGLES ±0.1°, DIM ±0.1mm FINISH CLEAN, REMOVE BURRS SURFACE TEXTURE 1.6um	TITLE:	Neutron piston-cylinder cell
	COMPONENT:	Plug -part A
	SCALE: 5 : 1	SHEET 2 OF 10

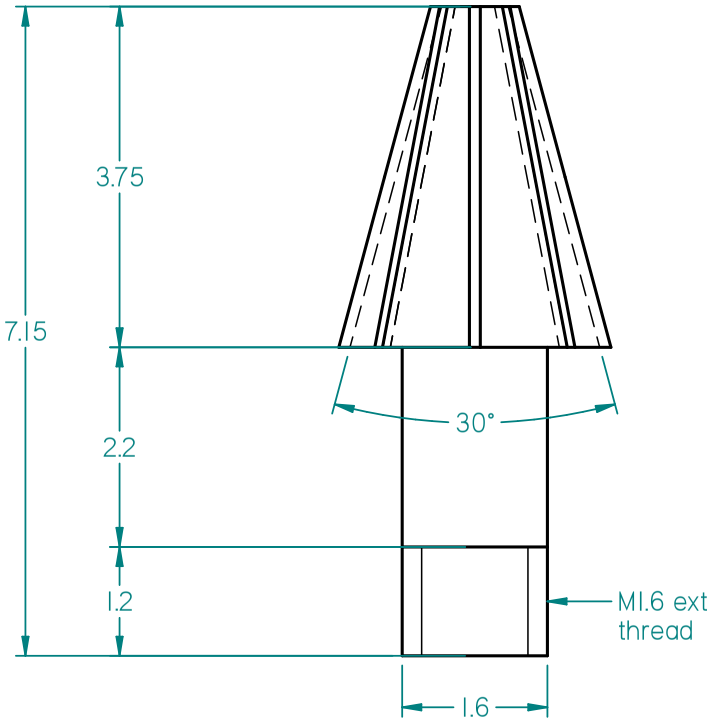

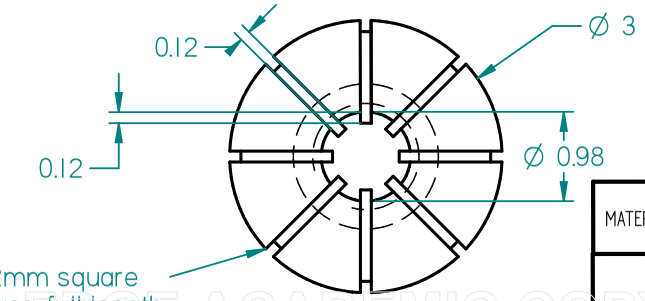

0.1mm diameter Polyimide-ML insulated wire
(Advent RM)

THE UNIVERSITY of EDINBURGH

MATERIAL: Berylco 25	DRAWN BY	Chris Ridley 26/04/16
DIMENSIONS ARE IN MILLIMETERS ANGLES ±0.1°, DIM ±0.1mm FINISH CLEAN, REMOVE BURRS SURFACE TEXTURE 1.6um	TITLE:	Neutron piston-cylinder cell
	COMPONENT:	Plug -part B
	SCALE: 15 : 1	SHEET 3 OF 10

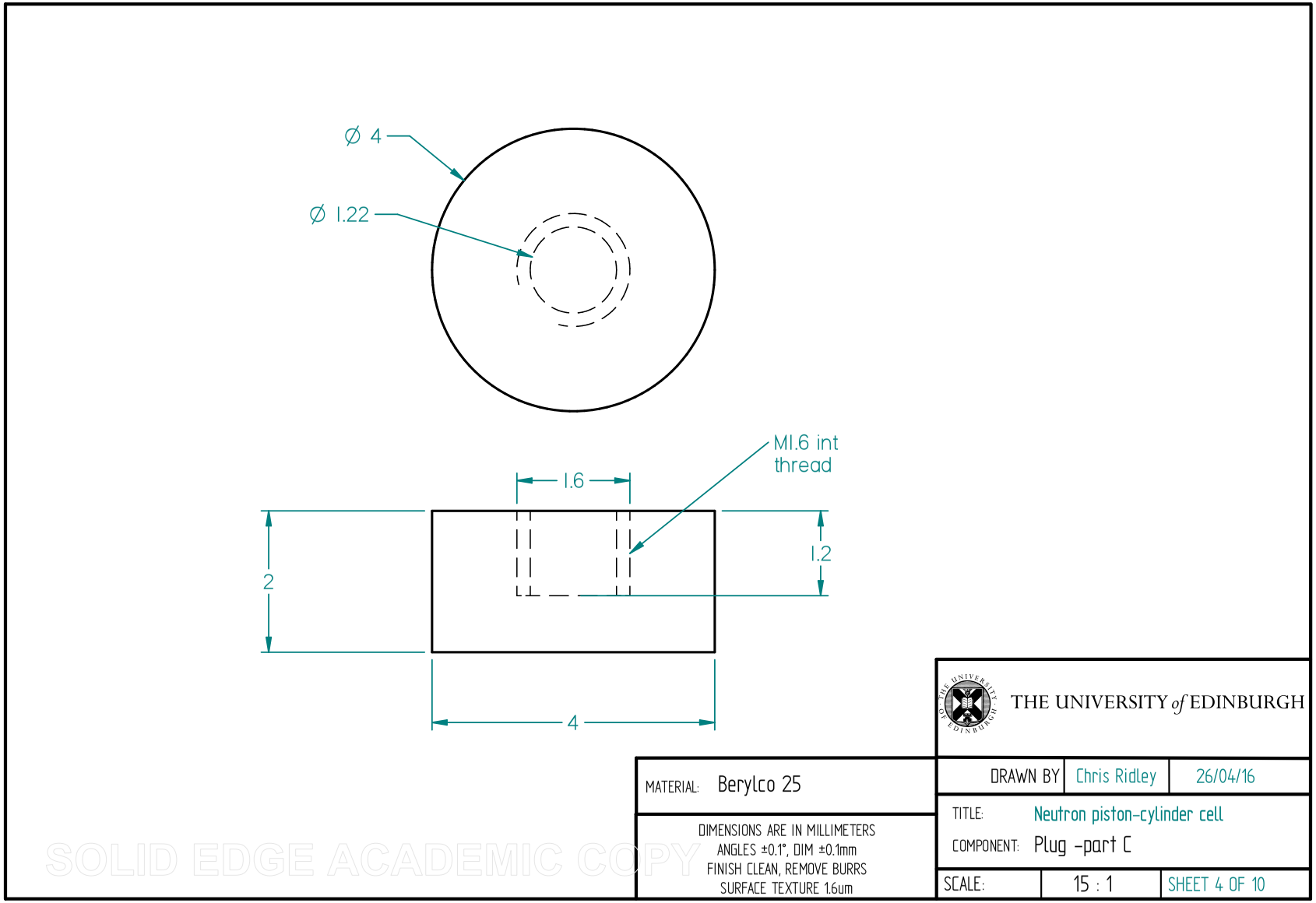

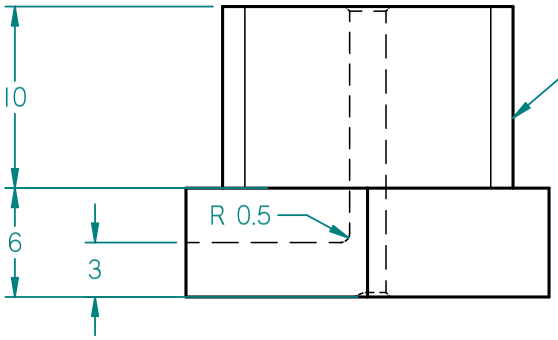

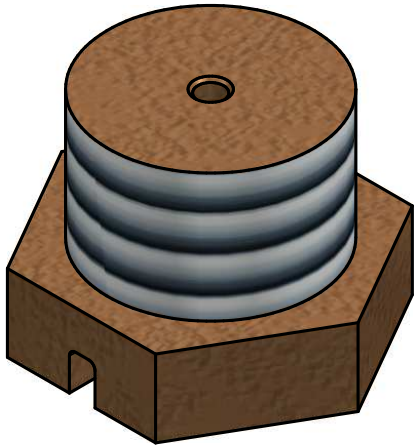

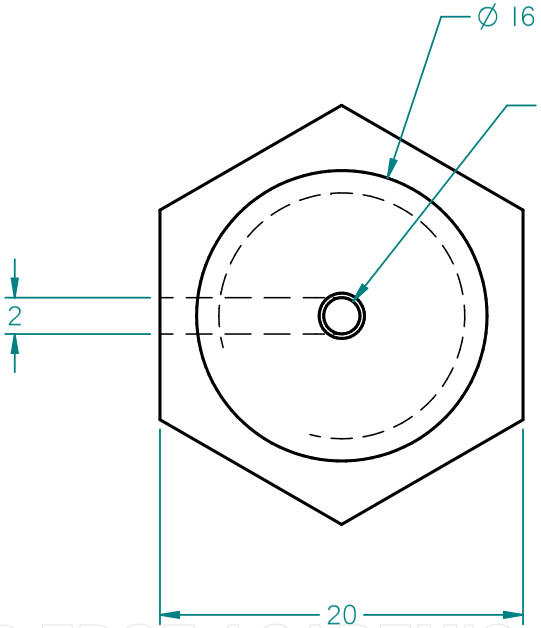

THE UNIVERSITY of EDINBURGH

MATERIAL: Berylco 25	DRAWN BY	Chris Ridley	26/04/16
DIMENSIONS ARE IN MILLIMETERS ANGLES ±0.1°, DIM ±0.1mm FINISH CLEAN, REMOVE BURRS SURFACE TEXTURE 1.6um	TITLE:	Neutron piston-cylinder cell	
	COMPONENT:	End nut - plug	
	SCALE:	3 : 1	SHEET 5 OF 10

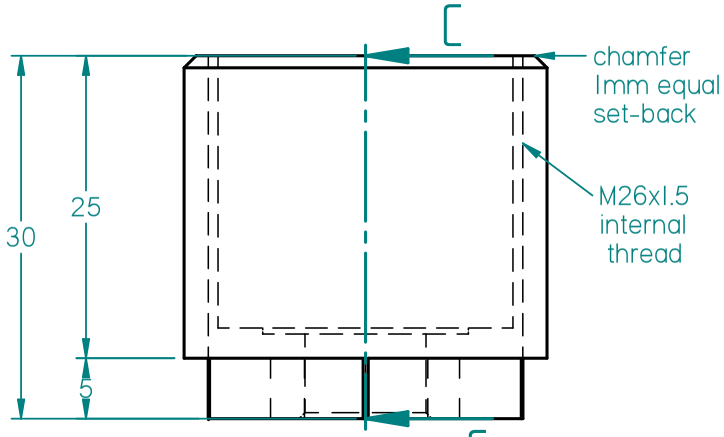

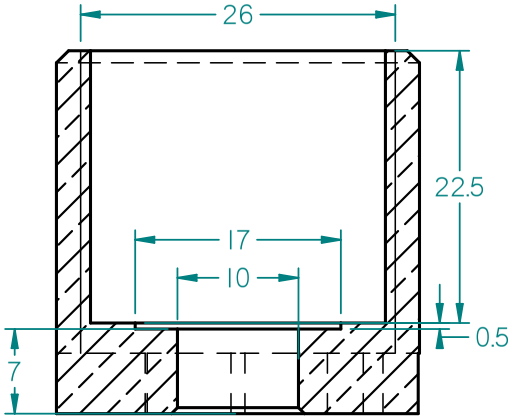

SECTION C-C

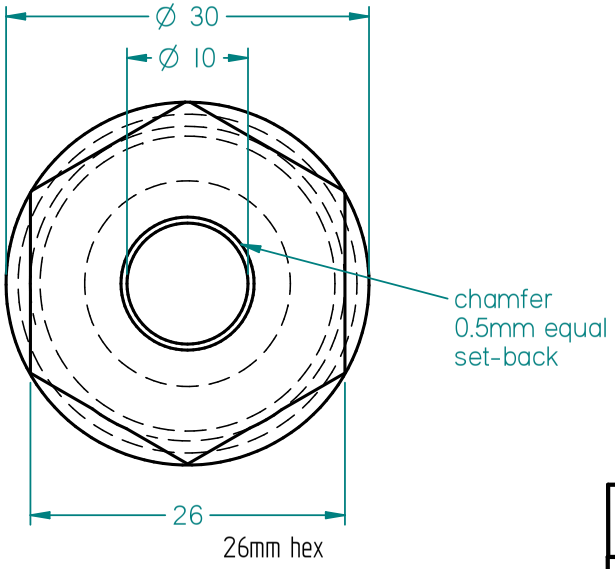

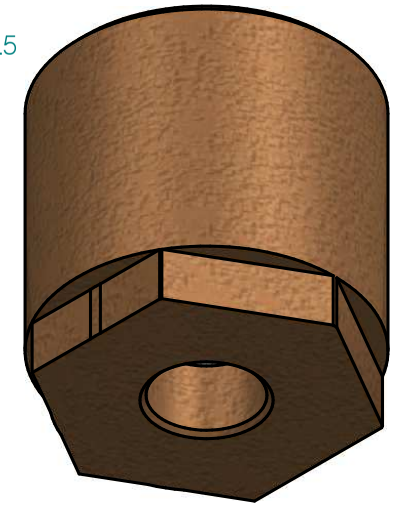

THE UNIVERSITY of EDINBURGH

MATERIAL: Berylco 25	DRAWN BY	Chris Ridley 26/04/16
DIMENSIONS ARE IN MILLIMETERS ANGLES ±0.1°, DIM ±0.1mm FINISH CLEAN, REMOVE BURRS SURFACE TEXTURE 1.6um	TITLE:	Neutron piston-cylinder cell
	COMPONENT:	End nut - piston
	SCALE:	2 : 1
	SHEET 6 OF 10	

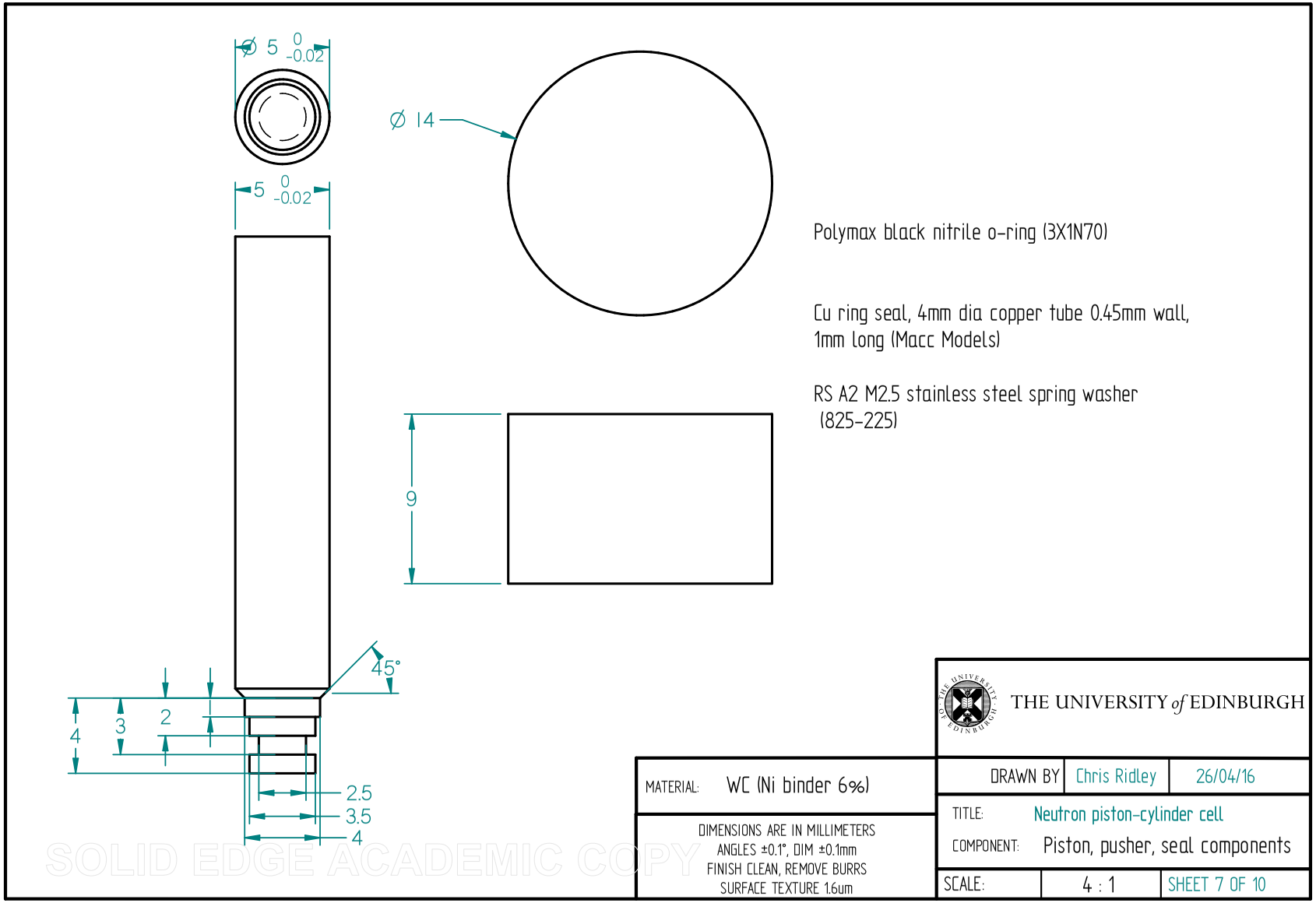

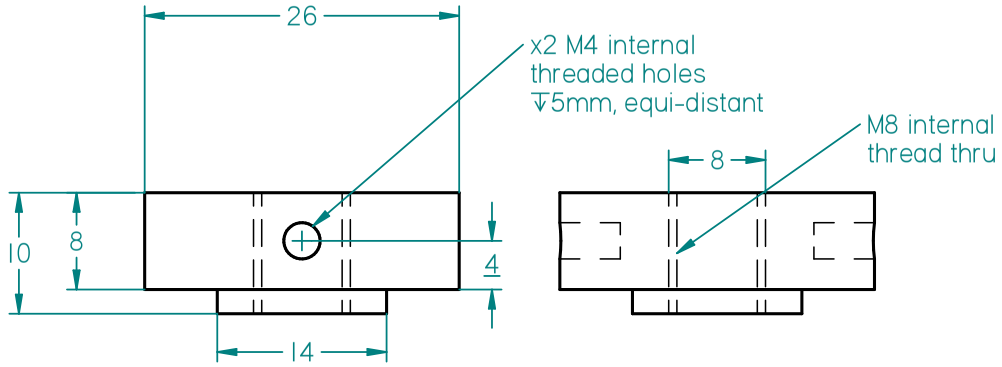

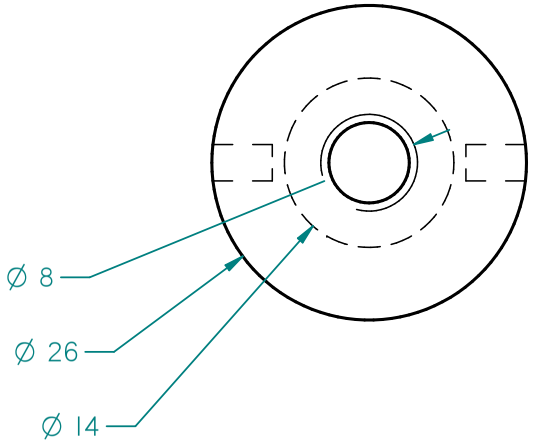

THE UNIVERSITY of EDINBURGH

MATERIAL: Stainless steel	DRAWN BY	Chris Ridley 26/04/16
DIMENSIONS ARE IN MILLIMETERS ANGLES ±0.1°, DIM ±0.1mm FINISH CLEAN, REMOVE BURRS SURFACE TEXTURE 1.6um	TITLE:	Neutron piston-cylinder cell
	COMPONENT:	Plug removal tool – A
	SCALE: 2 : 1	SHEET 8 OF 10

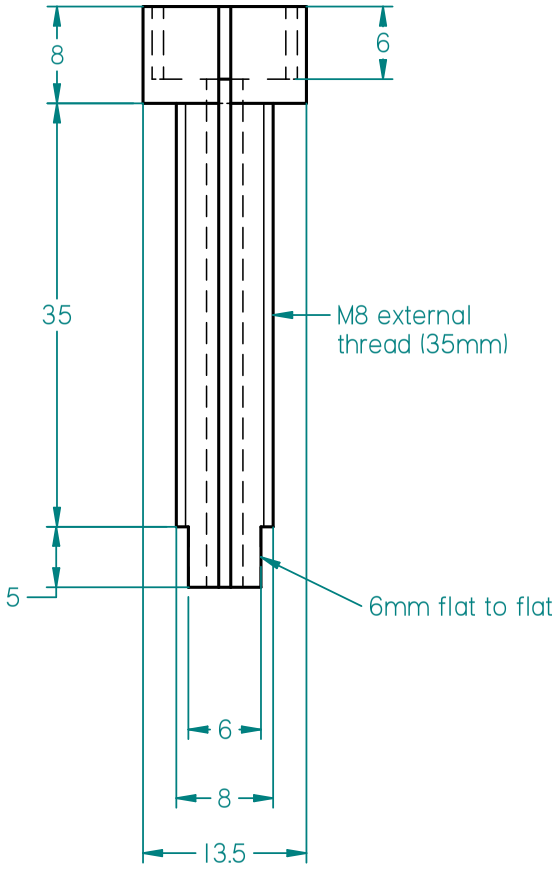

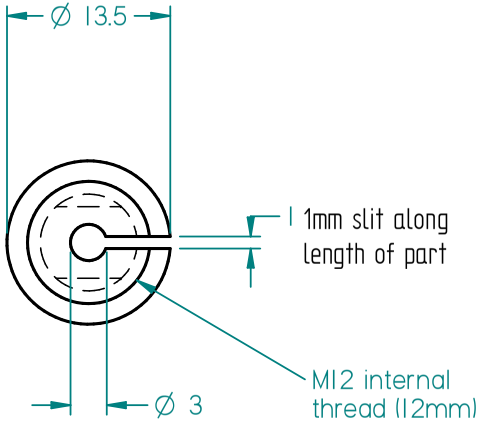

THE UNIVERSITY of EDINBURGH

MATERIAL: Stainless steel	DRAWN BY	Chris Ridley 26/04/16
DIMENSIONS ARE IN MILLIMETERS ANGLES ±0.1°, DIM ±0.1mm FINISH CLEAN, REMOVE BURRS SURFACE TEXTURE 1.6um	TITLE:	Neutron piston-cylinder cell
	COMPONENT:	Plug removal tool - B
	SCALE: 2 : 1	SHEET 9 OF 10

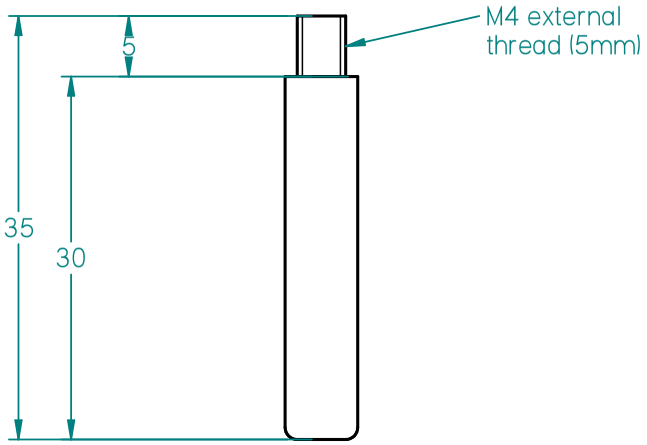

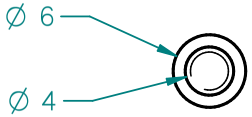

BREAK ALL EDGES

MATERIAL: Stainless steel - 2 of.		THE UNIVERSITY of EDINBURGH	
	DRAWN BY	Chris Ridley	26/04/16
DIMENSIONS ARE IN MILLIMETERS ANGLES ±0.1°, DIM ±0.1mm FINISH CLEAN, REMOVE BURRS SURFACE TEXTURE 1.6um	TITLE:	Neutron piston-cylinder cell	
	COMPONENT:	Plug removal tool - C	
	SCALE:	2 : 1	SHEET 10 OF 10

Appendix F

Technical drawings of spherical pressure cell & rotator mechanism

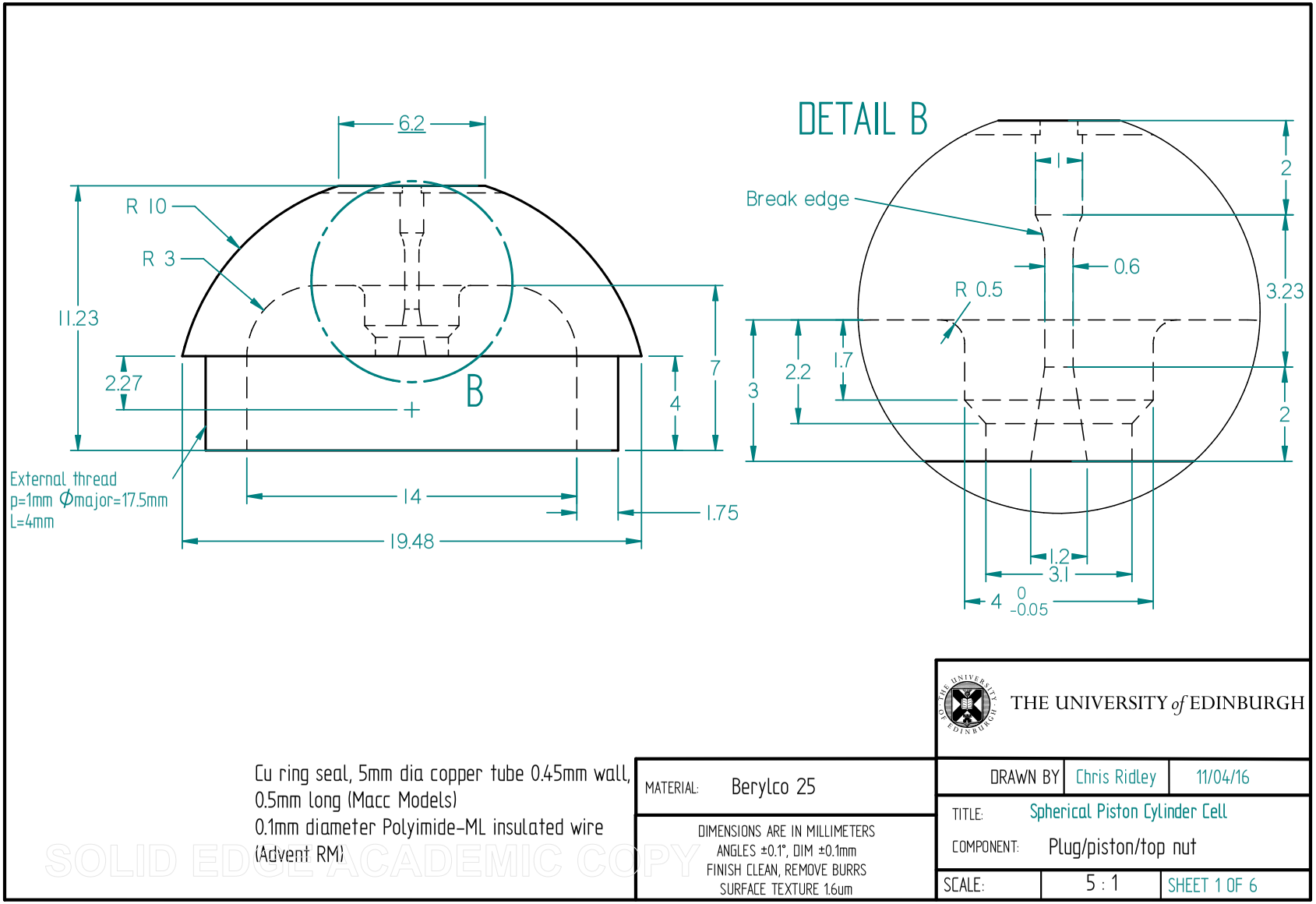

Cu ring seal, 5mm dia copper tube 0.45mm wall, 0.5mm long (Macc Models)
0.1mm diameter Polyimide-ML insulated wire (Advent RM)

MATERIAL: Berylco 25		DRAWN BY	Chris Ridley	11/04/16
DIMENSIONS ARE IN MILLIMETERS ANGLES ±0.1°, DIM ±0.1mm FINISH CLEAN, REMOVE BURRS SURFACE TEXTURE 1.6um		TITLE:	Spherical Piston Cylinder Cell
		COMPONENT:	Plug/piston/top nut
		SCALE:	5 : 1	SHEET 1 OF 6

THE UNIVERSITY of EDINBURGH

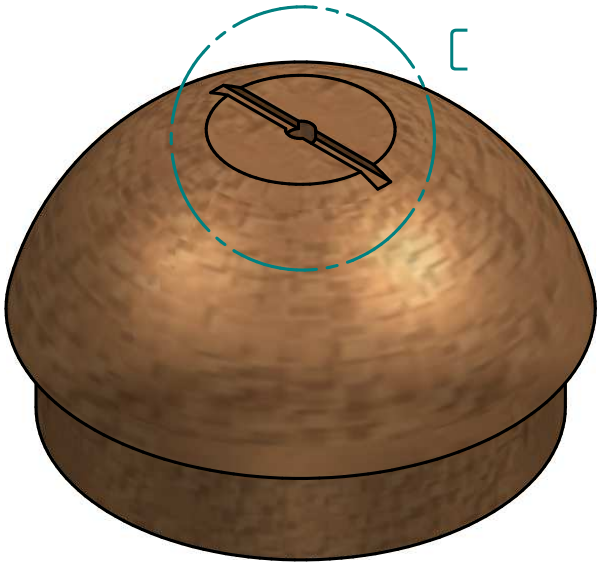

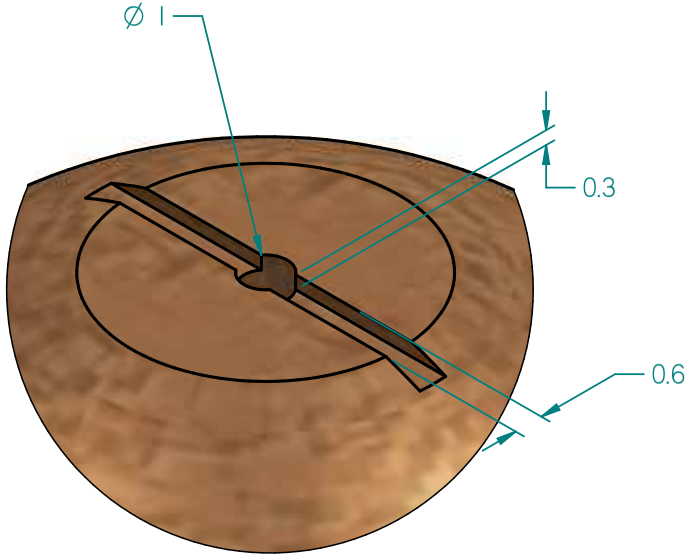

DETAIL C

THE UNIVERSITY of EDINBURGH

MATERIAL: Berylco 25	DRAWN BY: Chris Ridley	11/04/16
DIMENSIONS ARE IN MILLIMETERS ANGLES ±0.1°, DIM ±0.1mm FINISH CLEAN, REMOVE BURRS SURFACE TEXTURE 1.6um	TITLE: Spherical Piston Cylinder Cell COMPONENT: Outer detail – Plug/piston/top nut	
	SCALE: 5 : 1	SHEET 2 OF 6

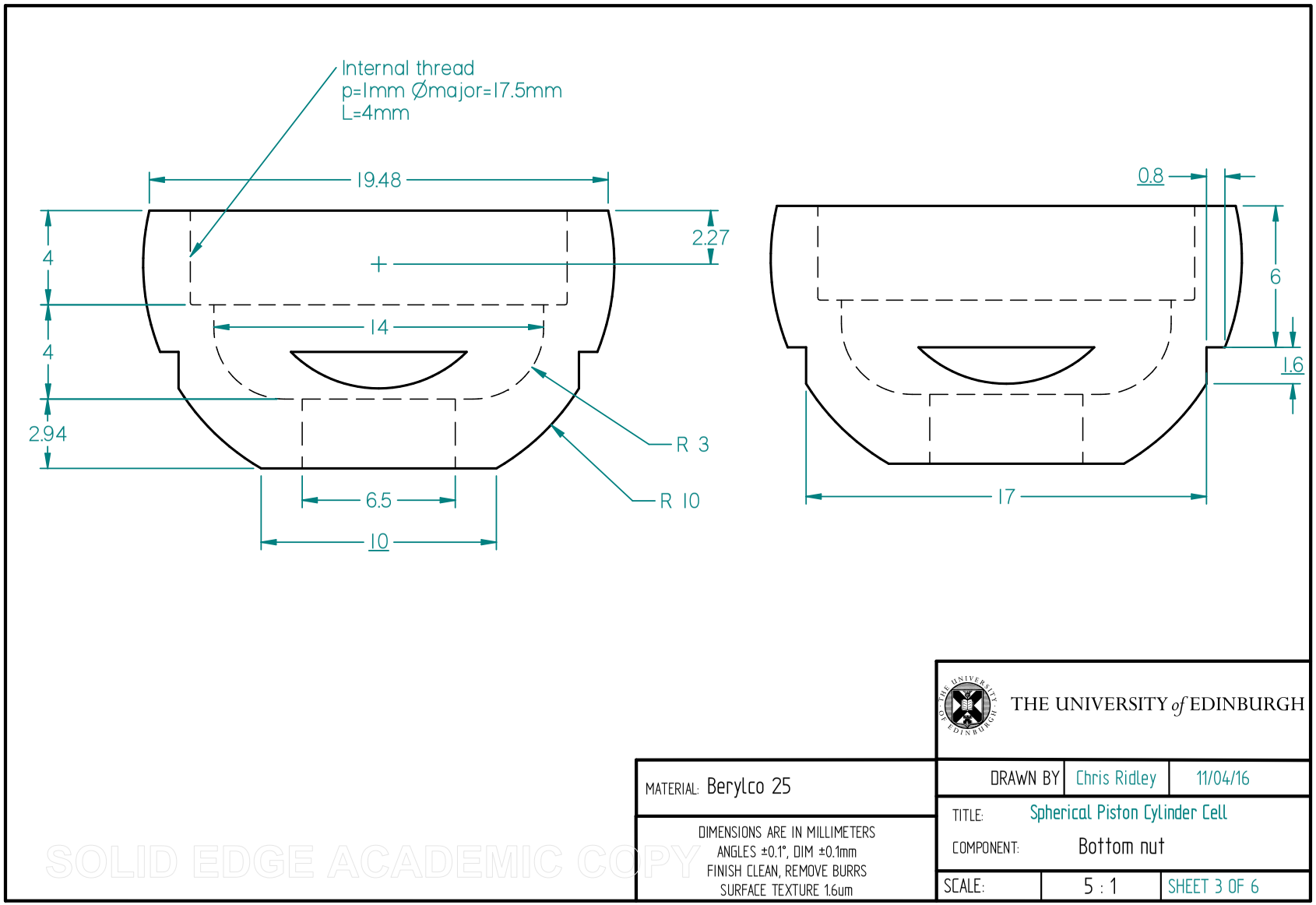

THE UNIVERSITY of EDINBURGH

MATERIAL: Berylco 25	DRAWN BY: Chris Ridley	11/04/16
DIMENSIONS ARE IN MILLIMETERS ANGLES ±0.1°, DIM ±0.1mm FINISH CLEAN, REMOVE BURRS SURFACE TEXTURE 1.6um	TITLE: Spherical Piston Cylinder Cell COMPONENT: Bottom nut	
	SCALE: 5 : 1	SHEET 3 OF 6

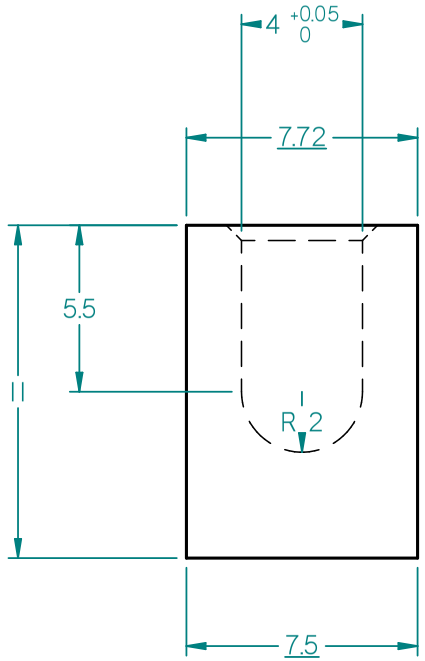

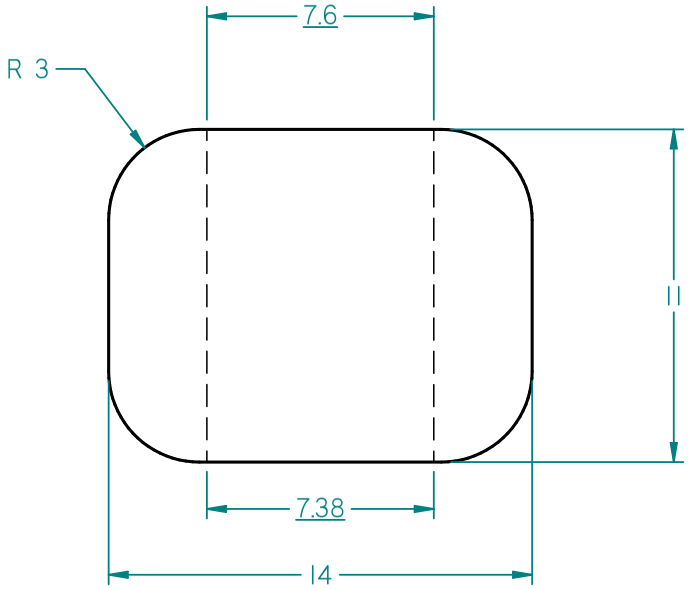

THE UNIVERSITY of EDINBURGH

MATERIAL: Berylco 25	DRAWN BY: Chris Ridley	11/04/16
DIMENSIONS ARE IN MILLIMETERS ANGLES ±0.1°, DIM ±0.1mm FINISH CLEAN, REMOVE BURRS SURFACE TEXTURE 1.6um	TITLE: Spherical Piston Cylinder Cell COMPONENT: Cylinder	
	SCALE: 5 : 1	SHEET 4 OF 6

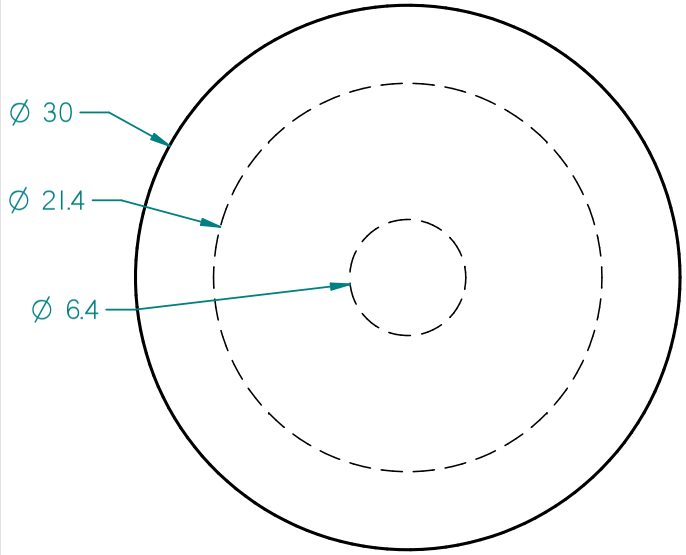

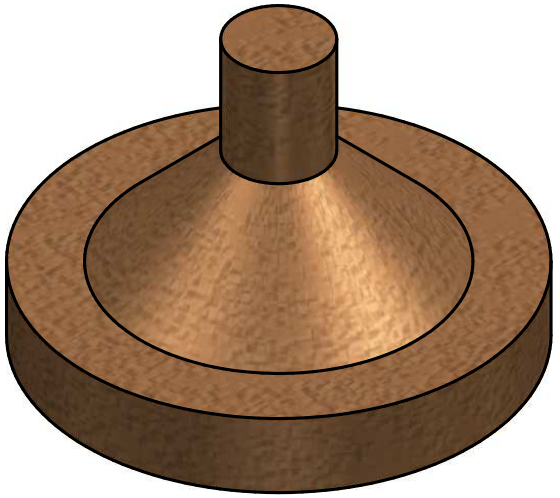

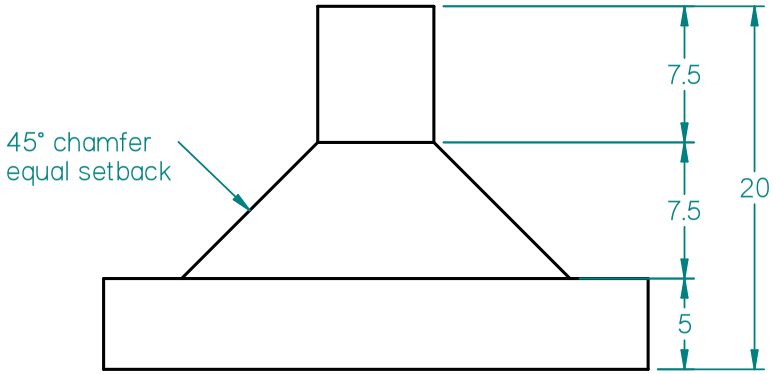

Chamfer all edges 0.25mm x 45°
unless specified otherwise

THE UNIVERSITY of EDINBURGH

MATERIAL: Berylco 25	DRAWN BY	Chris Ridley 11/04/16
DIMENSIONS ARE IN MILLIMETERS ANGLES ±0.1°, DIM ±0.1mm FINISH CLEAN, REMOVE BURRS SURFACE TEXTURE 1.6um	TITLE:	Spherical Piston Cylinder Cell
	COMPONENT:	Pusher tool
	SCALE: 3 : 1	SHEET 5 OF 6

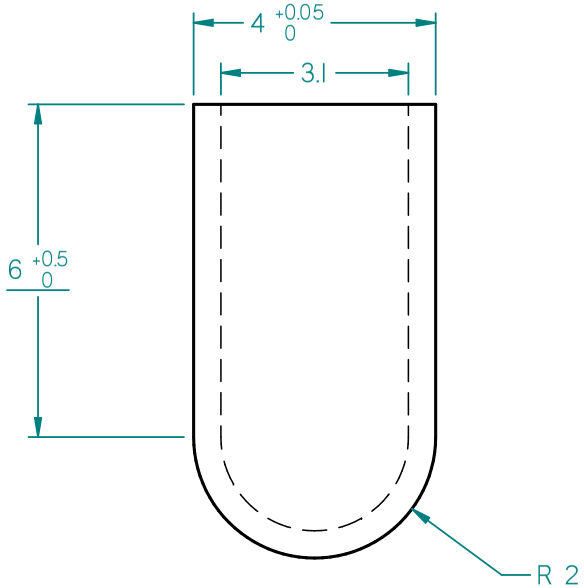

Teflon

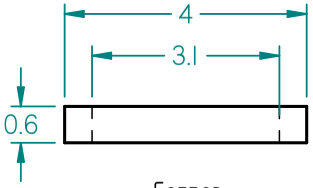

Copper

THE UNIVERSITY of EDINBURGH

MATERIAL: As indicated	DRAWN BY: Chris Ridley	11/04/16
DIMENSIONS ARE IN MILLIMETERS ANGLES ±0.1°, DIM ±0.1mm FINISH CLEAN, REMOVE BURRS SURFACE TEXTURE 1.6um	TITLE: Spherical Piston Cylinder Cell COMPONENT: Teflon sample capsule and Cu seal	
	SCALE: 10: 1	SHEET 6 OF 6

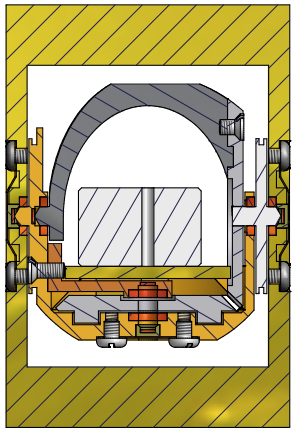

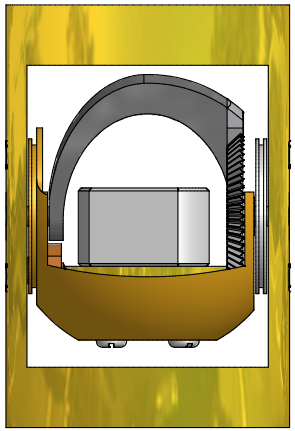

C-C (1 : 1)

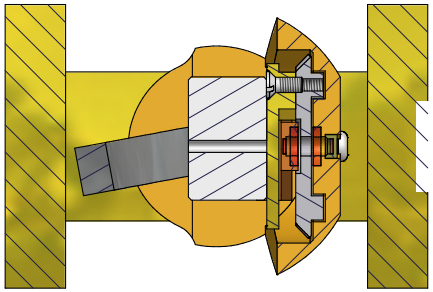

F-F (1 : 1)

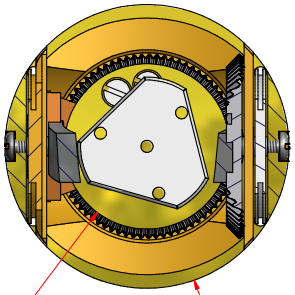

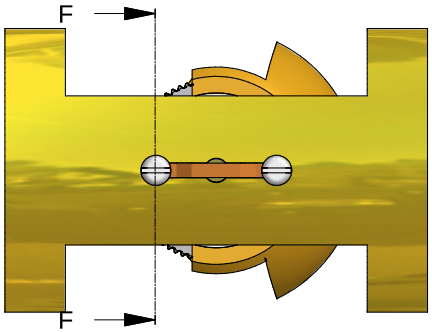

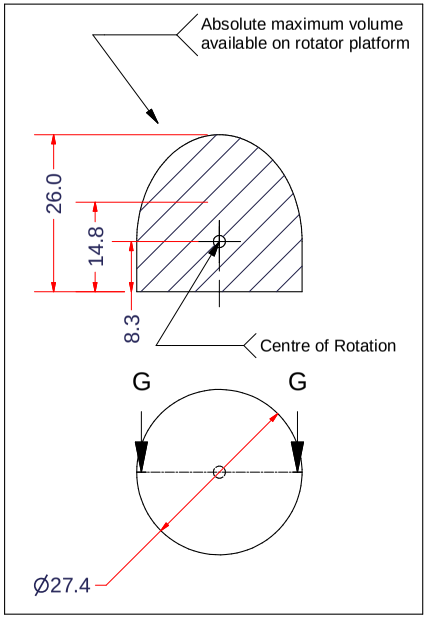

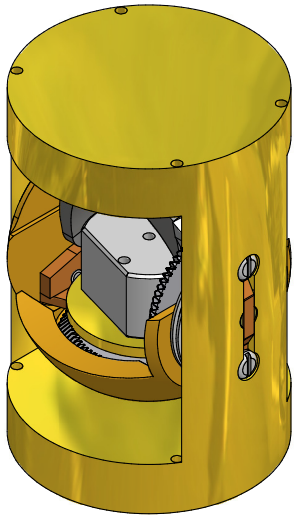

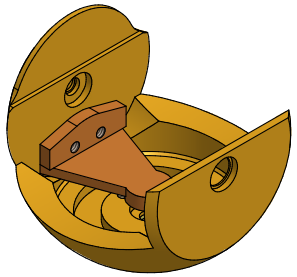

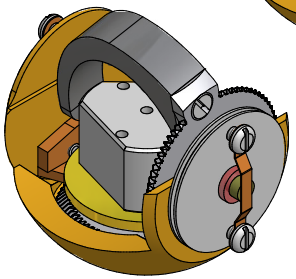

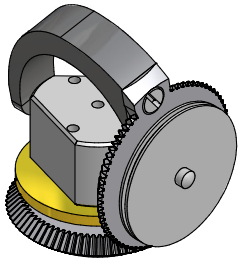

DRAWING No. Rotator ga		CRYOGENIC LTD	
SHEET 1 OF 1	FIRST DRAFT: 21/11/2013 THIS DRAFT: 25/11/2013		
STD.PART No.		MATERIAL SPECIFICATION	CUSTOM FINISH
THIRD ANGLE PROJECTION		DR rotator	
THIS DRAWING BELONGS TO CRYOGENIC LTD AND IS ISSUED ON THE CONDITION THAT IT IS NOT COPIED, REPRINTED OR DISCLOSED EITHER IN WHOLE OR IN PART TO A THIRD PARTY WITHOUT THE PRIOR CONSENT OF: CRYOGENIC LTD, ACTON PARK IND. ESTATE, THE VALE, LONDON W3 7QE		DIMENSION MM / TOLERANCE (UNLESS STATED) ± 0.1 / JOB NUMBER 3611	
14:48:30		DRAWN BY: JW / REVIEWED BY: / QUANTITY 1	

Bibliography

[1] M. L. Winterrose, M. S. Lucas, A. F. Yue *et al.*, "Pressure-induced invar behavior in Pd_3Fe," *Phys. Rev. Lett.*, vol. 102, p. 237202, Jun 2009.

[2] C. J. Ridley, M. K. Jacobsen, and K. V. Kamenev, "A finite-element study of sapphire anvils for increased sample volumes," *High Pressure Research*, vol. 35, no. 2, pp. 148–161, 2015.

[3] C. J. Ridley, P. Manuel, D. Khalyavin *et al.*, "A novel compact three-dimensional laser-sintered collimator for neutron scattering," *Review of Scientific Instruments*, vol. 86, no. 9, 2015.

[4] M. K. Jacobsen, C. J. Ridley, A. Bocian *et al.*, "High-pressure cell for neutron diffraction with in situ pressure control at cryogenic temperatures," *Review of Scientific Instruments*, vol. 85, no. 4, 2014.

[5] C. J. Ridley and K. V. Kamenev, "High pressure neutron and x-ray diffraction at low temperatures," *Zeitschrift für Kristallographie–Crystalline Materials*, vol. 229, no. 3, pp. 171–199, 2014.

[6] M. W. Kepa, C. J. Ridley, K. V. Kamenev *et al.*, "Piston cylinder cell for high pressure ultrasonic pulse echo measurements," *Review of Scientific Instruments*, vol. 87, no. 8, p. 085103, 2016.

[7] F. Bundy, "Designing tapered anvil apparatus for achieving higher pressures," *Review of Scientific Instruments*, vol. 48, no. 6, pp. 591–596, 1977.

[8] STFC, ISIS neutron facility, Sample Environment, "Orange cryostat operating instructions," http://www.isis.stfc.ac.uk/sample-environment/low-temperature/cryostats/files/orange-cryostat-operating-procedures11594.pdf, accessed: March 2016.

[9] R. Down, *Private communication*, ISIS neutron facility, cryogenics section, 2016.

[10] STFC, ISIS neutron facility, Sample Environment, "Low temperature dilution fridges," http://www.isis.stfc.ac.uk/sample-environment/low-temperature/dilution-refrigerators/dilution-refrigerators8825.html, accessed: March 2016.

[11] R. Tarumi, H. Ledbetter, H. Ogi *et al.*, "Low-temperature elastic constants of monocrystal corundum ($\alpha - Al_2O_3$)," *Philosophical Magazine*, vol. 93, no. 36, pp. 4532–4543, 2013.

[12] P. W. Bridgman *et al.*, "Physics of high pressure," 1952.

[13] A. Katrusiak and P. McMillan, *High-pressure crystallography*. Springer Science & Business Media, 2004, vol. 140.

[14] L. Dubrovinsky, N. Dubrovinskaia, E. Bykova *et al.*, "The most incompressible metal osmium at static pressures above 750 gigapascals," *Nature*, vol. 525, no. 7568, pp. 226–229, 2015.

[15] J. Tuoriniemi and T. Knuuttila, "Nuclear cooling and spin properties of rhodium down to picokelvin temperatures," *Physica B: Condensed Matter*, vol. 280, no. 1, pp. 474–478, 2000.

[16] W. A. Bassett, "Diamond anvil cell, 50th birthday," *High Pressure Research*, vol. 29, no. 2, pp. 163–186, 2009.

[17] M. Eremets, *High Pressure Experimental Methods*, ser. Oxford science publications. Oxford University Press, 1996.

[18] G. E. Bacon, *X-Ray and Neutron Diffraction: The Commonwealth and International Library: Selected Readings in Physics*. Elsevier, 2013.

[19] F. Pobell, *Matter and methods at low temperatures*. Springer Science & Business Media, 2007.

[20] S. Adenwalla, S. Lin, Q. Ran *et al.*, "Phase diagram of UPt_3 from ultrasonic velocity measurements," *Physical review letters*, vol. 65, no. 18, p. 2298, 1990.

[21] W. Cohn, "X-ray investigations at high pressures," *Phys. Rev*, vol. 44, pp. 326–327, 1933.

[22] R. B. Jacobs, "X-ray diffraction of substances under high pressures," *Physical Review*, vol. 54, no. 5, p. 325, 1938.

[23] R. M. Hazen, *The diamond makers*. Cambridge University Press, 1999.

[24] K. Entwistle, *Basic principles of the finite element method*. IOM Communications, 1999.

[25] B. Morosin and J. Schirber, "Low-temperature, high-pressure X-ray cell," *Journal of Applied Crystallography*, vol. 7, no. 2, pp. 295–296, 1974.

[26] H. T. Hall, "Ultra-high-pressure, high-temperature apparatus: the'belt'," *Review of Scientific Instruments*, vol. 31, no. 2, pp. 125–131, 1960.

[27] F. Bundy, "Phase diagrams of silicon and germanium to 200 kbar, 1000 C," *The Journal of Chemical Physics*, vol. 41, no. 12, pp. 3809–3814, 1964.

[28] P. F. McMillan, "New materials from high-pressure experiments," *Nature materials*, vol. 1, no. 1, pp. 19–25, 2002.

[29] D. P. Dobson, J. Mecklenburgh, D. Alfe *et al.*, "A new belt-type apparatus for neutron-based rheological measurements at gigapascal pressures," *High pressure research*, vol. 25, no. 2, pp. 107–118, 2005.

[30] M. v. Zimmermann, R. Nowak, G. Gu *et al.*, "A clamp-type pressure cell for high energy X-ray diffraction," *Review of Scientific Instruments*, vol. 79, no. 3, p. 033906, 2008.

[31] P. W. Bridgman, "Effects of high shearing stress combined with high hydrostatic pressure," *Physical Review*, vol. 48, no. 10, p. 825, 1935.

[32] P. W. Bridgman, "Explorations toward the limit of utilizable pressures," *Journal of Applied Physics*, vol. 12, no. 6, pp. 461–469, 1941.

[33] P. W. Bridgman, "An experimental contribution to the problem of diamond synthesis," *The Journal of Chemical Physics*, vol. 15, no. 2, pp. 92–98, 1947.

[34] P. F. McMillan, "Pressing on: the legacy of percy w. bridgman," *Nature materials*, vol. 4, no. 10, pp. 715–718, 2005.

[35] R. Fitch, T. Slykhouse, and H. Drickamer, "Apparatus for optical studies to very high pressures," *JOSA*, vol. 47, no. 11, pp. 1015–1017, 1957.

[36] S. Klotz, *Techniques in high pressure neutron scattering.* Boca Raton, Florida: CRC Press, Taylor & Francis Group, 2013.

[37] Y. Feng, R. Jaramillo, J. Wang *et al.*, "Invited article: High-pressure techniques for condensed matter physics at low temperature," *Review of Scientific Instruments*, vol. 81, no. 4, 2010.

[38] R. J. Angel, M. Bujak, J. Zhao *et al.*, "Effective hydrostatic limits of pressure media for high-pressure crystallographic studies," *Journal of Applied Crystallography*, vol. 40, no. 1, pp. 26–32, Feb 2007.

[39] S. Klotz, J.-C. Chervin, P. Munsch *et al.*, "Hydrostatic limits of 11 pressure transmitting media," *Journal of Physics D: Applied Physics*, vol. 42, no. 7, p. 075413, 2009.

[40] A. Bocian, C. L. Bull, H. Hamidov *et al.*, "Gas loading apparatus for the Paris-Edinburgh press," *Review of Scientific Instruments*, vol. 81, no. 9, 2010.

[41] N. Tateiwa and Y. Haga, "Evaluations of pressure-transmitting media for cryogenic experiments with diamond anvil cell," *Review of Scientific Instruments*, vol. 80, no. 12, 2009.

[42] B. A. Zakharov and A. F. Achkasov, "A compact device for loading diamond anvil cells with low-boiling pressure-transmitting media," *Journal of Applied Crystallography*, vol. 46, no. 1, pp. 267–269, Feb 2013.

[43] E. H. Abramson, "Melting curves of argon and methane," *High Pressure Research*, vol. 31, no. 4, pp. 549–554, 2011.

[44] K. Syassen, "Ruby under pressure," *High Pressure Research*, vol. 28, no. 2, pp. 75–126, 2008.

[45] J. C. Chervin, B. Canny, and M. Mancinelli, "Ruby-spheres as pressure gauge for optically transparent high pressure cells," *High Pressure Research*, vol. 21, no. 6, pp. 305–314, 2001.

[46] H. Mao, J.-A. Xu, and P. Bell, "Calibration of the ruby pressure gauge to 800 kbar under quasi-hydrostatic conditions," *Journal of Geophysical Research: Solid Earth*, vol. 91, no. B5, pp. 4673–4676, 1986.

[47] S. Dorfman, V. Prakapenka, Y. Meng *et al.*, "Intercomparison of pressure standards (Au, Pt, Mo, MgO, NaCl and Ne) to 2.5 Mbar," *Journal of Geophysical Research: Solid Earth*, vol. 117, no. B8, 2012.

[48] P. Lazzarin and P. Livieri, "Different solutions for stress and strain fields in autofrettaged thick-walled cylinders," *International journal of pressure vessels and piping*, vol. 71, no. 3, pp. 231–238, 1997.

[49] D. S. Tsiklis and T. Scott, "Handbook of techniques in high-pressure research and engineering," *Physics Today*, vol. 23, no. 5, pp. 68–69, 2008.

[50] V. Vullo, *Circular Cylinders and Pressure Vessels: Stress Analysis and Design.* Springer, 2014, vol. 3.

[51] S. P. Timoshenko and J. Goodier, "Theory of elasticity," *International Journal of Bulk Solids Storage in Silos*, vol. 1, no. 4, 2014.

[52] W. R. D. Manning and S. Labrow, *High pressure engineering.* L. Hill, 1971.

[53] M. F. Ashby, R. W. Messler, R. Asthana *et al.*, *Engineering Materials and Processes.* Butterworth-Heinemann, 2009.

[54] D. J. Dunstan, "Theory of the gasket in diamond anvil high-pressure cells," *Review of Scientific Instruments*, vol. 60, no. 12, pp. 3789–3795, 1989.

[55] J. Ekin, *Experimental Techniques for Low-Temperature Measurements: Cryostat Design, Material Properties and Superconductor Critical-Current Testing.* Oxford University Press, 2006.

[56] R. Powell, C. Y. Ho, and P. E. Liley, "Thermal conductivity of selected materials," DTIC Document, Tech. Rep., 1966.

[57] R. J. Corruccini and J. J. Gniewek, "Specific heats and enthalpies of technical solids at low temperatures: A compilation from the literature," National Bureau of Standards, Washington, DC, Tech. Rep., 1960.

[58] R. Berman, F. Simon, and J. Ziman, "The thermal conductivity of diamond at low temperatures," in *Proceedings of the Royal Society of London A: Mathematical, Physical and Engineering Sciences*, vol. 220, no. 1141. The Royal Society, 1953, pp. 171–183.

[59] K. D. Timmerhaus, *Advances in Cryogenic Engineering: Proceedings of the 1972. Cryogenic Engineering Conference. National Bureau of Standards. Boulder, Colorado. August 9–11, 1972.* Springer Science & Business Media, 2013, vol. 18.

[60] R. M. McClintock and H. P. Gibbons, *Mechanical properties of structural materials at low temperatures: a compilation from the literature.* National Bureau of Standards, 1960, vol. 13.

[61] T. S. DeSisto and L. Carr, *Low Temperature Mechanical Properties of 300 Series Stainless Steel and Titanium.* Springer, 1961.

[62] G. L. Squires, *Introduction to the theory of thermal neutron scattering.* Cambridge University Press, 2012.

[63] V. F. Sears, "Neutron scattering lengths and cross sections," *Neutron news*, vol. 3, no. 3, pp. 26–37, 1992.

[64] H. Rauch and W. Waschkowski, "Neutron scattering lengths in ILL neutron data booklet, edited by A.-J. Dianox & G. Lander," 2003.

[65] R. J. Hemley, H.-k. Mao, G. Shen *et al.*, "X-ray imaging of stress and strain of diamond, iron, and tungsten at megabar pressures," *Science*, vol. 276, no. 5316, pp. 1242–1245, 1997.

[66] M. Bruno and K. Dunn, "Stress analysis of a beveled diamond anvil," *Review of scientific instruments*, vol. 55, no. 6, pp. 940–943, 1984.

[67] K.-J. Dunn, "The yield stress of opposed anvils," *Journal of Applied Physics*, vol. 48, no. 5, pp. 1829–1832, 1977.

[68] D. M. Adams and A. C. Shaw, "A computer-aided design study of the behaviour of diamond anvils under stress," *Journal of Physics D: Applied Physics*, vol. 15, no. 9, p. 1609, 1982.

[69] D. M. Adams, A. G. Christy, and A. J. Norman, "Optimization of diamond anvil cell performance by finite element analysis," *Measurement Science and Technology*, vol. 4, no. 3, p. 422, 1993.

[70] N. Novikov, V. Levitas, S. Polotnyak *et al.*, "Numerical method for optimizing the design of a high-pressure apparatus with diamond anvils," *Strength of materials*, vol. 26, no. 4, pp. 294–302, 1994.

[71] W. C. Moss and K. A. Goettel, "Finite element design of diamond anvils," *Applied Physics Letters*, vol. 50, no. 1, pp. 25–27, 1987.

[72] S. Merkel, R. J. Hemley, and H.-k. Mao, "Finite-element modelling of diamond deformation at multi-megabar pressures," *Applied physics letters*, vol. 74, no. 5, pp. 656–658, 1999.

[73] H. Mao and P. Bell, "Generation of static pressures to 1.5 Mbar," *Carnegie Institution of Washington Year Book*, vol. 76, pp. 644–646, 1977.

[74] E. Bourgeat-Lami, J.-F. Chapuis, J. Chastagnier *et al.*, "Overview of the projects recently developed by the advanced neutron environment team at the ILL," *Physica B: Condensed Matter*, vol. 385&386, Part 2, pp. 1303 – 1305, 2006, proceedings of the Eighth International Conference on Neutron Scattering.

[75] S. Klotz, T. Strässle, B. Lebert *et al.*, "High pressure neutron diffraction to beyond 20GPa and below 1.8K using Paris-Edinburgh load frames," *High Pressure Research*, vol. 36, no. 1, pp. 73–78, 2016.

[76] A. J. Streiff, J. C. Zimmerman, L. F. Soule *et al.*, "Purification, purity, and freezing points of 30 hydro-carbons of the api-standard and api-nbs series," *Journal of Research of the National Bureau of Standards*, vol. 41, no. 4, pp. 323–357, 1948.

[77] W. Kuhs, F. Bauer, H. Ahsbahs *et al.*, "Neutron single crystal diffraction on kdp at 20k and 1.7GPa." *The Review of High Pressure Science & Technology*, vol. 7, pp. 307–309, 1998.

[78] V. Glazkov, I. Naumov, V. Somenkov *et al.*, "Superpositional many-detector systems and neutron diffraction of microsamples," *Nuclear Instruments and Methods in Physics Research Section A: Accelerators, Spectrometers, Detectors and Associated Equipment*, vol. 264, no. 23, pp. 367 – 374, 1988.

[79] V. Glazkov, I. Goncharenko, V. Irodova *et al.*, "Neutron diffraction study of molecular deuterium equation of state at high pressures*," *Zeitschrift für Physikalische Chemie*, vol. 163, no. Part 2, pp. 509 – 514, 1989.

[80] I. Goncharenko, "New techniques for high-pressure neutron and x-ray studies," *High Pressure Research*, vol. 27, no. 1, pp. 183 – 188, 2007.

[81] I. Goncharenko and I. Mirebeau, "Magnetic neutron diffraction under very high pressures. study of europium monochalcogenides." *The Review of High Pressure Science & Technology*, vol. 7, pp. 475–480, 1998.

[82] I. Goncharenko, "Neutron diffraction experiments in diamond and sapphire anvil cells," *High Pressure Research*, vol. 24, no. 1, pp. 193 – 204, 2004.

[83] I. Goncharenko, I. Mirebeau, and A. Ochiai, "Magnetic neutron diffraction under pressures up to 43GPa. study of the eux and gdx compounds," *Hyperfine Interactions*, vol. 128, no. 1, pp. 225 – 244, 2000.

[84] I. Goncharenko, I. Mirebeau, P. Molina *et al.*, "Focusing neutrons to study small samples," *Physica B: Condensed Matter*, vol. 234 - 236, pp. 1047 – 1049, 1997, proceedings of the First European Conference on Neutron Scattering.

[85] V. Somenkov, "High-pressure neutron scattering over the ages: In memory of Professor JM Besson and Professor J Rossat-Mignod." *Journal of Physics: Condensed Matter*, vol. 17, no. 40, p. S2991, 2005.

[86] V. Aksenov, A. Balagurov, V. Glazkov *et al.*, "DN-12 time-of-flight high-pressure neutron spectrometer for investigation of microsamples," *Physica B: Condensed Matter*, vol. 265, no. 1 - 4, pp. 258 – 262, 1999.

[87] T. Hattori, A. Sano-Furukawa, H. Arima *et al.*, "Design and performance of high-pressure PLANET beamline at pulsed neutron source at J-PARC," *Nuclear Instruments and Methods in Physics Research Section A: Accelerators, Spectrometers, Detectors and Associated Equipment*, vol. 780, pp. 55 – 67, 2015.

[88] W. Utsumi, "Strategy of high pressure research with neutron at J-PARC," *The Japan Society of High Pressure Science and Technology*, vol. 19, no. 1, pp. 10–14, 2009.

[89] A. Onodera, "Take-off for high-pressure neutron scattering experiment," *The Japan Society of High Pressure Science and Technology*, vol. 14, no. 2, pp. 135–142, 2004.

[90] T. Okuchi and H. Kagi, "High-pressure sciences of hydrogen compounds and expectations for the pulsed neutron source," *The Japan Society of High Pressure Science and Technology*, vol. 17, no. 1, pp. 65–72, 2007.

[91] T. Nagai, H. Arima, T. Okuchi *et al.*, "Introduction of the high pressure neutron diffraction projects in J-PARC," *Review of High Pressure Science and Technology*, vol. 19, no. 1, 2009.

[92] T. Osakabe, H. Yamauchi, and T. Okuchi, "Development of high-pressure technique for single-crystal magnetic neutron diffraction under 10GPa," *Review of High Pressure Science and Technology*, vol. 20, no. 1, 2010.

[93] T. Okuchi, S. Sasaki, Y. Ohno *et al.*, "Powder neutron diffraction using nano-polycrystalline diamond as opposed anvils," *Review of High Pressure Science and Technology*, vol. 20, no. 2, 2010.

[94] K. Furuno, A. Onodera, and S. Kume, "Sapphire-anvil cell for high pressure research," *Japanese journal of applied physics*, vol. 25, no. 8A, p. L646, 1986.

[95] A. Onodera, K. Furuno, Y. Ishii *et al.*, "Sapphire-anvil cell for neutron scattering at high pressure," *Japan Atomic Energy Research Institute - Review*, vol. JP9950100, 1999.

[96] T. Okuchi, S. Sasaki, T. Osakabe *et al.*, "Large-volume static compression using nano-polycrystalline diamond for opposed anvils in compact cells," in *Journal of Physics: Conference Series*, vol. 215, no. 1. IOP Publishing, 2010, p. 012188.

[97] T. Okuchi, M. Yoshida, Y. Ohno *et al.*, "Pulsed neutron powder diffraction at high pressure by a capacity-increased sapphire anvil cell," *High Pressure Research*, vol. 33, no. 4, pp. 777–786, 2013.

[98] T. Okuchi, S. Sasaki, Y. Ohno *et al.*, "Neutron powder diffraction of small-volume samples at high pressure using compact opposed-anvil cells and focused beam," in *Journal of Physics: Conference Series*, vol. 377, no. 1. IOP Publishing, 2012, p. 012013.

[99] R. Boehler, M. Guthrie, J. J. Molaison *et al.*, "Large-volume diamond cells for neutron diffraction above 90GPa," *High Pressure Research*, vol. 33, no. 3, pp. 546–554, 2013.

[100] R. Boehler and K. De Hantsetters, "New anvil designs in diamond-cells," *High Pressure Research*, vol. 24, no. 3, pp. 391–396, 2004.

[101] G. Batey, M. Buehler, M. Cuthbert *et al.*, "Integration of superconducting magnets with cryogen-free dilution refrigerator systems," *Cryogenics*, vol. 49, no. 12, pp. 727–734, 2009.

[102] P. Lisowski, C. Bowman, G. Russell *et al.*, "The los alamos national laboratory spallation neutron sources," *Nuclear Science and Engineering*, vol. 106, no. 2, pp. 208–218, 1990.

[103] S. Janssen, J. Mesot, and R. Hempelmann, "FOCUS: time-of-flight spectrometer for cold neutrons at SINQ," *New Instruments and Seienoe around SINQ*, p. 45, 1996.

[104] J. Ollivier, H. Mutka, and L. Didier, "The new cold neutron time-of-flight spectrometer IN5," *Neutron News*, vol. 21, no. 2, pp. 22–25, 2010.

[105] I. M. Sosnowska, "The birth of time-of-flight (TOF) neutron powder diffraction at pulsed neutron source," *Crystal Research and Technology*, vol. 50, no. 9-10, pp. 705–715, 2015.

[106] M. Arai and K. Crawford, "Neutron sources and facilities," in *Neutron imaging and applications*. Springer, 2009, pp. 13–30.

[107] L. C. Chapon, P. Manuel, P. G. Radaelli *et al.*, "WISH: The new powder and single crystal magnetic diffractometer on the second target station," *Neutron News*, vol. 22, no. 2, pp. 22–25, 2011.

[108] Y. Feng, D. Silevitch, and T. Rosenbaum, "A compact bellows-driven diamond anvil cell for high-pressure, low-temperature magnetic measurements," *Review of Scientific Instruments*, vol. 85, no. 3, p. 033901, 2014.

[109] C. Pfleiderer, E. Bedin, and B. Salce, "He activated loading device for low temperature uniaxial and anvil cell pressure experiments," *Review of Scientific Instruments*, vol. 68, no. 8, pp. 3120–3124, 1997.

[110] R. J. Chen and B. A. Weinstein, "New diamond-anvil cell design for far infrared magneto spectroscopy featuring in-situ cryogenic pressure tuning," *Review of Scientific Instruments*, vol. 67, no. 8, pp. 2883–2889, 1996.

[111] A. W. Webb, D. U. Gubser, and L. C. Towle, "Cryostat for generating pressures to 100 kilobar and temperatures to 0.03K," *Review of Scientific Instruments*, vol. 47, no. 1, pp. 59–62, 1976.

[112] A. Palmer, D. M. Silevitch, Y. Feng *et al.*, "Sub-kelvin magnetic and electrical measurements in a diamond anvil cell with in situ tunability," *Review of Scientific Instruments*, vol. 86, no. 9, 2015.

[113] W. B. Daniels and M. G. Ryschkewitsch, "Simple double diaphragm press for diamond anvil cells at low temperatures," *Review of Scientific Instruments*, vol. 54, no. 1, pp. 115–116, 1983.

[114] W. M. Howard, "An experimental investigation of pressure gradients due to temperature gradients in small diameter tubes," Ph.D. dissertation, California Institute of Technology, 1955.

[115] D. M. Stefanescu, *Handbook of force transducers: principles and components*. Springer Science & Business Media, 2011.

[116] National Instruments Application Note 078, *Strain Gauge Measurement: A Tutorial*. National Instruments, 1998.

[117] G. Shirane and Y. Yamada, "Lattice-dynamical study of the 110K phase transition in $SrTiO_3$," *Physical Review*, vol. 177, no. 2, p. 858, 1969.

[118] F. W. Lytle, "X-ray diffractometry of low-temperature phase transformations in strontium titanate," *Journal of Applied Physics*, vol. 35, no. 7, pp. 2212–2215, 1964.

[119] A. Hachemi, H. Hachemi, A. Ferhat-Hamida *et al.*, "Elasticity of $SrTiO_3$ perovskite under high pressure in cubic, tetragonal and orthorhombic phases," *Physica Scripta*, vol. 82, no. 2, p. 025602, 2010.

[120] A. Grzechnik, G. H. Wolf, and P. F. McMillan, "Raman scattering study of $SrTiO_3$ at high pressure," *Journal of Raman spectroscopy*, vol. 28, no. 11, pp. 885–889, 1997.

[121] D. Cabaret, B. Couzinet, A. Flank *et al.*, "Ti k pre-edge in $srtio_3$ under pressure: Experiments and full-potential first-principles calculations," *X-Ray Absorption Fine Structure–XAFS 13*, vol. 882, pp. 120–122, 2007.

[122] M. Guennou, P. Bouvier, J. Kreisel *et al.*, "Pressure-temperature phase diagram of $SrTiO_3$ up to 53GPa," *Physical Review B*, vol. 81, no. 5, p. 054115, 2010.

[123] A. Glazer, "Simple ways of determining perovskite structures," *Acta Crystallographica Section A: Crystal Physics, Diffraction, Theoretical and General Crystallography*, vol. 31, no. 6, pp. 756–762, 1975.

[124] M. Guthrie, C. G. Pruteanu, M.-E. Donnelly *et al.*, "Radiation attenuation by single-crystal diamond windows," *Journal of Applied Crystallography*, vol. 50, no. 1, pp. 76–86, 2017.

[125] K. Miyoshi, "Structures and mechanical properties of natural and synthetic diamonds," *Diamond Films and Technology*, vol. 8, pp. 153–172, 1998.

[126] J. Field and C. Pickles, "Strength, fracture and friction properties of diamond," *Diamond and related materials*, vol. 5, no. 6, pp. 625–634, 1996.

[127] R. Telling, C. Pickard, M. Payne *et al.*, "Theoretical strength and cleavage of diamond," *Physical Review Letters*, vol. 84, no. 22, p. 5160, 2000.

[128] J. Whitlock and A. L. Ruoff, "The failure strengths of perfect diamond crystals," *Scripta Metallurgica*, vol. 15, no. 5, pp. 525–529, 1981.

[129] X. Luo, Z. Liu, B. Xu *et al.*, "Compressive strength of diamond from first-principles calculation," *The Journal of Physical Chemistry C*, vol. 114, no. 41, pp. 17 851–17 853, 2010.

[130] M. A. Prelas, G. Popovici, and L. K. Bigelow, *Handbook of industrial diamonds and diamond films*. CRC Press, 1997.

[131] A. Neves and M. H. Nazaré, *Properties, growth and applications of diamond*. IET, 2001, no. 26.

[132] F. Schmid and D. C. Harris, "Effects of crystal orientation and temperature on the strength of sapphire," *Journal of the American Ceramic Society*, vol. 81, no. 4, pp. 885–893, 1998.

[133] E. R. Dobrovinskaya, L. A. Lytvynov, and V. Pishchik, *Sapphire: material, manufacturing, applications*. Springer Science & Business Media, 2009.

[134] A. Azhdari and S. Nemat-Nasser, "Experimental and computational study of fracturing in an anisotropic brittle solid," *Mechanics of Materials*, vol. 28, no. 1, pp. 247–262, 1998.

[135] A. B. Sinani, N. K. Dynkin, L. A. Lytvinov *et al.*, "Sapphire hardness in different crystallographic directions," *Bulletin of the Russian Academy of Sciences: Physics*, vol. 73, no. 10, pp. 1380–1382, 2009.

[136] J. W. Fischer, W. Compton, N. A. Jaeger *et al.*, "Strength of sapphire as a function of temperature and crystal orientation," in *San Dieg-DL Tentative*. International Society for Optics and Photonics, 1990, pp. 11–22.

[137] E. A. Jackman and J. Roberts, "The strength of single crystal and polycrystalline corundum," *The London, Edinburgh, and Dublin Philosophical Magazine and Journal of Science*, vol. 46, no. 378, pp. 809–811, 1955.

[138] R. Gentilman, E. Maguire, H. Starrett *et al.*, "Strength and transmittance of sapphire and strengthened sapphire," *Journal of the American Ceramic Society*, vol. 64, no. 9, 1981.

[139] J. Wachtman and L. Maxwell, "Strength of synthetic single crystal sapphire and ruby as a function of temperature and orientation," *Journal of the American Ceramic Society*, vol. 42, no. 9, pp. 432–433, 1959.

[140] T. Klünsner, S. Wurster, P. Supancic *et al.*, "Effect of specimen size on the tensile strength of WC-Co hard metal," *Acta Materialia*, vol. 59, no. 10, pp. 4244 – 4252, 2011.

[141] A. McKie, J. Winzer, I. Sigalas *et al.*, "Mechanical properties of cBN-Al composite materials," *Ceramics International*, vol. 37, no. 1, pp. 1 – 8, 2011.

[142] K. Liu, X. Li, M. Rahman *et al.*, "cBN tool wear in ductile cutting of tungsten carbide," *Wear*, vol. 255, no. 7, pp. 1344–1351, 2003.

[143] C. A. Klein, "Flexural strength of sapphire: Weibull statistical analysis of stressed area, surface coating, and polishing procedure effects," *Journal of applied physics*, vol. 96, no. 6, pp. 3172–3179, 2004.

[144] G. Dhatt, G. Touzot *et al.*, *Finite element method*. John Wiley & Sons, 2012.

[145] S. M. Wiederhorn, B. J. Hockey, and D. E. Roberts, "Effect of temperature on the fracture of sapphire," *Philosophical Magazine*, vol. 28, no. 4, pp. 783–796, 1973.

[146] J. Fang, C. L. Bull, J. S. Loveday *et al.*, "Strength analysis and optimisation of double-toroidal anvils for high-pressure research," *Review of Scientific Instruments*, vol. 83, no. 9, 2012.

[147] F. Mujika, "On the difference between flexural moduli obtained by three-point and four-point bending tests," *Polymer testing*, vol. 25, no. 2, pp. 214–220, 2006.

[148] P. Shipway and I. Hutchings, "Fracture of brittle spheres under compression and impact loading. ii. results for lead-glass and sapphire spheres," *Philosophical Magazine A*, vol. 67, no. 6, pp. 1405–1421, 1993.

[149] E. Lajtai, B. Carter, and M. Ayari, "Criteria for brittle fracture in compression," *Engineering Fracture Mechanics*, vol. 37, no. 1, pp. 59–74, 1990.

[150] N. E. Dowling, *Mechanical behavior of materials*. Pearson, 2012.

[151] J. Clayton, "A continuum description of nonlinear elasticity, slip and twinning, with application to sapphire," in *Proceedings of the Royal Society of London A: Mathematical, Physical and Engineering Sciences*, vol. 465, no. 2101. The Royal Society, 2009, pp. 307–334.

[152] D. J. Green, *An introduction to the mechanical properties of ceramics*. Cambridge University Press, 1998.

[153] D. Dunstan, "Recent developments in diamond-anvil cells," in *High Pressure Chemistry, Biochemistry and Materials Science*. Springer, 1993, pp. 79–99.

[154] S. Qiu, J. Yu, G. Zhu *et al.*, "Strategies for the synthesis of large zeolite single crystals," *Microporous and Mesoporous Materials*, vol. 21, no. 4–6, pp. 245 – 251, 1998.

[155] J. R. Santisteban, M. R. Daymond, J. A. James *et al.*, "ENGIN-X: a third-generation neutron strain scanner," *Journal of Applied Crystallography*, vol. 39, no. 6, pp. 812–825, Dec 2006.

[156] C. Carlile, P. Hey, and B. Mack, "High-efficiency soller slit collimators for thermal neutrons," *Journal of Physics E: Scientific Instruments*, vol. 10, no. 5, p. 543, 1977.

[157] C. Petrillo, E. Guarini, F. Formisano *et al.*, "A honeycomb collimator for the neutron brillouin scattering spectrometer BRISP," *Nuclear Instruments and Methods in Physics Research Section A: Accelerators, Spectrometers, Detectors and Associated Equipment*, vol. 489, no. 13, pp. 304 – 312, 2002.

[158] J.-L. Mutz, O. Bonnet, R. Fairbend *et al.*, "Micro-pore optics: from planetary X-rays to industrial market," in *Integrated Optoelectronic Devices 2007*. International Society for Optics and Photonics, 2007, pp. 64 790F–64 790F.

[159] A. S. Tremsin, D. F. Mildner, W. B. Feller *et al.*, "Very compact high performance microchannel plate neutron collimators," in *Nuclear Science Symposium Conference Record, 2003 IEEE*, vol. 1. IEEE, 2003, pp. 503–507.

[160] S. W. Wilkins, A. W. Stevenson, K. A. Nugent *et al.*, "On the concentration, focusing, and collimation of x-rays and neutrons using microchannel plates and configurations of holes," *Review of Scientific Instruments*, vol. 60, no. 6, pp. 1026–1036, 1989.

[161] M. Zhong, W. Liu, G. Ning *et al.*, "Laser direct manufacturing of tungsten nickel collimation component," *Journal of Materials Processing Technology*, vol. 147, no. 2, pp. 167 – 173, 2004.

[162] X. Yan and P. Gu, "A review of rapid prototyping technologies and systems," *Computer-Aided Design*, vol. 28, no. 4, pp. 307 – 318, 1996.

[163] M. Agarwala, D. Bourell, J. Beaman *et al.*, "Direct selective laser sintering of metals," *Rapid Prototyping Journal*, vol. 1, no. 1, pp. 26–36, 1995.

[164] Oracle, "JAVA SE, version 1.8.0," https://www.oracle.com/java/index.html, accesed August 2015.

[165] K. Lefmann and K. Nielsen, "Mcstas, a general software package for neutron ray-tracing simulations," *Neutron News*, vol. 10, no. 3, pp. 20–23, 1999.

[166] P. Andersen, K. Lefmann, L. T. Kuhn *et al.*, "Monte carlo simulations as a part of the configuration for neutron instruments," *Physica B: Condensed Matter*, vol. 350, no. 1–3, Supplement, pp. E721 – E724, 2004, proceedings of the Third European Conference on Neutron Scattering.

[167] D.-Q. Wang, X.-L. Wang, J. L. Robertson *et al.*, "Modeling radial collimators for use in stress and texture measurements with neutron diffraction," *Journal of Applied Crystallography*, vol. 33, no. 2, pp. 334–337, Apr 2000.

[168] A. Perin, R. Macisa Jareño, and L. Metral, "Study of materials and adhesives for superconducting cable feedthroughs," *LHC Project Report*, no. 504, pp. 1–8, 2001.

[169] K. J. Froelich and C. M. Fitzpatrick, "Lap shear strength of selected adhesives (epoxy, varnish, b-stage glass cloth) in liquid nitrogen and at room temperature," *Fusion Energy Division*, no. ORNL/TM-5658, pp. 1–20, 1976.

[170] Henkel, *Stycast 2850 FT and Catalyst 24 LV technical data.* Emerson & Cumming Ltd., 2015.

[171] J. Kamarád, *Private communication*, 2016.

[172] I. R. Walker, "Nonmagnetic piston-cylinder pressure cell for use at 35 kbar and above," *Review of Scientific Instruments*, vol. 70, no. 8, pp. 3402–3412, 1999.

[173] L. H. Dmowski and E. Litwin-Staszewska, "The variation of the pressure coefficient of manganin sensors at low temperatures," *Measurement Science and Technology*, vol. 10, no. 5, p. 343, 1999.

[174] B. Lüthi, "Ultrasonics at magnetic phase transitions," *Physical Acoustics in the Solid State*, pp. 93–108, 2005.

[175] M. Gauthier, D. Lheureux, F. Decremps *et al.*, "High-pressure ultrasonic setup using the Paris–Edinburgh press: Elastic properties of single crystalline germanium up to 6 GPa," *Review of scientific instruments*, vol. 74, no. 8, pp. 3712–3716, 2003.

[176] J. Chen, Y. Wang, S. Duffy *et al.*, *Advances in high-pressure techniques for geophysical applications*. Elsevier, 2011.

[177] O. F. Yagafarov, E. L. Gromnitskaya, A. G. Lyapin *et al.*, "Elastic properties of fullerites C_{60} and C_{70} under pressure," *Journal of Physics: Conference Series*, vol. 215, no. 1, p. 012054, 2010.

[178] S. Saxena, P. Agarwal, K. Ahilan *et al.*, "Superconductivity on the border of itinerant-electron ferromagnetism in UGe_2," *Nature*, vol. 406, no. 6796, pp. 587–592, 2000.

[179] A. D. Huxley, "Ferromagnetic superconductors," *Physica C: Superconductivity and its Applications*, vol. 514, pp. 368 – 377, 2015, superconducting Materials: Conventional, Unconventional and Undetermined.

[180] K. Kuwahara, T. Sakai, M. Kohgi *et al.*, "Elastic anomalies of UGe_2," *Journal of Magnetism and Magnetic Materials*, vol. 310, no. 2, pp. 362–364, 2007.

[181] P. Monthoux, D. Pines, and G. Lonzarich, "Superconductivity without phonons," *Nature*, vol. 450, no. 7173, pp. 1177–1183, 2007.

[182] A. Kornilov and V. Pudalov, "A spherical small-sized hydrostatic-pressure cell for measuring anisotropic galvanomagnetic effects," *Instruments and experimental techniques*, vol. 42, no. 1, pp. 127–129, 1999.

[183] H. Takahashi, K. Igawa, K. Arii *et al.*, "Superconductivity at 43K in an iron-based layered compound LaO1-xFxFeAs," *Nature*, vol. 453, no. 7193, pp. 376–378, 2008.

[184] A. B. Garg, V. Vijayakumar, and B. Godwal, "Electrical resistance measurements in a diamond anvil cell to 40GPa on ytterbium," *Review of scientific instruments*, vol. 75, no. 7, pp. 2475–2478, 2004.

[185] C. Gao, Y. Han, Y. Ma *et al.*, "Accurate measurements of high pressure resistivity in a diamond anvil cell," *Review of scientific instruments*, vol. 76, no. 8, p. 083912, 2005.

[186] L. Van der Pauw, "A method of measuring specific resistivity and hall effect of discs of arbitrary shape," *Philips Res. Rep*, vol. 13, pp. 1–9, 1958.

[187] T. Rikitake, *Magnetic and electromagnetic shielding*. Springer Science & Business Media, 1987.

[188] J. Heremans, C. H. Olk, and D. T. Morelli, "Magnetic susceptibility of carbon structures," *Phys. Rev. B*, vol. 49, pp. 15 122–15 125, Jun 1994.

[189] I. R. Walker, "Considerations on the selection of alloys for use in pressure cells at low temperatures," *Cryogenics*, vol. 45, no. 2, pp. 87 – 108, 2005.

[190] B. A. Jordan, "The development of an improved non-magnetic alloy based on the copper-beryllium system," *Journal of Materials Science*, vol. 4, no. 12, pp. 1097–1105, 1969.

[191] J. Kamarád, Z. Machátová, and Z. Arnold, "High pressure cells for magnetic measurements - destruction and functional tests," *Review of Scientific Instruments*, vol. 75, no. 11, pp. 5022–5025, 2004.

[192] *Beryllium Copper Alloys - Technical Guide.* NGK Berylco UK Ltd., 2014, vol. 1.

[193] J. J. Engelhardt, "Lattice parameters and superconductivity of the compounds U_6Mn, U_6Fe, U_6Co and U_6Ni and alloys between them," *Journal of Physics and Chemistry of Solids*, vol. 36, no. 3, pp. 123 – 126, 1975.

[194] E. Yamamoto, Y. Haga, A. Nakamura *et al.*, "Superconducting property of single crystal U_6Fe," *Physica B: Condensed Matter*, vol. 230–232, pp. 394 – 397, 1997, proceedings of the International Conference on Strongly Correlated Electron Systems.

[195] L. Dubrovinsky, N. Dubrovinskaia, I. A. Abrikosov *et al.*, "Pressure-induced invar effect in Fe-Ni alloys," *Phys. Rev. Lett.*, vol. 86, pp. 4851–4854, May 2001.

[196] A. Kussmann and K. Jessen, "INVAR-behaviour and magnetic moments of gamma-phase of iron-palladium alloys," *Journal of the Physical Society of Japan*, vol. 17, p. 136, 1962.

[197] J. R. Davis, "ASM specialty handbook: nickel, cobalt, and their alloys," *ASM International, Member/Customer Service Center, Materials Park, OH 44073-0002, USA, 2000. 442*, 2000.

[198] M. van Schilfgaarde, I. Abrikosov, and B. Johansson, "Origin of the invar effect in iron–nickel alloys," *Nature*, vol. 400, no. 6739, pp. 46–49, 1999.

[199] K. Lagarec, D. Rancourt, S. Bose *et al.*, "Observation of a composition-controlled high-moment/low-moment transition in the face centered cubic Fe-Ni system: Invar effect is an expansion, not a contraction," *Journal of Magnetism and Magnetic Materials*, vol. 236, no. 1–2, pp. 107 – 130, 2001.

[200] S. Khmelevskyi, I. Turek, and P. Mohn, "Large negative magnetic contribution to the thermal expansion in iron-platinum alloys: Quantitative theory of the Invar effect," *Physical review letters*, vol. 91, no. 3, p. 037201, 2003.

[201] N. Cowlam and A. Wildes, "A search for non-collinear ferromagnetism in INVAR," *Journal of Physics: Condensed Matter*, vol. 15, no. 3, p. 521, 2003.

[202] J. Buschbeck, I. Opahle, S. Fähler *et al.*, "Magnetic properties of Fe-Pd magnetic shape memory alloys: Density functional calculations and epitaxial films," *Physical Review B*, vol. 77, no. 17, p. 174421, 2008.

[203] D. Rancourt and M.-Z. Dang, "Relation between anomalous magnetovolume behavior and magnetic frustration in invar alloys," *Physical Review B*, vol. 54, no. 17, p. 12225, 1996.

[204] W. Stirling, R. Cowley, and M. Stringfellow, "Crystal dynamics of Pd_3Fe at 80K," *Journal of Physics F: Metal Physics*, vol. 2, no. 3, p. 421, 1972.

[205] B. Dutta, S. Bhandary, S. Ghosh *et al.*, "First-principles study of magnetism in Pd_3Fe under pressure," *Physical Review B*, vol. 86, no. 2, p. 024419, 2012.

[206] Y. Kvashnin, S. Khmelevskyi, J. Kudrnovskỳ *et al.*, "Noncollinear magnetic ordering in compressed $FePd_3$ ordered alloy: A first principles study," *Physical Review B*, vol. 86, no. 17, p. 174429, 2012.

[207] P. Franke and D. Neuschütz, *Binary systems. Part 3: Binary Systems from Cs-K to Mg-Zr: Phase Diagrams, Phase Transition Data, Integral and Partial Quantities of Alloys.* Berlin, Heidelberg: Springer Berlin Heidelberg, 2005, ch. Fe-Pd, pp. 1–5.

[208] P. Walker and W. H. Tarn, *CRC handbook of metal etchants.* CRC press, 1990.

[209] W. Whitley, C. Stock, and A. D. Huxley, "A laboratory-based Laue X-ray diffraction system for enhanced imaging range and surface grain mapping," *Journal of Applied Crystallography*, vol. 48, no. 4, pp. 1342–1345, 2015.

[210] P. Stetsenko and Y. Avksentev, "Hyperfine interactions in an ordering Pd3Fe alloy," *Sov Phys JETP*, vol. 33, no. 5, pp. 961–962, 1971.

[211] J. Mydosh, J. Budnick, M. Kawatra *et al.*, "Magnetic ordering in palladium-iron alloys," *Physical Review Letters*, vol. 21, no. 18, p. 1346, 1968.

[212] J. Cable, E. Wollan, and W. Koehler, "Atomic magnetic moments in dilute iron–palladium alloys," *Journal of Applied Physics*, vol. 34, no. 4, pp. 1189–1190, 1963.

[213] H. P. Wijn, *Magnetic properties of metals: d-elements, alloys and compounds.* Springer Science & Business Media, 2012.

[214] J. Crangle, "Ferromagnetism in Pd-rich palladium-iron alloys," *Philosophical Magazine*, vol. 5, no. 52, pp. 335–342, 1960.

[215] S. Pickart and R. Nathans, "Alloys of the first transition series with Pd and Pt," *Journal of applied physics*, vol. 33, no. 3, pp. 1336–1338, 1962.

[216] A. Men'shikov and V. Tsurin, "Influence of spin polarization on hyperfine interaction in iron–palladium alloys," *Phys. Met. Metallogr.*, vol. 47, no. 2, pp. 68–72, 1979.

[217] V. Tsurin, "Hyperfine interaction during ordering of alloy Pd3Fe," *Phys. Met. Metallogr.*, vol. 45, no. 3, pp. 82–88, 1978.

[218] M. Fallot, "The alloys of iron with metals of the platinum family," *Ann Phys*, vol. 10, pp. 291–332, 1938.

[219] J. Cable, E. Wollan, and W. Koehler, "Distribution of magnetic moments in Pd-3d and Ni-3d alloys," *Physical Review*, vol. 138, no. 3A, p. A755, 1965.

[220] T. F. Connolly, *Bibliography of magnetic materials and tabulation of magnetic transition temperatures.* Springer Science & Business Media, 2012.

[221] C. Bull, M. Guthrie, R. Nelmes *et al.*, "Time-of-flight single-crystal neutron diffraction to 10 GPa and above," *High Pressure Research*, vol. 29, no. 4, pp. 780–791, 2009.

[222] T. Strässle, S. Klotz, K. Kunc *et al.*, "Equation of state of lead from high-pressure neutron diffraction up to 8.9 GPa and its implication for the NaCl pressure scale," *Physical Review B*, vol. 90, no. 1, p. 014101, 2014.

[223] X. Wang, C. Chen, X. Huang *et al.*, "Acoustic and elastic properties of silicone oil under high pressure," *RSC Advances*, vol. 5, no. 48, pp. 38 056–38 060, 2015.

[224] D. D. Ragan, D. R. Clarke, and D. Schiferl, "Silicone fluid as a high-pressure medium in diamond anvil cells," *Review of scientific instruments*, vol. 67, no. 2, pp. 494–496, 1996.

[225] J. Ruiz-Fuertes, D. Errandonea, R. Lacomba-Perales *et al.*, "High-pressure structural phase transitions in $cuwo_4$," *Phys. Rev. B*, vol. 81, p. 224115, Jun 2010.

[226] J. Binns, K. V. Kamenev, G. J. McIntyre *et al.*, "Use of a miniature diamond-anvil cell in high-pressure single-crystal neutron Laue diffraction," *IUCrJ*, vol. 3, no. 3, pp. 168–179, May 2016.

[227] K. Komatsu, K. Munakata, K. Matsubayashi *et al.*, "Zr-based bulk metallic glass as a cylinder material for high pressure apparatuses," *High Pressure Research*, vol. 35, no. 3, pp. 254–262, 2015.

[228] R. L. Mills and E. Grilly, "Melting curves of He^3, He^4, H_2, D_2, Ne, N_2, and O_2 up to 3500 kg/cm^2," *Physical Review*, vol. 99, no. 2, p. 480, 1955.